Microstructured Bubbling Bed: Hydrodynamics and its Application in Flotation

Ritesh Prakash

Microstructured Bubbling Bed: Hydrodynamics and its Application in Flotation

THESIS

Submitted in Partial Fulfillment of the

Requirements for the Degree of

Doctor of Philosophy

in

Engineering

by

Ritesh Prakash

Roll No.: 156107030

Under the supervision of

Prof. Subrata Kumar Majumder

And

Prof. Anugrah Singh

DEPARTMENT OF CHEMICAL ENGINEERING

INDIAN INSTITUTE OF TECHNOLOGY GUWAHATI

GUWAHATI - 781039, INDIA

April 2021

DEPARTMENT OF CHEMICAL ENGINEERING
INDIAN INSTITUTE OF TECHNOLOGY GUWAHATI
GUWAHATI-781039, INDIA

DEPARTMENT OF CHEMICAL ENGINEERING

CERTIFICATE

This is to certify that the thesis entitled "**Microstructured bubbling Bed: Hydrodynamics and its Application in Flotation**" submitted by Ritesh Prakash in fulfillment of the requirement of the Degree of Doctor of Philosophy in Engineering, is a record of bonafide research work carried out by him, in the Department of Chemical Engineering, Indian Institute of Technology, Guwahati, under my guidance and supervision. The work documented in this thesis has not been submitted to any other University or Institute for the award of any degree or diploma. In my opinion, the thesis has reached the standard fulfilling the requirements of the Ph.D. degree as prescribed in the regulations of this institute.

Prof. Subrata Kumar Majumder
Professor
Department of Chemical Engineering
Indian Institute of Technology Guwahati
Guwahati – 781039, Assam , India

Prof. Anugrah Singh
Professor
Department of Chemical Engineering
Indian Institute of Technology Guwahati
Guwahati – 781039, Assam , India

ACKNOWLEDGEMENTS

I would like to express my gratitude to all those who helped me in different ways in completing this research work, directly or indirectly. First and foremost, I would like to express my deep felt gratitude to my supervisor, **Prof. Subrata Kumar Majumder** and **Prof. Anugrah Singh**, for providing me continuous inspiration and guidance throughout the entire course of work. In addition, their philosophical guidance has built up a momentum inside me. Their uncompromising approach to complete the experimental part, data analysis, writing manuscripts as well as thesis within the stipulated time period helped me a lot in completing my research work. The numerous brainstorming sessions during the project meetings with him were very useful in enriching my analytical power. I also remain indebted for their understanding, support, and caring during the times when I was really down and depressed due to personal problems. I also thank almighty for making me feel fortunate to work under their great stewardship.

I wish to acknowledge my respectful thanks to **Prof. Bishnupada Mandal**, former HOD, and **Prof. Anugrah Singh,** present HOD, Department of Chemical Engineering, for extending all the necessary facilities for carrying out my research work. I am also grateful to all the faculties in the department for their sincere cooperation.

I must also thank my doctoral committee members **Prof. Pallab Ghosh**, **Prof. Tapas Kumar Mandal** of the Department of Chemical Engineering, and **Dr. Amresh Dalal** of the Department of Mechanical Engineering, for their valuable suggestions and contribution towards my research work.

Last but not least, I wish to thank all the non-teaching staff of our department for the help received from them.

I would like to thank my co-researchers and friends Mr. Adhwarshu Bhattacharya, Mr. Jaspreet Singh Gaga, Mr. Sumit Kumar, Mr. Manisankar Majumder, Mr. Bongliba T. Sangtam, Mr. Kalicharan Hembrom, Mr. Bharath Kumar Goshika, Mr. Fahad M.K, Mr. Somen Mondal, Mr. Rupam Sinha, Mr. Bitang Kwrung Tripura, Mr. Kuldeep Roy, Mr. Pyarimohan Dehuri, Mr. Vikas Bindu Das, Miss. Surabhi Patel, Miss. Smita Medhi, Mr. Gaurav Singh, Mr. Babban Maurya, Mr. Santosh Deb Barma, Mr. Madhav P. Chavan, Mr. Manish Kumar for their enormous help and

support during research work. I would also like to express my gratitude to the former doctorate student, Dro. Rajeev Parmar for his suggestion during the research work. I am thankful to all my departmental friends, seniors, and juniors for their support and good wishes.

I would also like to thank my family, who have not only supported me in the completion of my Ph.D. but also have stood by me throughout my life. They have patiently supported me at all instances in my research work.

Ritesh Prakash

Date: 6th April, 2021

Place: IIT Guwahati

Brief Biodata

Name:	**Ritesh Prakash**
Date of Birth:	**25/12/1989**
Email:	**iit.ritesh@gmail.com**
Phone:	**+91-8638406349 or +91-9002497298**

Education

Ph.D. pursuing
Department of Chemical Engineering Indian, Institute of Technology Guwahati, Guwahati - 781039, Assam, India

M. Tech
Department of Chemical Engineering Indian, Institute of Technology Kharagpur, Kharagpur - 721302, West Bengal, India
2013 – 2015

B. Tech
Department of Chemical Engineering Indian, Institute of Technology Guwahati, Guwahati - 781039, Assam, India
2007 – 2011

Senior School Certificate Examination
Kendriya Vidyalaya BSF Meru Hazaribagh, Jharkhand, India
2004 – 2006

Secondary School Examination
Doon Public School Koyla Nagar, Dhanbad Jharkhand, India
2004

Awards and Scholarships

- Awarded 2nd position in poster presentation in Research Conclave, held during 14 – 17 March, 2019 at Indian Institute of Technology Guwahati, Assam, India.
- Awarded 2nd position in 7th National Science Olympiad, held on December 2, 2004, Kendriya Vidyalaya, Hazaribagh, Jharkhand, India.
- National Master Fellowship, Full-tuition scholarship with stipend awarded by MHRD, Jul 2013 – June 2015
- National Doctoral Fellowship, Full-tuition scholarship with stipend awarded by MHRD, Jul 2015 – July 2020.

List of Publications

- **Prakash, R.**, Majumder, S. K., & Singh, A. (2020). Bubble-slurry interfacial shear stress and frictional pressure drop in a rectangular column in the presence and absence of a surface-active agent, *Powder Technology*, *366*, 761 – 775. https://doi.org/10.1016/j.powtec.2020.03.015
- **Prakash, R.**, Majumder, S. K., & Singh, A. (2020). Dispersion characteristics in a counter-current microstructured slurry bubble column and its analysis based on the turbulence and circulation, *Industrial & Engineering Chemistry Research*, *59*, 8093 – 8111. https://doi.org/10.1021/acs.iecr.0c00834
- **Prakash, R.**, Majumder, S. K., & Singh, A. (2020). Bubble size distribution and specific bubble interfacial area in two–phase microstructured dense bubbling bed, *Chemical Engineering Research and Design*, *156*, 108 – 130. https://doi.org/10.1016/j.cherd.2020.01.032
- **Prakash, R.**, & Majumder, S. K. (2020). Effect of particle size and concentration on bubble size distribution and aspect ratio in a counter-current microstructured bubble column, *Journal of Industrial and Engineering Chemistry*, *90*, 105 – 116. https://doi.org/10.1016/j.jiec.2020.07.002
- **Prakash, R**., & Majumder, S. K. (2020). Experimental Investigation and its Analysis of Gas Holdup in a Three-phase Counter-current Microstructured Bubble Column. *Journal of Dispersion Science and Technology*, 42 (1), 1 – 16. DOI: 10.1080/01932691.2020.1839480
- **Prakash, R.**, Majumder, S. K., & Singh, A. (2019). Particle-laden bubble size and its distribution in microstructured bubbling bed in presence and absence of a surface active agent, *Industrial & Engineering Chemistry Research*, *58*, 3499 – 3522. https://doi.org/10.1021/acs.iecr.8b05625
- **Prakash, R.**, Majumder, S. K., & Singh, A. (2018). Flotation technique: Its mechanisms and design parameters. *Chemical Engineering and Processing-Process Intensification*, *127*, 249 – 270. https://doi.org/10.1016/j.cep.2018.03.029
- **Prakash, R.**, Majumder, S. K., & Singh, A. (2018). Gas holdup and frictional pressure drop contributions in microstructured two-and three-phase bubbling bed with Newtonian

and non-Newtonian liquids: Effect of coarse and fine particles with surface active agent. *Chemical Engineering and Processing-Process Intensification*, *133*, 40 – 57. https://doi.org/10.1016/j.cep.2018.09.020

Other Publications

- Sangtam, B.T., **Prakash, R**., & Majumder, S. K. (2020). Drop Sizes and Its Distribution in Jet-driven Liquid-Liquid Mixing Column: Substantial Application for the Liquid-Liquid Extraction Process. Chemical Engineering Research and Design. https://doi.org/10.1016/j.cherd.2021.02.029
- **Prakash, R.**, & Majumder, S. K. (2017). Analysis of particle recovery in flotation column based on information entropy theory, *Transactions of the Indian Institute of Metals*, *70*(2), 403 – 410. DOI 10.1007/s12666-016-0994-5
- Fahad, M. K., **Prakash, R.**, Majumder, S. K., & Ghosh, P. (2020). Dispersion characteristics in a gas–liquid–coal slurry flotation column and its analysis by the velocity distribution model, *Journal of Dispersion Science and Technology*, 1 – 15. https://doi.org/10.1080/01932691.2020.1737105
- Fahad, M. K., **Prakash, R.**, Majumder, S. K., & Ghosh, P. (2019). Gas holdup in the gas-liquid-coal slurry flow in a flotation column in presence of surface active agent, *Multiphase Science and Technology*, *31*(*3*), 199 – 214. DOI: 10.1615/MultScienTechn.2019029957
- Fahad, M. K., **Prakash, R.**, Majumder, S. K., & Ghosh, P. (2019). Frictional pressure drop in a flotation column: an experimental investigation in continuous mode and its prediction by a general model, *Multiphase Science and Technology*, *31*(*3*), 235 – 254. DOI: 10.1615/MultScienTechn.2019031051

Manuscript under Review

- **Prakash, R.**, & Majumder, S. K. (2020). Quality of Mixedness Using Information Entropy in a Counter-current Three-phase Bubble column. *Chemical Engineering & Technology* (Manuscript ID: ceat.202000241) DOI: 10.1002/ceat.202000241

Manuscript under Preparation

- **Prakash, R.**, Majumder, S. K & Singh, A. (2021). An analysis of mass transfer studies in a two-phase microstructured bubble column in the presence of different surfactants. (under preparation)
- **Prakash, R.**, Hembrom, K., Barma, S. D., Majumder, S. K., & Singh, A. (2021). Particle Recovery and its modelling and kinetic study in a microstructured column. (under preparation)
- Prakash, R., Hembrom, K., Majumder, S. K., & Singh, A.. Coal beneficiation using flotation technique. (under preparation)
- Sangtam, B. T., **Prakash, R**., & Majumder, S. K. Mixing Characteristic of Liquid-Liquid Dispersion in Jet-driven Mixing Column Developed for Separation of Organic Pollutants. (under preparation)
- Fahad, M. K., **Prakash, R**., Majumder, S. K., & Ghosh, P. Kinetics of Recovery of Fine Coal Particles by Flotation: Experiments and Modeling. (under preparation)
- Fahad, M. K., **Prakash, R**., Majumder, S. K., & Ghosh. P Effect of Different Variables on the Entrainment of Coal Particles in a Flotation Column. (under preparation)
- Fahad, M. K., **Prakash, R**., Majumder, S. K., & Ghosh Bubble size and its distribution in a coal slurry flotation column in the presence of surface active agent and its analysis by modelling. (under preparation)

Publication in Conference

- **Prakash, R.** & Majumder S K, 2013. Quality of mixing and its effect on particle separation in a flotation column, *26th International Mineral Processing Congress (IMPC)*, *Mineral Processing: Innovative Processing for Sustainable Growth*, *6*, 3107-3116.

Conferences

- **Prakash, R**., Sangtam, B. T., Barma, S. D., Hembrom, K., Majumder, S. K. and Singh, A. Bubble size analysis in a Two-phase Counter-current flow in the 2-D column, Fluid Mechanics and Fluid Power (FMFP), at Proceedings of the 8th International and 47th National Conference on Fluid Mechanics and Fluid Power (FMFP) December 9-11, 2020, IIT Guwahati, Guwahati-781039, Assam, India.

- **Prakash, R**., Majumder, S. K., and Singh, A., 2020. A study of bubble size and its distribution in a flotation column, RECYCLE 2020, 3rd international conference on waste management held during 13 – 14 February at Indian Institute of Technology Guwahati, Assam, India.
- **Prakash, R**., Majumder, S. K., and Singh, A., 2020. Dispersion characteristics in a counter-current three-phase column. International Conference on Advances in Chemical Engineering (AdChE), held during February 5 – 7 at Department of Chemical Engineering, University of Petroleum and Energy Studies (UPES), Dehradun, Uttarakhand, India.
- **Prakash, R.**, Majumder, S.K., Singh, A., 2019. Dispersion characteristics in a microstructured slurry bubble column. *First National Student Conference on "Advances in Chemical Engineering",* Department of Chemical Engineering, Assam Engineering College (TEQIP III), Guwahati, Assam, India.
- **Prakash, R**., Majumder, S. K., and Singh, A., 2019. Particle laden bubble size distribution in a microstructured slurry bubble column, Research Conclave, held during 14 – 17 March at Indian Institute of Technology Guwahati, Assam, India.
- **Prakash, R**., Majumder, S. K., and Singh, A., 2018. Pressure drop characteristics in presence of solid particle, Research Conclave held during 8 – 11 March at Indian Institute of Technology Guwahati, Assam, India.
- **Prakash, R**., Majumder, S. K., and Singh, A., 2018. Gas holdup and bubble size distribution in microstructured flotation column, XVII International Seminar on Mineral Processing Technology (MPT) held during 10 – 12 October at Indian Institute of Technology (ISM) Dhanbad, India.
- **Prakash, R**., Majumder, S. K., and Singh, A., 2017. Hydrodynamic characteristics in microstructure flotation column (MFC). Mineral Processing Technology (MPT) held during February 1 – 3 at Mahabalipuram, Chennai, India.
- **Prakash, R**., Majumder, S. K., and Singh, A., 2017. Bubble size & its distribution in presence of solid particle, Research Conclave held during 16 -19 March at Indian Institute of Technology Guwahati, Assam, India.

Abstract

Gas-slurry three-phase flow in the slurry bubble column has wide applications in the field of chemical, biochemical, petrochemical (Kim et al., 2017; Orvalho et al., 2018), metallurgical (Leonard et al., 2015), and wastewater treatment (Bartrand et al., 2009). Slurry bubble columns are advantageous to use due to the ease of thermal control, the high interfacial contact between the phases, the low-pressure drop, the good productivity, the low construction cost, and the effective heat and mass transfer coefficients (Barghi et al., 2004; Kim et al., 2014). Despite various advantages, their design and scale-up are not well understood due to the complex interaction of the phases (i.e., gas, liquid, and solid). Experimental studies in the slurry bubble column were largely conducted in semi-batch and co-current mode operation. Comparatively, few studies have been conducted in a counter-current mode (Trivedi et al., 2018). Substantial backmixing of the phases (both liquid and gas) is common in the cylindrical slurry bubble column (Shah et al., 2012). The efficiency of the slurry bubble column is affected by the degree of recirculation and the backmixing of the phases. Backmixing is known to increase drastically as the local liquid circulation develops. The most important changes occur in fluid mechanics when the geometry of the column changes from cylindrical to rectangular. Therefore, one of the most important factors in the design of the slurry bubble column is the effect of the geometric configuration on the flow behavior of the fluid. The rectangular column with considerable length and width, but with a small depth can be considered as the microstructured column. The small depth can be helpful in suppressing the backmixing and circulation of the phases, and can provide a uniform bubble size distribution.

The present study focuses on some of the important hydrodynamic characteristics and particle recovery in a three-phase counter-current microstructured column. Based on the literature survey and scope of the research, the following objectives of the work under this main objective are formulated as to study:

- Gas Holdup Characteristics and its Analysis
- Frictional Pressure Drop and Bubble-Slurry Interfacial Shear Stress
- Bubble Size Distribution and Bubble Aspect Ratio
- Dispersion Characteristics and its Analysis
- Particle Recovery in Microstructured Column

Chapter 2 reports the in-depth investigation of gas holdup in the three-phase counter-current system. This chapter is dedicated to studying the influence of superficial gas velocity, superficial slurry velocity, particle size, and particle concentration on gas holdup in a three-phase counter-current microstructured bubble column with and without surfactant. Slip velocity model was used to analyze the gas holdup characteristics. Correlations were also suggested for the gas holdup and slip velocity model parameters, taking into account the operating variables and the physical properties of the system.

Chapter 3 introduces the effect of different variables such as particle concentration, average particle size, slurry, and gas velocity on the gas-slurry interfacial shear stress and the frictional pressure drop. A mechanistic model is proposed based on the energy balance of gas and slurry flow by considering the energy dissipation rate because of bubble formation, the energy dissipation rate because of a slip of gas-slurry interface, and energy dissipation rate because of the wetting of a thin liquid layer with the column wall.

Chapter 4 aims to explore the effect of superficial gas and superficial slurry velocities, particle concentration, and particle size on the bubble size distribution (BSD) and bubble aspect ratio in a counter-current microstructured slurry column in the presence and absence of the surfactant. In addition, empirical correlations were also proposed for the Sauter mean bubble diameter and bubble size distribution function parameters as a function of the operating and physical properties of the system. An attempt was also made to develop a correlation for the aspect ratio based on the important dimensionless groups.

Chapter 5 aimed to study the mixing characteristics in the three-phase counter-current column. The effect of particle concentration, particle size, superficial gas, and slurry velocities on the axial and transverse dispersion coefficient, the dispersion due to circulation, the dispersion due to bubble motion, and the velocity distribution characteristic factor are analyzed in the presence of surfactant. An interpretation of the intensity of dispersion based on the liquid circulation and turbulence are also given. The velocity distribution model was also applied to analyze the dispersion of bubble motion in the column.

Chapter 6 analyze the particle separation efficiency of the microstructured column. The cleaning of coal samples has been reported in a microstructured column to understand the effects of various parameters such as collector concentration and surfactant doses, gas velocity and feed velocity on

the combustible recovery, the ash content in concentrate, yield, efficiency index, and induction time. An attempt was also made to optimize the reagent doses, and gas and feed velocity. The phenomenological kinetic model based on the consecutive sub-processes compromising of the bubble-particle collision, attachment, and detachment was used to enunciate the induction time. The present research will be useful for the process intensification of three-phase counter-current flow.

Contents

List of Figures

Chapter 1

Chapter 2

Chapter 3

Chapter 4

Chapter 5

Chapter 6

List of Tables

Chapter 2

Chapter 3

Chapter 4

Chapter 5

Chapter 6

Chapter 1

Background and Formulation of Research Work

1.1. Introduction

Three-phase columns are widely used in various industries such as coal beneficiation (Han et al., 2014), petrochemical (Kim et al., 2017; Orvalho et al., 2018), biochemical (Shaikh and Al-Dahhan, 2007), wastewater treatment (Bartrand et al., 2009) and chemical industries (Li and Prakash, 2000), etc. Three-phase columns are multiphase contactors wherein a gas phase is dispersed in the form of a bubble in a continuous slurry phase (Leonard et al., 2015). Three-phase columns are advantageous to use due to the ease of thermal control, the high interfacial contact between the phases, the low-pressure drop, the good productivity, the low construction cost, and the effective heat and mass transfer coefficients (Barghi et al., 2004; Kim et al., 2014). There are three modes of operation in the three-phase column, namely, semi-batch, co-current, and counter-current depending on the application. Despite several studies of hydrodynamic characteristics of the circular and rectangular columns, there is a lack of understanding of the hydrodynamic behavior (Götz et al., 2016; Kantarci et al., 2005; Kumar and Khanna, 2014). Hence, the correct interpretation of the design parameters is essential for the proper design, operation, modeling, control, scale-up, and optimization of a processing unit (Prakash et al., 2018a; Sheikhi et al., 2013). The complex nature of multiphase flow in the three-phase column is the result of the fluid flow that is affected by numerous design parameters. The three-phase columns are simple in construction; however, its scale-up is complicated because of the lack of adequate information on hydrodynamic characteristics (Barghi et al., 2004; Jakobsen et al., 2005; Prakash et al., 2018b). According to the literature, most of the experiments have been performed in the cylindrical column, in which the substantial backmixing of phase pccurs (both liquid and gas) (Shah et al., 2012), which reduces the process efficiency, decreases the overall performance of the system. The microstructured column (2D with very small width) can be useful to reduce the backmixing of the phases.

1.2. Design Parameters

Understanding of design parameters such as gas holdup characteristics, bubble size distribution, frictional pressure drop, and mixing characteristics is important for the enunciation of process efficiency of any column. The design parameters are dependent on each other. The in-depth analysis of the design parameters and the variables affecting it was discussed chapter wise. Different parameters and variables affecting the column performance are shown in Fig. 1.1.

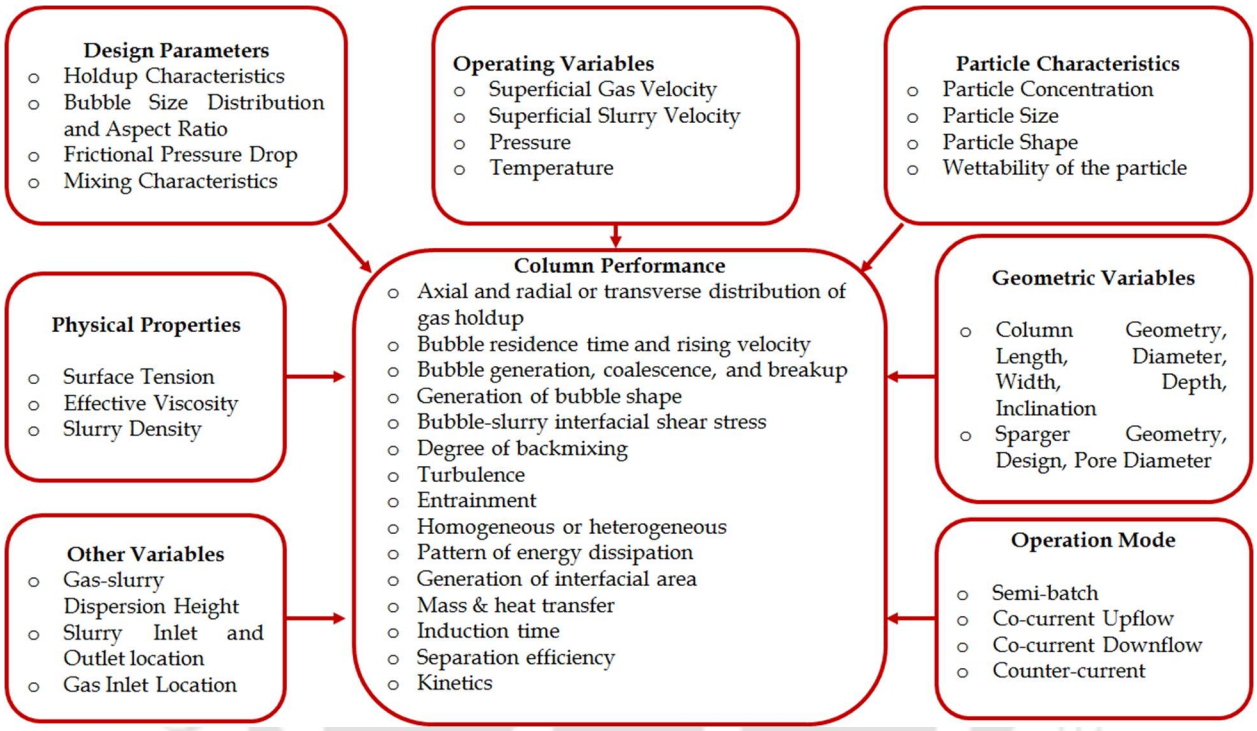

Fig. 1.1 Variables and parameters that affect the column performance.

The gas holdup can be expressed as the fraction of the volume occupied by the gas phase in the total volume of the two or three-phase mixture in the column. Gas holdup depends on bubbles, the local flow velocity, the presence of backmixing flow, and the rising velocity of the bubbles (Xia et al., 2011). The presence of internals also enhances the gas holdup charcteristics of a bubble column (Manjrekar et al., 2018). In the flotation process, the desired recovery is highly dependent on the gas holdup and flow regime. Particle and liquid residence time cannot be estimated without the knowledge of the gas holdup. Particle recovery is also dependent on gas flow rate and bubble diameter, both of which influence the gas holdup. Finch et al. (2000) observed a linear relationship between the bubble surface area flux and the gas holdup for different operating variables. There is a linear relationship between the flotation rate constant and gas holdup (Massinaei et al., 2009). Vinnett et al. (2016) reported an imaging technique to measure the local gas holdup in the flotation

process. This technique is based on the model structure, which is a function of the percent area occupied by gas bubbles in the binary images and the superficial gas velocity. Images were obtained using a bubble viewer, and over 250 bubble images were typically analyzed to obtain the correct percentage approximations of the area. The model structure was capable of measuring the gas holdup in the range of 2.5 to 15% in the laboratory column and 6.0 to 21.0% in the industrial column. Li et al. (2017b) studied the gas holdup in the presence of Carboxymethyl cellulose (CMC) and sodium dodecyl sulfate with nitrogen as the gas phase. They observed that the gas holdup increased with increasing superficial gas velocity and decreased with increasing CMC concentration. Bhunia et al. (2017) investigated the effect of the particle on gas holdup. The experimental result showed that the gas holdup decreased in the presence of the particle. This reduction was more on increasing the particle concentration and the presence of smaller particles resulted in a moderately higher gas holdup compared to larger particles. Particle addition increases the slurry viscosity as a result coalescence behavior of the gas bubble increases, contributing to a reduction in gas holdup. There are several methods available to measure the gas holdup. Some of the existing methods for measurement of the gas holdup are phase isolation technique, volume expansion technique, conductivity (Gomez et al., 2003), pressure drop (Tavera et al., 2001), electrical resistance tomography (Kumar et al., 1997; Vadlakonda and Mangadoddy, 2018; Veera and Joshi, 1999), dynamic gas disengagement (Sriram and Mann, 1977), an optical probe (Bakshi et al., 1995), γ ray densitometry (Shollenberger et al., 1997), etc. Measurement of gas holdup using pressure sensor required several pressure sensor and it cannot be used if the density of the liquid and solid is more or less same (Sines et al., 2019). The phase isolation technique is one of the simplest and most widely accepted techniques for measuring the gas holdup (Bhunia et al., 2017). Due to the limitation in the physical size of the sensors and sophisticated instrumentation, other techniques make the measurement of gas holdup tedious. Other techniques require sophisticated instrumentation and limitation on the physical size of the sensors is inadequate to estimate the gas holdup. In this work, the phase isolation technique is used to measure the gas holdup characteristics.

The interfacial area available for the adhesion of the particles to the gas bubble characterizes the separation efficiency of the system, which helps in the design, and scale-up of the system. High slurry concentration causes bubble coalescence, as a result small bubbles significantly reduced in number. Larger bubbles are practically independent of the gas velocity for solid holdup (> 0.05)

and gas velocity (> 0.1 m/s). The interfacial area directly affects the rate constant of the separation process (Gorain et al., 1997). The interfacial area depends on the bubble size, gas holdup, superficial gas velocity (Gomez and Finch, 2007), gas distributor design, physico-chemical properties of the phases, and column geometry (Camarasa et al., 1999). Smaller bubbles coalesce to form a larger bubble, decreasing the interfacial area for the bubble-particle collision, which causes a reduction in attachment probability of particle on the bubble and thus decreases the separation efficiency. Bubble formation process governs the initial bubble size and the rising velocity controls the contact time between the phases, which affects the interfacial transport process and mixing characteristics (Kulkarni and Joshi, 2005). Smaller and a stable bubble size can be obtained with decreasing surcae tendion and viscosity and increasing gas density at high pressure and high temperature (Schäfer et al., 2002). Since a decade, numerous intrusive and non-intrusive techniques are invented to measure the bubble sizes. Some of the methods like photographic technique Mie scattering technique (Hansen, 1985), Bayesian magnetic resonance technique (Holland et al., 2012), Coulter count method or pore electrical resistance method (Fujiwara, 2007), dynamic gas disengagement technique (Vadlakonda and Mangadoddy, 2017), acoustic (Kracht and Moraga, 2016), phase Doppler anemometry (Meng et al., 2016), drift flux analysis (Bhunia et al., 2017) is used to estimate the bubble size. Photographic technique is one of the simple techniques used to measure the bubble diameter. The high-speed camera captures the generated bubbles. The column wall should be transparent, so that the high-speed camera can capture the bubbles. A light source can be placed to get a clear picture of the bubbles. The captured images are analyzed by the image processing software to estimate the bubble size. Through this technique, the scale of the bubbles will be determined by manually identifying and marking each of the bubbles. Photographic technique is limited to resolve large bubble clusters (Besagni and Inzoli, 2016a) and captures only the bubbles located near the column wall.

Pressure drop determines the flow energy requirement for transporting fluids in the multiphase system. The notion of pressure drop provides the energy dissipation pattern, that allows to model and assesses the performance of the system (Majumder, 2016). The high flow rate or high viscosity contributes to a higher-pressure drop while a low flow rate lowers or no pressure drop.

Flow in columns never obeys the ideal flow pattern. The non-ideal behavior is due to (i) channel formation, (ii) recycling of fluid, (iii) vortices and turbulence at inlet and outlet of the vessel, (iv)

bypassing and short-circuiting of the fluid, and (v) formation of the dead zone at the corner of the vessel. The amount of time spent by the molecule in the vessel is called the residence time of the molecule. It is obvious that the different particles use different routes to pass through the column, takes a different amount of time, and due to this, there will be the distribution of residence time of the molecules within the vessel. The distribution of length of time spent by different molecules within the vessel is called the residence time distribution (RTD) or exit age distribution (E).

The simplest way to study the mixing phenomena is to detect the tracer particles during experimentation and analyze it using any suitable dispersion model. Tracer can be detected using both offline and inline techniques. The offline technique involves UV-absorption (Reitz et al., 2013), color intensity (Mu and Thompson, 2012), and radioactive radiation (Janssen et al., 1979), etc. The offline technique results in a gap between the actual process and the measured time. The product quality must be checked and controlled in real-time. In the inline technique, the inline probe associated with the data acquisition system directly detects and records the thermal, optical, and electrical signals of the tracer particles. This technique requires high-speed data sampling frequency and signal conversion (Gao et al., 2012). In the case of a radioactive tracer, the RTD can be determined by a non-invasive sensor located at the outlet of the vessel (Yianatos et al., 2005). The most frequently used liquid dispersion technique is residence time distribution (RTD), which is also a conductive detection technique or tracer technique (de Andrade Lima, 2006) based on the difference in electrical conductivity of the tracer particles and bulk flow.

The tracer technique is one of the simple methods to measure RTD (de Andrade Lima, 2006). The tracer should be non-reactive, should not be adsorbed to the vessel wall or other surfaces of the vessel, its physical property should be similar to the system, should be easily detectable, should be completely soluble in the system fluid. The pulse and step input methods are widely used for the RTD measurements. In the pulse input, the tracer is injected with feed at the time ($t = 0$) and the tracer concentration is measured at the outlet of the vessel as a function of time.

Mixing and dispersion are attributed to the pulp recirculation and turbulence of bubble and slurry motion in a three-phase system. Mixing affects the particle suspension, the generation of fine bubbles, and dispersion and, consequently, a bubble-particle collision takes place (Yianatos et al., 2005). Dispersion number is influenced by the bubble size, bubble number, particle settling velocity, slurry rate, collection zone height, and diameter of the column (Weijenberg et al., 2000).

The degree of mixing can be estimated using the residence time distribution (RTD) technique. The variation of gas holdup radially or axially induces pressure variation and is also responsible for the liquid circulation, and the back mixing of the phases (Majumder, 2016). Liquid circulation directs the rate of mixing and separation efficiency of the flotation process. Mills et al. (1992) examined the mixing characteristics using the RTD technique and concluded that the axial dispersion model controls the flow structure. The author claimed that the axial dispersion model is superior to other models dealing with a column diameter of 0.1 m to 1.5 m. To model the small-diameter column, either a dispersion model or tank in series model can be used. The particle dispersion coefficient is more than the liquid dispersion coefficient, and the particle dispersion coefficient increases with an increase in particle concentration in the laboratory test column, but remains unaltered in large columns (Mills et al., 1992). The intensity of axial mixing increases with the increase in the column diameter (Baird and Rice, 1975). The mixing of phases inside the flotation column significantly affects the bubble-particle attachment and bubble-particle detachment process.

1.3. Operation mode of columns

In a vertical column, there are primarily four modes of operation, namely: (i) semi-batch mode, (ii) co-current downflow, (iii) co-current upflow, and (iv) counter-current mode. Modes of operation are used for industrial purposes as per the requirement. In semi-batch mode, the slurry is in batch mode while the gas is in continuous mode. The direction of gas flow is upwards. In the co-current downflow column, both gas and slurry are in continuous mode, and the flow direction of both phases is downward. In the co-current upflow mode, the gas, and slurry flow continuously, and the flow direction of both phases are in the upward. In the case of the counter-current mode, both phases flow continuously, and the direction of gas flow is upward, and the flow of slurry is opposite to the gas phase. In the counter-current mode, the slurry inlet may be located at the top of the column or from the side of the column (at 2/3 height of the column from the base). If the slurry is introduced at the side of the column, it significantly disturbs the flow field, and it becomes tedious to interpret the hydrodynamic characteristics. Moreover, side slurry inlet also does not provide the actual realization of the influence of counter-current behavior on hydrodynamic characteristics. Therefore, in the present study, all the hydrodynamic characteristics have been carried out by taking the slurry inlet at the top of the column. In the case of enunciation of particle separation efficiency, the slurry inlet position is taken from the side of the column at 2/3 height

from the column base. The side inlet does not hinder the carrying capacity of particle-laden bubbles to the top of the column. Different operating modes in the vertical column are shown in Fig. 1.2.

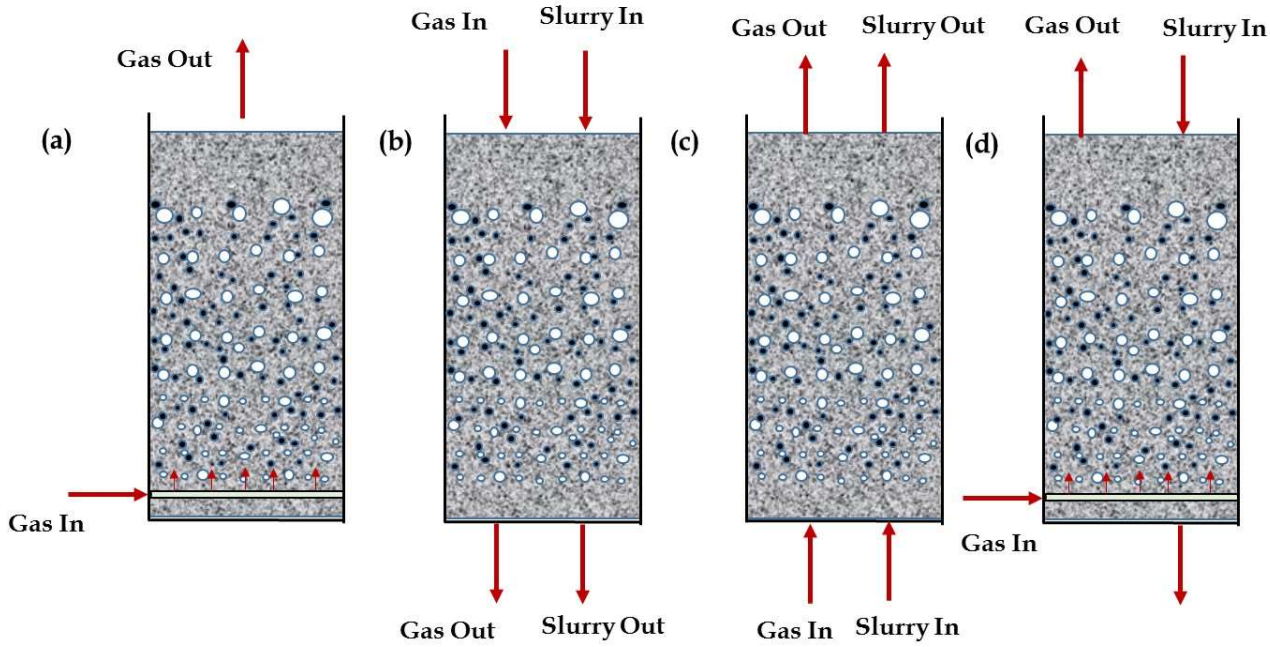

Fig. 1.2. Operation mode in vertical columns.

1.4. Map of three-phase slurry column

The three-phase flow columns are categorized into three classes, namely; the gas-sparged slurry column, the three-phase bubble column, and the three-phase fluidized bed as a function of the density difference between the particle and the fluid and the diameter of the particles (Tsutsumi et al., 1999). Fig. 1.3 represents the classification map of the three-phase flow column where published literature data and experimental data are plotted, and all data are categorized into three classes. The boundaries between the class *A* and class *B* sections, and class *B* and class *C* sections are indicated by two firm lines. The present study is based on class A, which is referred to as the gas-sparged slurry column.

Fig. 1.3. Classification map of three-phase flow columns (Tsutsumi et al., 1999). (a) Class A: gas-sparged slurry column, (b) Class B: three-phase bubble column, (c) Class C: the three-phase fluidized bed. (Copyright material)

1.5. Scope of the research work

The complex nature of multiphase flow in the three-phase column is the outcome of the fluid movement that is caused by numerous design parameters. Hence, the correct interpretation of the design parameters is essential for the proper design, operation, modeling, control, scale-up, and optimization of a processing unit (Sheikhi et al., 2013). The three-phase flow columns are simple in construction; however, the scale-up technique is complicated because of the lack of adequate information on hydrodynamic characteristics (Barghi et al., 2004; Jakobsen et al., 2005). Despite various advantages, their design and scale-up are not well understood due to the complex interaction between phases (i.e., gas, liquid, and solid).

Many industrial columns are subjected to low productivity or poor product quality because of the substantial backmixing of phases, the non-homogeneous bubble size distribution, the reduction in

interfacial area, the short residence time of bubbles, and irregular flow regime. Substantial backmixing of the phases (both liquid and gas) is common in the cylindrical column (Shah et al., 2012). The efficiency of the column is affected by the degree of recirculation and the backmixing of the phases. The backmixing has a negative effect on conversion and selectivity in many chemical reaction applications (Ekambara and Dhotre, 2010; Schmidt, 1998), mainly when intermediates are the desired products (Gao et al., 2012). Backmixing is known to increase drastically as the local liquid circulation develops (Cao et al., 2008). The most important changes occur in fluid mechanics when the geometry of the column changes from cylindrical to rectangular. Therefore, one of the most important factors in the design of the three-phase column is the effect of the geometric configuration on the flow behavior of the fluid. To offset these issues, a rectangular column (typically, with a considerable length (approximately 21 times of depth) and width (approximately 6.34 times of depth), but with a very small in depth) can be used to reduce the backmixing of the phases, channeling, the degree of bubble coalescence, and uneven distribution of gas bubbles. The small depth of the column helps to reduce the backmixing of the phases.

As per the literature review, it has been noticed that the none of the in-depth work in the microstructured column has been performed, which reflect the cumulative influence of the operating variables, physical properties of the system, and geometric variables on the hydrodynamic characteristics and separation efficiency in the presence and the absence of the surfactant. Therefore, the present work takes the task of an in-depth investigation of hydrodynamic characteristics in the microstructured slurry column.

1.6. Goal of the study

The primary goal of the present study is to enunciate the hydrodynamic characteristics of the three-phase flow in a microstructured column in the counter-current operating mode. Under this goal, the following components of the study are defined as objectives.

- Gas Holdup Characteristics and its Analysis
- Frictional Pressure Drop and Bubble-Slurry Interfacial Shear Stress
- Bubble Size Distribution and Bubble Aspect Ratio
- Dispersion Characteristics and its Analysis

- Particle Recovery in Microstructured Column

1.7. Thesis Organization

To understand the hydrodynamic behavior of the three-phase system (gas-liquid-solid) and the application for separation of particles, the present study has been organized as follows:

Chapter 1: Introduction

This chapter provides an overarching view of the background of the research study, a description of the three-phase columns, the interdependency of the design parameters, modes of operation, motivation, research gap, the scope of the research work, objectives, and thesis organization.

Chapter 2: Gas Holdup Characteristics

This chapter reports the in-depth investigation of gas holdup in the three-phase counter-current system. Gas holdup of the system governs the intensity of contact among the phases based on the mixing of the phases. As per literature, the study of gas holdup characteristics in a three-phase counter-current column is limited and not comprehensive. Most of the work was done with the two-phase flow in co-current mode. Only one publication is available that provides evidence of a gas holdup study in the three-phase counter-current mode in the presence of surfactant. Therefore, the purpose of this work is to study the influence of superficial gas velocity, superficial slurry velocity, particle size, and particle concentration on gas holdup in a three-phase counter-current microstructured bubble column with and without surfactant. Slip velocity model was used to analyze the gas holdup characteristics. Correlations were also suggested for the gas holdup and slip velocity model parameters, taking into account the operating variables and the physical properties of the system.

Chapter 3: Frictional Pressure Drop and Bubble-slurry Interfacial Shear Stress

This chapter introduces the effect of different variables such as particle concentration, average particle size, slurry, and gas velocity on the gas-slurry interfacial shear stress and the frictional pressure drop. A mechanistic model is proposed based on the energy balance of gas and slurry flow by considering the energy dissipation rate because of bubble formation, the energy dissipation rate because of a slip of gas-slurry interface, and energy dissipation rate because of the wetting of a thin liquid layer with the column wall.

Chapter 4: Bubble Size Distribution and Aspect Ratio

Knowledge of bubble size and aspect ratio are of paramount importance to enunciate the interfacial area and degree of uniformity of gas-phase distribution. It controls the residence time of the bubble in the column and influences the separation efficiency based on the probability of bubble-particle collision, attachment, and detachment. The interfacial area available for the particle adhesion characterizes the separation efficiency of the system, which helps in the design, and scale-up of the column. This chapter aims to explore the effect of superficial gas and superficial slurry velocities, particle concentration, and particle size on the bubble size distribution (BSD) and bubble aspect ratio in a counter-current microstructured slurry column in the presence and absence of the surfactant. In addition, empirical correlations were also proposed for the Sauter mean bubble diameter and bubble size distribution function parameters as a function of the operating and physical properties of the system. An attempt was also made to develop a correlation for the aspect ratio based on the important dimensionless groups.

Chapter 5: Mixing Characteristics

This chapter aimed to study the mixing characteristics in the three-phase counter-current column. The effect of particle concentration, particle size, superficial gas, and slurry velocities on the axial and transverse dispersion coefficient, the dispersion due to circulation, the dispersion due to bubble motion, and the velocity distribution characteristic factor are analyzed in the presence of surfactant. An interpretation of the intensity of dispersion based on the liquid circulation and turbulence are also given. The velocity distribution model was also applied to analyze the dispersion of bubble motion in the column.

Chapter 6: Particle Recovery

The last objective of the present work is to analyze the particle separation efficiency of the microstructured column. The cleaning of coal samples has been reported in a microstructured column to understand the effects of various parameters such as collector concentration and surfactant doses, gas velocity and feed velocity on the combustible recovery, the ash content in concentrate, yield, efficiency index, and induction time. An attempt was also made to optimize the reagent doses, and gas and feed velocity. The phenomenological kinetic model based on the

consecutive sub-processes compromising of the bubble-particle collision, attachment, and detachment was used to enunciate the induction time.

Chapter 7: Overall Conclusions, Limitations, and Future Recommendations

This chapter provides the overall conclusions, limitations, and future recommendations based on the present research in the three-phase microstructured column. This chapter highlighted the details of the hydrodynamic characteristics of two- and three-phase flow in the microstructured column. However, further works are required to have a complete idea in this field for proper designing, optimization, control, and scale-up of the column. Thus, possible recommendations for future research work in this system are summarized in this section.

Chapter 2

Gas Holdup and its Analysis

Abstract

In this chapter, the investigation of the gas holdup is reported in a three-phase counter-current microstructured bubble column with and without the presence of surfactant. The coal (specific gravity 1.4) was taken to prepare slurry (a mixture of water and coal), and Methyl Isobutyl Carbinol (MIBC) was used as a surfactant. The effects of the superficial gas velocity (i.e., air, u_{sg} = 0.011 – 0.075 m/s) and superficial slurry velocity (i.e., slurry, 0.018 - 0.057 m/s), particle concentration (i.e., 0.5 – 3.0 wt.%), and particle size (i.e., 63.01 – 517.0 μm) on gas holdup are studied. The gas holdup is analyzed with a slip velocity model. A novel correlation has been developed to predict the gas holdup and slip velocity model parameters.

Publication: Prakash, R., & Majumder, S. K. (2020). Experimental Investigation and its Analysis of Gas Holdup in a Three-phase Counter-current Microstructured Bubble Column. Journal of Dispersion Science and Technology, 42 (1), 1 – 16. DOI: 10.1080/01932691.2020.1839480

Prakash, R., Majumder, S. K., & Singh, A. (2018). Gas holdup and frictional pressure drop contributions in microstructured two-and three-phase bubbling bed with Newtonian and non-Newtonian liquids: Effect of coarse and fine particles with surface active agent. Chemical Engineering and Processing-Process Intensification, 133, 40 – 57. https://doi.org/10.1016/j.cep.2018.09.020

2.1. Introduction

Slurry bubble columns are extensively used in numerous applications in the fields of petrochemical (Gandhi et al., 1999b), biochemical (Shaikh and Al-Dahhan, 2007), chemical (Li and Prakash, 2000), and mineral beneficiation (Han et al., 2014) industries, etc. Slurry bubble columns are multiphase systems in which gas bubbles are introduced in a batch or continuous slurry phase (Leonard et al., 2015). Slurry bubble columns are operated in three distinct modes, viz., semi-batch, co-current, and counter-current. Several authors have reported hydrodynamic studies such as gas holdup in semi-batch slurry bubble column (Banisi et al., 1995b; Barghi et al., 2004; Gandhi et al., 1999b; Kim et al., 2014; Li et al., 2013; Ojima et al., 2014; Orvalho et al., 2018; Vadlakonda and Mangadoddy, 2018), semi-batch two-phase (Anastasiou et al., 2010; Azgomi et al., 2007; Kim et al., 2017; Li et al., 2017b), two-phase co-current (Rollbusch et al., 2015), three-phase co-current (Kumar and Khanna, 2014; Kumar et al., 2012), two-phase counter-current (Besagni et al., 2014; Besagni and Inzoli, 2017a, b; Trivedi et al., 2018), and three-phase counter-current mode (Bahri et al., 2013; Bhunia et al., 2017; Luewisutthichat et al., 1997; Shukla et al., 2010).

Enunciation of gas holdup helps in construction, scale-up, and efficiency evaluation of the slurry and flotation columns. Therefore, it is crucial to have a clear knowledge of the factors influencing the gas holdup in the slurry system. The current work, therefore, mainly focuses on the impact of the different operating variables and the physical properties of slurry on gas holdup in the counter-current slurry bubble column.

As per the literature, the majority of the experiments were conducted in the cylindrical column, renowned for extensive phase bacmixing (Shah et al., 2012), which reduced the transport efficiency of the column. The presence of the particle has a noteworthy influence on the hydrodynamic characteristic of a slurry bubble column. In the literature, several researchers have proposed a different hypothesis to clarify the impact of particles on gas holdup. Several authors have also clarified that the introduction of particle activates the bubble coalescence (Ojima et al., 2015) and contributes to a reduction in the gas holdup (Banisi et al., 1995b; Kuan and Finch, 2010; Lakhdissi et al., 2019; Mokhtari and Chaouki, 2019; Sarhan et al., 2018c). The increase in the bubble wake entrainment, the variation in radial holdup characteristics, and the flow profile reduces the average gas holdup in the column (Banisi et al., 1995a). Nevertheless, some researchers have suggested that gas holdup improves with the addition of particles (Fan et al., 2007; Mena et

al., 2005; Pandit and Joshi, 1984; Sada et al., 1986b). The cause for the enhancement in gas holdup is: (i) bubble breakup owing to the interaction of the particles (Yang et al., 2007), (ii) the attachment of the particles to the surface of the gas bubble upsurges the cumulative weight of the bubble-particle, thus lowers the velocity of the bubble (Tsutsumi et al., 1991; Uribe-Salas et al., 2003) and (iii) changes in the density and viscosity of the slurry (Kluytmans et al., 2001). The significant increase in the density and viscosity of the slurry around the gas bubble decreases the rising velocity of the gas bubbles and enhances the gas holdup (Kluytmans et al., 2001). The dual effect of particle concentration is reported by Mena et al. (2005). They noticed a substantial rise in the gas holdup upto a particle concentration of 5.0 vol. %, further exceeding the particle concentration above 5.0 vol. %, the gas holdup decreases substantially. The dual influence of particle concentration is attributed to the two opposing processes, stabilizing, and destabilizing the three-phase system (Mena et al., 2005). The addition of small particles (less than 10 μm) enhances the gas holdup at very low particle concentration, and the particle concentration with particle size greater than 50 μm leads to reduce the gas holdup (Sada et al., 1986b). According to Gandhi et al. (1999b), the addition of particle (at 40% vol.) reduces the bubble breakup rate; thus, the gas holdup decreases. Bińet al. (2001) reported that the gas holdup decreases in semi-batch and co-current mode, whereas it increased in counter-current mode. The change in gas holdup for counter-current and co-current operation was approximately 10%. Other researchers have also reported a similar trend (Jin et al., 2010; Uchida et al., 1989). Ityokumbul et al. (1995) observed the negligible change in a gas holdup with particle concentration, except near the sparger surface where the bubble coalescence probability is greater and the authors obtained the same results with the surfactant. A decrease in a gas holdup in the presence of the particle (0 −15% v/v) was observed by Banisi et al. (1995b). Vazirizadeh et al. (2016) reported the effect of two different particle particles: quartz (hydrophilic) and talc (hydrophobic), on gas holdup and bubble size distribution in the presence of the polyglycol surfactant. The presence of particles affects the gas holdup as; (i) it causes bubble breakup. Hence, the gas holdup increases (Yang et al., 2007), (ii) increases coalescence behavior of bubble which decreases gas holdup (Banisi et al., 1995b; Kuan and Finch, 2010), (iii) it enhances bubble wake entrainment so gas holdup decreases (Banisi et al., 1995b), (iv) it increases the apparent viscosity of the fluids leading to a decrease in gas holdup (Banisi et al., 1995b; Finch and Dobby, 1990), and (v) the particles attached to the bubble increases the weight of the bubble causing reduction in rising velocity leading to increase in the gas holdup (Tsutsumi et al., 1991;

Uribe-Salas et al., 2003). The effect of the particles, particle size, and particle concentration at the high gas temperature of a helium-water-alumina system was studied by Abdulrahman (2016). A decrease in gas holdup was observed by the addition of particles since the increase in slurry viscosity leads to promote the generation of substantial size gas bubbles while the breakup efficiency of the bubble reduces due to the reduction of instabilities at interfaces. Large bubbles have greater rise velocity and low residence time in the column, which leads to the reduction of the gas holdup. It was also observed that the effect of a change in the particle size on gas holdup was negligible. According to Abdulrahman (2016), the effect of particle size on the gas holdup was trivial. However, smaller particle size has a reasonably more gas holdup compared to the larger particle size (Bhunia et al., 2017). The same effect was found in both the presence and absence of surfactants in the system. The effect of large particles compared to the small is less significant because the smaller particle does not cause coalescence, but promote bubble breakup. According to Uribe-Salas et al. (2008), the rise velocity of bubble-particle aggregate increases as the bubble size increases. The viscosity of the slurry increases by lowering the particle size at a certain slurry concentration due to attractive particle concentration (Kawatra and Eisele, 1988a; Senapati et al., 2009; Shukla et al., 2008; Yoshida et al., 2013; Zhou et al., 1993). Banisi et al. (1995b) illustrated that particle concentration also stabilizes the bubble wake and bubble swarm velocity due to increased viscosity of the slurry. It causes an increase in the rising velocity of trailing bubbles due to inline bubble-bubble interaction. Kara et al. (1982) performed the experiment in batch mode and observed a reduction of the gas holdup with an increase in particles concentration and particle size. There was no significant difference observed in gas holdup characteristics of air-water and air-water-particle system when the particle size of 10 μm was used. However, the three-phase system indicated slightly larger gas holdup than two-phase in the presence of 10 μm particle. Khare and Joshi (1990) analyzed the enhancement in a gas holdup with an increase in particle size and particle concentration up to 67 μm and 0.6 vol.% respectively. A further increase in particle size and particle concentration causes a decrease in the gas holdup.

Characteristics of the sparger also play an important role in the estimation of the gas holdup. In a porous plate gas sparging media, the gas holdup tends to increase by 30% with a particle concentration of 0.1 wt.%, but the same trend of increase in gas holdup was not observed with perforated plate sparger (Sada et al., 1986b). An increase in particle concentration influences the viscosity and density of the system due to no-slip conditions on each particle (Mena et al., 2005).

It causes extra velocity gradient resulting in an increase of viscous dissipation and reduction in the rising velocity of the gas bubble. According to Luo et al. (1997), the mutual collision of bubbles and particles and hydrodynamic forces play a major role in decreasing the rising velocity of the bubbles.

Gas holdup study in the three-phase semi-batch 2D column (width × depth × height = 0.24 m × 0.04 m × 1 m) was studied by Hooshyar et al. (2010b). They noticed a 15% reduction in a gas holdup in a heterogeneous flow regime after the introduction of glass beads. Another study reported by Kluytmans et al. (2001) in semi-batch 2D slurry column (width × depth × height = 0.30 m × 0.015 m × 2.0 m) shows considerable enhancement in gas holdup with electrolyte (sodium gluconate) and particles (carbon particles, d_p = 30 μm, concentration 0.1 - 1.0 g/L). The enhancement in gas holdup is explained by three different mechanisms: (i) changes in the surface tension of the slurry with the electrolyte and the carbon particles, (ii) effect of particle wettability and ionic forces, and (iii) changes in the viscosity and density of the slurry. Stabilization and destabilization of the bubbles are due to the development of a layer of particles or electrolytes around the bubble, which either promotes or hinders the rate of bubble coalescence. The influence of wettable and non-wettable particles is demonstrated by Jamialahmadi and Müller-Steinhagen (1991). The wettable particles repel the gas bubbles interfaces, act as a buffer between gas bubbles, and hinder the coalescence, while the non-wettable particles have contradictory influence. Marrucci (1969) examined the mechanism of bubble coalescence for two approaching bubbles in the electrolyte solution and suggested that the presence of the ionic forces tends to reduce the film drainage speed between the two approaching gas bubbles. As a result, the coalesce rate reduces, and gas holdup enhances. In a 2D semi-batch slurry bubble column, the gas holdup was independent of slurry concentration (below 0.4 vol.%), and beyond 0.4 vol.% concentration, it decreases significantly (Ruthiya et al., 2006). The average gas holdup in the semi-batch 2D slurry bubble column shows a significant reduction in gas holdup as the particle concentrations increases in the range of 0 – 38.6 vol.% in paraffin oil slurry. The reduction in gas holdup was due to the depletion of the small bubbles (less than 10 mm) population.

Several investigators have demonstrated the influence of particle size on gas holdup (Kim et al., 1987; Mena et al., 2005; Ojima et al., 2015; Sarhan et al., 2018c). As per the literature, research on the impact of particle size on gas holdup is scarce and unclear. Some researchers have reported

a decrease (Sarhan et al., 2018c), while others have shown an increase (Banisi et al., 1995a) in the gas holdup. Fan et al. (1999) have reported a marginal impact of particle size on gas holdup. Gas holdup study in a semi-batch microstructured slurry bubble showed that the gas holdup is slightly higher for the large particle (d_p: 408.31 μm) than that of the small particle (d_p: 242.72 μm) (Prakash et al., 2018b). Kim et al. (1987) analyzed the impact of particle size (glass beads, d_p: 17 - 5000 μm) on gas holdup in the volume fraction range of 0 to 20 vol.% in co-current operation. The particle size in the range of 44 – 254 μm has an insignificant effect on gas holdup characteristics (Luo et al., 1999). Rabha et al. (2013a) demonstrated that a particle size less than 100 μm (at a concentration of < 3% by weight) had an insignificant impact on hydrodynamic behavior. They noticed a significant reduction in the gas holdup with larger particle diameter and particle concentration. A similar trend has been shown by other researchers, who illustrated that the gas holdup reduces as the particle size increases (Jamialahmadi and Müller-Steinhagen, 1991; Kim et al., 1987). So far, studies of gas holdup in the co- and counter-current mode in the two- and three-phase columns have been presented in Table 2.1.

Table 2.1 Summary of gas holdup studies in co- and counter-current mode in the two- and three-phase system.

System	Experimental condition	Sparger type and its characteristics	Measurement Technique	Operating mode	Remarks and correlation	Author
Gas: air, liquid: water, solid: none	u_{sg}: 0 – 0.06 m/s, u_l: 0.0035 – 0.0105 m/s, d_c: 0.159 m, h_c: 3.90 m, T: 298.15 K, P: 0.1 MPa, w_s : 0 wt.%	Perforated stainless steel plate (d_0: 2 mm, d_n: 200)	Pressure drop measurements	Co-current and counter-current	α_g increase with an increase in the gas velocity.	Eissa and Schügerl (1975)
Gas: air, liquid: water, mineral oil, solid: none	u_{sg}: 0 – 0.05 m/s, u_l: 0 – 0.017 m/s, d_c: 0.1016, 0.1397 m, h_c: 1.524, 2.134 m, P: 0.1 MPa, T: 298.15 K, w_s : 0 wt.%	Porous plate (d_0: 0.0017 mm), annular shear sparger (d_0: 0.002 mm), Membrane sparger	Differential pressure and volume expansion technique	Counter-current	Increasing the water jet velocity enhanced the α_g. The transition from the homogeneous to the heterogeneous flow regime was delayed in the shear sparger. No effect of column diameter on α_g observed.	Smith et al. (1996)
Gas: N_2, N_2/CO_2 mixture, liquid: water and aqueous solution of DEA+ ETG, solid: none	u_{sg}: 0 – 0.06 m/s, u_l: unknown, d_c: 0.156 m, h_c: 0.64 m, P: 0.1 – 7.0 MPa, T: 298.15 K, w_s : 0 wt.%	Perforated plate (d_0; 0.4 mm, d_n: 284)	Phase isolation	Counter-current	α_g increases with u_{sg}.	Stegeman et al. (1996)

Gas: Cyclohexane, Water, liquid: N_2 and CO_2, solid: none	u_{sg}: up to 0.14 m/s, u_l: up to 0.008 m/s, d_c: 0.2 m, h_c: 1.6 m, P: 0.1 MPa, T: 293.15 K, w_s : 0 wt.%	Toroidal gas spargers (d_0: 0.5 and 1 mm)	Differential pressure transducer	Co-current	A diminution in sparger d_0 contributes to a minor improvement in α_g at low u_{sg} and does not affect the heterogeneous regime. The α_g decreases as u_{sl} increases.	Chaumat et al. (2005)
Gas: air, liquid: water, solid: none	u_{sg}: 0.02 – 0.25 m/s, u_l: 0 – 0.011 m/s, d_c: 0.16 m, h_c: 2.5 m, P: 0.1 MPa, T: 295.15 K, w_s : 0 wt.%	Perforated plate (d_0: 1 mm, d_n: 55)	Electrical resistance tomography	Co-current	The u_l slightly influence the α_g and radial α_g distribution and the u_l can improve the transition u_{sg} for homogeneous to the heterogeneous regime. $\alpha_g = 1.042\, u_{sg}^{0.523} \left(\frac{h_c}{d_c}\right)^{-0.096}$	Jin et al. (2007)
Gas: air, liquid: water, solid: none	u_{sg}: 0.02 – 0.25 m/s, u_l: 0 – 0.011 m/s, d_c: 0.16 m, h_c: 2.5 m, P: 0.1 MPa, T: 295.15 K, w_s : 0 wt.%	Perforated plate (d_0 : 1 mm, d_n: 55)	Electrical resistance tomography	Counter-current	The α_g slightly increases with increasing downward u_l. The α_g in counter-current operation is more than batch and co-current mode. Meanwhile, the radial α_g profile becomes steeper in the central region of the column with a rise in the u_{sg}. Besides, the α_g in the center of the column becomes is steeper with increasing u_l. $\alpha_g = 0.9u_{sg}^{0.503}\left(\frac{h_c}{d_c}\right)^{-0.047} + 0.050u_l^{0.289}$	Jin et al. (2010)
Gas: air, liquid: water,	u_{sg}: 0.013 – 0.1628 m/s, u_l: 0 – 0.1604	Perforated plate (d_0: not given)	Differential pressure transducer	Co-current	For the semi-batch operation, the h_l did not affect the α_g. The α_g increases with an increase in u_{sg} for	Kumar et al. (2012)

solid: glass beads	m/s, d_c: 0.15 m, h_c: 2.72 m, h_l: 1 – 1.8 m, P: 0.1 MPa, T: 298.15 K, w_s : up to 9%, ρ_p: 2500 kg/m^3				both two and three-phase co-current columns. With an increase in w_s for co-current bubble column the α_g slightly increases or remains constant up to 5% concentration; beyond this concentration, there is a significant decrease in α_g.	
Gas: air, N_2, liquid: water, aqueous solution of polyethylene glycol, solid: none	u_{sg}: 0.021 – 0.1025, u_l: 0.0005 – 0.002 m/s, d_c: 0.29 m, h_c: 2 m, P: 0.1 MPa, T: 298.15 K, w_s : 0 wt.%	Perforated plate (d_0: 0.5 mm)	Hydrostatic pressure difference	Counter-current	The α_g increases with u_{sg}. At low u_{sg} (bubbly flow regime), the effect of the u_{sg} on α_g is more pronounced than at high u_{sg} (churn-turbulent regime). The α_g decreases as u_l increases. The α_g is more affected by the u_{sg} than the u_l. $\alpha_g = 0.072\left(\frac{u_{sg}^2}{gd_c}\right)^{0.5}\left(\frac{u_l^2}{gd_c}\right)^{-0.018}\left(\frac{g\rho_l^3 d_c^3}{\mu_l^2}\right)^{0.087}$	Shah et al. (2012)
Gas: O_2 and N_2, liquid: water, solid: none	u_{sg}: 9.44 × 10^{-5} – 6.61 × 10^{-4} m/s, u_l: 4.72 × 10^{-3} – 14.15 × 10^{-3} m/s, d_c: 0.15 m, h_c: 1 – 2 m, h_l: 0.5 – 1.850 m, P:	Single orifice (d_0 : 16 mm)	Phase isolation	Co-current	The value of α_g for the micro-bubbles slightly increased with increasing u_{sg} in the range of (u_{sg} < 5 × 10^{-4} m/s), then decreased with increasing u_{sg} in the range of (u_{sg} > 5 × 10^{-4} m/s). The values of α_g were not affected by the h_l.	Muroyama et al. (2013)

	0.1 MPa, T: 298.15 K, w_s : 0 wt.%					
Gas: O_2 and N_2, liquid: water and aqueous solution of ethanol (0.5 wt%), solid: none	u_{sg}: 0 – 0.15 m/s, u_l: 0 – 0.091 m/s, d_c: 0.1016 m, h_c: unknown, h_m: 1.8 m, P: 0.1 – 9.0 MPa, T: 297.15 K, w_s : 0 wt.%	Perforated plate (d_0: 3.175 mm, d_n: 23)	Differential pressure transmitter	Co-current	Increased u_{sg} resulted in higher α_g. Maximum local α_g was at the center of the column (r/R = 0). Bubble residence time in the column was shortened at the higher u_l.	Pjontek et al. (2014)
Gas: air, liquid: water, solid: none	u_{sg}: 0.046 – 0.206 m/s, u_l: 0.021 – 0.2 m/s, d_c: 0.10 m, h_c: 1.6 m, T: 298.15 K, P: 0.1 MPa, w_s : 0 wt.%	Not available	Gamma-ray densitometry	Co-current, counter-current and batch	The α_g increased with the u_{sg} for all modes of operation. The increases in α_g with increasing u_{sg} in the case of a semi-batch bubble column are greater than the co-current up-flow. The α_g decreased with the increasing u_l in co-current mode, while increases in the counter-current mode.	Hernandez-Alvarado et al. (2016)
Gas: air, liquid: water, aqueous solutions of sodium chloride, solid: none	u_{sg}: 0.004 – 0.23 m/s u_l: – 0.0846 m/s d_c: 0.24 m, h_c: 5.3 m, T: 295 K, P: 0.1 MPa, w_s : 0 wt.%	Spider-gas distributor (d_0: 2 – 4 mm)	Bed expansion	Batch and counter-current	In counter-current mode, α_g is higher and the homogeneous flow regime is destabilized. The existence of electrolytes enhances the α_g and stabilizes the homogeneous flow regime. The α_g decreases continuously when increasing the aspect ratio to the critical aspect ratio (AR = 5). Beyond AR = 5, there is no	Besagni et al. (2017a)

					noticeable change that appeared in the α_g values.	
Gas: air, liquid: water, aqueous ethanol solution (0.5 wt.%), solid: none	u_{sg}: 0 – 0.105 m/s, u_l: 0 – 0.107 m/s, d_c: 0.1016 m, h_c: 1.8 m, P: 0.1 – 6.5 MPa, T: 295.15 – 297.15 K, w_s : 0 wt.%	Perforated plate (d_0: 3.175 mm, d_n: 23)	Differential pressure transmitter and dynamic gas disengagement	Co-current	Elevated pressure and surfactant addition increases α_g.	Parisien et al. (2017)
Gas: air, liquid: water, solid: none	u_{sg}: 0.0023 – 0.0717 m/s, u_l: 0 – 0.0714 m/s, d_c: 89 mm, h_c: 1.85 m, T: 298.15 K, P: 0.1 MPa, w_s : 0 wt.%	Sintered glass disc (d_0: 0.04 – 0.09 mm)	Pressure drop	Counter-current	An increase in u_{sg} causes the α_g to increase throughout all the regimes because of an increase in bubble population in the column. The α_g increases with an increase in u_l.	Trivedi et al. (2018)
Gas: air, liquid: water, solid: coal, sphalerite	u_{sg}: 0.0063 – 0.0276 m/s, u_{sl}: 0.0106 – 0.0276 cm/s, d_c: 0.1 m, h_c: 1.68 m, c_s: 0 – 100 kg/m^3, surfactant (MIBC, c_f: 0 – 10 ppm)	ceramic porous sparger (d_0: 0.0009 – 0.0015 mm)	Phase separation or volume expansion	Counter-current	An almost linear increase in α_g with increasing u_{sg}. Pronounced reductions in α_g have been observed by increasing the particle concentration. The α_g in the case of sphalerite slurry is lower compared to the coal slurry. The smaller particle size shows slightly higher α_g with and without surfactant.	Bhunia et al. (2017)

Based on the above literature study, it is observed that the study of gas holdup in a three-phase counter-current bubble column is limited and not comprehensive. Most of the work was done with the two-phase flow in semi-batch and co-current mode. Therefore, the purpose of the current research is to investigate the influence of superficial gas and slurry velocities, particle size, and particle concentration on gas holdup in a three-phase counter-current microstructured bubble column with and without surfactant. Moreover, correlations are suggested for the gas holdup and slip velocity model parameters, taking into account the operating variables and the physical properties of the system.

2.2. Experimental facility

2.2.1. Description of the experimental setup

Fig. 2.1a displays the graphical description of the experimental setup. The experimental study was conducted in a Perspex sheet column of 0.63 m length, 0.19 m width, and 0.03 m depth. Atmospheric air, water, and coal are the gas, liquid, and solid phase, respectively. The experiments were conducted in counter-current mode at ambient pressure (1 atm) and room temperature (298.15 K). Throughout all experiments, the slurry dispersion level was kept at the height of 0.49 m. Air and slurry flow rate were measured with an air rotameter (Deluxe Industrial gases, range: 0 – 40 L/min) and an electromagnetic flowmeter (Adept Fluidyne, MagFlow 6410, range: 0 – 15 L/min, accuracy: ± 0.5%), respectively. Gas phase was distributed into the column by a stainless steel porous cylindrical sparger with a pore diameter of 20 μm, supplied by TFI Filtration, India, as depicted in Fig. 2.1b. The air flow was regulated by a needle valve. Three solenoid valves (quick closing valves) were used to quickly stop the flow of phases for the determination of gas holdup by the phase isolation technique. The ranges of superficial gas and slurry velocities, particle concentration, and particle size were 0.011 – 0.075 m/s, 0.018 – 0.057 m/s, 0.5 – 3.0 wt.%, and 61.30 – 517.0 μm, respectively. Methyl Isobutyl Carbinol (MIBC) was used as a surfactant (provided by Tokyo Chemical Industry Corporation Limited).

Fig. 2.1. (a) 3-D view of microstructured slurry column, (b) experimental setup: legends- 1. microstructured column, 2. Slurry inlet solenoid valve, 3. Electromagnetic flow meter, 4. Slurry bypass valve, 5. Slurry pump, 6. Storage tank, 7. Stirrer, 8. Slurry outlet control valve, 9. Slurry outlet solenoid valve, 10. Air rotameter, 11. Gas inlet solenoid valve, 12. Needle valve, 13. Compressor air control valve, 14. Compressor, 15. Light source, (c) image of sintered porous sparger (average pore diameter, 20 μm). (Copyright material)

2.2.2. Physical properties

Einstein (1906) equation was used to determine the effective slurry viscosity (μ_{eff}). The effective viscosity of slurry at a particle concentration of up to 1% by weight was determined using Eq. (2.1)

$$\mu_{eff} = \mu_l(1+2.5\alpha_s) \tag{2.1}$$

where μ_l is the liquid viscosity and α_s is the particle holdup. Thomas (1965) equation was used to estimate the slurry viscosity for a particle concentration higher than 1.0 wt.%

$$\mu_{eff} = \left(1+2.5\alpha_s+10.05\alpha_s^2\right)\mu_l \tag{2.2}$$

The particle density was 1400 kg/m^3. Four different particle fractions (< 150, 150 – 300, 300 – 425, and 400 – 600 µm) and particle concentrations (0.5, 1.0, 2.0, and 3.0) were taken for the experiments. The average particle sizes for particle fractions < 150, 150 – 300, 300 – 425, and 400 – 600 were 61.30 µm, 257.289 µm, 408.31 µm, and 517 µm, respectively. The average particle size was estimated using a laser particle size analyzer (make: Malvern, model: Master sizer 2000). A typical graph of the distribution of particle size is displayed in Fig. 2.2a. The particle shape was obtained by a field emission scanning electron microscope (FESEM) (make: Carl Zeiss, model: GeminiSEM 300). A typical image of the particle shape is illustrated in Fig. 2.2b.

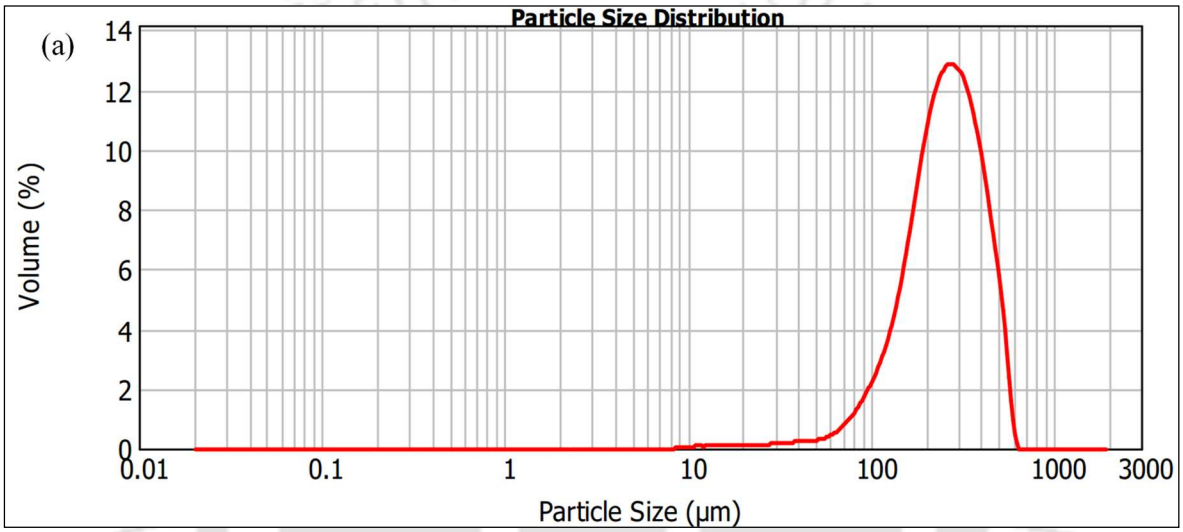

Fig. 2.2. (a) Particle size distribution (obtained by LPSA, for d_p = 257.289 μm) and (b) shape of the coal particles (obtained by FESEM, for d_p = 257.289 μm).

The particle holdup in the column was calculated using the following equation

$$\alpha_s = \frac{(m_s / \rho_s)}{(A_c h_m)} \tag{2.3}$$

where ρ_s, m_s, A_c, and h_m signify the particle density, mass of the particle, column cross-sectional area, and gas-slurry dispersion height, respectively. Slurry density (ρ_{sl}) was determined according to the Eq. (2.4)

$$\rho_{sl} = \frac{100}{w_s / \rho_s + (100 - w_s) / \rho_l} \tag{2.4}$$

where w_s is the particle concentration by weight (%) and ρ_l is the liquid density. Tensiometer (Make: M/s Kwoya, Japan, Model: DY300) was used to calculate the surface tension of the. The physical properties of the slurry (without surfactant) are given in Table 2.2. In the presence of surfactant, there is no appreciable change in the physical properties (i.e., slurry density and effective viscosity) of the slurry observed, except for the surface tension. The surface tension of the slurry in the presence of the surfactant is given in Table 2.3.

Table 2.2 Physical properties of the slurry without surfactant.

Material	Average particle diameter, d_p (μm)	Particle concentration, w_s (wt. %)	Slurry density, ρ_{sl} (kg/m^3)	Effective viscosity, $\mu_{eff} \times 10^4$ (Pa.s)	Surface tension, $\sigma_{sl} \times 10^3$ (N/m)
Slurry	242.72	0.5	1001.10	8.04	73.53
		1.0	1002.52	8.11	73.75
		2.0	1005.32	8.25	74.42
		3.0	1008.08	8.39	75.79
Water	–	–	999.68	7.97	69.95
Air	–	–	1.18	0.18	–

Table 2.3 Surface tension of slurry in the presence of surfactant.

Average particle diameter, d_p (μm)	Surface tension, $\sigma_{sl} \times 10^3$ (N/m)

	w_s (wt.%)	w_s (wt. %)	w_s (wt. %)	w_s (wt. %)
	0.5	1.0	2.0	3.0
65.29	72.30	72.49	73.33	74.17
242.72	70.87	71.22	71.93	72.63
408.31	69.00	70.93	71.87	72.80
517	70.33	70.66	70.93	71.20

2.2.3. Phase isolation technique

The gas holdup is expressed as the ratio of the volume of the gas phase to the total volume of the gas-liquid-solid mixture. The average gas holdup (α_g) of the system was calculated using the phase isolation technique, which is given by

$$\alpha_g = \frac{(h_m - h_l)}{h_m} \tag{2.5}$$

where h_m and h_l denote the gas-liquid-solid mixture height and slurry height, respectively. The scale was attached at the side of the column along with the axial height. During the operation, when the system reaches the steady-state, the image of the gas-slurry dispersion height at different time intervals was captured using the digital camera (Sony, DSC-H300). After capturing the image, the gas and slurry inlet and slurry outlet were suspended at a time using the solenoid valves installed in the pipelines, as displayed in Fig. 2.1b. As the inlet and outlet of slurry and gas flow are stopped, then the slurry level allows coming down as the gas phase escapes from the top side of the column, and the image of the clear slurry level was captured again using the digital camera. The same procedure was repeated for three-times for each experimental condition to obtain the average gas holdup. The ranges of uncertainties associated with the gas holdup are reported in Table 2.4.

2.2.4. Slip velocity model

In a counter-current operation, the important surface force acting on the interface of the gas-slurry flow is the interphase drag force. The prime reason for the interphase drag force is the slip between the gas and the slurry flow that takes place in the direction opposite to the slip velocity (Nagarajan et al., 2016). The slip velocity and the superficial gas velocity is (+) when moving in the direction

of the buoyancy, while the superficial slurry velocity is considered as (–) when the flow direction is opposite to the direction of buoyancy. For the counter-current operation, the slip velocity is expressed as

$$u_s = \frac{u_{sg}}{\alpha_g} + \frac{u_{sl}}{(1-\alpha_g)} \tag{2.6}$$

In a counter-current system, the interaction between the bubbles slows the rising velocity of bubbles, which can be considered as the multi-particle system. For this multi-particle effect, the slip velocity can be expressed as

$$u_s = k(1-\alpha_g)^n \tag{2.7}$$

where n and k can be evaluated by fitting the experimental data. As per Vinaya and Varma (1996), k does not have to be the rise velocity of the bubbles. Lapidus and Elgin (1957) have shown the interaction between bubbles as

$$u_s = u_b f(\alpha_g) \tag{2.8}$$

where u_b refers to the bubble terminal velocity, and $f(\alpha_g)$ represents the interaction between the gas bubbles. Wallis (1969) proposed the following relation that connects the slip velocity and terminal velocity of a bubble, which is expressed as

$$u_s = u_b(1-\alpha_g)^n \tag{2.9}$$

The slip velocity model was primarily developed for the two-phase system. Darton and Harrison (1975) have shown that this model can also be applied to the three-phase system.

The theory to calculate the uncertainty of the results is given in Appendix A. The ranges of experimental uncertainty analysis of the data points are given in Table 2.4.

Table 2.4 Uncertainties ranges of the gas holdup and operating variables.

Quantities	Mean, $\bar{x}$	STDEV	U	U_r (%)
α_g (without surfactant)	7.15×10^{-2} – 3.32×10^{-1}	1.0×10^{-2} – 9.40×10^{-2}	5.77×10^{-3} – 5.43×10^{-2}	1.52 – 1.67
α_g (with surfactant)	1.85×10^{-2} – 3.86×10^{-1}	5.03×10^{-4} – 1.10×10^{-2}	2.91×10^{-4} – 6.36×10^{-3}	1.57 – 1.91
u_{sg}	9.59×10^{-3} – 4.23×10^{-2}	9.06×10^{-4} – 1.53×10^{-3}	3.70×10^{-4} – 6.26×10^{-4}	8.74×10^{-1} – 6.54
u_{sl}	1.66×10^{-2} – 5.70×10^{-2}	1.71×10^{-3} – 1.92×10^{-3}	6.47×10^{-4} – 7.26×10^{-4}	1.27 – 3.89

2.3. Results and discussion

A comprehensive analysis of the variation in the gas holdup structure as a function of the superficial gas velocity, the superficial slurry velocity, the particle concentration, and the particle size with and without the presence of surfactant is discussed.

2.3.1. Variation of gas holdup under different experimental conditions

2.3.1.1. Variation of gas holdup as a function of superficial gas velocity

The effect of the superficial gas velocity at different particle concentrations, fixed superficial slurry velocity, and particle size on the gas holdup is given in Fig. 2.3. It is noticed that the gas holdup increases linearly with the increase in the superficial gas velocities at all particle concentrations. It is attributed to an increase in the quantity of gas by increasing the superficial gas velocity. The increase in the gas velocity contributes to the production of a huge number of gas bubbles, which are in the combination of small and large bubbles. The increase in the gas velocity causes bubble coalescence; as a result, bubble size increases. Due to the super porous pores of the sparger, the number of small gas bubbles in the present system is low compared to the larger bubbles. Details of bubbles size in the present experimental condition are reported in chapter 4. Due to a large number of small gas bubbles in the column, the gas holdup of the system was found to increase linearly. Other researchers have also found similar trends in their studies in counter-current operations (Besagni and Inzoli, 2016b; Jin et al., 2010; Vadlakonda and Mangadoddy, 2018). The gas holdup increases from 2.84 to 33.19% as the superficial gas velocities increase from 0.011 to 0.075 m/s (at w_s = 0.5 wt.%). The gas holdup changes from 2.2 to 25% for the same range of superficial gas velocity variation at 3.0 wt.% particle concentration.

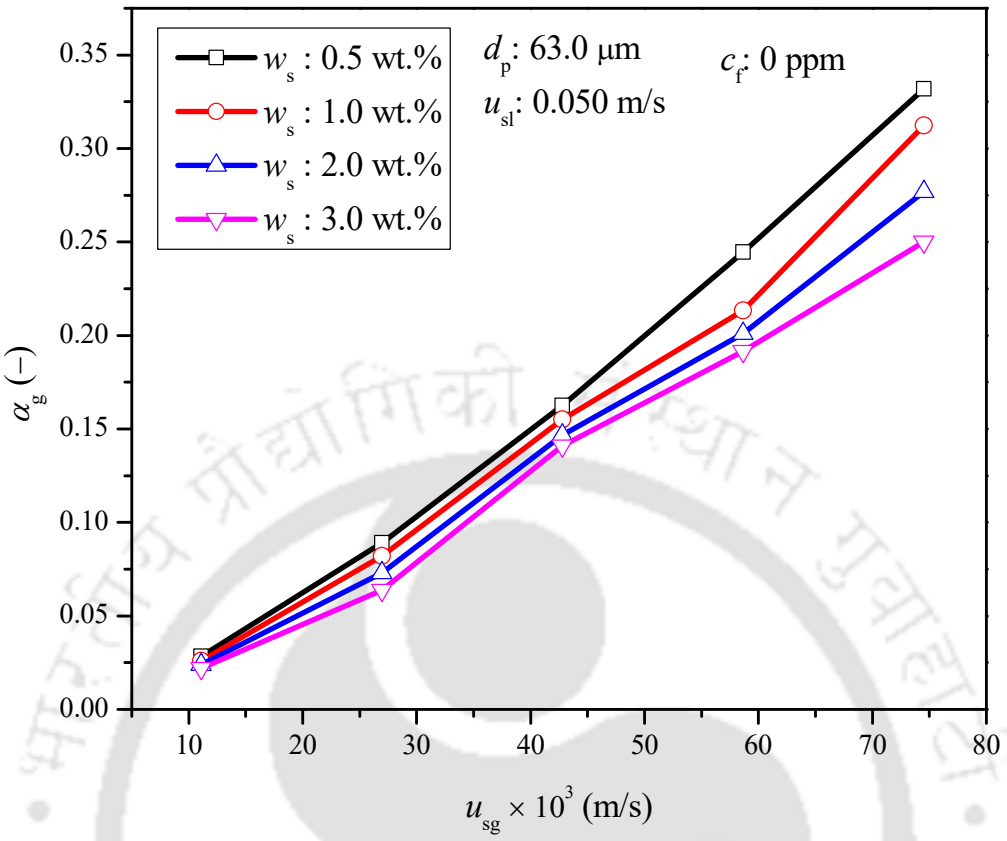

Fig. 2.3. Variation of gas holdup as a function of the superficial gas velocity.

2.3.1.2. Variation of gas holdup as a function of the superficial slurry velocity

The counter-current flow arrangement of the gas-slurry has a major influence on gas holdup characteristics. The relation between superficial slurry velocity and the gas holdup in various experimental conditions is given in Figs 2.4a and 2.4b. The gas holdup also increases with increasing superficial slurry velocities, as shown in Fig. 2.4a. In a counter-current mode, due to the counteractive liquid and gas flows, the bubble rise velocity is decreased, allowing more residence time for the bubbles in the column, thereby increasing the gas hold up. The retarding effects on the rising bubbles in counter-current operation, making the process of the column more efficient. Trivedi et al. (2018) also show the same trend of an increase in a gas holdup with slurry velocities in a counter-current mode. They explained that as the slurry velocity increases, it forces the rising bubbles to break into smaller bubbles, thereby decreasing the bubble diameter, creating more bubbles per unit volume. The variation in gas hold up is less at a lower superficial gas velocity, but it tends to increase rapidly at higher gas velocities. Furthermore, the same

investigation was conducted in the presence of different experimental conditions over the same range of slurry velocities. The maximum gas holdup was found to be 31.5% (Fig. 2.4a) at superficial slurry and gas velocity of 0.057 m/s and 0.075 m/s, respectively. The influence of the superficial slurry velocity on gas holdup at different particle concentrations (w_s = 0.5, 1.0, 2.0, and 3.0 wt.%) and fixed superficial gas velocity (u_{sg} = 0.043 m/s) and particle size (d_p = 61.30 µm) is shown in Fig. 2.4b. In Fig. 2.4b, the maximum gas holdup was found to be 17.10% (at w_s = 0.5 wt.%) at 0.057 m/s superficial slurry velocity. The impact of superficial slurry velocity on gas holdup was found to be less significant than that of superficial gas velocity.

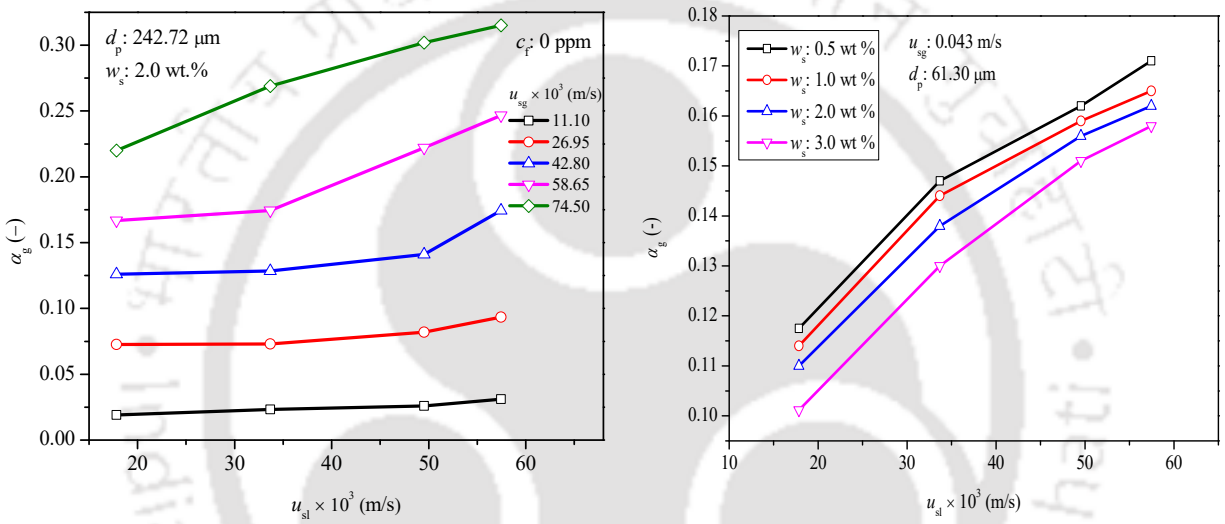

Fig. 2.4. (a) Gas holdup as a function of superficial slurry velocity (at d_p = 242.72 µm, w_s = 2.0 wt.%) and (b) gas holdup as a function of the superficial slurry velocity (at d_p = 61.30 µm, u_{sg} = 0.043 m/s).

2.3.1.3. Variation of gas holdup as a function of particle concentration

Gas holdup for different particle concentration at four different particle sizes at fixed superficial gas and slurry velocity is given in Fig. 2.5a. It is noticed that the gas holdup decreases profoundly with the particle concentration. The increase in particle concentration increases the slurry viscosity, leads to an increase in the bubble coalescence rate (Götz et al., 2017; Sarhan et al., 2016), causes the formation of large bubbles resulting in a reduction of the gas holdup. According to Gandhi et al. (1999b), increasing the particles concentration reduces the bubble breakup rate, hence reducing the formation of small bubbles while promoting the establishment of larger bubbles. The increase in the slurry viscosity stabilizes the gas-liquid interfaces and reduces the bubble breakup

rate (Rabha et al., 2013b). The reduction in gas holdup is approximately 13.19%, 11.04%, 10.71%, and 10.81% when the particle concentration changes from 0.5 to 3.0 wt.% in the 61.30 μm, 242.72 μm, 408.31 μm, and 517.0 μm particle sizes in the slurry, respectively. Comparison of gas holdup at w_s = 0.5 wt.% and w_s = 0 wt.% at two different superficial slurry velocities (u_{sl} = 0.018 and 0.040 m/s) as a function of the superficial gas velocity is shown in Fig. 2.5b. As expected, it was noticed that the gas holdup is higher at w_s = 0 wt.% compared to that of the system at w_s = 0.5 wt.% particle concentration.

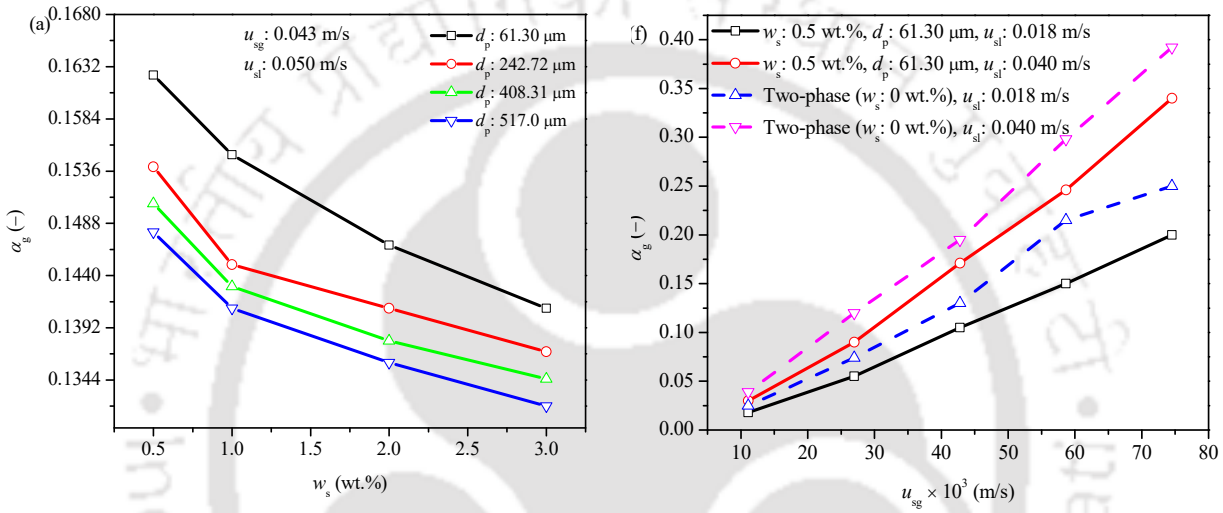

Fig. 2.5. (a) Gas holdup as a function of the slurry concentration at d_p = 61.30 – 517.0 μm and (b) comparison of gas holdup at w_s = 0 wt.% and w_s = 0.5 wt.% at different superficial gas and slurry velocities.

2.3.1.4. Variation in gas holdup as a function of particle size

The variation of gas holdup as a function of the average particle size at different particle concentration at a fixed superficial gas and slurry velocity is shown in Fig. 2.6. It is noticed that increasing the size of the particle tends to increase the gas holdup to a significant extent. At the particular slurry concentration, when the particle size decreases, the viscosity of the slurry increases due to the increase in particle-particle attraction (Kawatra and Eisele, 1988b; Senapati et al., 2009; Zhou et al., 1993). It can be explained in another way: in the case of the small size particles (as the number of particles increase), the particles are prone to get packed together closely, which increases in particle-particle and particle-fluid interaction. It increases the system viscosity. Overall observation indicates that the effect of the size of fine particles on gas holdup is

substantial. Increasing the slurry viscosity promotes the bubble coalescence (Ojima et al., 2014; Ojima et al., 2015); hence the gas holdup decreases. The enhancement in gas holdup is approximately 3.48% (at w_s = 0.5 wt.%), 2.73% (at w_s = 1.0 wt.%), 3.70% (at w_s = 2.0 wt.%), and 1.40% (at w_s = 3.0 wt.%) as the particle size changes from 61.30 to 517.0 μm. It is noticed that the improvement in gas holdup is not substantial with the increase in the particle size.

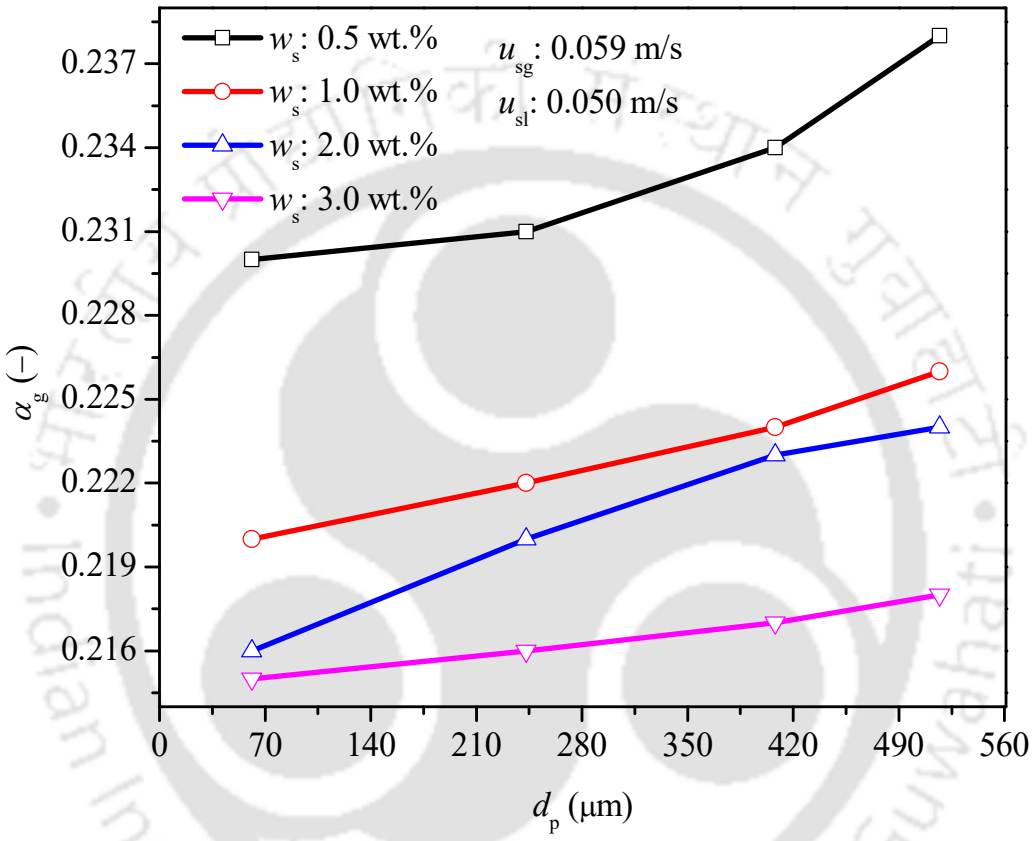

Fig. 2.6. Variation of the gas holdup with particle size (at w_s = 0.5 – 3.0 wt.%).

2.3.1.5. Effect of Sauter mean bubble size on the gas holdup

Gas holdup characteristics of the multiphase processes strongly depend on the bubble diameter. The photographic technique was followed to enunciate the bubble size. The influence of Sauter mean bubble diameter (d_{32}) on gas holdup (α_g) at different superficial slurry velocities and constant particle size and particle concentration is shown in Fig. 2.7a. As observed, the d_{32} is small at high u_{sl} compared to the low $u_{sl,}$ and the corresponding gas holdup is more at small d_{32} in comparison to that at large d_{32}. It is seen that the gas holdup is higher as the d_{32} decreases. At u_{sg} = 0.075 m/s, the d_{32} decreases from 3.45 (at u_{sl} = 0.018 m/s) to 2.63 mm (at u_{sl} = 0.057 m/s), leading to an

increase in gas holdup from 21.42 to 32.8%. Similarly, at u_{sg} = 0.011 m/s, the d_{32} decreases from 2.09 (at u_{sl} = 0.018 m/s) to 1.57 mm (at u_{sl} = 0.057 m/s), leads to enhance the gas holdup from 2.0 to 2.80%. Observation shows that a small change of d_{32} can significantly affect the gas holdup characteristics of the system. The effect of d_{32} on gas holdup at different particle concentrations and constant particle size and slurry velocity is illustrated in Fig. 2.7b. As noted, the d_{32} is large at a high particle concentration compared to the low particle concentration, and the corresponding gas holdup is low at a large d_{32}. The enhancement in d_{32} is due to a rise in the effective viscosity of the system. The increase in the effective viscosity enhances the bubble coalescence rate, consequently the bubble size upsurges. At u_{sg} = 0.075 m/s, the d_{32} enlarges from 3.55 mm (at w_s = 0.5 wt.%) to 4.19 mm (at w_s = 3.0 wt.%), causes a reduction in gas holdup from 33.19% to 25%. Similarly, at u_{sg} = 0.011 m/s, the d_{32} increases from 2.10 mm (at w_s = 0.5 wt.%) to 2.56 mm (at w_s = 3.0 wt.%), leads to reduce the gas holdup from 2.84% to 2.20%.

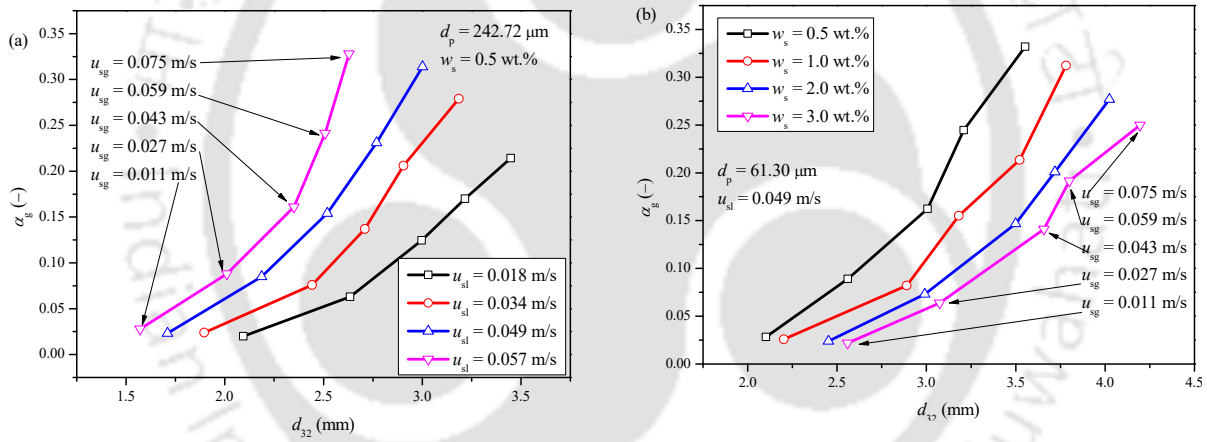

Fig. 2.7. Effect of d_{32} on gas holdup: (a) at different u_{sl} and (b) at different w_s.

2.3.1.6. Comparison of experimental gas holdup with literature data and interpretation of gas holdup by developing an empirical correlation

The present experimental gas holdup values (represented by the legend A in Fig. 2.8) at experimental conditions (d_p = 63.01 µm, w_s = 0.5 wt.%, u_{sg} = 0.011 – 0.075 m/s, u_{sl} = 0.018 m/s) are compared with the literature data of counter-current three-phase systems such as Bhunia et al. (2017) (legend: B, 0 ppm surfactant, w_s = 10 wt.% and legend: C, 10 ppm MIBC as frother, d_p: 63.0 and 138.0 µm and w_s = 5%), Fahad et al. (2019b) (legend: G, d_p = 63.22 µm, c_{sl} = 10.89 kg/m^3, surfactant = 10 gm/m^3, CTAB as surfactant), Prakash et al. (2018b) (legend: I, d_p = 4.85 –

52.26 μm, legend: J, d_p = 408.31 μm, 0.8 wt.% (coal particle)), Shukla et al. (2010) (legend: K, u_{sl} = 0.0191 m/s, c_s = 50 kg/m^3, coal particle, legend: L, u_{sl} = 0.0191 m/s, c_s = 100 kg/m3 coal particle), co-current three-phase flow Kumar et al. (2012) (legend: M, w_s = 0.5 wt.%, glass beads, d_p: 35 μm, u_{sl} = 0.0207 m/s (water), co-current mode), and two-phase counter-current system as Rollbusch et al. (2015) (legend: D, u_l = 0.0014 m/s, water), Besagni et al. (2014) (legend E, u_l = 0.04 m/s water), Otake et al. (1981) (legend: F, u_l = 0.03 m/s, water), and Jin et al. (2010) (legend: H, u_l = 0.0028 m/s (water)). It is seen that the experimental values of Prakash et al. (2018b) (legend: I) and Shukla et al. (2010) (legend: L) are close to the present experimental values. Some literature values of Bhunia et al. (2017) (legend: C), Fahad et al. (2019b) (legend: G), Bhunia et al. (2017) (legend: B), and Shukla et al. (2010) (legend: K) over predict while Kumar et al. (2012) (legend: M) under predict the gas holdup values. Some of the literature gas holdup values of Rollbusch et al. (2015) are close to the present experimental values below u_{sg} < 0.03 m/s and deviates potentially above u_{sg} > 0.03 m/s. The deviation of literature values from the present experimental data is because of a different experimental condition such as the different slurry or liquid velocity, the flow arrangements such as semi-batch, co-current, and counter-current, the sparger geometry and pore size, the column dimension and geometry and the particle size and its density.

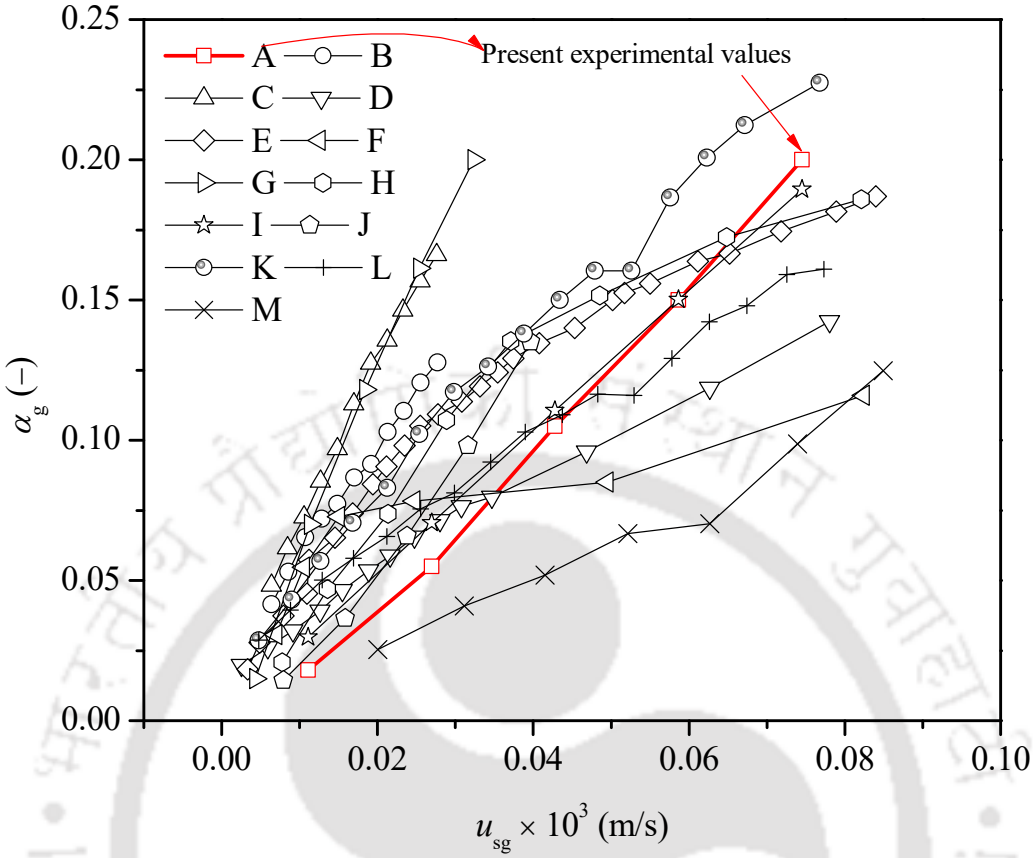

Fig. 2.8. Comparison of experimental and literature gas holdup values in a counter-current slurry bubble column and air-water system, legends: A: present experimental value (u_{sl} = 0.018 m/s, w_s = 0.5 wt.%, d_p = 63.01 µm), B: 0 ppm surfactant, w_s =10 wt.% (Bhunia et al., 2017), C: 10 ppm surfactant, MIBC, w_s = 5.0 wt.% (Bhunia et al., 2017), D: u_l = 0.001 m/s, water (Rollbusch et al., 2015), E: u_l = 0.040 m/s, water (Besagni et al., 2014), F: u_l = 0.030 m/s, demineralized water (Otake et al., 1981), G: d_p = 63.22, c_{sl} = 10.89 kg/m^3, surfactant = 10 gm/m^3, CTAB (Fahad et al., 2019b), H: u_l = 0.0028 m/s, water (Jin et al., 2010), I: d_p = 4.85 – 52.26 µm (Prakash et al., 2018b), J: d_p= 408.31 µm, 0.8 wt.% (coal particle) (Prakash et al., 2018b), K: u_{sl} = 0.019 m/s, c_s = 50 kg/m^3, coal particle (Shukla et al., 2010), L: u_{sl} = 0.019 m/s, c_s = 100 kg/m3 coal particle (Shukla et al., 2010), and M: w_s = 0.5 wt.% (glass beads, d_p: 35 µm), u_{sl} =0.021 m/s (water), co-current mode (Kumar et al., 2012).

It was noticed that the literature values of some authors are in accordance with the present system, but, to improve the accuracy of the interpretation of the gas holdup in the present system, it is essential to develop an empirical correlation. In the present system, the potential parameters, which

affect the system holdup characteristics, are the superficial gas velocity (u_{sg}), the superficial slurry velocity (u_{sl}), the particle diameter (d_p), the slurry surface tension (σ_{sl}), the slurry density (ρ_{sl}), the column diameter (d_c), and acceleration due to gravity (g). Based on the experimental observations, the gas holdup can be expressed as the functionality of

$$\alpha_g = f\left(u_{sg}, u_{sl}, \sigma_{sl}, \rho_{sl}, d_p, d_c, g\right) \tag{2.10}$$

Applying Buckingham's pi theorem and multiple regression analysis on the 557 experimental data yields the following generalized correlation for the three-phase counter-current flow

$$\alpha_g = 7.752 \left(\frac{d_p \rho_{sl} u_{sl}^2}{\sigma_{sl}}\right)^{0.078} \left(\frac{g d_c}{u_{sg}^2}\right)^{-0.639} \tag{2.11}$$

Detail theory of multiple linear regression analysis is provided in Appendix as section B. The correlation coefficient was found to be 0.99 (for Eq. 2.11). The validity range of the proposed correlation (Eq. 2.11) is: $0.018 \le \alpha_g \le 0.34$; $2.277 \times 10^{-4} \le d_p \rho_{sl} u_{sl}^2 / \sigma_{sl} \le 2.43 \times 10^{-2}$; and $91.445 \le g d_c / u_{sg}^2 \le 4122.476$. The gas holdup correlation (Eq. 2.11) is appropriate for the analysis of gas holdup in the three-phase (with and without surfactant) system. Experimental values are in ± 19.99% error with respect to the predicted values. The parity between the experimental and the predicted values of a gas holdup is shown in Fig. 2.9.

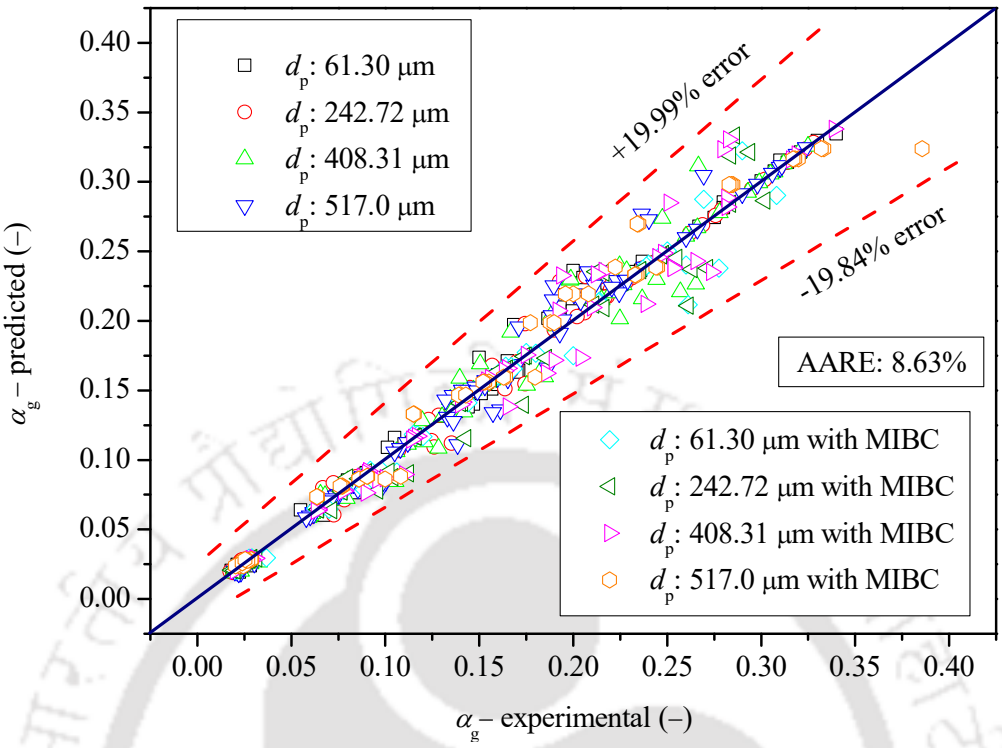

Fig. 2.9. Parity plot between the experimental and predicted (calculated from Eq. 2.11) gas holdup values.

2.3.1.7. Assessment of gas holdup using a slip velocity model

As per the slip velocity model (Eq. 2.9), the gas holdup is a function of two parameters: u_b and n. Vinaya and Varma (1996) reported the value of 'n' as 1.84 (for $\alpha_g \leq 0.15$) for bubbly flow. In the current work, the exponent (n) was in the range of 0.948 – 2.075 (with surfactant) and 0.925 – 2.036 (without surfactant) for the three-phase counter-current system. Parameter ranges are based on the 526 experimental data points. The range of parameters reported in this section was based on a wide range of superficial gas and slurry velocity, particle concentration, and particle size. The higher range in the absence of surfactant reflects the higher interaction of the rising gas bubbles with the neighboring bubbles and the surrounding medium. Godfrey and Slater (1991) and Richardson and Zaki (1954) used Eq. (2.7) for liquid-liquid and gas-solid systems. The values of 'n' for the pulse column, the spray column, and the rotating disc contactor are in the range of 0.3 – 0.51, 0.2 – 1.5, and 0.6 – 3.5, respectively (Godfrey and Slater, 1991). The range of values of n as per Richardson and Zaki (1954) for the gas-solid system is 1.39 – 3.65. Yerushalmi and Cankurt (1979) also reported the negative value of n and deduced that the formation of a particle cluster is

the main reason for a negative value. In the case of a churn turbulent flow, the negative value is probably due to the agglomeration of bubbles. Vinaya and Varma (1996) studied the gas holdup in a co-current up-flow two-phase system in the presence of four different liquid systems and five different particles with air as the dispersed phase. They developed a correlation for interpretation of slip velocity and reported that the influence of gas flow rate on slip velocity was dominant in comparison to the liquid velocity. The gas holdup and the liquid velocity have a negative impact on the slip velocity. Sada et al. (1986a) reported an analysis of gas holdup in semi-batch with two- and three-phase systems using the slip velocity model. They noticed the values of exponent '*n*' as –4 and –3 for the two- and three-phase system, respectively.

The u_b value for a three-phase system was 0.396 – 0.586 (without surfactant) and 0.393 – 0.556 (with surfactant). The range of u_b in the presence of surfactant is low compared to the absence of the surfactant. The lower value attributed to the creation of a large number of small bubbles by surfactant addition. As per Deckwer (1985), the bubble swarm velocity (u_{bs}) is estimated as $u_{bs} = u_{sg}/\alpha_g$. Rollbusch et al. (2015) used the Deckwer (1985) relation and reported u_{bs} in the range of 0.476 – 0.693 (in perforated plate sparger) in the u_{sg} range of 0.005 – 0.079 m/s (at u_l = 0.0014 m/s) in a cylindrical column with a diameter of 0.16 m. (Hooshyar et al. (2010a)) reported the value of u_b as 0.21 – 0.231 m/s and *n* as 0.73 – 1.08 in a semi-batch 2D slurry bubble column in the particle volume fraction range of 0 – 10%. In the case of the cylindrical column (semi-batch mode), the authors reported values of u_b as 0.24 – 0.255 and *n* as 0.655 – 1.570 in the range of 0 to 40% volume fraction of the particle. The following correlation is suggested for the parameter u_b to interpret the gas holdup using the slip velocity model:

$$\frac{u_b}{u_{sg}} = 2.527 \left(\frac{\rho_{sl} u_{sl}^2 d_p}{\sigma_{sl}} \right)^{-0.248} \left(\frac{g d_p}{u_{sg}^2} \right)^{0.436} (1 - w_s)^{-0.037} \qquad (2.12)$$

The correlation coefficient (R^2) and the standard error of Eq. (2.12) are 0.94 and 0.234, respectively. The range of correlation (for Eq. 2.12) is $2.27\times10^{-4} \le \rho_{sl} u_{sl}^2 d_p / \sigma_{sl} \le 2.431\times10^{-2}$; $1.11\times10^{-1} \le g d_p / u_{sg}^2 \le 41.190$, and $0.970 \le 1 - w_s \le 0.995$. Similarly, a correlation is also developed for exponent *n*, which can be expressed as

$$n = 0.404\left(\frac{\rho_{sl}u_{sl}^2 d_p}{\sigma_{sl}}\right)^{-0.218}\left(\frac{gd_p}{u_{sg}^2}\right)^{0.038}(1-w_s)^{0.638} \quad (2.13)$$

The experimental values satisfactorily follow the correlation (Eq. 2.13) with a standard error of 0.124 and a correlation coefficient of 0.90. The gas holdup ($\alpha_{g,\,slip}$) using a slip velocity model can be obtained by substituting Eq. (2.12) and Eq. (2.13) into Eq. (2.14)

$$\alpha_{g,slip} = 1 - \left(\frac{u_s}{u_b}\right)^{\frac{1}{n}} \quad (2.14)$$

The absolute average relative error (AARE) between experimental and predicted gas holdup as per Eq. (2.11) is 4.76% with a deviation in values are ± 19.93%, while AARE, according to the slip velocity model, is approximately 9.76% with a deviation within ± 19.80%. Experimental and predicted gas holdup (using a slip velocity model) is shown in Fig. 2.10.

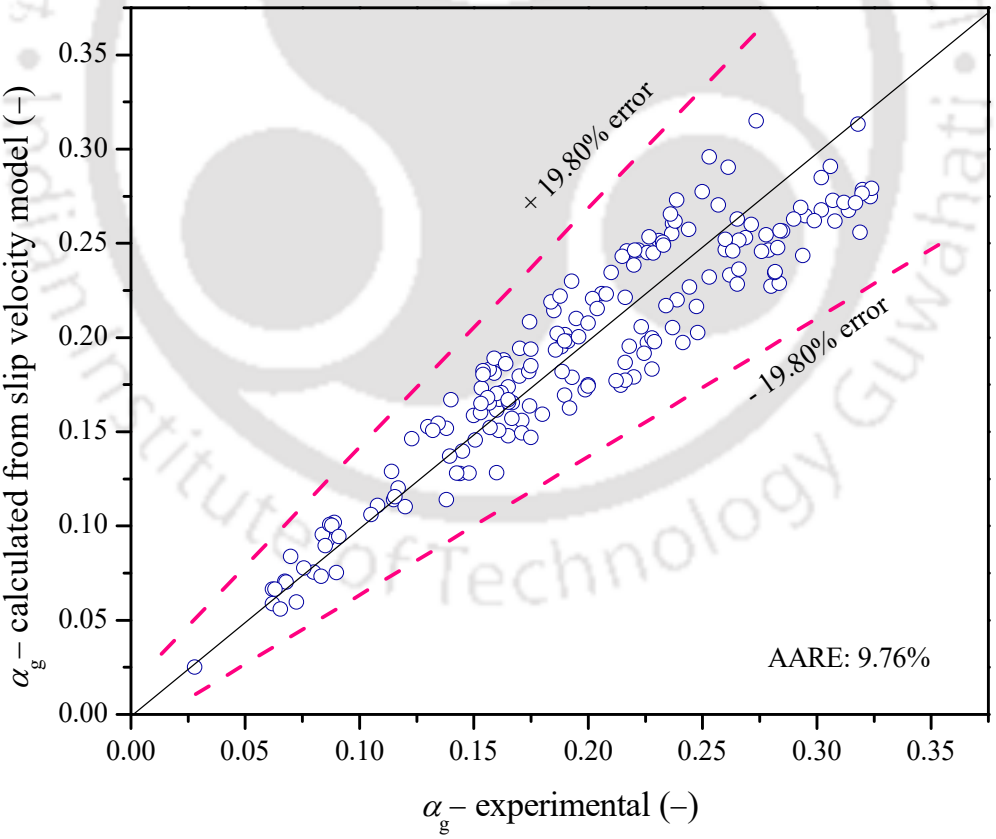

Fig. 2.10. Parity of experimental and predicted (calculated using Eq. 2.14) gas holdup using slip velocity model.

Some typical values of gas holdup and Sauter mean bubble diameter are given in Table 2.5.

Table 2.5 Some typical values of the gas holdup and Sauter mean bubble diameter in the different experimental conditions.

System	Superficial slurry velocity, $u_{sl} \times 10^3$ (m/s)	Superficial gas velocity, $u_{sg} \times 10^3$ (m/s)	Particle concentration, w_s (wt.%)	Particle diameter, d_p (μm)	Gas holdup, α_g (–)
Air-water-particle (without surfactant)	17.83	11.10	0.5	61.30	0.018
	17.83	42.80	0.5	61.30	0.105
	17.83	74.50	0.5	61.30	0.200
	49.54	58.65	0.5	61.30	0.244
	57.46	74.50	1.0	61.30	0.330
	49.54	11.10	2.0	61.30	0.024
	33.69	26.95	3.0	61.30	0.072
	49.54	74.50	3.0	242.72	0.295
	57.46	58.65	2.0	408.31	0.199
	17.83	74.50	3.0	408.31	0.237
	17.83	42.80	0.5	517.0	0.112
	33.69	58.65	1.0	517.0	0.195
	49.54	26.95	2.0	517.0	0.098
	57.46	74.50	3.0	517.0	0.269
Air-water-particle (with surfactant)	17.83	11.10	0.5	61.30	0.021
	33.69	26.95	1.0	61.30	0.089
	49.54	42.80	3.0	61.30	0.156
	57.46	74.50	2.0	408.31	0.311
Air-water	17.83	11.10	–	–	0.018
	33.69	42.80	–	–	0.120
	49.54	42.80	–	–	0.143

2.4. Conclusions

The present research reports an experimental analysis of gas holdup in a three-phase counter-current microstructured slurry bubble column with and without surfactant. An extensive investigation is performed to assess the effect of operating variables and physical properties on gas holdup characteristics. The maximum gas holdup in the column with and without the surfactant is 38.570% and 33.195%, respectively. The increase in the superficial gas velocity, superficial slurry velocity, and particle size enhances the gas holdup, while it decreases with the increase in the

particle concentration. The effect of superficial gas velocity, superficial slurry velocity, and particles concentration on gas holdup is more pronounced compared to particle size. The analysis of holdup characteristics by the slip velocity model enunciates two critical parameters (u_b and n), demonstrating that the ranges of the two parameters are higher in the three-phase without surfactant as compared to the three-phase with a surfactant. Higher values of the parameter 'n' in the absence of surfactant reflect that the rising bubbles are exposed to more interaction with the neighboring bubbles and surrounding fluids. Correlations has been proposed for the interpretation of the parameters of the gas holdup and slip velocity model. The proposed correlation satisfactorily fits the experimental values well in the error range of ± 20% and AARE less than 20%.

Chapter 3

Bubble-Slurry Interfacial Shear Stress and Frictional Pressure Drop in the Presence and Absence of a Surface-Active Agent

The present chapter enunciates the experimental studies to examine the gas-slurry interfacial shear stress and frictional pressure drop in the presence and absence of surfactant in a rectangular slurry column. A novel mechanistic model has been proposed by considering the energy dissipation rate because of bubble formation, a slip of gas-slurry interface, and the wetting of a thin liquid layer with the column wall. A comprehensive investigation was carried out to enunciate the effect of particle concentration, particle size, bubble size, and surfactant on the frictional pressure drop and bubble-slurry interfacial shear stress. Generalized empirical correlations were also developed based on the dynamic variables, geometric variables, and physical properties of the system.

Publication: Prakash, R., Majumder, S. K., & Singh, A. (2020). Bubble-slurry interfacial shear stress and frictional pressure drop in a rectangular column in the presence and absence of a surface-active agent, Powder Technology, 366, 761 – 775. https://doi.org/10.1016/j.powtec.2020.03.015

3.1. Introduction

The complex nature of multiphase flow in the slurry bubble column is the result of the fluid flow that is affected by numerous design parameters. Hence, the correct interpretation of the design parameters is essential for the proper design, operation, modeling, control, scale-up, and optimization of a processing unit (Sheikhi et al., 2013). The slurry bubble columns are simple in construction; however, the scale-up technique is complicated because of the lack of adequate information on hydrodynamic characteristics (Barghi et al., 2004; Jakobsen et al., 2005). The accurate design and scale-up of the slurry bubble columns require the knowledge on the effects of various hydrodynamic characteristics (i.e., frictional pressure drop, bubble size distribution, gas holdup, flow regime, and mixing characteristics) on the design parameters. The knowledge of pressure drop characteristics is essential in analyzing the impact of the hydrodynamic characteristics of a multiphase system, since, it influences the rate of productivity, processing cost, corrosion rate, and shear stresses (Biria, 2013).

The pressure drop characterizes the total amount of energy dissipation by the fluid in a multiphase process. Energy dissipation is the result of frictional losses (viz. viscous dissipation) on column walls and internals (Charton et al., 2017). The influence of frictional pressure drop becomes crucial when the phase velocity and system viscosity change (Descamps et al., 2008). Prediction of the drop in frictional pressure in multiphase flow is complicated because of the additional pressure drop due to slippage (Biria, 2013). Slippage in a multiphase system is due to the difference in velocities of the phases. The variation in slip velocity significantly affects the pressure drop characteristics of a multiphase process (Griffith, 1962).

Many authors have conducted experiments to determine the frictional pressure drop in both the Newtonian and non-Newtonian systems (Majumder et al., 2011; Majumder et al., 2006, 2007; Mandal et al., 2004; Mittal and Zhang, 2007; Shannak, 2008; Yao et al., 2018). The variation in bubble size and buoyancy influences the frictional pressure drop in in the vertical column (Yao et al., 2018). It was reported that the buoyancy of the bubbles results in increased frictional losses, especially when the larger bubbles are present in the system. Tang et al. (2013) reported the influence of superficial gas velocity and superficial liquid velocity on the frictional pressure drop. The authors reported that at high Reynolds number, the bubbles closer to the column wall affect the wall shear stress. A detailed study of the contributions of friction because of the liquid phase,

form drag, and bubble formation to total frictional pressure drop is reported by Majumder et al. (2006). They suggested that the form drag and pressure drop is because of the bubble formation, which increases with increasing gas and liquid flow. Drag force experienced on the gas bubbles depends on the rising velocity of a swarm of bubbles, which causes the dissipation of viscous and inertial energy (Stewart, 1969).

According to Peker et al. (2008), the pressure drop in the slurry system is because of the particle-particle collision, the particle interaction with the column wall, and the liquid friction on the column surface. Prakash et al. (2018b) investigated the fluid-wall, the particle-fluid, and the fluid-particle components of the frictional pressure drop in a semi-batch slurry column. They observed that the fluid-wall frictional pressure drop is nearly 99% of the frictional pressure drop, and the remaining is caused by the cumulative effect of both fluid-particle and particle-wall interactions. Nagarajan et al. (2016) described the impact of operating variables, i.e., the liquid flow rate, the mass flow rate of particles, the size, and density of the particles on the pressure drop in counter-current operation. They concluded that the pressure drop increased with increasing phase velocity and decreased with the particle size and particle density. The presence of particles substantially affects the frictional pressure drop characteristics. Many authors have reported that the frictional pressure drop increases with increasing particle concentration (Peker et al., 2008; Shukla et al., 2010; Wilson et al., 2006). As the surfactant added to the liquid, the frictional pressure drop decreases and alters the flow pattern and liquid holdup (Liu et al., 2014). A reduction in pressure drop is strongly based on the drag force and liquid holdup, and on their weighting coefficients.

Interfacial shear stress is profoundly based on gas-liquid interfacial structures (Fukano and Furukawa, 1998). Shear stress exerted by each phase in the multiphase system is different due to its velocities and properties (Biria, 2013). Hanratty and Engen (1957) and Smith and Tait (1964) have demonstrated the more interfacial shear stress in the case of gas flow over the irregular gas-liquid mixture interface compared to a smooth plane surface. Smith and Tait (1966) reported that the interfacial shear stress caused by the momentum transfer is dependent on the relative velocity of the phases. As the fluid flows past a smooth boundary, a molecular diffusion through the boundary laminar sublayer occurs. Consequently, a flux of momentum takes place. Diffusion between the phases results in a secondary momentum transport due to the interchange of particles

between the phases. Summary on some important frictional pressure drop and bubble-liquid interfacial shear stress study related to the present work is given in Table 3.1.

Table 3.1. Summary on some important studies on the frictional pressured drop and bubble-liquid interfacial shear stress.

System	Type	Apparatus & Condition	Key Finding	References
Air, Triton X-100, corn syrup,	Co-current upflow	u_l = upto 0.05 m/s, u_{sg} = upto 0.30 m/s, d_c = 0.229 m, h = 9.14 m, w_s = 0 wt.%	Pressure drop	Miller (1980)
Air–CMC	vertically upward	u_l = 0.023 – 0.10 m/s, u_{sg} = 0.02 – 1.0 m/s, w_s = 0 wt.%	Frictional pressure drop	Chandrakar et al. (1985)
Air-slurry	Vertical upflow and downflow	u_{sl} = 0 – 8 m/s, u_{sg} = 0 – 8 m/s, d_c = 0.015 and 0.026 m, h = 2.785 and 2.797 m, d_c = 0.015 m and 0.026 m, glass beads, d_p = < 30, 63, and < 100 μm, w_s = 0 – 65.0 wt.%	Frictional pressure drop	Hatate et al. (1986)
Air–PAA	Vertically upward	u_l = 0.01 – 0.10 m/s, u_{sg} = 7.7 – 12.8 m/s, w_s = 0 wt.%	Frictional pressure drop	Akagawa et al. (1989)
Air–water	Multi-stage bubble column	u_l = 0.003 – 0.005 m/s, u_{sg} = 0.11 – 0.20 m/s, w_s = 0 wt.%	Frictional pressure drop	Meikap (2000)
Air–water	Vertically upward co-current annular flow	u_l = 0.05 – 0.22 m/s, u_{sg} = 10 – 35 m/s, d_c = 0.029 m, h = 3 m, w_s = 0 wt.%	Interfacial friction factor	Wongwises and Kongkiatwanitch (2001)
Air–water	Co-current gas–liquid annular two-phase flow	u_l = 0.1 – 1.0 m/s, u_{sg} = 1.42 – 28.87 m/s, d_c = 0.1016 m, h = 4 m, w_s = 0 wt.%	Interfacial friction factor	Aliyu et al. (2015)
Air-water-CMC	Downflow bubble column	u_l = 0.035 – 0.167 m/s, u_{sg} = 0.002 – 0.062 m/s, d_c = 0.05 m, h = 1.60 m, w_s = 0 wt.%	Pressure drop and bubble-liquid interfacial shear stress	Majumder et al. (2007)
Air-slurry, air-slurry with surfactant (MIBC)	Counter-current	u_{sl} = 0.013 – 0.028 m/s, u_{sg} = 0.009 – 0.050 m/s, d_c = 0.1 m, h =1.68 m, coal particle, d_p = 63.0 μm, c_s = 0 – 200 kg/m^3	Frictional pressure drop	Shukla et al. (2010)

Air-water, amyl alcohol, glycerin, and CMC	Co-current upflow	u_l = 0.536 – 2.245 m/s, u_{sg} = 0.168 – 0.643 m/s, d_c = 0.020 m, h = 3.4 m, w_s = 0 wt.%	Frictional pressure drop	Majumder et al. (2011)
Air-water-slurry and air-glycerol-slurry	Ejector induced slurry bubble column	u_{sl} = 0.009 – 0.026 m/s, u_{sg} = 0.04 – 0.14 m/s, d_c = 0.05 m, h = 1.6 m, Zinc oxide (d_p = 2.21 μm), Kieselguhr (d_p = 19.39 μm) and Aluminum oxide (d_p = 96.0 μm), w_s = 0.1 – 1.0 wt.%	Frictional pressure drop	Sivaiah and Majumder (2012)
Air-water, Air-water-surfactant	Vertical phase flow	u_l = 0.00001 – 0.2 m/s, u_{sg} = 0.1 – 20 m/s, w_s = 0 wt.%	Frictional pressure drop	Liu (2014)
Air-water-SDS, Air-water-CMC	Semi-batch	u_l = 0 m/s, u_{sg} = 0.008 – 0.040 m/s, h = 0.63 m, w = 0.19 m, d = 0.03 m, w_s = 0 wt.%	Frictional pressure drop	Prakash et al. (2018b)
Air-slurry	Semi-batch	u_{sl} = 0 m/s, u_{sg} = 0.008 – 0.040 m/s, h = 0.63 m, w = 0.19 m, d = 0.03 m, Al_2O_3 (d_p = 52.26 μm), CuO (d_p = 10.16 μm), SiO_2 (d_p = 5.01 μm), ZnO (d_p = 4.85 μm), w_s = 0.2 – 3.0 wt.%	Frictional pressure drop	Prakash et al. (2018b)
Air-slurry	Semi-batch	u_{sl} = 0 m/s, u_{sg} = 0.008 – 0.040 m/s, h = 0.63 m, w = 0.19 m, d = 0.03 m, coal particle, d_p = 242.72 and 408.31 μm, w_s = 0.2 – 0.8 wt.%	Frictional pressure drop	Prakash et al. (2018b)
Air-water-slurry with and without surfactant	Counter-current column	u_{sl} = 0.007 – 0.035 m/s, u_{sg} = 0.007 – 0.035 m/s, coal particle, d_c = 0.055 m, h = 0.91 m, d_p = 63.22, 235.61, 404.97 and 507.67 μm, c_s = 1.5 – 10.89 kg/m^3	Frictional pressure drop	Fahad et al. (2019a)

From the literature, it is noticed that the hydrodynamic characteristic of a rectangular slurry column is limited and not comprehensive. Most studies are limited to certain aspects of the design

parameters. However, some work has been done in a counter-current conventional bubble column. None of the work in the literature has reported the effect of different variables such as particle concentration, average particle size, slurry, and gas velocity on the gas-slurry interfacial shear stress and the frictional pressure drop. Some researchers have attempted to study the influence of operating variables and physical properties of the phases on the bubble-liquid interfacial shear stress in the gas-liquid system (Majumder et al., 2006, 2007).

The majority of studies conducted in the past are related to the assessment of the frictional pressure drop in the horizontal and vertical two-phase cylindrical column. However, no research article was found that shows the measurement of gas-slurry interfacial shear stress and frictional pressure drop in a counter-current rectangular slurry bubble column. Therefore, this work primarily aims to study the impact of the operating variable, physical properties, and geometric variable of the system on the frictional pressure drop and gas-slurry interfacial shear stress in a rectangular slurry bubble column. A mechanistic model is also proposed based on the energy balance of gas and slurry flow by considering the energy dissipation rate because of bubble formation, the energy dissipation rate because of a slip of gas-slurry interface, and energy dissipation rate because of the wetting of a thin liquid layer with the column wall.

3.2. Experimental arrangement

The schematic diagram of the experimental setup is shown in Fig. 3.1. The rectangular column used in this study was made of the Perspex sheet. Perspex was chosen as the construction material for the column to visualize the hydrodynamic characteristics. The length, depth, and width of the rectangular column were 0.63, 0.03, and 0.19 m, respectively. The experiments were performed by varying the superficial gas velocity from 0.011 to 0.075 m/, superficial slurry velocity from 0.018 to 0.057 m/s, and particle concentration from 0.5 to 3.0 wt.%. Cationic surfactant MIBC (Methyl Isobutyl Carbinol, molecular weight: 102.18, specific gravity: 0.81) with a purity greater than 98.0% was purchased from Tokyo Chemical Industry Co. Ltd. The experiments were carried out in the three-phase in the presence and absence of a surfactant. Pressure drop was measured using two horizontally installed pressure transmitters (Make: Gems Sensors & Controls, Model: 3500 B 0002G 01 B) P_1 and P_2. The distance of pressure transmitter ports, P_1, and P_2 was about 0.162 m and 0.365 m from the lower end of the column. Two pressure transmitters were coupled with the pressure meter, which was further coupled with the computer through a cable (RS-232)

for transferring data. The slurry inlet was at the top of the column, while the outlet was at the bottom of the column, as shown in Fig. 3.1. The slurry was prepared using tap water, and coal particles and the gas phase was the atmospheric air. In all the experimental work, the gas-slurry dispersion height was kept at 0.49 m from the lower end of the column. The gas-slurry dispersion height in the column was controlled using the controlled valve installed in the bottom outlet line. Slurry pump (power: 1 HP, 0.75 kW, pressure range: 2.1 bar, maximum flow rate: 24 liters/minute) was used to transport the slurry into the column. The flow rate of the slurry was measured by an electromagnetic flowmeter (Adept Fluidyne, MagFlow 6410). A direct driven air compressor (Model: XLBM24, Power: 2 HP, Pressure: 8 bar, Tank volume: 24 liters, Speed: 2850 RPM, Capacity: 195 liters/minute) was used to deliver the compressed air to the sparger.

Fig. 3.1. Schematic of the experimental arrangement. (Copyright material)

A calibrated air rotameter (range 0 – 10 liter/minute, full-scale accuracy ± 5%) was used to estimate the air flow rate. A needle valve was connected prior to the air rotameter to control the air flow rate. A cylindrical sintered stainless steel sparger (make: TFI filtration, SS316 L) with an average pore size 20 μm (indicated by the manufacturer) was used to distribute the gas as a dispersed bubble phase in the slurry column. The length, inner diameter, and outer diameter of the

stainless steel sintered sparger were 175 mm, 10 mm, and 14 mm, respectively. To ensure that the pores are not clogged, it was cleaned with the aqueous solution of HCl (40% HCl + 60% water) before each run of the experiment.

3.3. Physical properties of the system

The composition and physical properties of the slurry used in the current study are given in chapter 2, as Table 2.2 and Table 2.3. It was found that the surface tension of the slurry in the absence of surfactant varies with only particle concentration, but in the case of slurry with a surfactant, the slurry surface tension varies with both the particle concentration and particle size. The surface tension of slurry with and without the MIBC surfactant was measured by a tensiometer (Make: Kwoya, Model: DY300). The slurry viscosity and density did not vary with the surfactant. All the physical properties were determined at 25 ± 1 °C.

3.4. Theoretical background

In a vertical multiphase system, the total pressure drop (ΔP_T) can be defined as the summation of the frictional pressure (ΔP_f), the hydrostatic pressure (ΔP_h), and the pressure drop because of acceleration (ΔP_a). The total pressure drop is expressed as

$$\Delta P_T = \Delta P_f + \Delta P_h + \Delta P_a \tag{3.1}$$

According to Hughmark and Pressburg (1961), the pressure drop caused by the acceleration in a column with a uniform cross-sectional area is insignificant compared to the total pressure drop, and therefore, it was ignored. The hydrostatic pressure drop or potential energy component depends on the gas-liquid-solid mixture density, which is expressed as

$$\Delta P_h = (\rho_g \alpha_g + \rho_l \alpha_l + \rho_s \alpha_s) g \Delta Z \tag{3.2}$$

where ΔZ is the distance between the pressure ports. Finally, Eq. (3.1) yields the frictional pressure drop as

$$\Delta P_f = \Delta P_T - (\rho_g \alpha_g + \rho_l \alpha_l + \rho_s \alpha_s) g \Delta Z \tag{3.3}$$

3.4.1. Development of a mechanistic model

The analysis of interfacial shear stress between the gas bubbles and slurry was done based on the mechanistic model. Mechanistic model was applied based on the following assumption (Majumder, 2018): (i) flow of the phases in the column is steady and isothermal, (ii) holdup calculated is assumed to be average at a particular superficial gas and slurry velocity, (iii) the effect of acceleration is considered insignificant without mass transfer between phases, and (iv) the frictional loss is assumed to be the same for a particular superficial gas and slurry velocity.

3.4.1.1. Mechanical energy balance

The mechanical energy balance of the gas phase flow is given by

$$-\Delta P_T \alpha_g A_c u_{sg} + g\Delta Z A_c \alpha_g \rho_g u_{sg} + E_g = 0 \tag{3.4}$$

In Eq. (3.4), the first term denotes the energy dissipation because of the gas flow, the second term is potential energy, and the third term is frictional energy loss because of gas flow. In the same way, for the slurry phase flow, the mechanical energy balance can be expressed as

$$-\Delta P_T (1-\alpha_g) A_c u_{sl} + g\Delta Z A_c (1-\alpha_g) \rho_{sl} u_{sl} + E_{sl} = 0 \tag{3.5}$$

where E_{sl} represents the frictional energy dissipation rate because of the slurry flow. Addition of Eq. (3.4) and Eq. (3.5) yields

$$-\Delta P_T \left((1-\alpha_g) u_{sl} + \alpha_g u_{sg}\right) + \left(\rho_{sl} u_{sl} (1-\alpha_g) + \alpha_g \rho_g u_{sg}\right) g\Delta Z + (E_{sl} + E_g)/A_c = 0 \tag{3.6}$$

The total energy dissipation rate in the three-phase system is contributed by frictional dissipation by gas and slurry flow, energy dissipation as a result of the formation of gas bubbles, energy dissipation because of a slip of gas-slurry interface, and energy dissipation caused by wetting of column wall. Therefore, the expression for ($E_{sl} + E_g$) can be written as

$$E_{sl} + E_g = \Delta P_{fsl} A_c (1-\alpha_g) + \Delta P_{fg} A_c \alpha_g u_{sg} + E_b + E_{slip} + E_w \tag{3.7}$$

where ΔP_{fsl} and ΔP_{fg} are the frictional pressure drop because of slurry flow and gas flow, respectively. E_b, E_{slip}, and E_w denote the energy dissipation rate due to the formation of gas bubbles,

the energy dissipation rate caused by a slip of gas-slurry interface, and the rate of energy because of the wetting column wall, respectively. Substitution of the Eq. (3.7) into Eq. (3.6) yields

$$-\Delta P_T\left[\frac{L_s}{\rho_{sl}}+\frac{G}{\rho_g}\right]+\left[L_s+G\right]g\Delta Z+\frac{\Delta P_{fg}G}{\rho_g}+\frac{\Delta P_{fsl}L_s}{\rho_{sl}}+\frac{E_b+E_{slip}+E_w}{A_c}=0 \tag{3.8}$$

where L_s, G, ΔP_{fg}, and ΔP_{fsl} denote the mass flux of slurry, the mass flux of gas phase, the frictional losses due to gas phase only, and the frictional losses due to the slurry flow only, respectively. The mass flux of slurry was defined by

$$L_s=(1-\alpha_g)u_{sl}\rho_{sl} \tag{3.9}$$

Similarly, the mass flux of the gas flow was defined as

$$G=\alpha_g u_{sg}\rho_g \tag{3.10}$$

3.4.1.2. Energy dissipation because of skin friction

To estimate the frictional dissipation by both the gas and slurry flow in the column, a model is established considering the following assumptions:

(i) In a three-phase system, the friction factor for individual gas or slurry phase is α' times of the factor where only the individual phase is flowing in the column.

(ii) In the three-phase process, the contact area of each gas or slurry phase is α'' times of that when only the individual phase flows through the column. Similarly, during the flow of the gas phase, the magnitude of both parameters α' and α'' are defined based on the bubble contacts with the column wall. Taking into account both assumptions, the slurry phase momentum balance equation can be expressed as follows:

$$\frac{\Delta P_{fsl}(\text{cross}-\text{sectional area})_T}{\Delta P_{fsl0}(\text{cross}-\text{sectional area})_{sl0}}=\frac{(\text{wall shear stress})_T}{(\text{wall shear stress})_{sl0}}\times\frac{(\text{Area of contact with wall})_T}{(\text{Area of contact with wall})_{sl0}}$$

$$\frac{\Delta P_{fsl}A_c(1-\alpha_g)}{\Delta P_{fsl0}A_c}=\frac{(0.5f\rho_{sl}u_{sl}^2)_T}{(0.5f\rho_{sl}u_{sl}^2)_{sl0}}\times\frac{(\text{Area of contact with wall})_T}{(\text{Area of contact with wall})_{sl0}}=\frac{f_{slg}}{f_{sl0}}\frac{(u_{sl}^2)_T}{(u_{sl}^2)_{sl0}}\times\alpha''_{sl}$$

$$\Rightarrow \frac{\Delta P_{fsl} A_c (1-\alpha_g)}{\Delta P_{fsl0} A_c} = \alpha'_{sl} \frac{1}{(1-\alpha_g)^2} \alpha''_{sl} = \frac{\alpha_{sl}}{(1-\alpha_g)^2}$$

$$\Rightarrow \frac{\Delta P_{fsl}}{\Delta P_{fsl0}} = \frac{\alpha_{sl}}{(1-\alpha_g)^3} \tag{3.11}$$

where ΔP_{fsl0} represents a frictional pressure drop because of slurry flow only in the column. The subscript 'T', 'sl0', and 'sl' refer to the slurry-gas three-phase, slurry phase only, and slurry actual velocity, $(u_{sl})_{tp} = (u_{sl})_{l0} / (1-\alpha_g)$, respectively. The quantity α_{sl} is equal to $\alpha'_{sl}\alpha''_{sl}$. The cross-sectional area for slurry flow is $(1-\alpha_g)$ times the cross-sectional area of the column. The parameter α'_{sl} represents the ratio f_{slg} / f_{sl0} and α''_{sl} is (area of contact)$_T$ / (area of contact)$_{sl0}$. It was also presumed that the contact area of the liquid phase with the column in the three-phase system is equal to the contact area of slurry with the column wall when only the slurry flows. In a similar way, after performing an overall momentum balance for a gas phase in a three-phase system, the following relation can be obtained

$$\frac{\Delta P_{fg}}{\Delta P_{fg0}} = \frac{\beta_g}{\alpha_g^3} \tag{3.12}$$

where ΔP_{fg0} denotes the frictional pressure drop when only gas-phase flows in the column. The parameter β_g is defined by

$$\beta_g = \alpha'_g \alpha''_g \tag{3.13}$$

where α''_g is the parameter related to the gas phase and its magnitude is based on the number of gas bubbles which are in contact with the column wall. Pressure drop due to only slurry flow in the column can be calculated as

$$\Delta P_{fsl0} = \frac{2 f_{sl0} \rho_{sl} u_{sl}^2 \Delta Z}{d_{be}} \tag{3.14}$$

where f_{sl0} denotes the friction factor when the only slurry flows. Similarly, the pressure drop because of the only gas flow in the column can be estimated as

$$\Delta P_{fg0} = \frac{2 f_{fg0} \rho_g u_{sg}^2 \Delta Z}{d_{be}} \tag{3.15}$$

where f_{fg0} is friction factor when the only gas flows in the column. Friction factor for the laminar flow condition can be calculated as (Majumder, 2016)

$$f_0 = \frac{16}{\mathrm{Re}_0} \qquad \mathrm{Re}_0 < 2100 \tag{3.16}$$

for transition flow

$$f_0 = 0.125(0.0112 + \mathrm{Re}_0^{-0.3185}) \qquad 2100 < \mathrm{Re}_0 < 4000 \tag{3.17}$$

for turbulent flow condition

$$f_0 = \frac{0.079}{\mathrm{Re}_0^{0.25}} \qquad \mathrm{Re}_0 > 4000 \tag{3.18}$$

3.4.1.3. Energy dissipation by phase interaction

In a three-phase counter-current vertical system, bubbles and slurry flow in the opposite direction, resulting in a significant phase interaction. Therefore, it is important to consider the pressure drop that is caused by the phase interaction. The pressure drop as a result of the phase interaction can be expressed as (Majumder et al., 2006)

$$\Delta P_{FD} = \frac{1}{8} c_d \rho_{sl} u_s^2 \tag{3.19}$$

where c_d and u_s stand for drag coefficient and slip velocity, respectively. The relative velocity between the gas bubble and slurry is known as slip velocity. For a counter-current flow system, slip velocity is defined by

$$u_s = \frac{u_{sg}}{\alpha_g} + \frac{u_{sl}}{(1-\alpha_g)} \tag{3.20}$$

The rate of energy dissipation based on the slip of phases is given by

$$E_{slip} = \Delta P_{FD} Q_m = \frac{1}{8} c_d \rho_{sl} u_s^2 A_c \left(\frac{G}{\rho_g} + \frac{L_s}{\rho_{sl}} \right) \tag{3.21}$$

The following correlations can be used to calculate the drag coefficient as per experimental conditions (Joshi et al., 1998)

$$c_d = 24/\mathrm{Re}_b \qquad \mathrm{Re}_b \le 1 \tag{3.22}$$

$$c_d = 14\mathrm{Re}_b^{-0.53} \qquad 1 \le \mathrm{Re}_b \le 14.5 Mo^{-0.154} \tag{3.23}$$

$$c_d = 0.115\mathrm{Re}_b^{1.25} Mo^{0.27} \qquad 14.5 Mo^{-0.154} \le \mathrm{Re}_b \le 17.95 Mo^{-0.1985} \tag{3.24}$$

$$c_d = 2.66 \qquad \mathrm{Re}_b \ge 17.95 Mo^{-0.1985} \tag{3.25}$$

where Re_b and Mo are the bubble Reynolds number and Morton number, respectively. The Bubble Reynolds number is defined by

$$\mathrm{Re}_b = \frac{\rho_{sl} u_s d_{32}}{\mu_{sl}} \tag{3.26}$$

where d_{32} is the Sauter mean bubble diameter. The Morton number is defined as

$$Mo = \frac{g\mu_{sl}^4 (\rho_{sl} - \rho_g)}{\rho_{sl}^2 \sigma_{sl}^3} \tag{3.27}$$

3.4.1.4. Energy dissipation because of bubble generation

The energy dissipation rate during the generation of gas bubbles is equal to the rate of bubble formation times the energy dissipation in the generation of a single gas bubble. Bubble generation rate is the ratio of gas flow rate and volume of a single bubble. The rate of bubble generation can be expressed as

$$N_b = \frac{6GA_c}{\rho_g \pi d_{32}^3} \tag{3.28}$$

where N_b represents the bubble generation rate. The amount of energy loss for the generation of a single bubble is given as $\sigma_{sl}\pi d_{32}^2$. So, the total amount of energy loss in the generation of N number of bubbles is (Majumder, 2016)

$$E_b = N_b \sigma_{sl} \pi d_{32}^2 \tag{3.29}$$

Hence, substituting Eq. (3.28) into Eq. (3.29) yields the energy dissipation rate by bubble generation as

$$E_b = \frac{6GA_c\sigma_{sl}}{\rho_g d_{32}} \tag{3.30}$$

3.4.1.5. Energy dissipation due to wetting

The energy dissipation rate because of liquid wettability (E_w) of the column wall can be expressed as (Parmar and Majumder, 2014)

$$E_w = \frac{\pi d_{be} u_{sl} \sigma_{sl}}{1-\alpha_g} \tag{3.31}$$

where d_{be} is an equivalent column diameter.

3.4.1.6. Estimation of the parameter of the model

Rearrangement of Eq. (3.8) yields the following equation (Eq. 3.32)

$$\Delta P_T\left[\frac{L_s}{\rho_{sl}}+\frac{G}{\rho_g}\right]-(L_s+G)g\Delta Z-\frac{\Delta P_{fg}G}{\rho_g}-\frac{(E_b+E_{slip}+E_w)}{A_c}=\frac{\Delta P_{fsl}L_s}{\rho_{sl}} \tag{3.32}$$

All the terms on the left-hand side of the Eq. (3.32) can be calculated using the experimental data. Putting the frictional pressure drop due to slurry flow, Eq. (3.11) into Eq. (3.12), yields

$$\Delta P_T\left[\frac{L_s}{\rho_{sl}}+\frac{G}{\rho_g}\right]-(L_s+G)g\Delta Z-\frac{\Delta P_{fg}G}{\rho_g}-\frac{(E_b+E_{slip}+E_w)}{A_c}=\frac{\Delta P_{fsl0}\alpha_{sl}L_s}{(1-\alpha_g)^3\rho_{sl}} \tag{3.33}$$

In Eq. (3.33), all terms are known except α_{sl}, which can be expressed as

$$\alpha_{sl} = \frac{(1-\alpha_g)^3 \rho_{sl}}{\Delta P_{fsl0} L_s}\left[\Delta P_T\left(\frac{L_s}{\rho_{sl}} + \frac{G}{\rho_g}\right) - [L_s + G]g\Delta Z - \frac{\Delta P_{fg} G}{\rho_g} - \frac{(E_b + E_{slip} + E_w)}{A_c}\right] \tag{3.34}$$

The value of α_{sl} can be obtained from the experimental value. Once, the value of α_{sl} is evaluated, the three-phase effective friction factor, f_T, can be deduced from the following relation

$$f_T = \frac{\alpha_{sl}}{\alpha_l''} f_{sl0} \tag{3.35}$$

The bubble-slurry interfacial shear stress (τ_i) is coupled with the three-phase effective friction factor (f_T), which can be expressed as

$$\tau_i = \frac{0.5 f_T \rho_{sl} (u_{sl} - u_{sg})^2}{(1-\alpha_g)^2} \tag{3.36}$$

Substituting the value of three-phase effective friction factor from Eq. (3.35) into Eq. (3.36), the interfacial shear stress can be represented by

$$\tau_i = \frac{0.5\alpha_{sl} f_{sl0} \rho_{sl} (u_{sl} - u_{sg})^2}{\alpha_l''(1-\alpha_g)^2} \tag{3.37}$$

3.5. Uncertainty analysis

The ranges of mean, standard deviation, standard uncertainty, and the relative uncertainty of experimentally determined quantities are given in Table 3.2.

Table 3.2 The range of uncertainties of the experimentally determined quantities.

Quantities	Mean, $\bar{x}$	*STDEV*	*U*	U_r (%)
ΔP_f (without surfactant)	2.72 – 26.9	2.81×10^{-1} – 3.14×10^{-1}	1.26×10^{-1} – 1.40×10^{-1}	4.50 – 4.66
ΔP_f (with surfactant)	2.57 – 22.3	2.75×10^{-1} – 2.32	1.23×10^{-1} – 1.04	4.65 – 4.77
τ_i (without surfactant)	3.12×10^{-3} – 27.0	9.71×10^{-4} – 1.55	4.34×10^{-4} – 6.93×10^{-1}	2.57 – 13.94
τ_i (with surfactant)	3.27×10^{-3} – 1.01×10^{1}	2.09×10^{-4} – 2.15×10^{-1}	9.33×10^{-5} – 9.63×10^{-2}	0.96 – 2.86

u_{sg}	$4.23 \times 10^{-2} - 9.59 \times 10^{-3}$	$9.06 \times 10^{-4} - 1.53 \times 10^{-3}$	$3.70 \times 10^{-4} - 6.26 \times 10^{-4}$	$8.74 \times 10^{-1} - 6.54$
u_{sl}	$1.66 \times 10^{-2} - 5.70 \times 10^{-2}$	$1.71 \times 10^{-3} - 1.92 \times 10^{-3}$	$6.47 \times 10^{-4} - 7.26 \times 10^{-4}$	1.27 – 3.89

3.6. Results and discussion

3.6.1. Effect of different variables on the frictional pressure drop

Frictional pressure drop is an important design parameter that must be taken into account during the multiphase flow. Frictional pressure drop characteristics in the three-phase flow are completely different from that of the two-phase flow. So, a detailed analysis of the effect of the superficial gas velocity, the superficial slurry velocity, the particle concentration, the particle size, and the bubble size on the frictional pressure drop has been presented in the following sections.

3.6.1.1. Influence of superficial gas and slurry velocity on frictional pressure drop

Influence of superficial gas velocity (u_{sg}), at different superficial slurry velocities (u_{sl} = 0.018 – 0.057 m/s) on the frictional pressure drop (ΔP_f) at a fixed particle concentration (w_s = 3.0 wt.%) and particle size (d_p = 65.29 μm) is shown in Fig. 3.2. It is seen that the ΔP_f increases with an increase in the u_{sg}, while it decreases with an increase in the u_{sl}. The increase in the ΔP_f with the u_{sg} is because of the generation of a substantial amount of gas bubbles, which increases the actual liquid velocity in the column and consecutively increases the interaction between the fluid and column wall. In a counter-current operation, the bubbles move upward, while the slurry in a downward direction. Therefore, a bubble has to overcome the drag forces exerted by the slurry. It was noted that in the three-phase semi-batch operation, the ΔP_f was the sum of the cumulative effect of the fluid-wall, particle-wall, and fluid-particle frictional losses (Prakash et al., 2018b). The ΔP_f of the fluid-wall has reportedly contributed around 99%, and the particle-wall and fluid-particle frictional pressure has contributed to the remaining 1%. In the case of continuous counter-current operation, however, the interaction between the slurry and the gas phase must be greater than that of semi-batch operation. A bubble in a multiphase system contains pressure energy at the bottom and potential energy at the top (Vitankar et al., 2002). As the bubble rises, the potential energy increases gradually, whereas the pressure energy decreases. So, when the gas bubble rises, the energy associated with the bubble decreases, and the same amount disappears in the form of

friction between the bubble and the slurry (Vitankar et al., 2002). The reduction in the ΔP_f with an increase in the u_{sl} is due to the increase in the drag experienced by the gas bubbles and bubble coalescence rate. As the bubble size increases, the ΔP_f decreases. Several researchers (Majumder et al., 2007; Mandal et al., 2004; Tang et al., 2013) have also reported a similar trend in ΔP_f characteristics with superficial gas and liquid velocity.

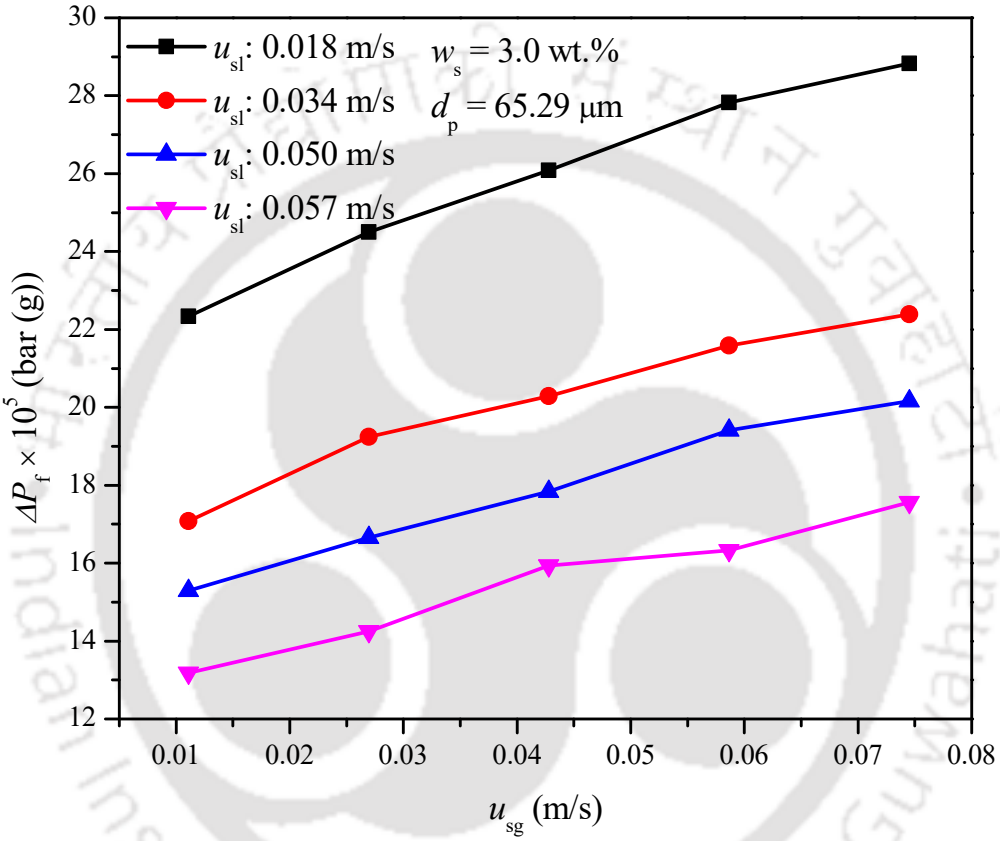

Fig. 3.2. Influence of superficial gas and slurry velocity on the ΔP_f.

3.6.1.2. Influence of particle concentration on frictional pressure drop

Variation in ΔP_f with the particle concentration (at w_s = 0.5 – 3.0 wt.%) at different u_{sg} = 0.011 – 0.075 m/s and fixed d_p = 242.72 μm and u_{sl} = 0.018 m/s is presented in Fig. 3.3. It is noticed that the ΔP_f is increasing with an increase in the w_s at all the u_{sg}. Several authors have reported a direct proportionality of w_s to the ΔP_f (Peker et al., 2008; Wilson et al., 2006). The ΔP_f contribution becomes significant when the slurry velocity or viscosity of the system is changed (Descamps et al., 2008). Present experimental results follow the same trend of other researchers (Chung et al.,

1998; Ferre and Shook, 1998; Sivaiah and Majumder, 2012), where they reported that the increase in apparent density and the total wall stress of the column cause an increase in the ΔP_f. As particle concentration increases, the slurry viscosity and density also increase, which intensifies the bubble coalescence rate, therefore, the bubble size increases (Li and Prakash, 2000; Manjrekar and Dudukovic, 2015; Moshtari et al., 2007; Orvalho et al., 2018; Tyagi and Buwa, 2017).

The ΔP_f is also influenced by the viscous sub-layer characteristics and boundary layer thickness. Moreover, if the intensity of the drag in the viscous sub-layer is reduced, it directly affects the degree of reduction in ΔP_f. According to Nouri et al. (2013), the reduction in ΔP_f is more effective if the bubble size in the vicinity of a wall is smaller than the boundary layer thickness and larger than that of the viscous sub-layer. So, it can be deduced that the presence of particles causes an increase in the bubble size, which in turn increases the slurry momentum, consequently, increases the ΔP_f.

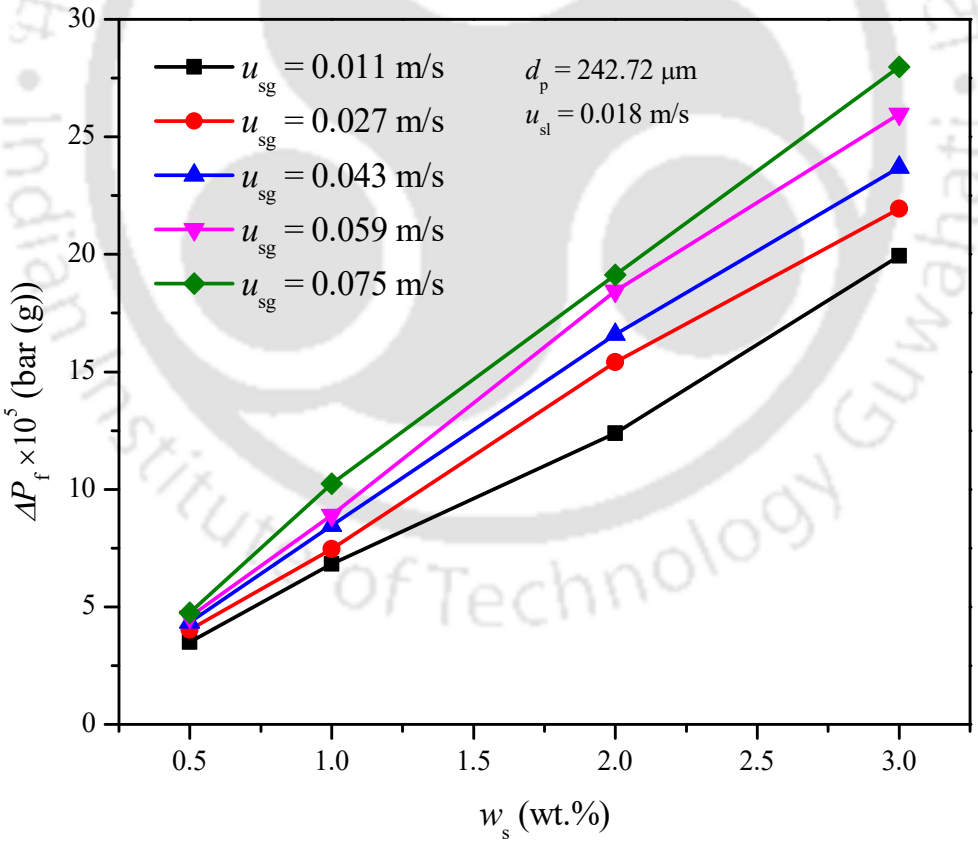

Fig. 3.3. Variation of the ΔP_f with particle concentration.

Comparison of the ΔP_f with and without surfactant is presented in Fig. 3.4. It is noticed that the increase in the particle concentration from 0.5 to 3.0 wt.% (in both with and without surfactant) increases the ΔP_f at all the u_{sg}. It is also noted that the ΔP_f is lower for a surfactant solution (MIBC, c_f = 6 ppm) at all particle concentrations compared to that of a surfactant-free system. At minimum particle concentrations, say 0.5 wt.%, the difference in ΔP_f in the presence and absence of surfactant is small. The reduction in ΔP_f is approximately 14.81% (at w_s = 0.5 wt.%), 10.33% (at w_s = 1.0 wt.%), 4.03% (at w_s = 2.0 wt.%), and 8.79% (at w_s = 3.0 wt.%) at u_{sg} of 0.075 m/s.

The decrease in both the bubble-slurry interface drag and near-wall drag after surfactant addition is attributed to a reduction in the fluid-wall ΔP_f. According to Wilson (1989), drag reduction is attributed to the thickening of the near-wall sublayer in the case of laminar flow. A drag reducing element (i.e., surfactant) improves the viscosity of the liquid, thereby, reducing the transport of both momentum and vorticity in the turbulent region. A large number of gas bubbles rise in the middle of the column in the surfactant-free solution, while a small number of bubbles in the vicinity of the wall move downward and circulate. The circulation of bubbles in the wall region increases the slurry momentum. As a result, the ΔP_f increases. However, in the surfactant solution, the bubbles are smaller and more homogenous in size, so that the bubble size distributions in the column is almost narrow. Consequently, the circulation velocity nearby the wall reduces, resulting in a reduction in the ΔP_f. According to Guin et al. (1996), drag reduction depends on the position of the maximum number of bubbles in the column. They stated that the degree of drag reduction reduces as the bubbles move away from the column wall. However, Merkle and Deutsch (1989) and Shen et al. (2006) observed that the drag reduction depending on the flow characteristics rather than any specific bubble size. Fontaine et al. (1999) reported that a reduction in bubble size resulted in a reduction in drag force. For effective drag reduction, the size of the bubble must be greater than the viscous sub-layer and less than the thickness of the boundary layer (Nouri et al., 2013). When the bubble diameters exceed the boundary layer thickness by a certain value, the skin friction decreases irrespective of the flow rate.

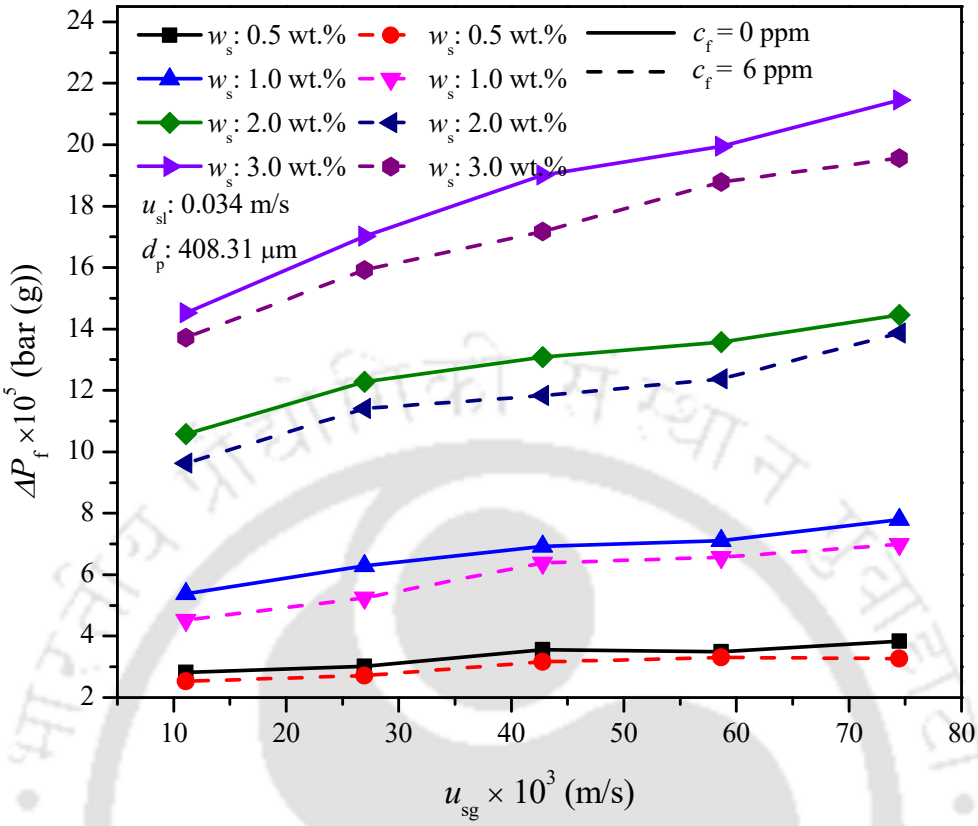

Fig. 3.4. Comparison of the ΔP_f with (c_f = 6 ppm) and without (c_f = 0 ppm) surfactant.

3.6.1.3. Influence of particle size on frictional pressure drop

Particle size in the counter-current slurry system also plays an important role all through its operation for solid handling. Therefore, it is essential to assess the influence of the particle size on the ΔP_f. The influence of different particle sizes (at d_p = 65.29, 242.72, 408.31, and 517 µm) at various u_{sg} on the ΔP_f at fixed u_{sl} = 0.018 m/s and fixed w_s = 3.0 wt.% is given in Fig. 3.5. The ΔP_f reduces as the average particle size increases for all u_{sg}. The behavior of ΔP_f characteristics in the presence of MIBC surfactant and in the absence of particles (without MIBC) is also shown in Fig. 3.5. It was noticed that the ΔP_f was lower in the case of a system with MIBC for all the u_{sg}. In the absence of particles (without MIBC), the ΔP_f was lower compared to that of the presence of particles. As particle size changes from 65.29 to 517.0 µm, the decrease in ΔP_f was noticed to be 14.24% and 9.18% at u_{sg} = 0.011 m/s and u_{sg} = 0.057 m/s, respectively. Similarly, in the case of the presence of a surfactant, a reduction in ΔP_f was 16.07% and 12.56% at u_{sg} = 0.011 m/s and u_{sg} = 0.057 m/s, respectively. A similar trend of a reduction in the ΔP_f with an increase in particle size

at a fixed w_s = 1.0 wt.% with a surfactant (MIBC) is shown in Fig. 3.6. Many authors have also confirmed that an increase in the pressure drop after particle loading is due to increased bulk density and wall shear stresses (Chung et al., 1998; Ferre and Shook, 1998; Sivaiah and Majumder, 2012).

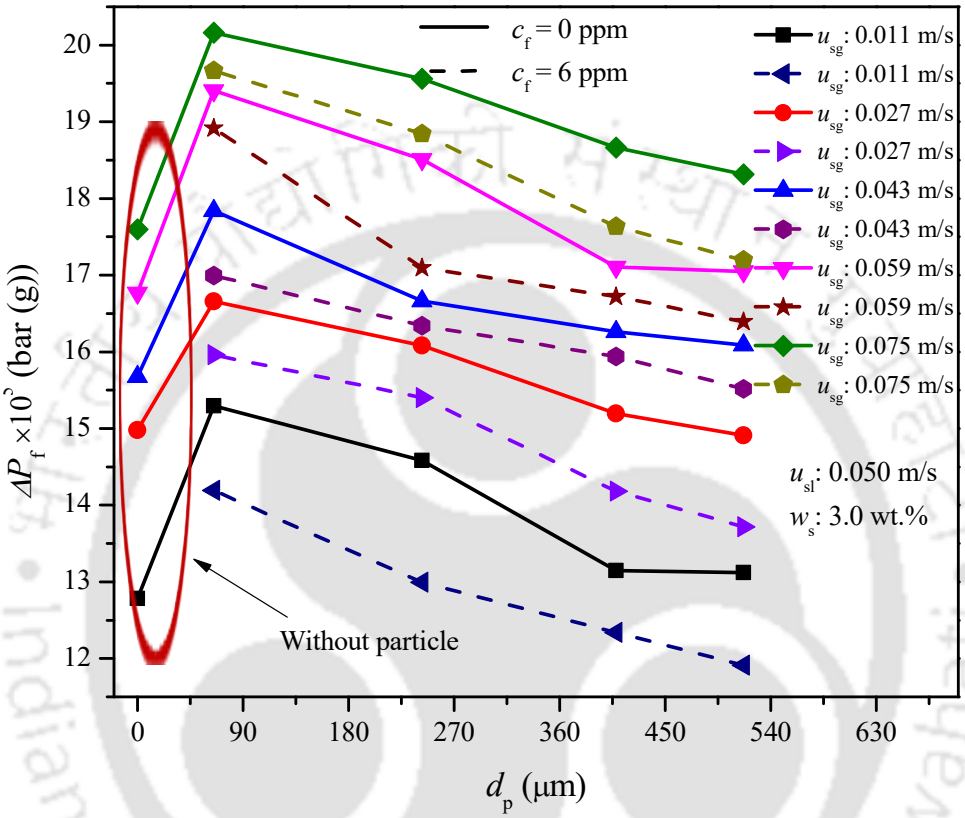

Fig. 3.5. Frictional pressure drop in the presence and absence of surfactant and particle, respectively.

Change in slurry viscosity is an imperative factor that alters the ΔP_f behavior of the slurry column. Higher slurry viscosity in the case of small particle sizes is because of attractive particle interaction (Kawatra and Eisele, 1988b; Senapati et al., 2009; Zhou et al., 1993). At the fixed mass of particles, if the particle size is reduced, the net result will be an increase in the number of particles. Hence, it is worth to say that the system viscosity is higher with the fine particles compared to coarser particles.

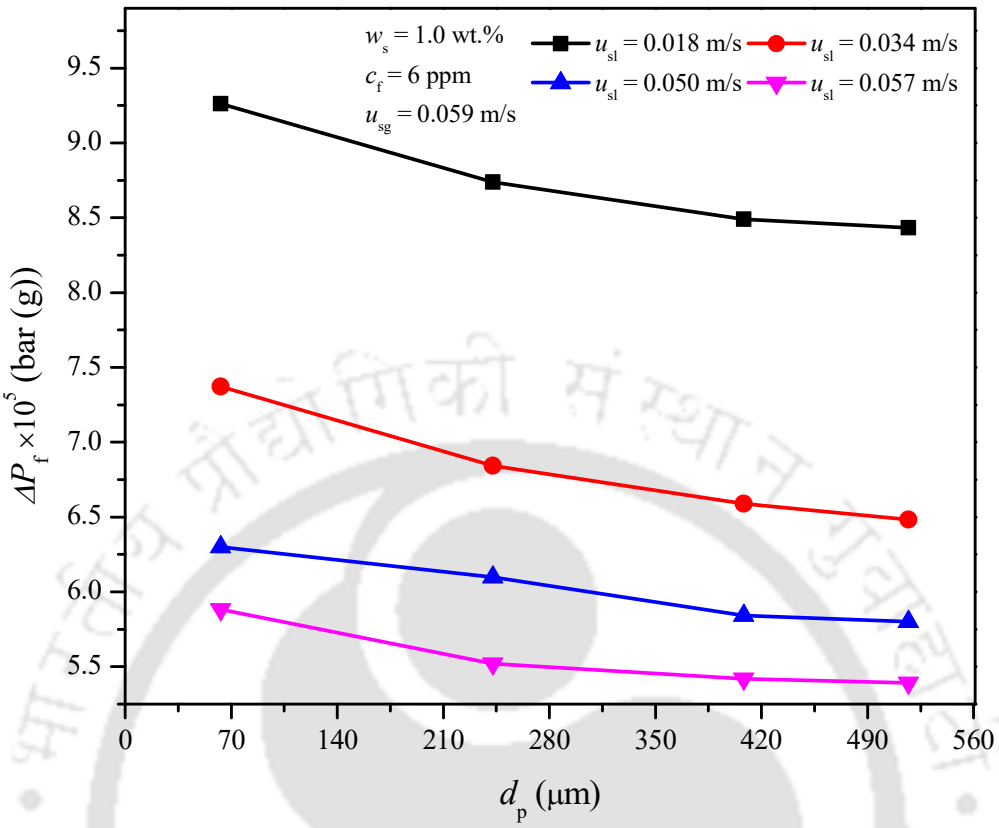

Fig. 3.6 Variation of the ΔP_f at various particle sizes in the presence of a surfactant.

3.6.1.4. Effect of bubble size on frictional pressure drop

Effect of the Sauter mean bubble diameter (d_{32}) on ΔP_f in the presence of a particle (at d_p = 65.29 μm and w_s = 2.0 wt.%) for the u_{sl} range of 0.018 – 0.057 m/s is shown in Fig. 3.7. It is noticed that the ΔP_f increased with the increase in d_{32}. The larger bubble does not significantly reduce the drag and causes more turbulence, resulting in an increased ΔP_f. Yao et al. (2018) also reported that larger bubbles increase ΔP_f. The presence of small bubbles effectively reduces the pressure drop as compared to larger bubbles (Guet et al., 2003). A reduction of pressure drop in the presence of microbubble is also reported by Nouri et al. (2013). According to Nouri et al. (2013), a pressure reduction of 35% and 13% is seen at 9% and 0.6% void fraction, respectively. According to Li et al. (2016), the bubble-induced pressure is the cumulative effect of the unbalanced pressure between the gas bubbles and the ambient fluid flow, which estimates the influence of the high-pressure gas to the dynamic pressure and the high-speed fluid motion around the bubbles. Local high pressure is generated when a spherical gas bubble collapses (Rayleigh, 1917). The generated local high

pressure can affect the surrounding fluid medium (Harrison, 1952). The pressure field around a non-spherical bubble differs completely from the spherical bubble. There are two main reasons for the bubble induced pressure: (i) the first is due to the pressure of the gas bubble, and (ii) the second is caused by the bubble movement.

Larger bubbles produce higher velocity fluctuations in the middle zone of the column due to the higher slip velocity of the bubbles. Both primarily disturb the flow and creates more vorticity in the system. The important role of the gas bubbles is to decrease the weight of the mixture in the core zone, and when it is in hydrostatic equilibrium, no lateral transport of the bubbles occurs. If the Stokes numbers ($St = \tau_b / \tau_k$) for the bubble sizes are more than 1, the bubble-response time-scales are greater than the Kolmogorov time-scale (Lu and Tryggvason, 2007). Consequently, the bubbles do not follow the surrounding liquid and are not trapped by the coherent vortices near the walls. Here, all bubbles move to the central zone of the column because of the lift force induced by the high shear stress close to the column wall. In the central part of the column, the vorticity is because of the bubble motion. Tomiyama et al. (2002) also studied the effect of bubble size on phase flow behavior. They used a wide range of bubble sizes to investigate the transverse movement of bubbles in an upward shear flow. The author pointed out that the lateral movement of the gas bubbles depends on bubble size, viz., in the upward column, the small gas bubbles prone to move to the column wall and result in a wall-peaked bubble distribution, but the large bubbles tend to move to the center of the column, resulting in a core-peaked bubble distribution. The lateral movement of the bubble near the wall is dominated by the shear-induced lift force (Auton, 1987), which consists of the bubble slip velocity and the flow circulation around the bubble. The bubble slip velocity significantly affects the lift force, so that the small bubbles tend to move towards the wall (Fujiwara et al., 2004).

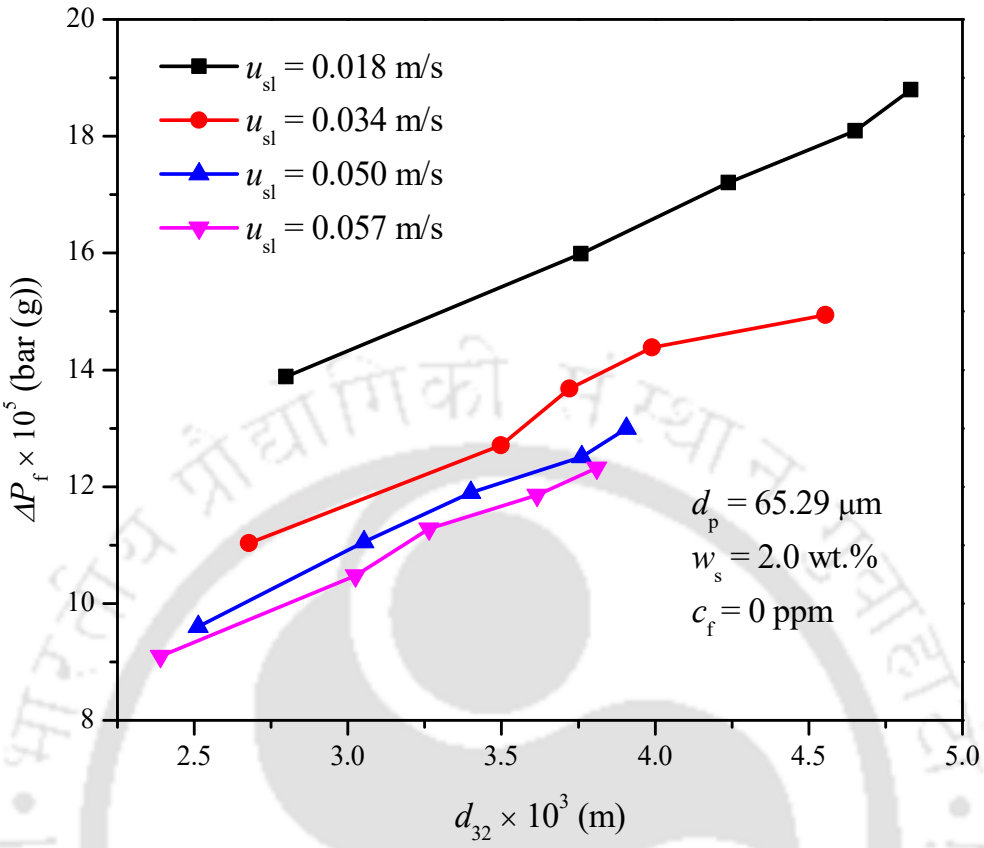

Fig. 3.7. Effect of Sauter mean bubble diameter on the ΔP_f in the absence of surfactant.

3.6.1.5. Development of the correlation model

The ΔP_f is influenced by various process variables such as superficial gas (u_{sg}) and slurry velocity (u_{sl}), slurry density (ρ_{sl}), particle diameter (d_p), slurry surface tension (σ_{sl}), particle concentration (c_s), column diameter (d_c) and distance between the pressure ports (ΔZ). Therefore, the proposed empirical correlation for the ΔP_f is expressed as follows:

$$\frac{\Delta P_{frictional} d_c}{\Delta Z \rho_{sl} u_{sg}^2} = 1.108 \left(\frac{u_{sg}}{u_{sl}}\right)^{-0.767} \left(\frac{\rho_{sl} u_{sl}^2 d_p}{\sigma_{sl}}\right)^{-0.565} \left(\frac{g d_p}{u_{sg}^2}\right)^{0.537} \left(\frac{c_s}{\rho_{sl}}\right)^{0.952} \quad (3.38)$$

The correlation coefficients (R^2) and the standard error of Eq. (3.38) is 0.99 and 0.034, respectively. The validity range of the individual dimensionless group was reported in the Eq. (3.38) is: $0.193 \le u_{sg}/u_{sl} \le 4.178$, $2\times10^{-4} \le \rho_{sl} u_{sl}^2 d_p / \sigma_{sl} \le 2.43\times10^{-2}$, $0.111 \le g d_p / u_{sg}^2 \le 41.191$, and $0.015 \le c_s/\rho_{sl} \le 0.088$. The correlation (Eq. 3.38) satisfactorily predicts the experimental

values in the error range of ± 19.83% and the absolute average relative error (AARE) of about 6.34%. Parity of the experimental and predicted result (obtained from Eq. (3.38)) is presented in Fig. 3.8.

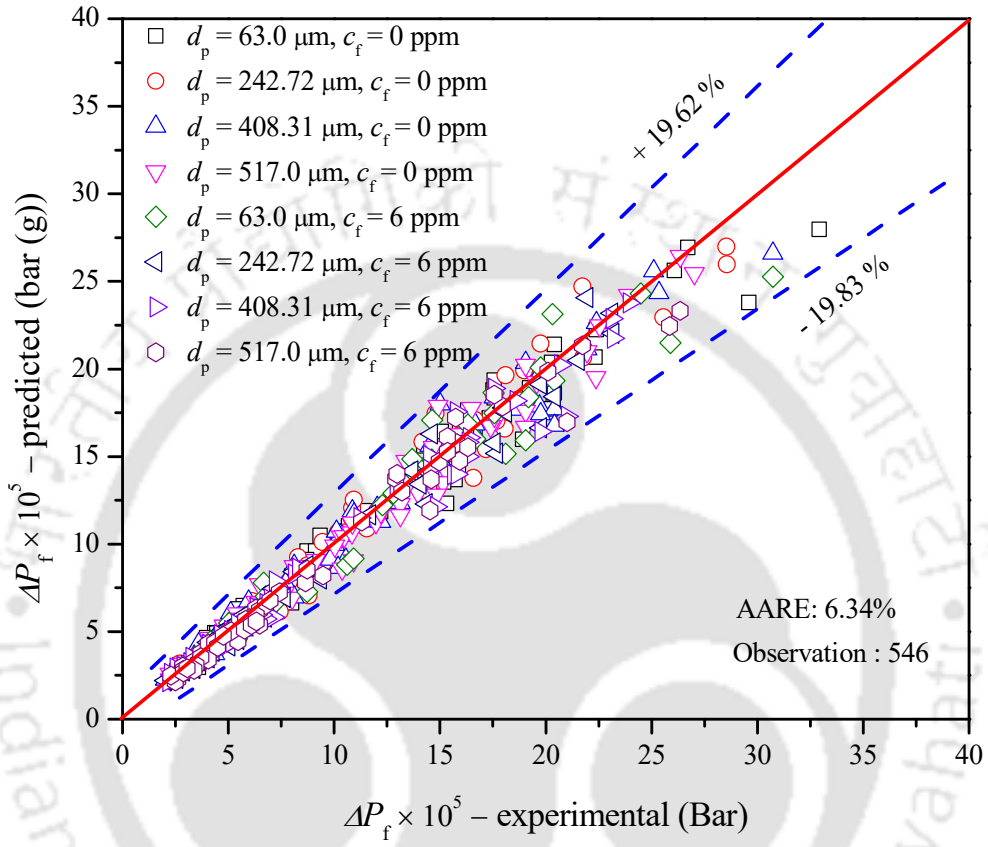

Fig. 3.8. Comparison between the experimental and the predicted value of ΔP_f.

3.6.2. Effect of different variables on interfacial shear stress

The interfacial shear stress characteristic of the slurry system is different from the two-phase system. It has been noted that the surfactant addition has a dramatic effect on the vertical counter-current gas-slurry flow. Experimental data for the total pressure drop in different operating conditions were obtained for the rectangular counter-current slurry column. The bubble-slurry interfacial shear stress was calculated based on the developed mechanistic model (section 4.1), which includes a mechanical energy balance of both the gas and the slurry phase considering the energy dissipation rate because of the generation of gas bubbles, the energy dissipation rate as a

result of a slip of gas-slurry interface, and energy dissipation rate caused by wetting of the column wall using experimentally calculated total pressure drop, gas holdup, and bubble size.

3.6.2.1. Effect of superficial gas and slurry velocity on interfacial shear stress

Effect of both superficial gas (u_{sg} = 0.011 – 0.075 m/s) and slurry velocities (u_{sl} = 0.018 – 0.057 m/s) in the presence of particles (at d_p = 65.29 μm) at a fixed particle concentration (w_s = 2.0 wt.%) on the bubble-slurry interfacial shear stress is shown in Fig. 3.9. It is noted that interfacial shear stress increases with an increase in the u_{sg}, while it decreases with an increase in the u_{sl}. A complex interaction between the bubble-slurry interfaces occurs in the vertical counter-current flow. The intensity of interfacial bubble-slurry interactions depends on the magnitude of gas and slurry, the flow direction, the particle concentration, the average particle size, the slurry viscosity, the slurry surface tension, and the bubble size. At the lower u_{sg}, the interaction of bubbles between the phases is weak. Although, with an increase in the u_{sg}, the bubble number density appears to be large when the bubble begins to interact with each other and with slurry directly or indirectly (due to the bubble-bubble collision or bubble-slurry interactions), and effects of wakes produced by other bubbles. Therefore, the bubble-slurry interfacial shear stress increases with an increase in the u_{sg}. Bubble-slurry interfacial shear stress varies non-linearly at lower slurry velocities because the drag exerted by the slurry on the bubbles is significantly low. The rising velocities of the bubbles are higher (due to the low u_{sl}), and there is an almost homogeneous concentration of bubbles in the column. As the u_{sl} increases, the drag offered to the bubbles is significantly higher, which reduces the rising velocity of the gas bubbles. This produces a very dense bubble population at the lower segment of the column. It causes an axial imbalance in the gas bubbles along the length of the column. The variation of the bubble concentration results in a non-linear gas-slurry interfacial shear stress. It is seen that the increase in the interfacial shear stress is more at a lower u_{sl} = 0.018 m/s compared to a higher u_{sl} > 0.018 m/s. An increase in the u_{sl} can also cause bubbles to break up, which can also contribute to a decrease in interfacial shear stress. The rising velocity of bubbles at a low u_{sl} is high in comparison to the high u_{sl} due to the increased drag on bubbles, and this may also reduce the interfacial shear stress. Typical values of interfacial shear stress, energy dissipation rate because of the slip of gas-slurry interface, energy loss because of wetting, and friction factor is shown in Table 3.3.

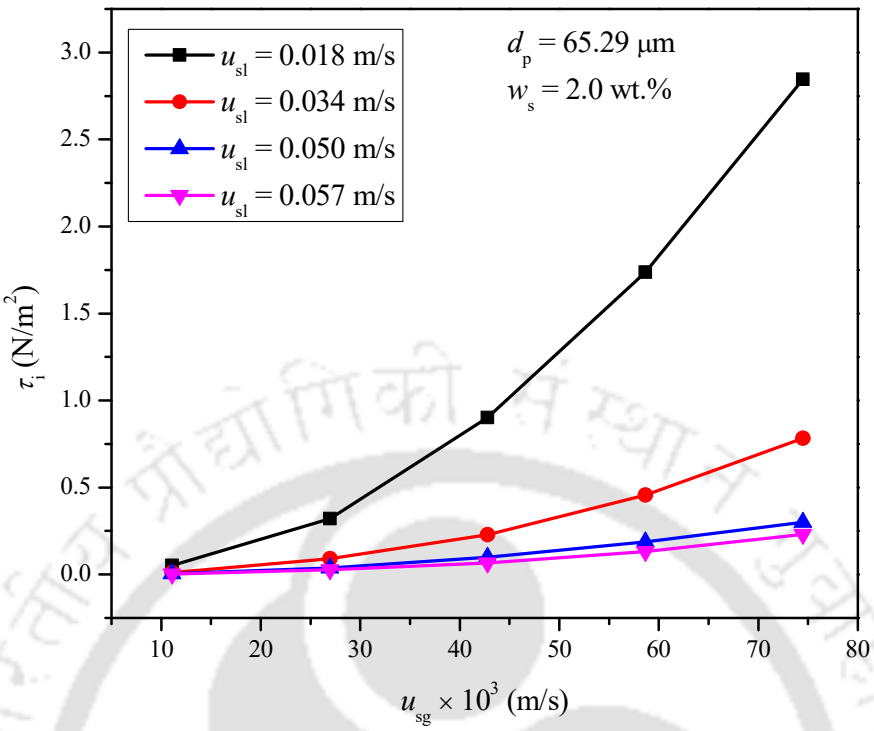

Fig. 3.9. Effect of superficial gas and slurry velocity on the interfacial shear stress in the surfactant-free system.

Table 3.3 Typical values of the interfacial shear stress, frictional pressure drop, energy dissipation due to slip, wetting, and friction factor in different experimental conditions.

Superficial gas velocity $\times 10^2$, u_{sg} (m/s)	Superficial slurry velocity $\times 10^2$, u_{sl} (m/s)	Surfactant concentration, c_f (ppm)	Particle concentration, w_s (wt.%)	Particle diameter, d_p (μm)	Interfacial shear stress, τ_i (N/m^2)	Frictional pressure drop, ΔP_f (bar (g))	Energy dissipation rate due to slip of gas-slurry interface $\times 10^3$, E_{slip} (Nm/s)	Energy loss because of wetting $\times 10^4$, E_w (Nm/s)	Friction factor, $\alpha_{sl} f_{sl0} / \alpha''_l$ (–)
1.10	1.80	0	0.5	65.29	0.054	3.675	6.66	2.24	251.210
4.30	3.40	0	0.5	65.29	0.193	3.597	1.78	4.87	7.399
7.50	5.70	0	0.5	65.29	0.198	3.052	2.68	0.11	0.437
7.50	1.80	0	1.0	65.29	2.71	5.458	2.21	2.88	11.498
5.80	1.80	0	2.0	65.29	1.736	20.325	1.63	2.92	20.549
5.80	1.80	0	3.0	242.72	8.015	25.970	1.55	3.07	19.548
7.50	3.30	0	3.0	408.31	5.604	21.453	1.70	6.58	2.2864
7.50	5.00	0	0.5	517.0	2.579	3.052	2.01	8.86	0.612
5.80	5.80	0	3.0	517.0	1.331	19.047	2.40	0.11	1.039
5.80	3.40	6	3.0	242.72	1.544	20.407	1.54	5.07	3.614
4.28	3.36	6	0.5	242.72	1.590	3.165	1.74	4.40	6.113
4.20	1.80	6	1.0	242.72	5.739	7.204	1.49	2.32	29.293
1.10	1.80	6	0.5	517.0	0.439	3.385	2.78	2.08	207.272
4.28	1.78	6	3.0	517.0	7.069	21.734	1.47	2.33	29.171

3.6.2.2. Effect of surfactant addition on interfacial shear stress

The presence of a surfactant significantly influences the flow characteristics of the phases in the rectangular slurry bubble column. Effect of the presence and absence of surfactant as a function of the u_{sg} at fixed u_{sl} and fixed average d_p at two different w_s = 0.5 and 3.0 wt.% on interfacial shear stress is shown in Fig. 3.10. It is noticed that interfacial shear stress in the presence of surfactant is lower than that of an absence of surfactant at both w_s = 0.5 and 3.0 wt.% for all u_{sg}. A negligible difference in interfacial shear stress is observed in the presence of surfactant at 0.5 wt.% and 3.0 wt.% particles. It shows that the surfactant addition has a substantial effect on the bubble-slurry interfacial shear stress. It implies that the particle concentration effect on the interfacial shear stress is independent of the particle concentration in the presence of the surfactant. Therefore, it can be concluded that the surfactant addition can prominently reduce the interfacial shear stress between bubbles and slurry. The addition of a surfactant to the liquid significantly reduces the surface tension, resulting in a large number of bubbles. The influence of surfactant is usually interconnected to the following series of events: the surfactant adsorbs on the air-water interface and is concentrated to the rear surface of a rising gas bubble due to the mobility of its surface; as a result, a surface tension gradient is created that generates a force that opposes the motion, then there is a resultant increase in drag coefficient which causes a reduction in the rising velocity (Dukhin et al., 1998). Reducing the surface tension of the liquid improves the gas bubble's breakup rate, which in turn promotes the existence of smaller bubbles when the breakage rate surpasses the bubble coalescence rate. The bubble generation rate also improves by reducing the surface tension due to the requirement of less momentum to detach the gas bubbles from the sparger pores and also the time for the bubble growth before detachment reduces (Kulkarni and Joshi, 2005).

The presence of particles increases the apparent viscosity of the system, thus, the bubble coalescence rate intensifies (Orvalho et al., 2018; Sarhan et al., 2018c). Nevertheless, surfactant addition reduces the bubble coalescence rate, thus, produces small bubbles. As it was concluded in an earlier discussion that the small bubble is more useful for reducing drag, frictional pressure drop, and interfacial shear stress. Therefore, the same argument can be applied to the reason for reducing interfacial shear stress in the presence of a surfactant. After surfactant addition a reduction in interfacial shear stress was approximately 6.78% at 0.5 wt.% particle concentration (at u_{sg} = 0.075 m/s). Similarly, after surfactant addition, a reduction in interfacial shear stress was

about 20.5% at 3.0 wt.% particle concentration at the same superficial gas velocity (at u_{sg} = 0.075 m/s).

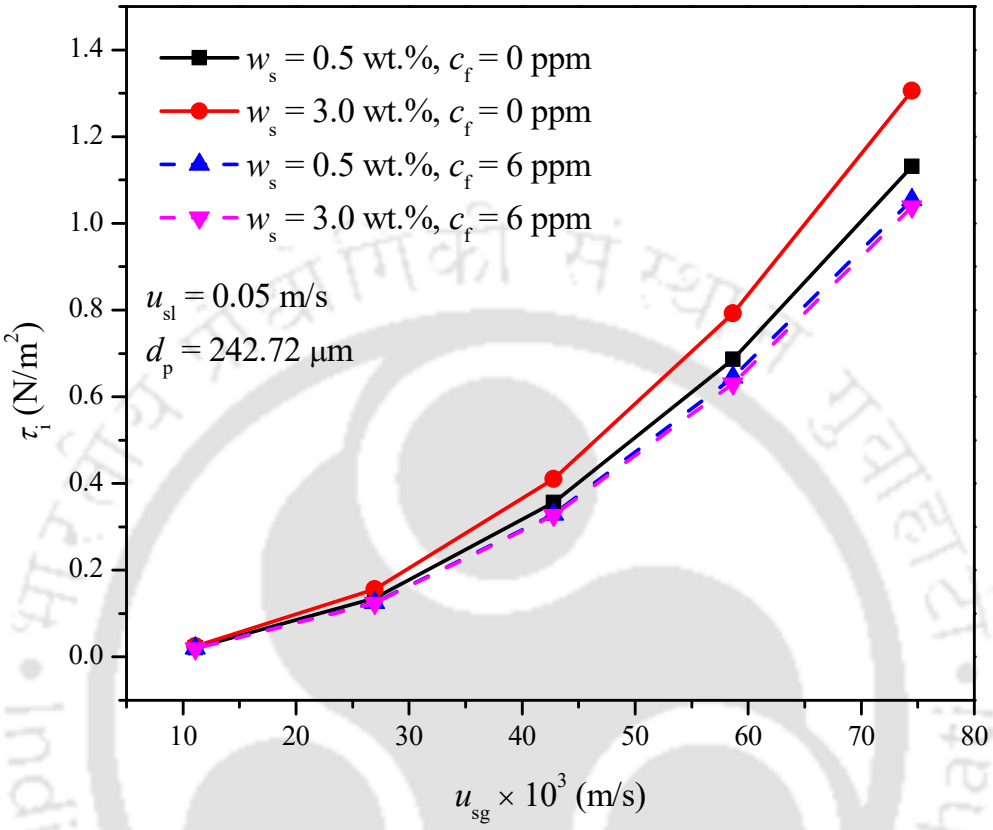

Fig. 3.10. Effect of surfactant on the bubble-slurry interfacial shear stress.

3.6.2.3. Effect of particle concentration on interfacial shear stress

Particle concentration in the slurry column significantly impacts the bubble-slurry interfacial shear stress. Influence of the particle concentration on the bubble-slurry interfacial shear stress at fixed d_p = 242.72 μm and at various u_{sg} are shown in Fig. 3.11. It is noted that the interfacial shear stress increases with an increase in particle concentration for all u_{sg}. The increase in interfacial shear stress was found to be about 2.96%, 5.82%, and 4.69% as the particle concentration varied from 0.5 to 1.0 wt.%, 1.0 to 2.0 wt.%, and 2.0 to 3.0 wt.%, respectively at a u_{sg} of 0.075 m/s. Increased slurry viscosity is one of the prime reasons of bubble coalescence, therefore, the bubble size increases (Ojima et al., 2015; Orvalho et al., 2018; Sarhan et al., 2018c), henceforth, the interfacial shear stress. It is also noticed that the increase in the bubble-slurry interfacial shear stress is in the

range of 14 – 32 % when the slurry concentration changed from 0.5 to 3.0 wt.% irrespective of the u_{sg}.

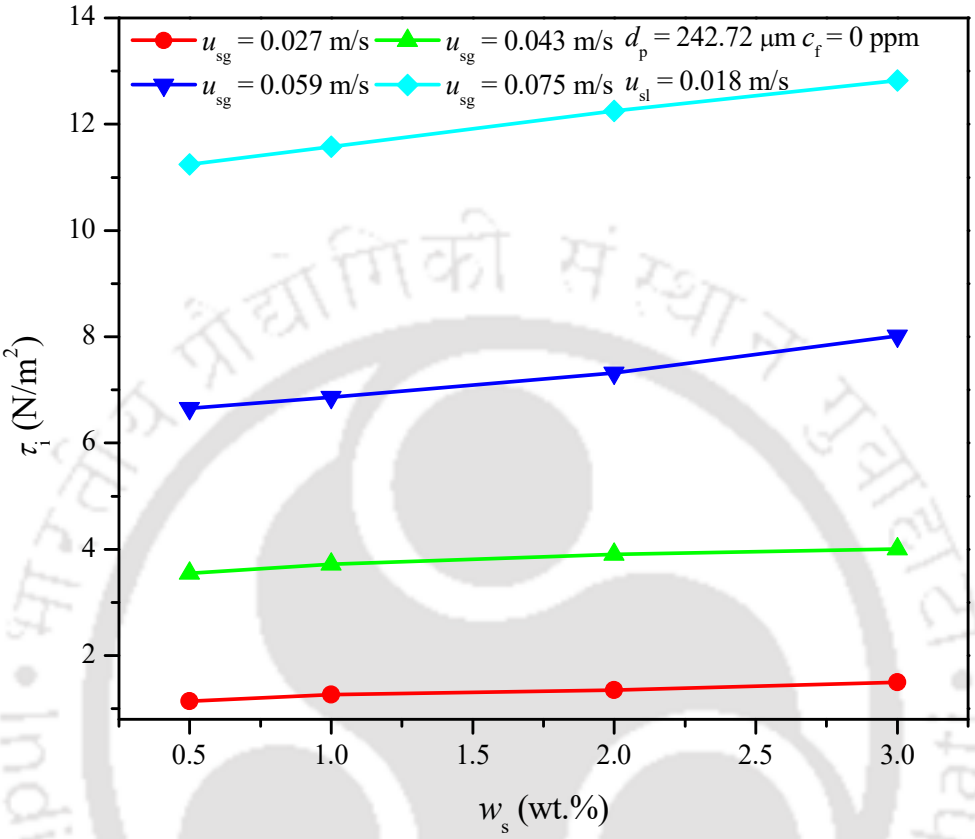

Fig. 3.11. Effect of particle concentration on interfacial shear stress in the surfactant-free system.

3.6.2.4. Effect of particle concentration on the rate of energy loss because of the wetting of the column wall

The wetting phenomena in a multiphase system are important because of the dissipation of a certain amount of energy in liquid-wall wetting (Parmar and Majumder, 2014). The effect of particle concentration with and without surfactant on the rate of energy loss because of the wetting of a thin liquid layer with the column wall as a function of u_{sg} at a fixed u_{sl} = 0.050 m/s and d_p = 517.0 µm is depicted in Fig. 3.12. It is noted that the energy dissipation rate because of the wetting of the column wall is more at a higher w_s = 3.0 wt.% as compared to the lower w_s = 0.5 wt.%. It is also seen that the rate of energy loss because of the wetting of a thin liquid layer with the column with surfactant is lower than that of the other particle concentrations (at w_s = 0.5 and 3.0 wt.%) without surfactant. It is observed that the surface tension is increasing with particle concentration

and decreases with the addition of a surfactant (as shown in Table 3.2 and Table 3.3). The addition of a surfactant enhances the affinity of wetting phenomena of the liquid to the particle surface. Therefore, the energy dissipation rate attributed to the wetting of the thin liquid film with the column wall increases with particle concentration, while it is lower with the surfactant addition. At 0.5 wt.% particle concentration, the average reduction in the rate of energy loss because of the wetting of solid wall with surfactant for all u_{sg} is about 7.16%, whereas the average reduction is approximately 18.04% at 3.0 wt.% particle concentration. Similarly, the average difference in energy dissipation rate because of the wetting of a thin liquid film with the column wall at 0.5 wt.% and 3.0 wt.% particle concentrations without surfactant is approximately 14.86%.

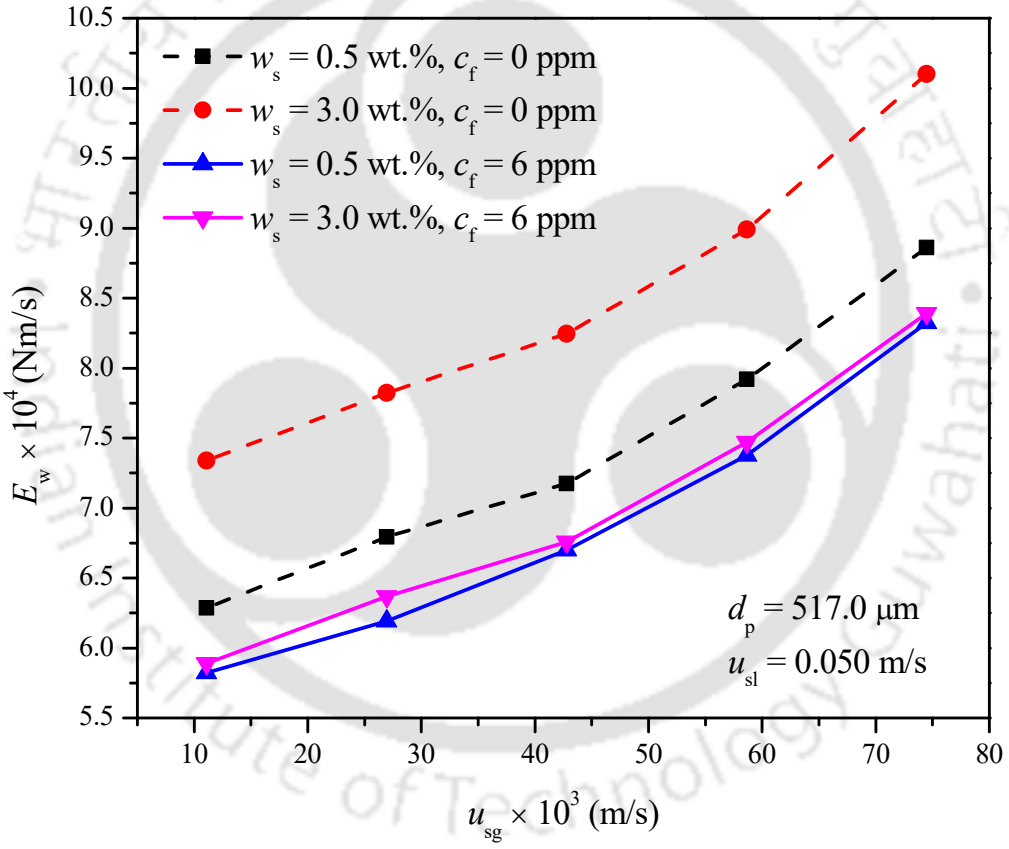

Fig. 3.12. Effect of particle concentration on the rate of energy loss because of the wetting of solid wall in the presence and absence of surfactant.

3.6.2.5. Variation of the friction factor as a function of the rate of energy loss because of wettability

Change in the friction factor $(\alpha_{sl} f_{sl0} / \alpha_l'')$ with the energy loss because of the wettability at different particle concentrations in the surfactant and the surfactant-free system is shown in Fig. 3.13. It is observed that the friction factor reduced with an increase in energy loss because of wettability for all the particle concentrations. Friction factor is more for a higher particle concentration than for a lower particle concentration. The friction factor is lower in the case of the surfactant addition. As the solid concentration increases, both the surface tension and slurry viscosity increase. These two factors (viscosity and surface tension) reduce the affinity of the wettability of the liquid for the column wall. Therefore, the rate of energy loss because of wettability increases.

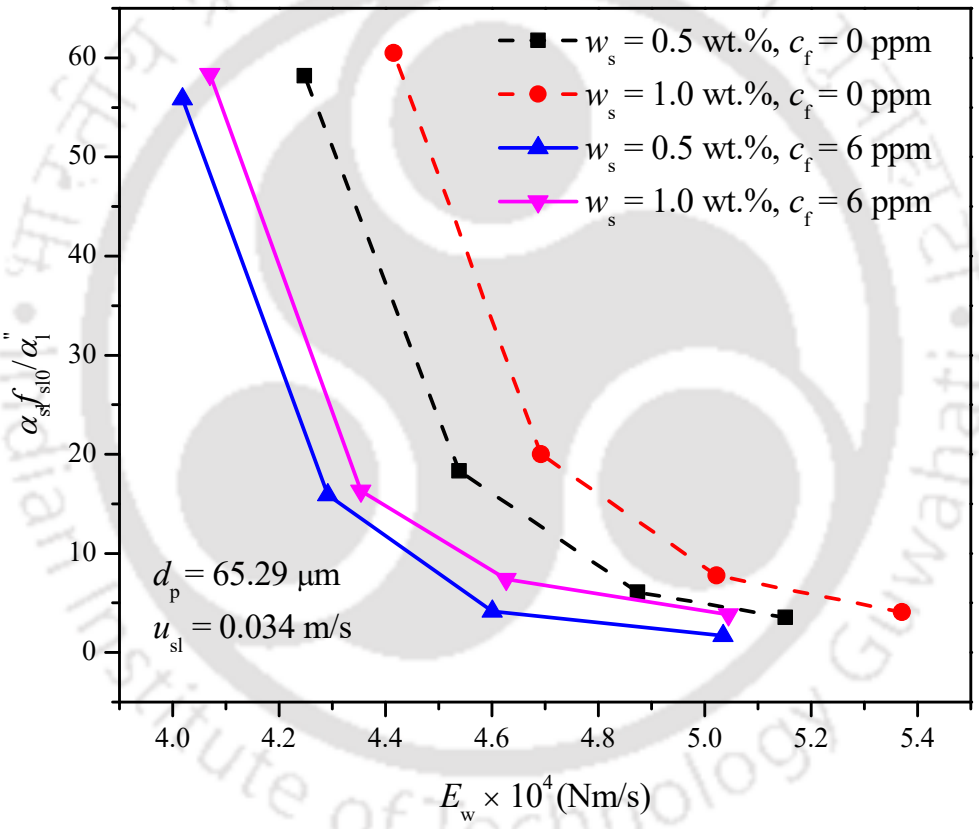

Fig. 3.13. Variation of the friction factor as a function of the rate of energy loss because of the wettability at various particle concentrations with and without surfactant.

3.7. Development of an empirical correlation

It was noticed that the superficial gas and the slurry velocity, the slurry surface tension, the particle diameter, the effective slurry viscosity, the slurry density, the slurry viscosity, and the acceleration

due to gravity influence the interfacial shear stress. The generalized correlation for the interfacial shear stress is expressed as follows:

$$\frac{\tau_i}{\rho_{sl}u_{sl}^2} = 1.07\times10^{-5}\left(\frac{u_{sg}}{u_{sl}}\right)^{4.264}\left(\frac{gd_p}{u_{sg}^2}\right)^{1.075}\left(\frac{g\mu_{sl}^4}{\rho_{sl}\sigma_{sl}^3}\right)^{-0.388} \quad (3.39)$$

The range of validity of different dimensionless parameters in Eq. (3.39) are: $0.193 \le u_{sg}/u_{sl} \le 4.177$, $0.111 \le gd_p/u_{sg}^2 \le 41.190$, and $6.853\times10^{-12} \le g\mu_{sl}^4/\rho_{sl}\sigma_{sl}^3 \le 1.180\times10^{-11}$. The value of correlation coefficients (R^2) and standard error of the proposed correlation (Eq. (3.39)) are 0.99 and 0.233, respectively. The developed correlation (Eq. 3.39) predicts the experimental values within the error range of ± 19.94%. Absolute average relative error (AARE) between experimental and predicted bubble-slurry interfacial shear stress is approximately 5.68%. The parity of the experimental and predicted interfacial shear stress (using Eq. (3.39)) is shown in Fig. 3.14.

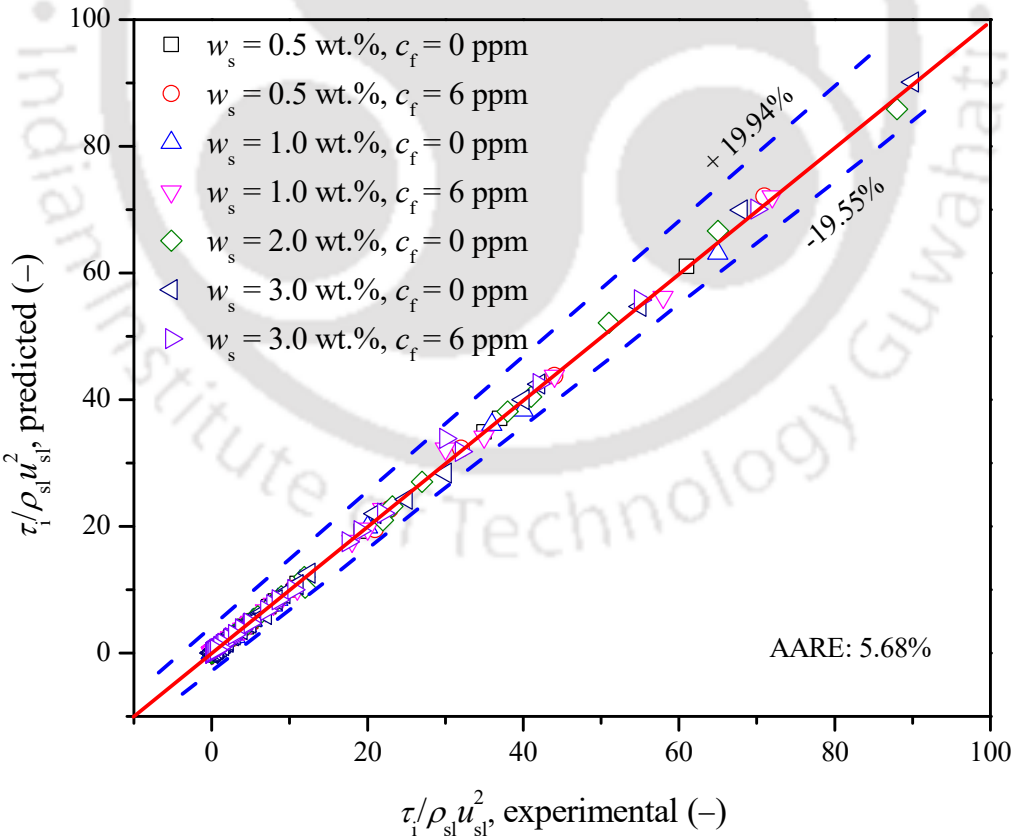

Fig. 3.14. Parity plot of the bubble-slurry interfacial shear stress.

3.8. Conclusions

The present work reports the frictional pressure drop and the bubble-slurry interfacial shear stress in a rectangular counter-current slurry bubble column with and without surfactant. A thorough investigation was conducted to analyze the effect of superficial gas velocity, superficial slurry velocity, particle size, and particle concentration on the frictional pressure drop and bubble-slurry interfacial shear stress. A mechanistic model was developed to estimate the bubble-slurry interfacial shear stress. Based on the experimental study, the following conclusion can be made:

- Frictional pressure drop observed to increase with an increase in the superficial gas velocity, the particle concentration, and the bubble size, while it reduces by increasing the superficial slurry velocity and the average particle diameter, respectively. A reduction in the frictional pressure drop was about 34.46% when the superficial slurry velocity increases from 0.018 to 0.057 m/s and an increase was approximately 35.38% when the superficial gas velocity increases from 0.01 to 0.075 m/s (at d_p = 65.29 μm and w_s = 3.0 wt.%). The addition of the surfactant reduces the frictional pressure drop as compared to that of the system without surfactant.
- Bubble-slurry interfacial shear stress increases with an increase in the superficial gas velocity and particle concentration while decreasing with an increase in the superficial slurry velocity. The bubble-slurry interfacial shear stress was lower in the presence of surfactant as compared to the surfactant-free system. A considerable change of approximately 15.04% (without surfactant) was noticed in the interfacial shear stress as the particle concentration varied from 0.5 to 3.0 wt.%, but this change is insignificant and reduced to 1.61% in the presence of a surfactant.
- The impact of the bubble size on the rate of energy loss because of a slip of the gas-slurry interface was lower in the case of the surfactant solution. The rate of energy loss because of the gas-slurry interface decreased to about 50.21% as the bubble size increased by 8.01% in the presence of the surfactant.
- The rate of energy loss due to the wetting of a thin liquid layer with the column wall increases to approximately 14% in the particle concentration range of w_s = 0.5 – 3.0 wt.% (at u_{sg} = 0.075 m/s without surfactant), and the increase is less than 1% in the presence of the surfactant.

- Friction factor decreases drastically with an increase in the rate of energy loss because of wettability. Friction factor was more in the presence of higher particle concentration and decreased in the presence of the surfactant.
- Developed empirical correlation satisfactorily predicts the frictional pressure drop and gas-slurry interfacial shear stress within an error range of ± 20%, which may be used for the analysis of multiphase behavior in the rectangular counter-current slurry bubble column.

Chapter 4

Bubble Size Distribution and Aspect Ratio

The present chapter enunciates the bubble size and its distribution, and bubble aspect ratio in two (air-water) and three-phase (air-water-coal particle) in a counter-current microstructured bubble column with and without surfactant. The effects of dispersed and continuous phase velocity, particle concentration, and particle size are investigated. The aspect ratio of the bubble was interpreted as a function of Eötovos number, and its shape is plotted in the grace diagram, indicating that the bubbles cover both the spherical and ellipsoidal shape regimes. A generic empirical correlation is proposed for the Sauter mean bubble diameter and distribution function parameters in terms of operating conditions and physical properties of the system. Experimental data and correlations from the literature, and this study were compared with the results of the proposed correlation.

Publication: Prakash, R., Majumder, S. K., & Singh, A. (2020). Bubble size distribution and specific bubble interfacial area in two–phase microstructured dense bubbling bed, *Chemical Engineering Research and Design*, *156*, 108 – 130. https://doi.org/10.1016/j.cherd.2020.01.032

Prakash, R., & Majumder, S. K. (2020). Effect of particle size and concentration on bubble size distribution and aspect ratio in a counter-current microstructured bubble column, Journal of Industrial and Engineering Chemistry, 90, 105 – 116. https://doi.org/10.1016/j.jiec.2020.07.002

Prakash, R., Majumder, S. K., & Singh, A. (2019). Particle-laden bubble size and its distribution in microstructured bubbling bed in presence and absence of a surface active agent, *Industrial & Engineering Chemistry Research*, *58*, 3499 – 3522. https://doi.org/10.1021/acs.iecr.8b05625

4.1. Introduction

Slurry bubble columns are widely used in various industries such as coal beneficiation (Han et al., 2014), petrochemicals (Gandhi et al., 1999a), biochemical (Shaikh and Al-Dahhan, 2007), and the chemical industries (Li and Prakash, 2000), etc. Slurry columns are multiphase contactors wherein a gas phase is dispersed as a bubble in a continuous slurry phase (Leonard et al., 2015). There are three types of operating modes in the slurry bubble column, namely, semi-batch, co-current, and counter-current. The bubble size distribution (BSD) studies were conducted in three-phase semi-batch (Zhang et al., 2008), two-phase semi-batch (Azgomi et al., 2007), and two-phase counter-current operation (Besagni et al., 2014; Besagni and Inzoli, 2017a, b). Knowledge of the bubble size and their distribution is of the utmost importance when assessing performance, scale-up, and design of a slurry bubble column and flotation devices. It is, therefore, essential to understanding the factors that influence the bubble size and its distribution in the slurry system. The present study focuses primarily on the effects of various operating variables and physical properties of the system on hydrodynamic characteristics such as the bubble size distribution and aspect ratio in a counter-current slurry bubble column.

According to the literature, most of the bubble size measurement experiments have been performed in the cylindrical column, which is known for the substantial backmixing of phases (both liquid and gas) (Shah et al., 2012), which reduces the process efficiency, and decreases the overall performance of the bubble column. In the cylindrical geometry, the performance of the column is mainly limited by the interfacial mass transfer rate. The microstructured column (2D with small depth) nowadays are gaining importance to the scientific community for its ability to reduce the backmixing of the phases. The hydrodynamic studies in the microstructured are carried out so that in future research, the influence of studied variables and design parameters can be enunciated on the mineral beneficiation studies. Reducing backmixing of the phases will be helpful in improving the recovery of the valuable particles from the gangue particles (i.e., unwanted particles). The use of the microstructure column can be an attractive way of upgrading the low-grade to higher-value products.

Numerous techniques for the measurement of bubble size and its distribution have been used by many researchers. Some of the techniques as Mie scattering technique (Hansen, 1985), pressure fluctuations (Chilekar et al., 2005), Bayesian magnetic resonance technique (Holland et al., 2012),

resistivity probes (Zhang et al., 2010), Coulter count method or pore electrical resistance method (Fujiwara, 2007), optical probe (Xue et al., 2008), two-point conductivity method (Buchholz et al., 1979), photographic technique (Lau et al., 2010), and x-ray tomography (Rabha et al., 2013b) are used for estimation of bubble size. Intrusive techniques (e.g., optical probe) disturb the flow hydrodynamics, therefore non-intrusive methods (e.g., photographic technique) are favored over intrusive technique (Guet et al., 2005). The simplest technique to obtain the bubble size from an image is to manually draw lines on the bubble interface (Winkel et al., 2004).

The interfacial area available for a process is a crucial variable for design and scale-up purposes. The lower the bubble size is, the higher the interfacial area is, which improves the process performance. The interfacial area depends on the bubble size, gas holdup, sparger design, property of phases, and column geometry. Bubble size in the three-phase system depends on the physico-chemical property of the system and the type of gas distributor used (Camarasa et al., 1999). Passos et al. (2015) reported the measurement of the bubble size by an optical technique in a non-Newtonian solution. The addition of non-ionic surfactant (Triton X-100) results in a reduction in bubble size as well as the transition of homogenous to the heterogeneous regime is shifted to a higher gas flow rate. When smaller bubbles coalesce to form a bigger bubble, the surface area for bubble-particle interaction decreases, thus, process efficiency reduces (Ata et al., 2003). Grau and Heiskanen (2005) studied the bubble size distribution and observed that reagents control the bubble size by decreasing the coalescence behavior. The mean bubble size was found to increase with quartz particle addition and an increase in air flow rate. Yianatos et al. (1988) observed increased slurry density by an increase in the particle concentration, which results in an increase in the bubble rise velocity (Bhunia et al., 2017). The rising velocity of the large bubble is higher than the small bubble (Manjrekar and Dudukovic, 2015; Moshtari et al., 2007), hence the residence time of the bubble decreases, which impacts the system performance (Luo et al., 1999).

Since the past few years, several efforts have been carried out to investigate the bubble size and its distributions in the slurry system. The influence of slurry concentration and particle diameter on the bubble size has been studied by many investigators (Manjrekar and Dudukovic, 2015; Moshtari et al., 2007; Tyagi and Buwa, 2017). Numerous researchers deduced that the addition of particles causes the generation of bigger bubbles (Li and Prakash, 1997; Li and Prakash, 2000; Luo et al., 1999; Manjrekar and Dudukovic, 2015; Moshtari et al., 2007; Tyagi and Buwa, 2017).

The increase in bubble size was because of the rise in the viscosity and mixture density of the slurry after particle addition (Manjrekar and Dudukovic, 2015). The increase in liquid viscosity generally increases the bubble coalescence rate, consequently enlarge the gas bubble size (Kato et al., 1972; Li and Prakash, 1997; Sehabiague and Morsi, 2013). In contrast, Götz et al. (2016) reported that the small concentration of fine particles (<<100 μm) reduces the bubble coalescence phenomena otherwise enhance the bubble coalescence. Particle size also influences the hydrodynamics behavior of the slurry column. The contrary effect of particle concentration on slurry hydrodynamics is also reported in the literature. Small particles (<100 μm) with a particle concentration range of 0 to 3.0 wt.%, has no influence on hydrodynamic behavior (Rabha et al., 2013a). Usually, when the gas velocity increases, the bubble size also increases, but few researchers observed a reduction in bubble diameter attributable to bubble breakup due to augmentation of bubble-eddies collision frequency (Banisi et al., 1995a, 1995b). Vazirizadeh et al. (2016) investigated the influence of particle on BSD and observed that the BSD of the system becomes a little wider in the presence of particles. Published literature shows that BSD measurement was conducted in the low particle concentration ($c_s < 15\%$) and low superficial gas velocity ($u_{sg} < 0.1$ m/s) (Chilekar et al., 2005; Lau et al., 2010; Wang et al., 2001). Few researchers carried out the measurement of BSD in a high slurry concentration (Luo et al., 1999; Xue et al., 2008; Zhang et al., 2010). Understanding of bubble size in both radial and axial directions is essential for the improvement of process efficiency. Few authors have investigated the axial variation of BSD in the slurry column (Lau et al., 2010; Zhang et al., 2008). Tyagi and Buwa (2017) studied the BSD at different axial locations in the presence of gas velocity and particle concentration range of 0.05 to 0.3 m/s and 0 to 40 vol.%, respectively. They have noticed that as the gas velocity and concentration increase, the bubble size and its distribution change from smaller bubbles to larger bubbles, and BSD shifted from narrow to wide. Sarhan et al. (2018c) observed a rise in the bubble coalescence rate with the particle addition ($0 \leq c_s \leq 40$ vol.%) at different particle diameters. They also reported a diminishing mean bubble size with the increment in the particle size. The occurrence of larger particles causes a decrease in the bubble coalescence time, which in turn leads to a decrease in the bubble coalescence rate. A similar trend of reduction in bubble diameter with the increase in particle size is also reported by Ojima et al. (2015).

Besagni and Inzoli (2016a) elucidated that the liquid in counter-current operation does not allow bubbles to escape out easily. The bubbles group and coalesce together and form large bubbles. In a two-phase, counter-current flow, Besagni and Inzoli (2016b) reported a higher number of distorted or ellipsoidal bubbles compared to spherical bubbles, due to higher shear stress between the phases. The important hydrodynamic characteristics such as bubble size distribution and holdup are required for modeling, control, and optimization of the two- and three-phase bubble column. Theses hydrodynamic characteristics usually explained, taking into account the physic-chemical properties of the system, such as its viscosity and surface tension. De Guido and Pellegrini (2017) reported the effect of monoethylene glycol surfactant on the surface tension and viscosity of the liquid. It has been elucidated that the addition of surfactant to the liquid significantly lowers the surface tension of the liquid, while the viscosity of the liquid increases substantially. They also attempted to produce the gas holdup data using a dynamic surface tension model for the binary liquid mixture (water + monoethylene glycol) in a large diameter bubble column. Their investigation suggests that the dynamic surface tension model qualitatively suitable to generate the gas holdup values, but no quantitative agreement exists due to the overprediction of the maximum frothing ability of monoethylene glycol. The dual effect of viscosity in the presence of an aqueous solution of monoethylene glycol on gas holdup and BSD is elucidated by Besagni et al. (2017b). They delineated that the low viscosity liquids ($\mu_l \leq 1.01$ mPa.s) increased gas holdup and were characterized by a larger number of small bubbles. Whereas, the moderate or high viscosity liquids ($1.01 < \mu_l \leq 7.96$ mPa.s) reduce the gas holdup, and the bubble size distribution has shifted to larger bubbles. Vazirizadeh et al. (2016) analyzed the effect of the particle on bubble size and shape and observed that the small bubbles are more spherical in comparison to large bubbles. Maldonado et al. (2013) confirmed that the spherical bubble has a lower rise velocity than the flattened bubble.

The ratio between the major and minor axes of the bubble is known as the aspect ratio. Most of the research is conducted on a single rising bubble (Aoyama et al., 2018; Bozzano and Dente, 2001; Zhen et al., 2019) and dense bubble two-phase (Besagni and Inzoli, 2016a) system. In recent years, some experiments have also been performed to study the aspect ratio of bubbles rising in a line (Li et al., 2017a), in bubbly or dense flow in the two-phase batch mode (Besagni and Inzoli, 2019).

Based on the literature as mentioned above, this study aims to explore the effect of dispersed gas and continuous slurry velocities, particle concentration, and particle size on the BSD and bubble aspect ratio in a counter-current microstructured slurry bubble column in the presence and absence of the surfactant. In addition, empirical correlations are proposed for the Sauter mean bubble diameter and BSD function parameters as a function of the operating and physical properties of the system. An attempt is also made to develop a correlation for the aspect ratio based on the important dimensionless groups. Some important studies regarding the bubble size measurement in the three-phase and two-phase systems with their experimental conditions are given in Table 4.1 and Table 4.2, respectively.

Table 4.1 Some important literature on bubble size measurements in the three-phase system.

System	Type of column	Operation mode	Experimental condition	Sparger	Technique	Remarks and correlations	Author
Liquid: water and glycerol (5 – 50 vol.%, , solid: glass beads	Cylindrical, d_c: 0.15 m, L_c: 1.2 – 3.2 m	Co-current up flow	u_{sg}: 0.01 – 0.08 m/s, u_l: 0.001 – 0.05 m/s, P: 0.1 MPa, T: 293.05 K, d_p: 56 – 460 μm, μ_l: 1.20 – 6.60 mPa.s, σ_l: 72.4 – 68.8 mN/m, ρ_l: 1012 – 1127 kg/m^3)) r/R: 0, 47, and 67 mm	Multi-nozzle gas distributor (d_{pore}: 2.6 mm, 8 nozzles)	Dual-electroresistivity probe	The influence of particles on bubble is insignificant as d_p reduces or the liquid viscosity increases. Addition of particles at low u_{sg} BSD widens and flow pattern changes from homogeneous to heterogeneous. $d_{32} = \frac{0.59}{g}\left(\frac{V_D}{\alpha_g}\right)^2$	Fukuma et al. (1987)
Gas: N_2, liquid: water, solid: glass beads	2D column, L_c: 2.16 m, w: 0.56 m,	Semi-batch and continuous mode (co-current)	u_{sg}: 0 – 0.00046 m/s, u_l: 0.0122 – 0.078 m/s, P: 0.1 MPa, T: 293.05 K, Two and three-phase system, d_p: 88 – 2700	Multi-nozzle gas distributor (d_{pore}: 4 mm, 13 nozzles)	Image analysis	BSD obtained in semi-batch and continuous mode follows the log-normal distribution. In the case of the small particle system, bubble behavior is the same as that of the two-phase system. In the case of the large particle system, broad BSD occurs. An increase in u_{sg} increases d_{32} while decreases by increasing the u_l	Luewisutthichat et al. (1997)

			μm, ρ_p: 2500 kg/m^3			(for d_p: 500 μm and 2700 μm). The effect of particle size range was different for each particle size range.	
Gas: N_2, liquid: Paratherm NF, solid: alumina	Cylindrical, d_c: 0.102 m, L_c: 1.37 m	semi-batch	u_{sg}: 0 – 0.045 m/s, u_l: 0 m/s, P: 0.1 – 5.6 MPa, T: 301 – 351 K, d_p: 100 μm, ρ_p: 2440 kg/m^3, h_0: 0.5 m, α_s: 0.081 – 0.191	Perforated sparger (d_{pore}: 1.5 mm, 120 holes)	Fiber-optic probe	Elevated pressures lead to smaller d_b and narrower BSD. d_b increases significantly with increasing w_s at ambient pressure, while at high pressures, this effect is less pronounced.	Luo et al. (1999)
Gas: air, liquid: water-fiber slurry	Cylindrical column, L_c: 0.15 – 0.4 and 1.15 – 1.40 m	Co-current up flow	u_{sg}: 0.01-0.04 m/s, u_l: 0.01 – 0.02 m/s, w_s: 0 – 1.5 wt.%, P: 0.1 MPa, T: 298.15 K	Sintered polyethylene aerator (d_{pore}: 50 μm)	Flash X-ray radiography	Bubbles are divided into d_b < 10 mm or d_b > 10 mm. BSD is characterized by a lognormal distribution. Large bubble size and population increases with column height, u_{sg}, and fiber concentration.	Heindel (2002)
Gas: nitrogen, liquid: slurry, surfactant: Dowfroth 250 (c_f: 30 ppm)	Cylindrical flotation column, d_c: 0.05 m, L_c: not given	Co-current up flow	u_{sg}: 0.012 m/s, Q_{sl}: 0.0108 l/s, flotation cell consists of a 150-mm diameter	Not given	Photographic technique	The d_{32} in the froth increases with increasing height above the froth-pulp interface. The major increase in d_{32} occurs with particles of the lowest contact angle. In the presence of particles with strong hydrophobicity, bubbles coalesce more	Ata et al. (2003)

			stirred vessel connected to a 50 mm diameter, Silica (d_{50}: 5 μm), glass sphere (d_{50}: 68 μm, d_{80}: 82 μm), glass particle of different hydrophobicity (50^0, 66^0 and 82^0), w_s: 7.5 wt.%, P: 0.1 MPa, T: 298.15 K			rapidly than in the presence of the moderately hydrophobic particle, but less rapidly than in the presence of the weakly hydrophobic particles. The rate of change in the d_{32} is highest with the weakly hydrophobic particles and lowest in the case of the intermediate hydrophobic particles.	
Gas: air, liquid: wastewater, an aqueous solution of carboxymethylcellulose, solid: glass bead	Three-phase circulation fluidized bed, cylindrical, d_c: 0.102 m, L_c: 3.5 m	Three-phase circulation, riser column, gas-liquid-solid separator and solid recycle device	u_{sg}: 0.01-0.07 m/s, u_{sl}: 0.17-0.23 m/s, , d_p: 1000 μm, ρ_p: 2500 kg/m^3, circulation rate: 2.0 kg/m^2.sec, σ_l: 72.9 – 73.6 mN/m, ρ_l: 1000 –	Not given	Dual electrical resistivity probe	BSD is measured in the riser of the three-phase circulatory fluidized bed. The d_b increased with increasing gas velocity and liquid viscosity, while decreases with increasing liquid velocity. BSD widens with increasing gas velocity or liquid viscosity.	Son et al. (2007)

			1003 kg/m^3), μ_l: 0.96 – 38 mPa·s, P: not given, T: not given				
Gas: air, liquid: water, solid: glass beads	Cylindrical, d_c : 0.1 m, L_c: 1.50 m	Semi-batch	u_{sg}: 0.01 – 0.064 m/s, u_{sl}: 0 m/s, (d_p: 2 – 50 µm, $d_{p,\ average}$: 17.82 µm, ρ_p: 2200 kg/m^3), α_s: 0 – 30 %, radial position (r/R) : 0, 0.4 and 0.7, h_0: 1 m, $M_{position}$: 0.6 m	Perforated plate sparger (d_{pore}: 1 mm, 100 holes)	Four channels dual-tip conductivity probe	Bubbles are grouped into two size classes, small bubbles with chord length < 10 mm and large bubbles with chord length > 10 mm. Increasing u_{sg} and α_s increase the bubble size and number of large bubbles. At low α_s BSD is well predicted by lognormal or gamma distributions. The effect of r/R on bubble size distribution is slight.	Zhang et al. (2008)
Gas: air, liquid: water, solid: alumina	Cylindrical, d_c: 0.102 m, L_c: 1.05 m		u_{sg} : 0.013 – 0.13 m (covers both bubbly and churn turbulent flow regime), u_{sl}: 0 m/s, h_0: 0.90 m, $d_{p,}$	Perforated plate sparger (d_{pore}: not given)	Four-point optical probe	With an increase in particle concentration, bubble frequency decreased, while bubble chord length increases and the bubble chord length distribution widens. In both the bubble and the slurry bubble column, bubble chord lengths in the center and wall	Wu et al. (2008)

			$_{average}$: 75 µm, c_v: 9 – 25 vol.%, P: 0.1 MPa, T: 298.15 K			regions increase with u_{sg}. Bubble chord length increases as u_{sg} increases.	
Gas: air, liquid: slurry, solid: soda lime glass sphere	Cylindrical, d_c: 0.14 m, L_c: 1.50 m	semi-batch	u_{sg}: 0.0325 – 0.108 m/s, u_{sl}: 0 m/s, soda-lime glass spheres ($d_{p-average}$: 425 –600 µm, ρ_p: 2480 kg/m^3), w_s: 5.0 wt.%	Perforated plate sparger (d_{pore}: 3 mm)	Image analysis	Particle addition enhances the d_b, and the effect is less significant at higher u_{sg}. At a fixed initial liquid height, the d_b is higher in the sparger zone in comparison to the central region. A reduction of column aspect ratio reports small bubbles. At low aspect ratio, BSD is narrow in comparison to that of the higher aspect ratio.	Lau et al. (2010)
Gas: air, liquid: water, solid: glass beads	Both 2D (w: 0.24 m, d: 0.04 m, L_c: 1 m) and 3D column (d_c: 0.15 m, L_c: 2 m)	semi-batch	u_{sg} : 0 - 0.10 m/s (for 2D column), and : 0 - 0.106 m/s (for 3D column), column, $d_{p,average}$: 108 µm (for 2D column), 78 µm (3D column), w_s : 0 -10	Needle sparger (for 2D column, 95 needles, d_{pore}: 0.8 mm), for 3D column (559 needles)	Four point optical probe	An increase in particles volume fraction shifts the transition point from homogeneous to heterogeneous flow to a lower gas velocity. BSD widen when increasing the dispersed phase flow rate for all three particles concentrations. Addition of particle enhances the bubble rising velocity, however, it has insignificant impact on mean bubble chord length.	Hooshyar et al. (2010a)

			wt.% for (2D system) and 0 -20 wt.% (for 3D system), u_{sl}: 0 m/s ρ_p: 2500 kg/m^3, P: not given, T: not given				
Gas: air, liquid: water, solid: glass beads	Cylindrical, d_c: 0.07 m, L_c: 1.5 m	Semi-batch	u_{sg}: 0.02 – 0.05 m/s, u_{sl}: 0 m/s, d_p: 100 µm, ρ_p: 2500 kg/m^3, P: 0.1 MPa, T: 298.15 K, c_v: 0.05 – 0.36 vol.%	Perforated plate (d_{pore}: 1 mm, 95 holes)	Ultrafast electron beam X-ray tomography	As u_{sg} increases, transitions from homogeneous to heterogeneous and churn-turbulent regimes are observed. The d_{32} increases with u_{sg}. The addition of particles leads to bubble coalescence at low concentration and u_{sg}.	Rabha et al. (2013b)
Gas: He/ N_2, liquid: molten wax, solid: iron catalyst	Cylindrical, d_c: 0.29 m, L_c: 3 m	Semi-batch	u_{sg}: 0.1 -0.3 m/s, u_{sl}: 0 m/s, P: 4 – 31 bar, T : 380 – 500 K, w_s: 0 -45 wt.%, ρ_p: 3380 kg/m^3, $d_{p,\,average}$: 81 µm)	Spider sparger (d_{pore}: 5 mm, 108 orifices)	Dynamic Gas Disengagement (DGD)	Reported correlation for large diameter bubbles. The d_{32} of gas bubbles increased with increasing the concentration of particles. The d_{32} decrease with increasing temperature.	Sehabiague et al. (2015)
Gas: air, liquid: slurry, solid: quartz, talc	Cylindrical flotation		u_{sg}: 0.01 m/s, u_{sl}: 0.101 –	Frit-and-sleeve sparger	Image analysis (bubbles	d_{32} and BSD are higher and wider in three-phase than the two-phase system.	Vazirizadeh et al. (2016)

	column, d_c: 0.056 m, L_c: 6.50 m		0.404 m/s, surfactant (polyglycol, F150, c_f: 5 – 25 ppm), w_s: 0 – 4 wt.%	consist of porous stainless steel ring (d_{pore}: 10 µm, sparger diameter: 0.025 m, length: 0.04 m)	sampled in bubble viewer)		
Gas: air, liquid: water, solid: sludge	Cylindrical column, d_c: 0.09 m, L_c: 1.75 m,	Semi-batch	u_{sg}: 0.005 – 0.07 m/s, u_{sl}: 0 m/s, sludge mixed with suspended particle (1.082 to 10.82 g/L), h_0: 1.30 m, P: 0.1 MPa, T: 293.15 K	Perforated plate sparger (d_{pore}: 0.5 mm)	Dual-tip electro resistivity probe	An increase in sludge concentration resulted in an increase in the bubble chord length.	Jamshidi and Mostoufi (2017)
Gas: air, liquid: water, solid: glass beads	Rectangular column, L_c: 1.40 m, w: 0.2 m, d: 0.05 m	Semi-batch	u_{sg}: 0.05 – 0.30 m, c_v: 0 – 40 vol.%, d_p: 0.25 mm, ρ_p: 2400 kg/m^3, average dispersion height	Sparger (lengh: 0.1 m, width: 0.05 m, d_{pore}: 1 mm, 50 holes)	Dual–tip voidage (conductivity) probes	As particle holdup and u_{sg} increase, the chord length of the bubble increases.	Tyagi and Buwa (2017)

			maintained at 0.90 m				
Gas: air, liquid: water and aqueous solution of SDS (anionic) and Tween 20 (non-ionic) surfactant), solid: coal	Rectangular column, L_c: 0.63 m, w: 0.19 m, d: 0.03 m	Semi-batch	u_{sg}: 0.008 - 0.040 m/s, u_{sl}: 0 m/s, w_s: 0.2-0.8 wt.%, P: 0.1 MPa, T: 298.15 K, AR: 3 , 7.8, , c_f: 0 – 6 ppm, $d_{p,\,average}$: 242.72 µm, 408.31 µm	Cylindrical sparger (d_{pore}: 20 µm)	Photographic	The d_b and BSD increased and widens, respectively with axial distance from the sparger and u_{sg}. BSD is wider in three-phase in comparison to the two-phase system. BSD is approximated by beta (air-slurry-Tween 20), log-logistic (air-slurry-SDS), and Weibull (air-slurry). $\frac{d_{32}}{Z} = 1.79\times10^{-11}\left(\frac{u_{sg}d_p\rho_m}{\mu_{sl}}\right)^{4.033}\left(\frac{u_{sg}^2 d_p\rho}{\sigma_{sl}}\right.$ $\left(\frac{u_{sg}^2}{gd_p}\right)^{1.786}\left(\frac{z}{d_p}\right)^{-0.936}\left(\frac{c_s}{\rho_m}\right)^{0.006}$	Prakash et al. (2019)
Gas: air, liquid: aqueous solution of DF250 surfactant, solid: quartz	d_c: 0.027 m, L_c: 2.50 m	Continuous	u_{sg}: 0.001 m/s, u_{sl}: 0.002 m/s, , P: 0.1 MPa T: 295.15 K, c_f: 3.8 – 154.80 ppm, $d_{p,\,average}$: 41.6, 199, 254.5, 345.5 µm, ρ_p: 2650 kg/m^3, w_s: 10 % wt.%	Stainless-steel porous sparger (porous tube with 15 mm diameter, 30 mm length, and 2.3 mm wall thickness)	Image analysis	The d_b was measured before they entered the column. The d_b decreased quickly at first, then slowly at higher surfactant dose, tending to a constant value.	Seger et al. (2019)

4.2. Experimental facility

4.2.1. Description of the experimental setup

The schematic diagram of the experimental apparatus is illustrated in Fig. 4.1. The column used for the current study was made of a Perspex sheet with a length, width, and depth of 0.63 m, 0.19 m, and 0.03 m, respectively. All the experiments were performed in a counter-current mode, with slurry as the continuous phase, while the air was the dispersed phase with and without surfactant. The ranges of dispersed gas velocities and slurry velocities, particle concentration, and particle size were 0.011 – 0.075 m/s, 0.018 – 0.057 m/s, 0.5 – 3.0 wt. %, and 61.30 – 517.0 μm, respectively. Methyl Isobutyl Carbinol (MIBC) (purity > 98.0%) provided by Tokyo chemical industry corporation limited was used as a surfactant. The flow rate of the slurry was measured by the digital electromagnetic flowmeter (Adept Fluidyne, MagFlow 6410) in a range of 0 – 15 L/min and accuracy ± 0.5%. Air was supplied by the compressor, and a calibrated air rotameter was used to measure the flow. The airflow was controlled and maintained using the needle valve. The air bubble in the column was produced by the stainless steel cylindrical porous sparger (supplied by TFI filtration, India). The inner and outer diameter and length of the sparger were 0.01 m, 0.014 m, and 0.175 m, respectively, and the pore size was 20 μm. The physical properties of the slurry system are given in chapter 2 (as Table 2.2 and Table 2.3). The Morton number of the slurry and uncertainty analysis of measured quantities are given in Table 4.2 and 4.3, respectively.

Fig. 4.1. Schematic of the experimental arrangements.

Table 4.2 Physical properties of the slurry and their composition.

Material	Average particle diameter, d_p (μm)	Particle concentration, w_s (wt. %)	$\log_{10}(Mo)$
Slurry	242.72	0.5	–10.987
		1.0	–10.977
		2.0	–10.960
		3.0	–10.957
Water	–	–	–10.937
Air	–	–	–

Table 4.3 Ranges of uncertainties of the measured quantities.

Quantities	Mean, $\overline{x}$	STDEV	U	U_r (%)
d_{32} (without surfactant)	1.76 – 2.54	5.17×10^{-2} – 5.33×10^{-2}	2.99×10^{-2} – 3.08×10^{-2}	1.18 – 1.75
d_{32} (with surfactant)	1.78 – 2.50	2.52×10^{-2} – 5.0×10^{-2}	1.45×10^{-2} – 2.89×10^{-2}	0.81– 1.16
u_{sg}	9.59×10^{-3} – 4.23×10^{-2}	9.06×10^{-4} – 1.53×10^{-3}	3.70×10^{-4} – 6.26×10^{-4}	8.74×10^{-1} – 6.54
u_{sl}	1.66×10^{-2} – 5.70×10^{-2}	1.71×10^{-3} – 1.92×10^{-3}	6.47×10^{-4} – 7.26×10^{-4}	1.27 – 3.89

4.2.2. Image analysis procedure

In spite of various bubble size measurement techniques, a precise assessment of the bubble size in a wide range of experimental conditions is complicated due to the advantage and disadvantages associated with each measurement technique. In the current experiment, the bubble diameter was obtained by the photographic method. A digital camera (make: Sony, model: DSC H300, 20.1 megapixels) was placed at a distance of 300 mm from the front section of the microstructured column. A halogen lamp (500 w, Havells) was used for the illumination purpose and focused on the measurement location. A black sheet was used behind the column to achieve better contrast and superior images. About 5 – 10 images were taken for each experimental condition, and out of these images, the best quality image was selected and used to analyze by the image analysis software (Digimizer, V 2.0). The images were enhanced with the help of software that allows us to distinguish and mark the boundaries of the bubbles. About 150 – 250 bubbles were marked for

each experimental condition to quantify the Sauter mean bubble diameter. The variation in the number of bubbles marking was attributed to the absence of a proper visualization of the bubble boundaries with higher particle concentration (at $w_s > 2.0$ wt. %). A total number of approximately 59000 bubbles were marked for the complete analysis in this experimental study. It is a well-known fact that not all bubbles are spherical, some bubbles are ellipsoid in shape. Spherical bubbles were marked directly using the image analysis software (as shown in Fig. 4.2), while measuring the size of the ellipsoidal bubble, the major ($d_{b,\,max}$), and the minor ($d_{b,\,min}$) axis of the bubbles were measured. The following equation (Eq. 4.1) was used to determine the equivalent diameter (d_{eq}) of the bubble

$$d_{eq} = \sqrt[3]{d_{b,\max}^2 d_{b,\min}} \tag{4.1}$$

Sauter mean bubble diameter (d_{32}) of the bubbles was calculated by

$$d_{32} = \frac{\sum_{i=1}^{n} n_i d_{bi}^3}{\sum_{i=1}^{n} n_i d_{bi}^2} \tag{4.2}$$

where n_i denotes the number of bubbles with diameter d_{bi}. The required number of bins to investigate the BSD is a matter of argument in the research publication. As per Sturge's criteria, the number of bins can be estimated as (Passos et al., 2015)

$$n_c = 1 + \log_2 s \tag{4.3}$$

where n_c and s denote the number of bins and sample size, respectively. The sample size (s) refers to the number of bubbles in a bin. The ranges of experimental uncertainty analysis of quantities such as d_{32}, u_{sg}, and u_{sl} are given in Table 4.3).

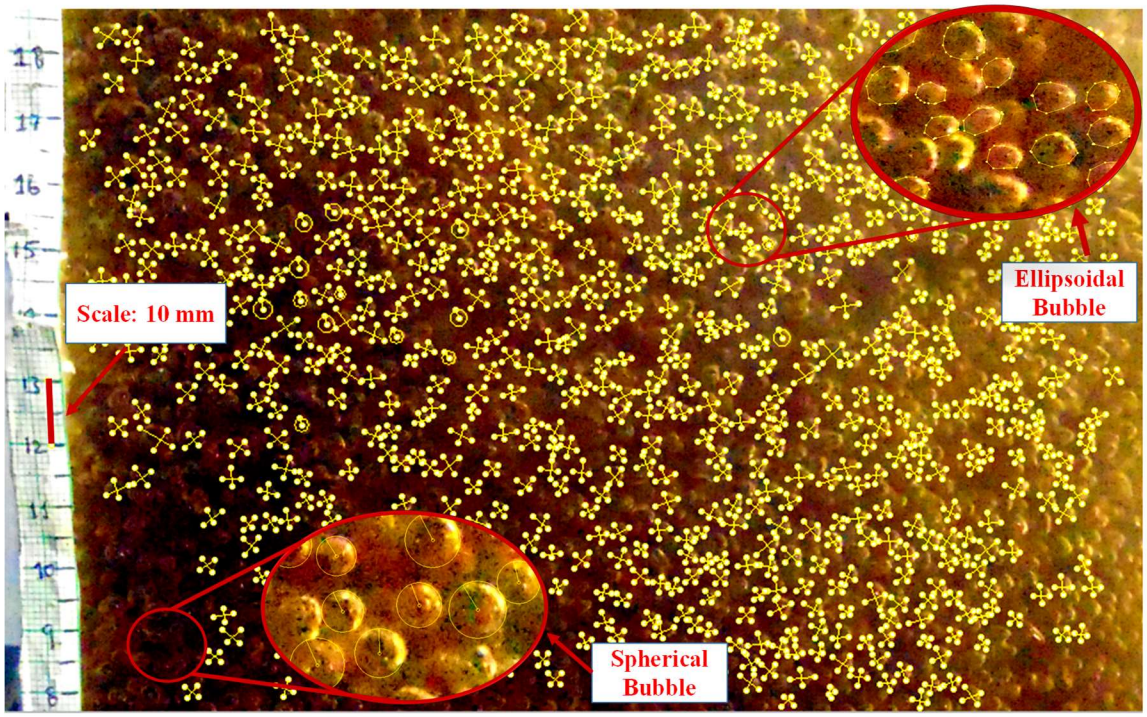

Fig. 4.2. A typical outline for measuring the bubble size.

4.3. Results and discussion

4.3.1. Influence of different variables on the Sauter mean bubble diameter

This section presents a comprehensive analysis of the impact of different variables such as dispersed gas and continuous slurry velocity, particle concentration, particle size, and surfactant on the Sauter mean bubble diameter. Some typical images of bubbles in various experimental conditions are displayed in Fig. 4.3.

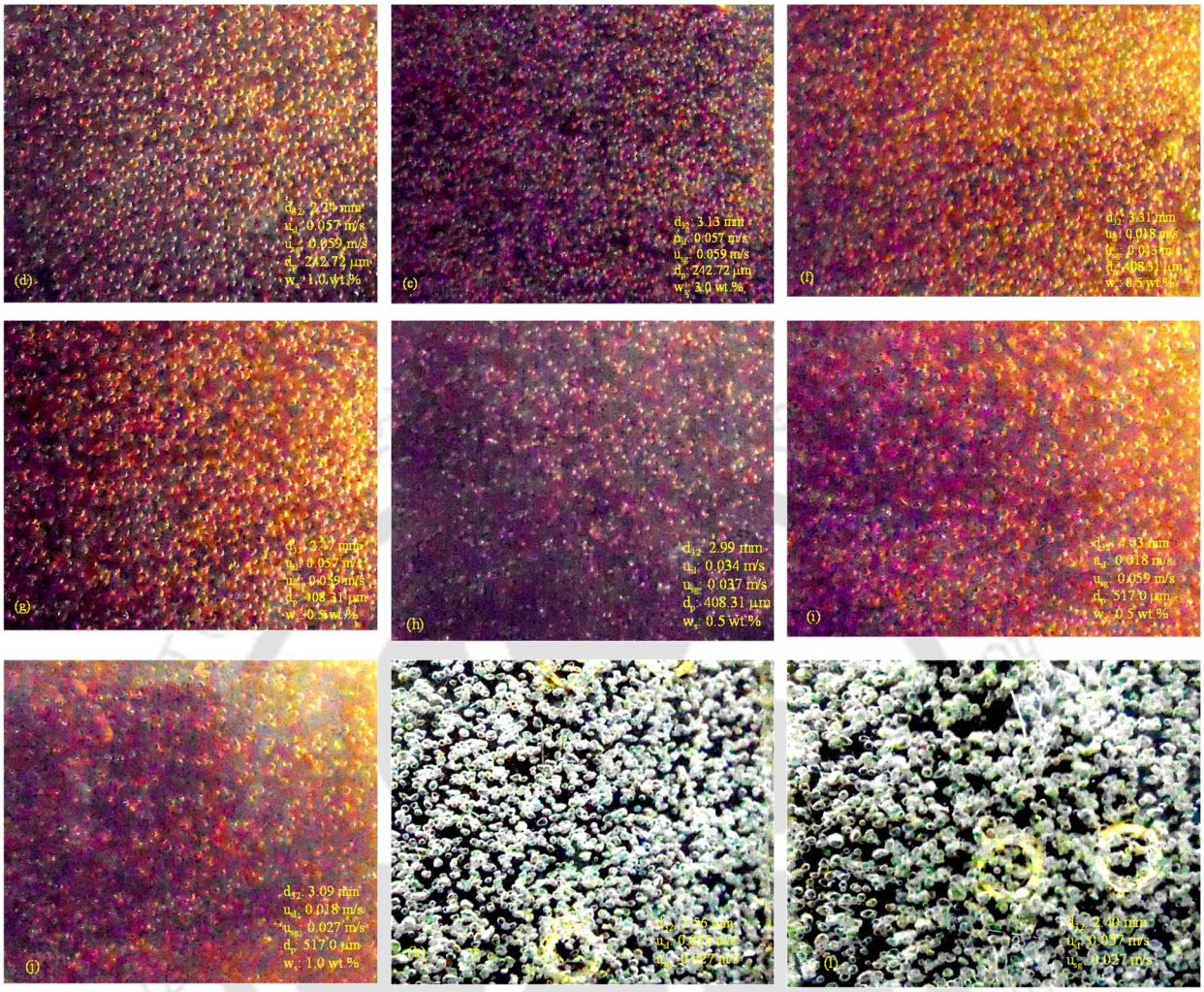

Fig. 4.3. A typical snapshot of bubbles in various experimental conditions.

4.3.1.1. Influence of dispersed phase and slurry velocity on Sauter mean bubble diameter

Influences of continuous slurry velocity ($0.018 \leq u_{sl} \leq 0.057$ m/s) on Sauter mean bubble diameter (d_{32}) at various dispersed gas velocities ($0.011 \leq u_{sg} \leq 0.075$ m/s) and at fixed particle concentration (w_s: 0.5 wt.%) and particle size (d_p: 242.72 μm) are shown in Fig. 4.4a. It is perceived that d_{32} increases as the u_{sg} increases, although it decreases with an increase in u_{sl}. The increase in the bubble size with an increase in the u_{sg} is mainly due to the bubble coalescence (Zhang et al., 2008). Bubble coalescence theory reports bubbles of different diameters will have different rise velocity due to the buoyant force, which causes a collision of bubbles and coalescence occurs (Shukla et al., 2008). The random motion of bubbles causes turbulence, which also promotes collision. Azad and Syeda (2006), reported the mechanism of bubble coalescence, this

occurs by three approaches, a collision of the bubble and entrapment of liquid between them, flattening of the bubble, and drainage of trapped liquid and then coalescence of the bubble. In the counter-current flow arrangement, as the u_{sl} increases, the drag on the rising bubbles increases, which reduces the rising velocity of the bubbles. As a result, the bubble size decreases. Variations in the rising velocity also intensify the rate of bubble coalescence (Shukla et al., 2008; Yoshida et al., 2013). A similar result is observed by Luewisutthichat et al. (1997), where they reported that the increase and decrease in the d_{32} with u_{sg} and u_{sl}, respectively, in the counter-current three-phase (glass beads of d_p: 500 and 2700 μm) bubble column. The d_{32} decreases from 2.09 to 1.57 mm, (approximately 24.95%, at u_{sg}: 0.011 m/s) as the u_{sl} increases from 0.018 to 0.057 m/s. Similarly, the decrease in d_{32} is around 23.70% (at u_{sg}: 0.075 m/s) in the same range of change in u_{sl}. So, it can be deduced that the impact of an increase in gas velocity on d_{32} is more prominent than that of an increase in the slurry velocity.

4.3.1.2. Influence of particle concentration on Sauter mean bubble diameter

The effects of particle concentration (w_s: 0.5 – 3.0 wt.%) on d_{32} at a different dispersed gas velocities ($0.011 \leq u_{sg} \leq 0.075$ m/s) and at fixed continuous slurry velocity (u_{sl}: 0.057 m/s) and particle size (d_p: 517.0 μm) are shown in Fig. 4.4b. It is noted that the rise in particle concentration results in an increase in the d_{32}. The increase in the d_{32} is attributed to the increase in the apparent viscosity of the slurry with an increase in the particle concentration. The increase in viscosity enhances the bubble coalescence, and hence the d_{32} increases. According to Behkish et al. (2007), the increase in particle concentration shortens the liquid drainage time between the gas bubbles and promotes the bubble coalescence. It is well known that the increase in the degree of viscosity of fluids affects the bubble size in the gas-liquid-solid dispersion. Even little magnitudes of enhancement in system viscosity can have a significant effect. Increased viscosity augments the bubble coalescence behavior of the system, which increases the bubble size. The difference in the rising velocity of various size bubbles also leads to intensified bubble coalescence (Shukla et al., 2008), therefore bubble size enlarges. An increase in the liquid viscosity not only alters the shape of the bubbles, but also affects the bubble trajectories as well as the rising velocity of the bubble (Xu et al., 2017). The minimum and maximum d_{32} were observed to be 1.44 mm (at u_{sg}: 0.011 m/s and w_s: 0.5 wt. %) and 4.09 mm (at u_{sg}: 0.075 m/s and w_s: 3.0 wt. %), respectively.

4.3.1.3. Influence of particle size on Sauter mean bubble diameter

From the literature review, it has been seen that the particle size is an important parameter that influences the bubble size behavior in a counter-current gas-slurry flow. The effect of particle size ($61.30 \leq d_p \leq 517.0$ μm) on d_{32} at different dispersed gas velocities ($0.011 \leq u_{sg} \leq 0.075$ m/s) and fixed particle concentration (w_s: 0.5 wt.%) and continuous slurry velocity (u_{sl}: 0.034 m/s) is demonstrated in Fig. 4.4c. It is seen that the d_{32} reduces at all the dispersed phase velocities by increasing the particle size. Adding larger particles increases the bubble coalescence time, which lowers the coalescence rate. Another possible reason for the reduction in d_{32} is a reduction in slurry viscosity with an increase in the particle size. Attractive particle interaction is the reason for the higher viscosity in the case of the smaller particle size compared to that of the coarser particle (Kawatra and Eisele, 1988b; Senapati et al., 2009; Zhou et al., 1993). The d_{32} reduces from 2.49 to 1.50 mm (at u_{sg}: 0.011 m/s), which is a reduction of about 39.69% when the particle size increases from 61.30 to 517.0 μm. Similarly, at a dispersed gas velocity (u_{sg}: 0.075 m/s), the decrease in the d_{32} is approximately 34.87% when the d_p increases from 61.30 to 517.0 μm.

4.3.1.4. Comparison of Sauter mean bubble diameter with and without particle and surfactant

The influences of the presence and the absence of particle and surfactant on Sauter mean bubble diameter is shown in Fig. 4.4d. It is noticed that the Sauter mean bubble diameter in the two-phase (air-water) is smaller than that of the three-phase system (in both the presence and absence of surfactant). As expected, in the three-phase system, the Sauter mean bubble diameter without surfactant is larger than that in the presence of surfactant. At a dispersed gas velocity (u_{sg}: 0.011 m/s), the Sauter mean bubble diameter increases from 2.03 (air-water) to 2.09 mm (air-water-solid, with surfactant), that is approximately an increase of 3.12%. Similarly, the Sauter mean bubble diameter increases from 2.09 (air-water-solid-surfactant) to 2.25 mm (air-water-solid, without surfactant); the increase is about 7.42% at a dispersed gas velocity of 0.011 m/s. When the Sauter mean bubble diameter in the air-water system is compared with air-water-solid (without surfactant), the increment is approximately 10.78%. Similarly, Sauter mean bubble diameter at a dispersed gas velocity (u_{sg}: 0.075 m/s), increases from 3.32 (air-water) to 3.46 (air-water-solid, with surfactant) and to 3.59 mm (air-water-solid, without surfactant), the increment is approximately 4.22% and 3.59%, respectively. The increase in the Sauter mean bubble diameter

was about 7.97% when 61.30 µm particle sizes added to the air-water system at a dispersed gas velocity of 0.018 m/s.

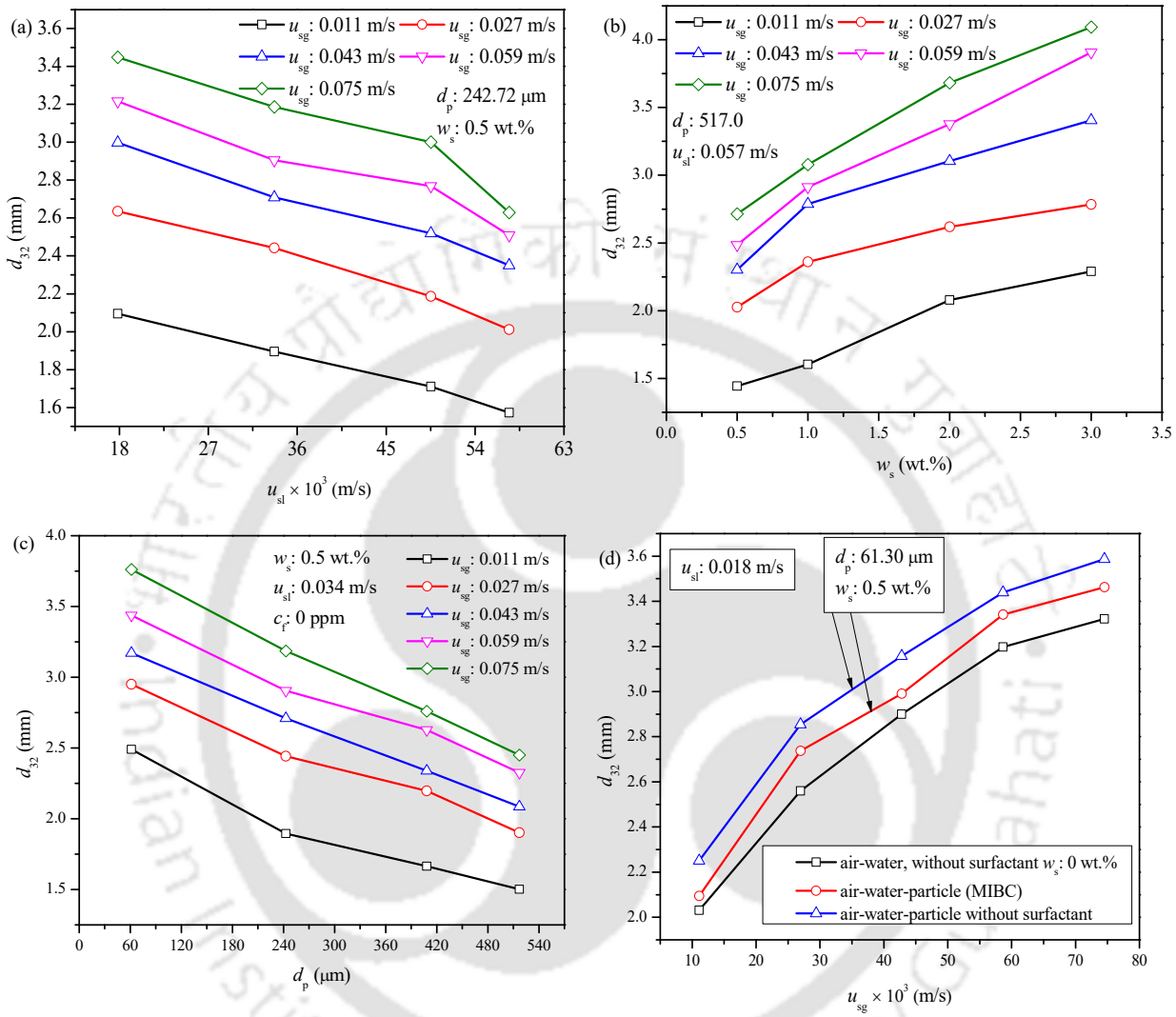

Fig. 4.4 Influence of: (a) continuous slurry and dispersed gas velocity on d_{32}, (b) slurry concentration on d_{32}, (c) particle diameter on d_{32}, and (d) comparison of d_{32} in the presence and absence of particle and surfactant.

4.3.1.5. Sauter mean bubble diameter correlation

The literature lacks the reports of the influence of various variables such as particle concentration, particle size, dispersed gas, and continuous slurry velocity on d_{32} in the three-phase counter-current bubble column. However, some experiments have been performed in the two-phase counter-current cylindrical bubble column (Besagni et al., 2014). To check the scope of validity range of

this experimental result (at u_{sl}: 0.018 m/s, d_p: 63.01 μm, w_s: 0.5 wt.%), the current experimental values are compared with the experimental data from Besagni et al. (2014) (two-phase counter-current system, experimented at u_l: 0.04, 0.08, and 0.11 m/s) and Prakash et al. (2019) (semi-batch microstructured slurry bubble column, at different w_s: 0.2, and 0.8 wt. %, d_p: 242.72 and 408.31 μm, with and without surfactant) (as shown in Fig. 4.5a). It is observed that the experimental values of Besagni et al. (2014) (at u_l: 0.08 m/s) and Prakash et al. (2019) (at w_s: 0.8 wt. %, 242.72 μm, SDS 3 ppm) lie below the current experimental d_{32}. The experimental values of Besagni et al. (2014) at u_{sg}: 0.02, 0.03, and 0.04 m/s (for u_l: 0.04 m/s) are close to the present experimental values whereas at u_{sg}: 0.01, the d_{32} value is less than the experimental value. For u_l: 0.11 m/s (at u_{sg}: 0.020 m/s), the experimental value of Besagni et al. (2014) is close to the present experimental value of d_{32}, but at u_{sg}: 0.011and 0.040 m/s, the deviation in values from experimental data is very large. Consequently, it is deduced that there is a lack of a robust correlation that can accommodate all essential parameters that can precisely interpret the experimental d_{32} values. To accurately predict d_{32} for current experimental conditions, it is essential to develop a new empirical correlation. The proposed correlation (based on 557 sets of experimental data) for d_{32} is as follows

$$\frac{d_{32}}{d_c} = 0.06 \left(\frac{g d_p}{u_{sg}^2} \right)^{-0.124} \left(\frac{\rho_{sl} u_{sl}^2 d_c}{\sigma_{sl}} \right)^{-0.018} (1 - w_s)^{-4.963} \qquad (4.4)$$

The ranges of validity of the correlation (Eq. 4.4) is: $0.193 \leq u_{sg}/u_{sl} \leq 4.177$; $0.111 \leq g d_p / u_{sg}^2 \leq 41.190$; $0.187 \leq \rho_{sl} u_{sl}^2 d_c / \sigma_{sl} \leq 2.480$; and $0.970 \leq 1 - w_s \leq 1.0$. The absolute average relative error (AARE) between experimental and predicted Sauter mean bubble diameter using Eq. (4.4) is 2.52%. The correlation (Eq. 4.4) is reliable for interpreting the Sauter mean bubble diameter in the error range of ± 19.88%. Parity of experimental and predicted (from Eq. 4.4) Sauter mean bubble diameter with a correlation coefficient of 0.99, and a standard error of 0.132 is given in Fig. 4.5b.

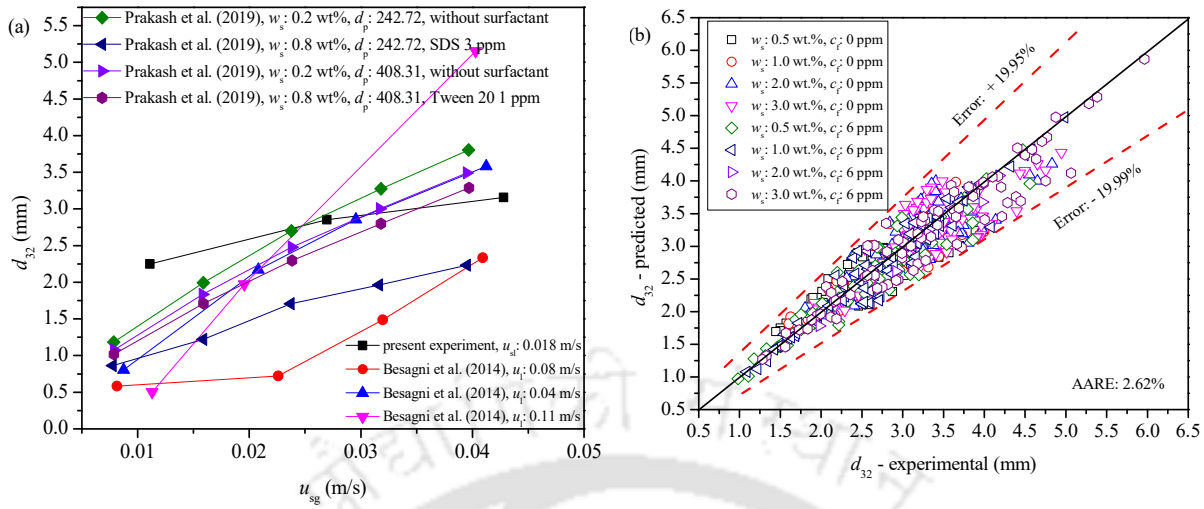

Fig. 4.5 (a) Comparison of the experimental d_{32} with literature values and (b) parity of predicted d_{32} with the experimental values in the three-phase system.

Some typical values of d_{32} are given in Table 4.4.

Table 4.4 Some typical values of Sauter mean bubble diameter in the various experimental condition.

System	Superficial slurry velocity, $u_{sl} \times 10^3$ (m/s)	Superficial gas velocity, $u_{sg} \times 10^3$ (m/s)	Particle concentration, w_s (wt.%)	Particle diameter, d_p (μm)	Sauter mean bubble diameter, d_{32} (mm)
Air-water-particle (without surfactant)	17.83	11.10	0.5	61.30	2.25
	17.83	42.80	0.5	61.30	3.158
	17.83	74.50	0.5	61.30	3.587
	33.69	26.95	0.5	61.30	2.950
	49.54	58.65	0.5	61.30	3.129
	57.46	74.50	1.0	61.30	3.221
	49.54	11.10	2.0	61.30	2.614
	33.69	26.95	3.0	61.30	3.060
	57.46	26.95	0.5	242.72	2.011
	17.83	11.10	1.0	242.72	2.459
	49.54	74.50	3.0	242.72	3.032
	57.46	58.65	2.0	408.31	3.249
	17.83	74.50	3.0	408.31	3.183
	17.83	42.80	0.5	517.0	2.519
	33.69	58.65	1.0	517.0	3.103
	49.54	26.95	2.0	517.0	2.722
	57.46	74.50	3.0	517.0	4.094
	17.83	11.10	0.5	61.30	2.095

Air-water-particle (with surfactant)	33.69	26.95	1.0	61.30	3.119
	49.54	42.80	3.0	61.30	3.274
	57.46	74.50	2.0	408.31	4.181
	17.83	11.10	–	–	2.091
Air-water	33.69	42.80	–	–	2.801
	49.54	42.80	–	–	2.694

4.3.1.6. Aspect ratio of gas bubbles

The ratio of the minor axis and the major axis of the bubble is defined as the aspect ratio (ϕ) of the bubble, which is used to characterize the bubble shape. The ϕ of bubble gradually decreases with an increase in *Eo*. The bubble shape is influenced by the surface tension force, inertial force, buoyant force, and viscous force that act on it. These forces can be characterized by a dimensionless number such as Reynolds number (*Re*), Weber number (*We*), Eötovos number (*Eo*), and Morton number (*Mo*). Several studies on *E* has been conducted to enunciate the influence of gas velocity and physical properties on it (Aoyama et al., 2018; Besagni and Deen, 2019; Besagni and Inzoli, 2019; Huang et al., 2018; Li et al., 2017a; Zhen et al., 2019). Several researchers have suggested a correlation for *E* in terms of *Eo* (Besagni and Inzoli, 2016a, 2019; Okawa et al., 2003), *We* (Legendre et al., 2012; Raymond and Rosant, 2000; Wellek et al., 1966) and as a function of *Mo* and *Re* (Fan and Tsuchiya, 1990; Myint et al., 2007; Takahashi et al., 1976), *Re* and *Eo* (Aoyama et al., 2016; Besagni and Deen, 2019; Tian et al., 2019), *We* and *Re* (Raymond and Rosant, 2000), *Mo* and *Eo* (Bozzano and Dente, 2001), *Wi*, *We*, and *Re* (Acharya et al., 1977; Gupta and Wanchoo, 2009). Most of the developed correlations are suggested for a single bubble rising in an infinite medium. Few authors have developed a correlation for swarms of gas bubbles (Besagni and Deen, 2019; Besagni and Inzoli, 2016a, 2019; Besagni et al., 2017b). The variation of ϕ as a function of d_b at different experimental conditions is shown in Fig. 4.6. Fig. 4.6a – 4.6d shows ϕ for the two-phase system in a counter-current mode. At u_{sg} = 0.011 m/s and u_l = 0.018 m/s, approximately 47.39% of the bubbles can be approximated as a sphere with $0.9 \leq \phi \leq 1.0$ and remaining bubbles are in the range of $0.5 \leq \phi < 0.9$ (as shown in Fig. 4.6a). No bubbles are observed below ϕ of 0.5. When the u_{sg} increases to 0.075 m/s, with the same value u_l = 0.018 m/s, the bubbles with $0.9 \leq \phi \leq 1.0$ reduces to 42.80%, while the remaining bubbles were in the range of $0.5 \leq \phi < 0.9$ (as shown in Fig. 4.6b). The reduction in the bubble number density is attributed

to the distortion of the bubble shape due to an increase of u_{sg}. By comparing ϕ at same u_{sg}: 0.043 m/s, but at different u_l: 0.034 and 0.057 m/s, it was seen that the bubbles with $0.9 \leq \phi \leq 1.0$ are 48.54% and 41.64%, respectively (as shown in Figs 4.6c and 4.6d). Here also, it has been observed that the sphericity of the bubbles reduces as the u_l increases in the counter-current mode. Fig. 4.6e to 4.6i shows the behavior of ϕ in a three-phase counter-current flow in the presence of MIBC surfactant (6 ppm). Figures 4.6e and 4.6f reflect the influence of an increase in particle concentration on the ϕ of the bubbles. About 65.09% (at 0.5 wt. %, u_{sg}: 0.043 m/s, u_{sl}: 0.018 m/s) and 51.93% (at 3.0 wt. %, u_{sg}: 0.043 m/s, u_{sl}: 0.018 m/s) bubbles are in the range of $0.9 \leq \phi \leq 1.0$. The increase in particle concentration also reduces the sphericity of the bubbles. Figures 4.6g and 4.6h show the influence of particle size on the ϕ of the bubbles. It was found that about 54.30% (at d_p: 150 – 300 µm, u_{sg}: 0.043 m/s, u_{sl}: 0.050 m/s) and 60.07% (at d_p: 300 – 425 µm, u_{sg}: 0.043 m/s, u_{sl}: 0.050 m/s) bubbles are present with $0.9 \leq \phi \leq 1.0$. It deduced that with larger particle size, the bubble shape distortion is lower in comparison with that of smaller particle size. In the case of a particle size $dp > 425$ µm, at u_{sg}: 0.075 m/s, u_{sl}: 0.075 m/s (Fig. 4.6i), approximately 54.80% of the bubbles are with $0.9 \leq \phi \leq 1.0$ and remaining was with $0.4 \leq \phi < 0.9$.

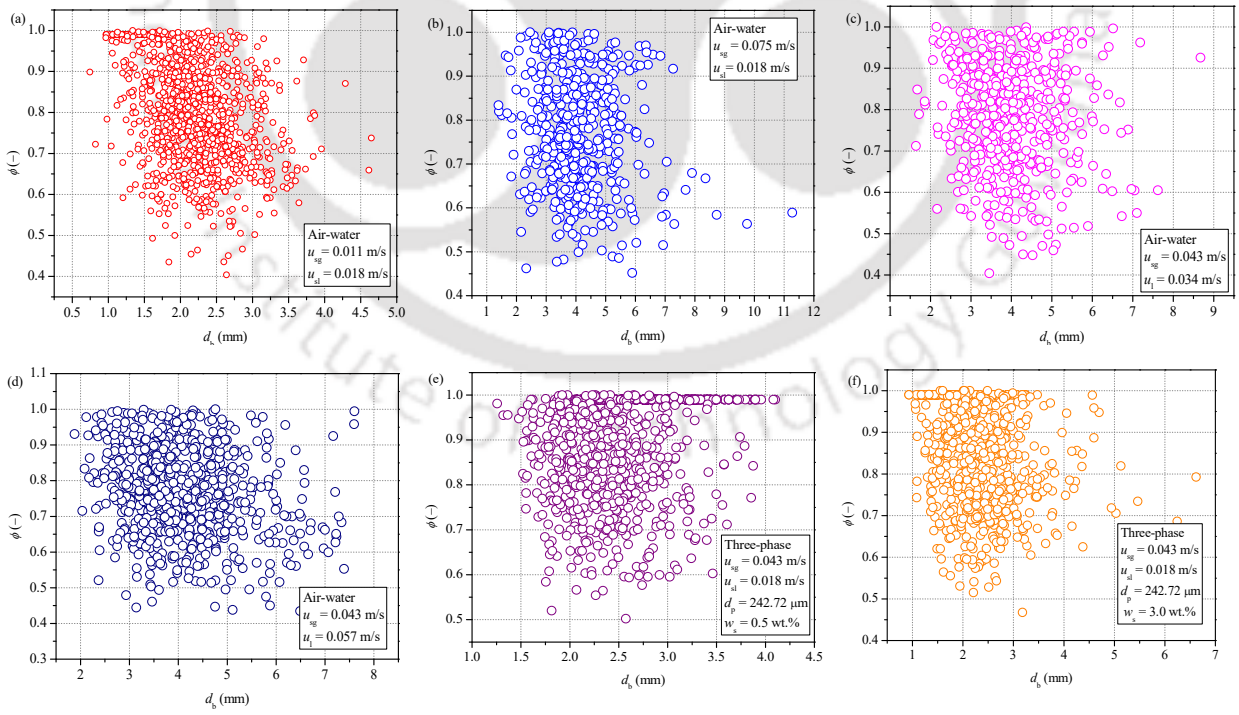

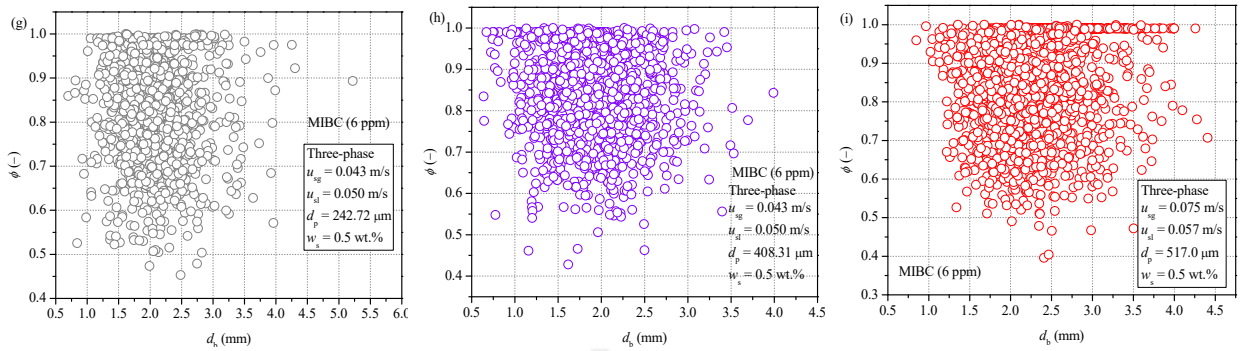

Fig. 4.6 Some typical results of ϕ as a function of d_b in various experimental conditions: (6a – 6d) aspect ratio in the two-phase system, (6e – 6i) aspect ratio in the three-phase system.

4.3.1.7. Aspect ratio correlation

Several correlations have been suggested to interpret the ϕ of the bubbles in terms of different dimensionless groups such as *We* (Sugihara et al., 2007), *Eo* (Besagni and Inzoli, 2016a; Li et al., 2017a; Okawa et al., 2003), *Ta* (Fan and Tsuchiya, 1990; Vakhrushev and Efremov, 1970) and a combination of *Re* and *Eo* (Aoyama et al., 2016; Besagni and Deen, 2019; Dong et al., 2010; Tian et al., 2019), *Mo* and *Eo* (Bozzano and Dente, 2001). An attempt was made to develop the correlation by incorporating the multiple dimensionless groups by applying multiple linear regression analysis, but it was statistically less significant. Consequently, correlations are developed by taking the *Eo* and *Re* for the two-phase (without surfactant) (Eq. 4.5) and three-phase (with surfactant) system (Eq. 4.6).

$$\phi = \frac{1}{(1+1.795Eo^{2.207}\,\mathrm{Re}^{0.43})^{0.081}} \tag{4.5}$$

$$\phi = \frac{1}{(1+0.9Eo^{2.9}\,\mathrm{Re}^{0.5})^{0.08}} \tag{4.6}$$

The correlations (Eq. 4.5 and Eq. 4.6) are strictly valid for dense bubbly flow conditions in a counter-current mode. The developed correlation for the counter-current two-phase system is compared with the published correlations, as shown in Fig. 4.7a. The AARE between the present proposed correlation and the available correlations is reported in Table 4.5. It is noticed that the correlations of Bozzano and Dente (2001) (for the single bubble motion), Li et al. (2017a) (for the methane bubble covered with a hydrating film), Besagni and Inzoli (2016a) (for air-water), Wellek

et al. (1966) (for drop), Besagni and Inzoli (2019) (for air-water and air-water-ethanol), and Vakhrushev and Efremov (1970) (for a single bubble) fit the present proposed correlation with AARE < 15.0%. The correlation proposed by Bozzano and Dente (2001) fits well the current data with the AARE of 4.314%. Similarly, the correlation developed for the three-phase is also compared with the published correlations, as shown in Fig. 4.7b. For the case of a three-phase system, the correlations of Bozzano and Dente (2001), Li et al. (2017a), Wellek et al. (1966), and Prakash et al. (2019) (for three-phase batch mode) are close to present developed correlation with the AARE < 9.0%. Also, in the three-phase system, the correlation of Bozzano and Dente (2001) satisfies well the presently developed correlation with AARE of 1.964%.

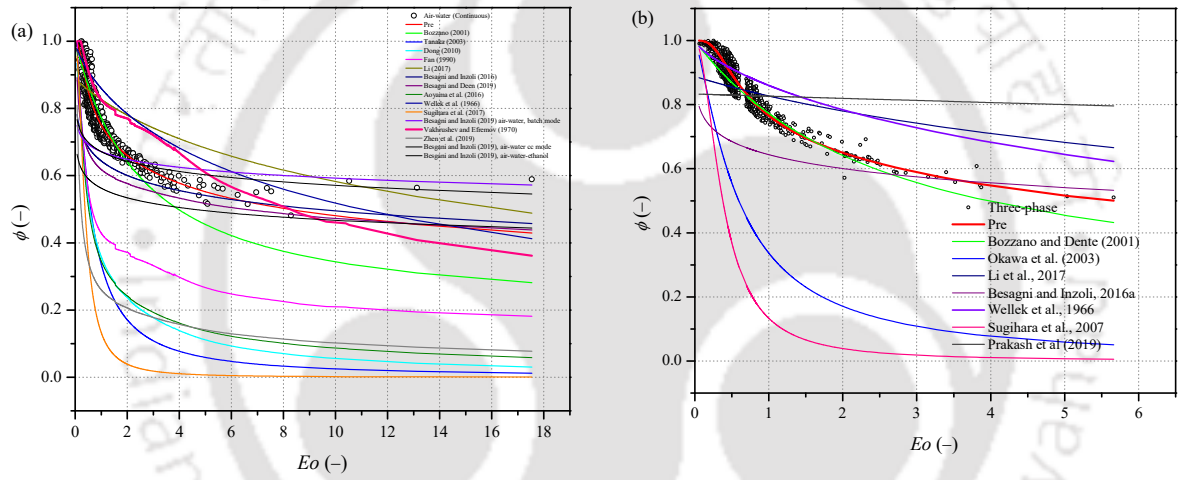

Fig. 4.7 comparison of the measured ϕ with the available correlations as a function of *Eo*: (a) for the two-phase system and (b) for the three-phase system.

Table 4.5 Error between the available correlations and the presently developed correlation for the two- and three-phases.

Author	Experimental condition	AARE (%) for counter-current air-water	AARE (%) for counter-current three-phase
Bozzano and Dente (2001)	–	4.314	1.964
Okawa et al. (2003)	–	58.700	44.443
Dong et al. (2010)	–	54.093	–
Fan and Tsuchiya (1990)	–	40.154	–
Li et al. (2017a)	–	12.992	6.717

Besagni and Inzoli (2016a)	Air-water, $\log_{10} Mo$ (-10.781)	12.809	20.156
Besagni and Deen (2019)	$\log_{10}$ (*Mo*): -10.8 and 2.3, single bubbles and dense bubbly flows	15.424	–
Aoyama et al. (2016)	Air and the aqueous solution of glycerol, $\log_{10}$ (*Mo*): −6.6, −5.5, −4.9, and −3.9. The maximum bubble diameter in the present experiment was 6.11 mm. The tank size was, therefore, large enough to make the wall effect on the bubble motion and shape negligible.	53.907	–
Wellek et al. (1966)	–	13.539	6.973
Sugihara et al. (2007)	–	77.807	65.835
Besagni and Inzoli (2019)	Air-water, batch mode, -10.781	10.477 (for air-water)	–
Besagni and Inzoli (2019)	Air-water-ethanol, batch mode, (0.05%wt), $\log_{10}$ (*Mo*): −10.665	9.983 (air-water ethanol, batch mode)	–
Besagni and Inzoli (2019)	Air-water counter-current mode	23.078	
Zhen et al. (2019)	For low *We* (*We* < 12) and *Mo* (*Mo* < 3), both viscous and surface tension are important. Thus the bubble shape relies on *Eo* number and *Re*.	64.999	–
Vakhrushev and Efremov (1970)	–	11.558	–
Prakash et al. (2019)	–	–	8.179

4.3.1.8. Grace diagram for the shape of gas bubbles

A general graphical shape regime in terms of *Eo*, *Re,* and *Mo* for the bubble in an infinite medium is given by Grace (1976) and Clift et al. (1978). This graphical shape regime diagram can be used to determine the bubble shape and terminal velocity of the bubbles. The graphical layout was developed for the single rising bubble in the infinite medium instead of that for the dense bubbly regime. Clift et al. (1978) reported the influence of the column wall on the rising gas bubbles as per ratio λ, which is the ratio of the bubble to the column diameter. If the value of λ is less than 0.6, this reflects an insignificant impact of the wall on the rising gas bubbles, and the bubble can be considered as rising in the infinite medium. In the analysis, the maximum bubble size is 11.28 mm (for the two-phase without surfactant), and the equivalent column diameter is 0.052 m, hence as per the relation, the λ is 0.22. Consequently, it has a negligible influence of the wall on the gas bubbles. The present experimental data for the two-phase (for $\log_{10}(Mo) = -10.937$) and the three-phase (for $\log_{10}(Mo) = (-10.957) - (-10.987)$) system is presented in the grace diagram (as shown in Fig. 4.8). It is noticed that the bubbles cover both the spherical and ellipsoidal shape regime.

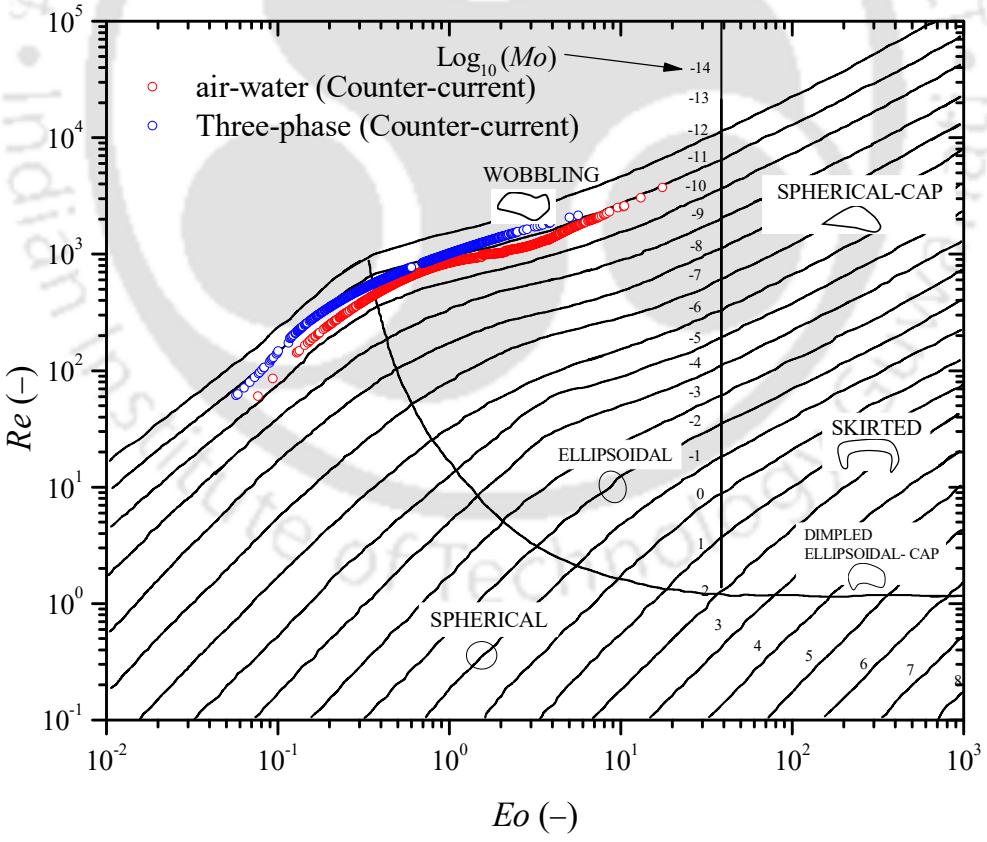

Fig. 4.8 Grace diagram for estimation of a bubble shape (adapted from Prakash et al. (2020)).

4.3.1.9. Error in image analysis

A total of 300 bubbles were marked, and the bubble size was measured. As expected, the relative standard deviation (RSD) was observed to be higher for smaller bubbles, and it decreases with a larger bubble, as shown in the Supporting Information. It indicates that the smaller the bubble size, the higher the estimation error. The present result is consistent with Besagni and Inzoli (2016a) and Prakash et al. (2020). The maximum relative standard deviation (RSD) is 6.88%. Selected image for error in image analysis and relative standard deviation (RSD) as a function of bubble size is shown in Fig. 4.9a and 4.9b, respectively.

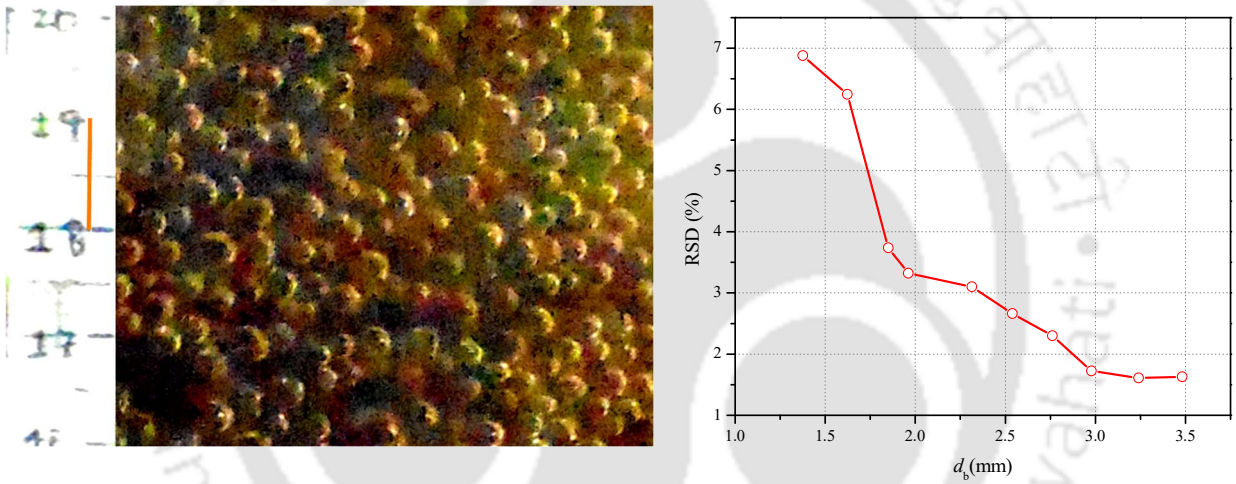

Fig. 4.9 (a) Selected image for error in image analysis and (b) relative standard deviation (RSD) as a function of d_b.

4.3.2. Influence of numerous variables on the bubble size distribution

This section discusses the influences of various variables (i.e., u_{sg} and u_{sl}, w_s, and d_p) on bubble size distribution (BSD). The BSD is expressed in terms of percentage relative frequency (RF). In different environments, the BSD can have different shapes due to operating variables and the physical properties of the system. In the research articles, both unimodal (Smith et al., 1996) and bimodal (Lau et al., 2013; Parthasarathy and Ahmed, 1994; Wongsuchoto et al., 2003) type of BSD has been observed depending on the operating variables and gas distributor design. A transition from unimodal BSD to bimodal BSD has been observed with an increase in the

superficial gas velocity (Lau et al., 2013; Wongsuchoto et al., 2003). To obtain consistent BSD, the number of bubbles taken into consideration is the matter of debate in the research articles (Honkanen et al., 2005). Many authors reported sample size of bubbles for BSD analysis is 50−100 (Lage and Espósito, 1999), 100 (Passos et al., 2015), 200 (Wongsuchoto et al., 2003), and 250−300 (Al-Oufi, 2011). In this present analysis, for each system, at least 250 to at most 400 bubbles were marked for an individual region. In this present work, all the BSD plots show a unimodal form of BSD. In the subsequent section, the bubble diameter is used as the characteristics size for the BSD in the slurry system. The subsequent section describes the type of BSD and its prediction.

4.3.2.1. Bubble size distribution as a function of dispersed gas velocity

The BSD gives an idea of interfacial forces and interaction among the phases, plays an essential role in the determination of the hydrodynamic characteristics of the slurry column (Rabha et al., 2013b). A typical percentage relative frequency versus bubble diameter result obtained from the photographic measurement technique is shown in Fig. 4.10. On the *x*-axis, the region associated with "1.60" represents all bubbles with $d_b \leq$ 1.60 mm, and the next region represents bubbles with 1.60 mm ≤ d_b ≤ 1.98 mm (Fig. 4.10a). The influences of three different dispersed gas velocities (u_{sg}: 0.043, 0.059, and 0.075 m/s) on the BSD in the presence of 0.5 wt. % particle concentration, 0.018 m/s u_{sl}, and 242.72 μm d_p are illustrated in Fig. 4.10a. At a u_{sg}: 0.043 m/s, the BSD is unimodal with a maximum relative frequency (RF) peak at d_b: 3.12 mm. The further increase in the u_{sg}, say at 0.059 m/s, the RF peak moves to the larger bubble diameter (at d_b: 3.50 mm). With a further increase in the u_{sg}, say 0.075 m/s, no change in the RF peak is observed. The BSD curve shifted towards the large d_b as u_{sg} increases from 0.043 to 0.059 m/s; however, further, the rise in the u_{sg} does not show any appreciable change. In Fig. 4.10a, at a low dispersed gas velocity (u_{sg}: 0.043 m/s), the RF of small bubbles (< 3.50 mm) is approximately 76.77% compared to 46.34% and 39.9% at u_{sg}: 0.059 m/s and 0.075 m/s, respectively. Fig. 4.10b also shows the influence of u_{sg} on BSD at u_{sl}: 0.034 m/s. The RF of smaller bubbles, say < 3.62 mm is about 96.77%, 73.88%, and 75.73% at the u_{sg}: 0.043, 0.059, and 0.075 m/s, respectively.

4.3.2.2. Bubble size distribution as a function of continuous slurry velocity

The effect of slurry velocity (0.018 ≤ u_{sl} ≤ 0.057 m/s) on BSD at u_{sg}: 0.027, d_p: 242.72 μm, and w_s: 0.5 wt. % is shown in Fig. 4.10c. It is seen that the BSD is shifted to the small bubble diameters

(to the left) when the u_{sl} increases from 0.018 to 0.057 m/s. The shifting of the BSD to the small bubble is attributed to a reduction in the bubble coalescence rate as the u_{sl} increases. In a counter-current flow arrangement, as the u_{sl} increases, the rising bubbles are exposed to a higher drag force, which in turn reduces the rising velocity. With a low rising velocity, the intensity of bubble collision decreases, leading to a decrease in the bubble coalescence. As the u_{sl} increases, the turbulence in the column increases, causing the bubble breakup, leading to the generation of small bubbles. The maximum RF is at d_b: 2.85 mm, 2.28 mm, and 1.72 mm at 0.018, 0.034, and 0.057 m/s u_{sl}, respectively.

4.3.2.3. Bubble size distribution as a function of particle concentration

Influence of slurry concentration (w_s: 0.5, 1.0, and 3.0 wt. %) on BSD at u_{sg}: 0.043 m/s and u_{sl}: 0.050 m/s and d_p: 242.72 μm is shown in Fig. 4.10d. It is seen that with an increase in the particle concentration, BSD is shifting to large bubble diameters. The shifting of the BSD towards the large bubble is because of the increase in the bubble size. The apparent viscosity of the slurry increases, leading to an increase in the bubble coalescence, and consequently, the bubble size increases. The maximum RF peak increases from 2.73 to 3.20 and to 3.66 mm as the slurry concentration increases from 0.5 to 1.0 and to 3.0 wt. %, respectively. At particle concentrations (w_s: 0.5 wt. %), the RF of the bubbles (d_b < 3.20 mm) is approximately 66.14%, 36.45%, and 12.98% at 0.5, 1.0 and 3.0 wt. % particle concentration, respectively. The RF of small bubbles decreases by increasing the particle concentration. Similarly, Fig. 4.10e shows the effect of particle concentration at two different u_{sl}: 0.034 and 0.057 m/s and d_p: 408.31 μm and u_{sg}: 0.059 m/s. In the case of particle concentration, 0.5 wt. % (at u_{sl}: 0.034 m/s), the maximum RF is at d_b: 2.60 mm, while it is 2.92 mm at 1.0 wt. % (at u_{sl}: 0.034 m/s) particle concentration. Similarly, at $u_{sl:}$ 0.057 m/s and at 0.5 wt. % particle concentration, the maximum RF is at d_b: 1.96 mm, while it is 2.28 mm at 1.0 wt. % particle concentration. At u_{sl}, say 0.034 m/s, at d_b: 2.60 mm, the RF of the bubble is approximately 40.26% (at w_s: 0.5 wt. %), but it is about 10.96% at 1.0 wt. % particle concentration. Similarly, it was 75.92% (at w_s: 0.5 wt. %) and 56.60% (at w_s: 1.0 wt. %) at u_{sl}: 0.057 m/s.

4.3.2.4. Bubble size distribution as a function of particle size

The influences of three different particle sizes (d_p: 242.72, 408.31, and 517.0 μm) on BSD at a fixed particle concentration (w_s: 0.5 wt. %) and superficial slurry (u_{sl}: 0.034 m/s) and dispersed

gas velocity (u_{sg}: 0.075 m/s) are shown in Fig. 4.10f. It is seen that with a decrease in the particle size, BSD shifts to a large bubble diameter. It is attributable to an increase in the bubble diameter with a decrease in particle size. At a fixed quantity of the particle, if the particle size is reduced, the net result is an increase in the particle count; consequently, slurry viscosity increases. The apparent viscosity of the slurry is more in small particle size because of a more attractive particle interaction (Kawatra and Eisele, 1988b). A system with a smaller particle size produces larger diameter bubbles (Ojima et al., 2015; Sarhan et al., 2018c). According to Sarhan et al. (2018c), the presence of larger particle size, the bubble coalescence rate decreases, which can be attributed to the coalescence of gas bubbles in the presence of larger particles, takes more time in comparison to small particles. The maximum RF of the bubbles is at d_b: 3.52 mm, 3.10 mm, and 2.67 mm in the presence of 242.72, 408.31, and 517.0 µm particle sizes, respectively. The RF of bubbles at d_b < 3.52 mm is approximately 91.08%, 82.18%, and 48.53% at 517.0, 408.31, and 242.72 µm particle size, respectively. Figure 4.11g also reports the influence of particle size on BSD at u_{sl}: 0.018 m/s, u_{sg}: 0.059 m/s, and w_s: 0.5 wt. %. It is observed that BSD shifts to a larger bubble diameter as the d_p decreases from 517.0 to 242.72 µm. The RF of bubbles at d_b < 3.62 mm is 51.88% (at d_p = 242.72 µm), 87.87% (at d_p = 408.31 µm), and 92.67% (at d_p = 517.0 µm). The maximum RF of the bubbles is at 3.62 mm, 3.18 mm, and 2.73 mm at 242.72 µm, 408.31 µm, and 517.0 µm, respectively.

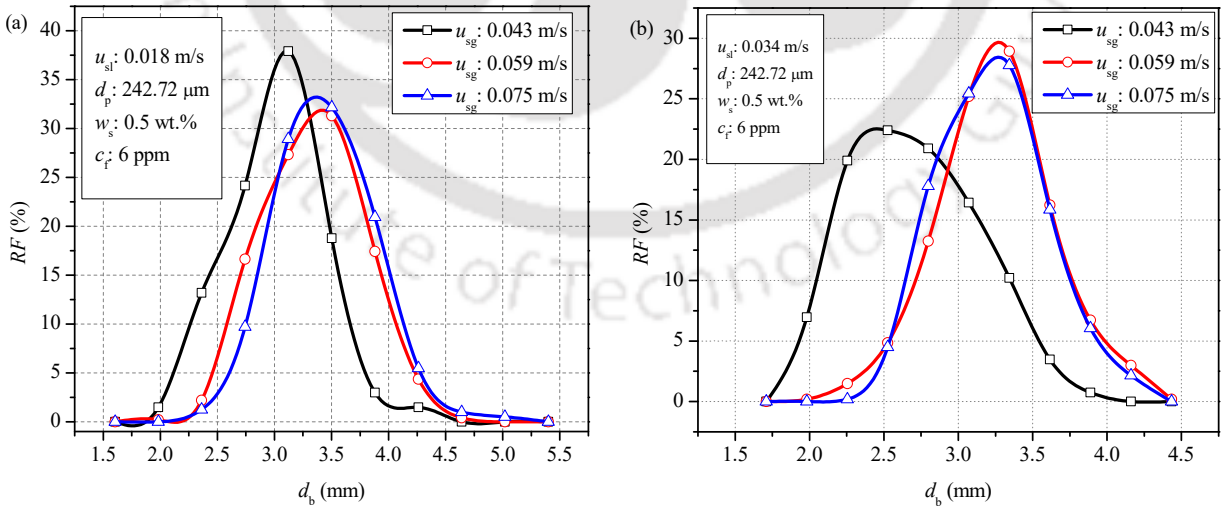

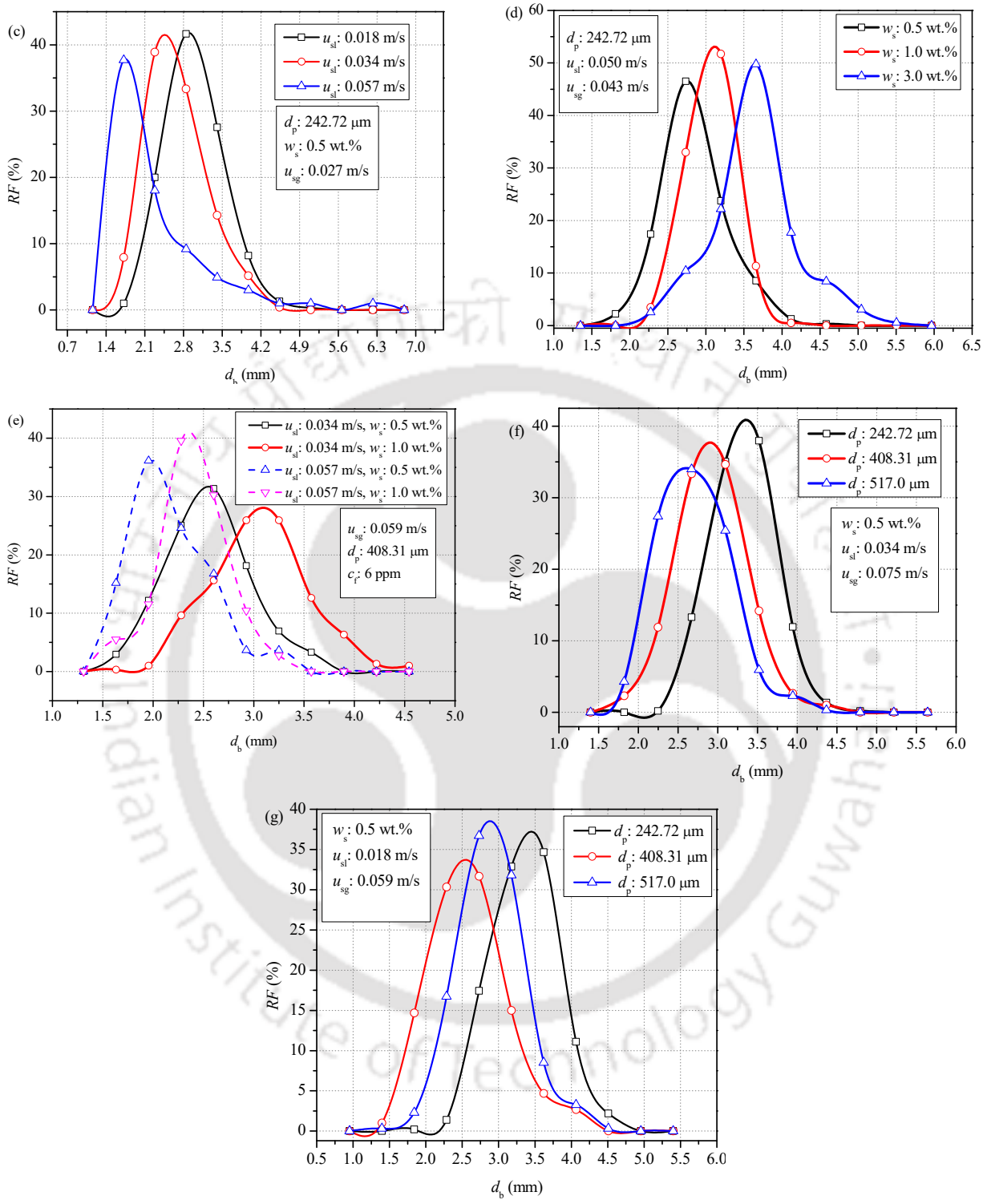

Fig. 4.10 (a) BSD as a function of (a) dispersed gas velocity (at w_s: 0.5 wt.%, u_{sl}: 0.018 m/s, d_p : 242.72 μm), (b) dispersed gas velocity (at w_s: 0.5 wt.%, u_{sl}: 0.034 m/s, d_p: 242.72 μm), (c) continuous slurry velocity (at w_s: 0.5 wt.%, u_{sg}: 0.027 m/s, d_p: 242.72 μm), (d) slurry concentration (at u_{sl}: 0.050 m/s, u_{sg}: 0.043 m/s, d_p: 242.72 μm), (e) slurry concentration (at u_{sg}: 0.059 m/s, d_p:

408.31 μm), (f) particle size (at w_s: 0.5 wt.%, u_{sl}: 0.034 m/s, u_{sg}: 0.075 m/s), and (g) particle size (at w_s: 0.5 wt.%, u_{sl}: 0.018 m/s, u_{sg}: 0.059 m/s).

4.3.2.5. Prediction of BSD

In the current study, the size of the experimentally measured bubble was analyzed using the STAT::FIT software. It was observed that the log-logistic distribution function describes the BSD well with the least error in all sets of values. The goodness of the fit for BSD is decided based on the statistical analysis of chi-squared, Kolmogorov Smirnov, and Anderson Darling test. The log-logistic probability density function is represented by

$$F(d_b) = \frac{\alpha}{\beta}\left(\frac{d_b}{\beta}\right)^{\alpha-1}\left(1+\left(\frac{d_b}{\beta}\right)^{\alpha}\right)^{-2} \tag{4.7}$$

where F(d_b), α and β denote the bubble distribution function, the bubble shape parameter and the bubble scale parameter, respectively. The cumulative distribution function (CDF) for log-logistic BSD can be expressed as

$$F(d_b) = \frac{1}{1+\left(\frac{\beta}{d_b}\right)^{\alpha}} \tag{4.8}$$

The previous article reports the log-logistic BSD function (in air-water-SDS (surfactant)-particle (d_p: 150 – 425 μm)) (Prakash et al., 2019). However, other experimental conditions follow the Weibull and Beta distribution. Other researchers reported a log-normal BSD function (Luewisutthichat et al., 1997). The type of BSD in two (air-water) and the three-phase (air-water + MIBC + solid) system follow the log-logistic BSD. Typical results for three and two-phase BSD fitting are shown in Figs. 4.11a and 4.11b, respectively.

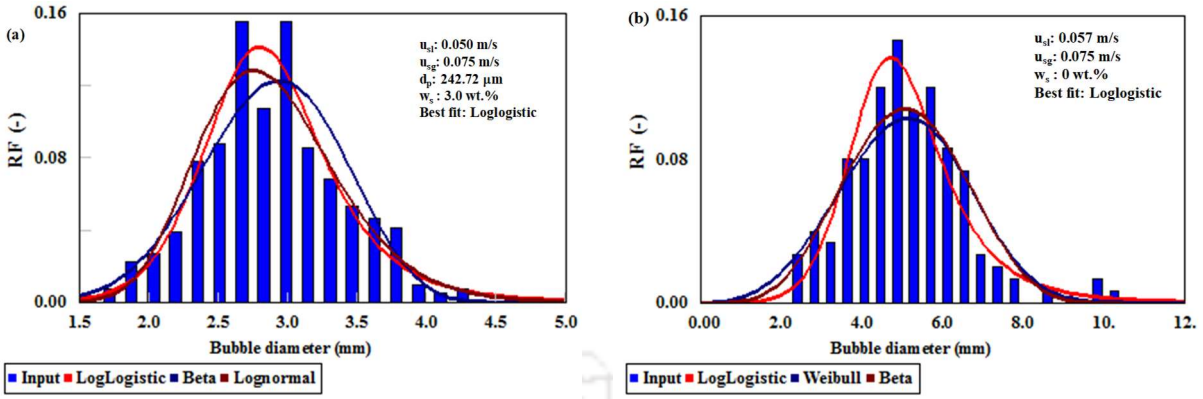

Fig. 4.11 Typically fitted bubble size distribution: (a) three-phase, best fit: LogLogistic (at u_{sl}: 0.050 m/s, u_{sg}: 0.075 m/s, d_p: 242.72 µm, and w_s: 3.0 wt. %) and (b) two-phase, best fit: LogLogistic (at u_{sl}: 0.057 m/s, u_{sg}: 0.075 m/s, and w_s: 0 wt. %).

Developed correlation for the bubble shape parameter (for the three-phase with MIBC) is represented by

$$\alpha = 41.549\left(\frac{\rho_{sl}u_{sl}^2 d_c}{\sigma_{sl}}\right)^{0.251}\left(\frac{gd_p}{u_{sg}^2}\right)^{-0.009}(1-w_s)^{15.613}\left(\frac{\rho_{sl}u_{sl}d_p}{\mu_{sl}}\right)^{-0.442} \quad (4.9)$$

The range of validity of the correlation (Eq. 4.9) follows:

$0.231 \le \rho_{sl}u_{sl}^2 d_c/\sigma_{sl} \le 2.480$; $0.429 \le gd_p/u_{sg}^2 \le 41.190$; $0.970 \le 1-w_s \le 1.0$; $5.366 \le \rho_{sl}u_{sl}d_p/\mu_{sl} \le 37.044$. Experimental values of the bubble shape parameter satisfy the correlation (Eq. 4.9) with a correlation coefficient of 0.90 and a standard error of 0.079, respectively. The recommended correlation for the scale parameter (β) is represented by

$$\beta = 34.773\left(\frac{\rho_{sl}u_{sl}^2 d_c}{\sigma_{sl}}\right)^{0.262}\left(\frac{gd_p}{u_{sg}^2}\right)^{-0.033}(1-w_s)^{2.742}\left(\frac{\rho_{sl}u_{sl}d_p}{\mu_{sl}}\right)^{-0.458} \quad (4.10)$$

The correlation (Eq. 4.10) successfully interprets the experimental values with a correlation coefficient and standard error of 0.85 and 0.047, respectively. The correlation ranges are the same as for Eq. 4.9. Similarly, for the two-phase system, the correlations are developed for the bubble shape parameter (α) and the scale parameter (β). The suggested correlation for α can be expressed as

$$\alpha = 4.245\left(\frac{u_{sl}^2 d_c \rho_l}{\sigma_l}\right)^{0.062}\left(\frac{g d_c}{u_{sg}^2}\right)^{0.119} \tag{4.11}$$

The suggested correlation for the interpretation of the bubble shape parameter in the two-phase system is suitable for predicting experimental values with a standard error and a correlation coefficient of 0.105 and 0.90, respectively. The correlation ranges (for Eq. 4.11) for the different parameters are as follows: $0.416 \le u_{sl}^2 d_c \rho_l / \sigma_l \le 4.315$; $91.444 \le g d_c / u_{sg}^2 \le 4122476$. The correlation developed for β (two-phase) is given by

$$\beta = 31.125\left(\frac{u_{sl}^2 d_c \rho_l}{\sigma_l}\right)^{-0.005}\left(\frac{g d_c}{u_{sg}^2}\right)^{-0.364} \tag{4.12}$$

Equation 4.12 interprets the bubble scale parameter for two-phase with 0.171 as the standard error and 0.97 as the correlation coefficient. The range of variables of correlation (Eq. 4.12) is the same as for the parameter α (Eq. 4.11). Parity of experimental and predicted log-logistic cumulative distribution function (CDF) is shown in Figs 4.12a, 4.12b, and 4.13c. Experimental (calculated from Eq. 4.8) and predicted (calculated from Eq. 4.8 by incorporating Eq. 4.9 and 4.10) values of CDF obey the AARE of 18.87% (at w_s: 0.5 wt. %) and 18.30% (at w_s: 1.0 wt. %) as shown in Fig. 4.12a. In Fig. 4.12b, the AARE is 29.67% (at w_s: 0.5 wt. %, d_p: 408.31 μm) and 8.32% (at w_s: 1.0 wt. %, d_p: 408.31 μm). Similarly, for the two-phase system, the predicted values are evaluated by incorporating Eq. (4.11) and Eq. (4.12) into Eq. (4.8). Figure 4.12c shows the parity of CDF in the air-water system at various experimental conditions. The AARE is 8.74%, 27.16%, and 28.12% at 0.011, 0.043, and 0.075 m/s dispersed gas velocity, respectively.

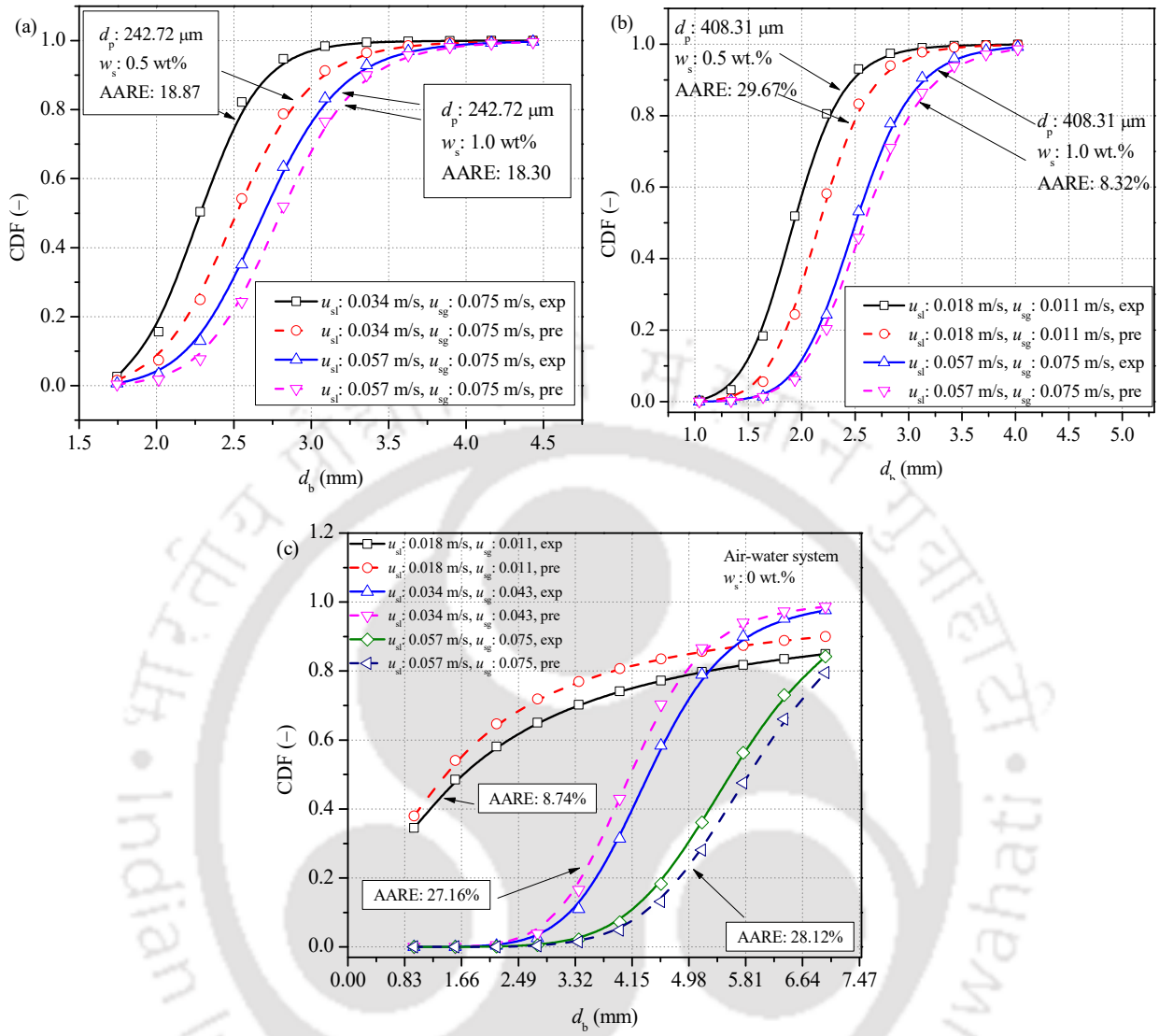

Fig. 4.12 Parity of cumulative distribution function in various experimental conditions: (a) at d_p: 242.72 µm at 0.5 and 1.0 wt. % particle concentration, (b) at dp: 408.31 µm at 0.5 and 1.0 wt. % particle concentration, and (c) air-water system (at w_s: 0 wt. %).

4.4. Conclusions

The present work reports an experimental study of the bubble size and its distribution and aspect ratio in a counter-current microstructured slurry column in the presence and absence of a surfactant. In-depth analysis is carried out to enunciate the influence of physical properties, operating, and dynamic variables on hydrodynamics characteristics. Based on the experimental result, the following conclusions can be drawn:

- Sauter mean bubble diameter decreases with an increase in the continuous slurry velocity and particle size, while it increases as the dispersed gas velocity and particle concentration increase.
- The aspect ratio of the bubble gradually decreases with an increase in Eötovos number. Here also, it has been observed that the sphericity of the bubbles reduces as the dispersed gas and continuous slurry velocity and particle concentration increase. In the presence of the large particle size, the bubble shape distortion is low compared to that of the small particle size.
- Bubble size distribution in the two- and three-phase systems (with and without surfactant) satisfactorily follow the log-logistic distribution function.
- Bubble size distribution became wider and shifted towards the larger bubble diameter as the particle concentration and dispersed gas velocity increased, whereas it was narrower and moved to a smaller bubble size with an increase in the continuous slurry velocity and particle size.
- New empirical correlations were proposed for the prediction of Sauter mean bubble diameter, bubble aspect ratio, and bubble size distribution function parameters. The proposed correlations satisfactorily fit the experimental values well within the error range of ± 20% and AARE less than 20%.

The present experimental analysis will be useful for improving the processes of three-phase counter-current flow columns, for intensifying in the chemical engineering process related to the multiphase system.

Chapter 5

Dispersion Characteristics and Its Analysis

This chapter aims to quantify the degree of axial and transverse slurry dispersion in the counter-current microstructured slurry bubble column within the ranges of particle concentration 0.5 – 3.0 wt. %, particle size 63 – 408 μm, superficial gas velocity 0.011 – 0.074 m/s, and slurry velocity 0.018 – 0.058 m/s. A model was developed to interpret the intensity of the dispersion based on liquid turbulence and circulation. The degree of dispersion was also analyzed by the velocity distribution model.

Publication: Prakash, R., Majumder, S. K., & Singh, A. (2020). Dispersion characteristics in a counter-current microstructured slurry bubble column and its analysis based on the turbulence and circulation, Industrial & Engineering Chemistry Research, 59, 8093 – 8111. https://doi.org/10.1021/acs.iecr.0c00834

5.1. Introduction

Substantial backmixing of the phases (both liquid and gas) is common in the cylindrical slurry bubble column (Shah et al., 2012). The efficiency of the slurry bubble column is affected by the degree of recirculation and the backmixing of the phases. The backmixing has a negative effect on the conversion and selectivity in many chemical reaction applications (Ekambara and Dhotre, 2010; Schmidt, 1998), mainly when intermediates are the desired products (Gao et al., 2012). Backmixing is known to increase drastically as the local liquid circulation develops (Cao et al., 2008). The most important changes occur in fluid mechanics when the geometry of the column changes from cylindrical to rectangular. Therefore, one of the most important factors in the design of the slurry bubble column is the effect of the geometric configuration on the flow behavior of the fluid. The rectangular column with considerable length and width, but with a small depth can be considered as the microstructured column. The small depth can be helpful in suppressing the backmixing and circulation of the phases and can provide a uniform bubble size distribution. Another way to reduce the backmixing is the use of internals such as horizontal perforated sieve plate (Palaskar et al., 2000a), packing (Bhatia et al., 2004), channels (Wu et al., 2009). The backmixing of the phases can be interpreted by studying the mixing characteristics in terms of axial dispersion coefficient, mixing time, and dispersion number (Buwa and Ranade, 2003; Rampure et al., 2007). The degree of backmixing can be quantified by the Peclet number (*Pe*). The high value of *Pe* indicates low backmixing (Zhang et al., 2019). Mixing is primarily caused by turbulent eddies, molecular diffusion, and convection due to the entrainment of liquid behind the wakes of rising gas bubbles (Ekambara and Joshi, 2003; Yang et al., 1992).

The simplest way to study mixing phenomena is to detect tracer the particles during the experiment and analyze them using any suitable dispersion model. Tracer detection techniques can be classified into offline and inline methods. The offline technique includes UV-absorption (Reitz et al., 2013), color intensity (Mu and Thompson, 2012), radioactive radiation (Janssen et al., 1979). The offline technique results in a gap between the actual process and the measured time. The product quality must be checked and controlled in real-time. In the inline technique, the inline probe associated with the data acquisition system directly detects and records the thermal, optical, and electrical signals of the tracer particles. This technique requires high-speed data sampling frequency and signal conversion (Gao et al., 2012). The most frequently used liquid dispersion

technique is residence time distribution (RTD), which is also a conductive detection technique based on the difference in electrical conductivity of the tracer particles and bulk flow.

Numerous studies are available on the mixing characteristics in the two-phase semi-batch (Muhsin and Mohammad, 2008), co-current (Ekambara and Joshi, 2003; Reitz et al., 2013), downflow (Majumder, 2008), and counter-current mode (Ansari et al., 2018; Janssen et al., 1979; Muhsin and Mohammad, 2008; Reitz et al., 2013). The behavior of the phase flow and its interactions becomes complex when the third phase (as a particle) is introduced into the column. Some mixing studies have been reported in the three-phase cylindrical columns with co-current up-flow (Kelkar et al., 1984; Pareek et al., 2001), three-phase downflow (Sivaiah and Majumder, 2013a), and counter-current flow (Fahad et al., 2020; Kumar et al., 2017; Pareek et al., 2001). As noticed, there is a scarcity of studies regarding the mixing characteristics in the three-phase counter-current mode. Based on the literature review, this work is mainly focused on research on the hydrodynamic behavior (i.e., mixing characteristics) of a system containing two- and three-phase. The influence of the gas velocity on the axial dispersion coefficient in the two- and the three-phase system has been studied by several researchers and noted that the axial dispersion coefficient increases with the gas velocity irrespective of the operating mode (Abdulrazzaq, 2015; Eissa and Schügerl, 1975; Kelkar et al., 1984; Moustiri et al., 2001; Muhsin and Mohammad, 2008; Wadaugsorn et al., 2018). The axial dispersion coefficient increases with the column diameter in a two-phase semi-batch mode (Moustiri et al., 2001), co-current up-flow mode (Eissa and Schügerl, 1975), and three-phase semi-batch mode (Abdulrazzaq, 2015). The formation of large circulation cells increases as the column diameter increases, resulting in more axial mixing (Moustiri et al., 2001). The axial dispersion coefficient decreases with the continuous phase velocity in two-phase co-current up-flow mode (Eissa and Schügerl, 1975), increases in two-phase with both co- and counter-current modes (Eissa and Schügerl, 1975), and independent of the slurry velocity in the three-phase co-current column (Kelkar et al., 1984). Muhsin and Mohammad (2008) showed that the axial dispersion coefficient was more near the gas distributor and in the center of the column. Most of the studies in the literature focus on the influence of gas velocity, liquid velocity, and column diameter, rather than the effect of particle concentration, particle size, slurry viscosity, and slurry surface tension. However, some research has been found in the literature on the dispersion behavior of slurry in the presence of particles (Abdulrazzaq, 2015; Ityokumbul et al., 1995; Kelkar et al., 1984; Kumar et al., 2017; Pareek et al., 2001; Sivaiah and Majumder, 2013a, b). The effect of

particle size, particle concentration, interfacial tension, and slurry viscosity on the axial slurry dispersion coefficient was examined in the three-phase co-current column by Kelkar et al. (1984). They reported that the axial slurry dispersion coefficient was not significantly affected by the particle size and particle concentration. Ityokumbul et al. (1995) reported an increase in the liquid dispersion coefficient by adding a surfactant to the liquid. They also analyzed the influence of the particle addition on the liquid dispersion coefficient and noted that the liquid dispersion coefficient decreases by 40%. This effect is attributed to increased radial mixing. Yang et al. (1992) investigated the axial and radial dispersion coefficient using a computer-automated radioactive particle tracking technique. The axial dispersion coefficients were much higher than the radial values. The study of the axial dispersion coefficient in a slurry bubble column with and without internals is reported by Forret et al. (2006). They reported that the axial dispersion coefficient increases with an increase in the column diameter. Eissa and Schügerl (1975) noted that the dispersion coefficient was much higher in the counter-current mode. They reported that the initial liquid height in the semi-batch operation also affects the dispersion behavior of the liquid in the column. Wadaugsorn et al. (2018) numerically studied the effect of the initial liquid height on the axial dispersion coefficient and stated that the axial dispersion coefficient could be improved by increasing liquid height in the column. Deckwer (1992) noted that the radial dispersion coefficient is always less than one-tenth of the axial dispersion coefficient value. Rubio et al. (2004) also confirmed that the radial dispersion coefficient values were approximately 1% of the axial dispersion coefficient. Based on the literature review, it is noticed that some researchers have studied the mixing characteristics in a three-phase semi-batch and co-current operation mode. Studies in the three-phase counter-current mode have been completely ignored. Reported studies regarding the effect of gas velocity on axial dispersion are clear, whereas, in the case of liquid or slurry velocity, it changes with the operating mode. In addition, the effect of particle concentration, particle size, slurry viscosity, slurry surface tension, the axial and radial or transverse position is still not clear.

Apart from particle flows, the bubble flow is equally important since the dispersion coefficient is sensitive to changes in the gas input as well as changes in the particle characteristics. The convective motion is caused by the bubble-bubble interaction, the relative motion of the bubbles and liquid phases, and the transport of liquids behind the wakes of the rising bubbles (Rubio et al., 2004). The dispersion coefficient in the counter-current mode has a multi-scale connection since

the bubble motion distracts the down flowing liquid, which in turn causes the bubble coalescence or bubble breakup and variation in the rising velocity. Dispersion phenomena are highly dependent on the gas volume fraction, the bubble flow, and the bubble size distribution (BSD) in a multiphase flow system. At low liquid velocity, gas volume fraction does not have much effect because of the low liquid velocity in comparison to the bubble rise velocity (Akita and Yoshida, 1973; Rollbusch et al., 2015). Higher liquid velocity influences the gas volume fraction, and it increases in counter-current mode (Besagni and Inzoli, 2016b; Trivedi et al., 2018), while it decreases in co-current mode (Pjontek et al., 2014; Shah et al., 2012). In the downflow column, the bubble size is larger at a lower liquid velocity compared to that at a higher liquid velocity (Zhu et al., 2019). In counter-current mode, the bubble size is smaller than that of the semi-batch mode (Besagni and Inzoli, 2016b). Pallapothu and Taweel (2012) noted the effect of the surfactant (0 – 50 ppm of sodium dodecyl sulfonate) on the bubble size, the gas volume fraction, and the liquid circulation. A 5-fold increase in the gas volume fraction and an 8-fold increase in the liquid circulation velocity indicate good mixing and mass transfer performance. In the semi-batch operation, in the middle of the column, the liquid flows upwards, while it is in the downward direction in the vicinity of the column wall. As a result, the large bubbles are pushed to the center of the column, while the small bubbles move close to the column wall because of the lift force (Besagni and Inzoli, 2016b; Besagni et al., 2019). Besagni et al. (2019) have shown that increasing liquid velocity in counter-current operation only shifts the liquid velocity profile downwards. In the co-current flow, the rising bubbles are pushed towards the wall, while in the counter-current flow, the bubbles are pushed away from the column wall (Giusti et al., 2005). In the absence of surfactant or salt in the liquid, the turbulence intensity in the axial direction reduces, as a result, bubble diameter increases (Turney et al., 2019). The presence of particles reduces the turbulent intensity of the continuous phase if the ratio of the particle size and turbulence scale is less than unity (Kawamura et al., 2004). It indicates that the turbulence in the liquid phase is weak in the presence of small particles. Moreover, it is assumed that the small bubbles disperse faster compared to the large bubbles. The dispersion of the bubbles results in a reduction of the void fraction near the wall.

Apart from these experimental studies, efforts have been made to simulate the flow behavior in the column using computational fluid dynamics (CFD) (Sarhan et al., 2020; Sarhan et al., 2017a, 2018a, b). For example, Sarhan et al. (2017a) have employed an Eulerian multi-fluid approach to study the influence of particle type, the wettability, the particle concentration on gas volume

fraction, and the bubble characteristics such as bubble size and the attached particle density. In another study, the population balance equation was used to study the influence of particles on the bubble breakup, the bubble coalescence, and the bubble-particle attachment and detachment at the various gas inlet (Sarhan et al., 2016). It is also reported that the small bubble size in the presence of larger particles is the reason for the reduced bubble coalescence. Sarhan et al. (2017b) reported that the influence of the particle addition facilitates bubble size reduction. Ahmadi and Zhang (2005) developed the computational model by assuming that the shape of the bubbles did not change during the process and found that the size of the bubbles has a significant effect on the flow behavior in a three-phase system. Wadaugsorn et al. (2018) conducted an experimental study and a CFD simulation to investigate the mixing characteristics in large reactors. They used the virtual tracer technique and noted that an increase in gas inlet increases the liquid circulation velocity and dispersion of the liquid phase. Moreover, they observed that an increase in the initial liquid height reduces the gas volume fraction, while the liquid dispersion, the gas velocity, and the liquid circulation increase. They also observed that the circulation velocity increases by 70% when the column diameter increases from 0.14 to 0.30 m.

Extensive research has been done on the axial mixing characteristics in the two- and three-phase semi-batch mode. However, these researches mainly focus on semi-batch operating conditions in a cylindrical column rather than the counter-current microstructured slurry bubble column. There is also a lack of research on the interpretation of intensity of dispersion, the applicability of the velocity distribution model, and the axial and transverse dispersion characteristics in a counter-current slurry bubble column. Therefore, the main aim of the present work is to study the mixing characteristics in the three-phase counter-current slurry bubble column. The effect of particle concentration, particle size, superficial gas, and slurry velocities on the axial and transverse dispersion coefficient, the dispersion due to circulation, the dispersion due to bubble motion, and the velocity distribution characteristic factor are analyzed in the presence of surfactant. An interpretation of the intensity of dispersion based on the liquid circulation and turbulence are also given. The velocity distribution model is applied to analyze the dispersion of bubble motion in the column.

5.2. Theoretical background

5.2.1. Theory to estimate the intensity of dispersion

Axial dispersion model (ADM) was used to estimate the axial dispersion of the slurry phase in the counter-current slurry bubble column. The underlying assumptions for applying ADM are as follows: (i) the velocity distribution of the liquid is uniform throughout the column, (ii) the bulk flow exists only in the axial direction, (iii) the axis-symmetric tracer concentration distribution exists, and (iv) the liquid phase dispersion exists only in the axial direction (Palaskar et al., 2000a). Axial dispersion model describing the tracer concentration with time over the length of the column is expressed as shown in Eq. 5.1 (Majumder, 2019)

$$\frac{\partial C}{\partial t} = E_z \frac{\partial^2 C}{\partial z^2} - \frac{u_{sl}}{1-\alpha_g}\frac{\partial C}{\partial z} \tag{5.1}$$

where C, t, z represent the tracer concentration, the time, and the axial distance between the tracer input and the measurement point, respectively. The dimensionless form of Eq. (5.1) is

$$\frac{\partial \psi}{\partial \theta} = \frac{1}{Pe}\frac{\partial^2 \psi}{\partial Z^2} - \frac{\partial \psi}{\partial Z} \tag{5.2}$$

where $\theta = t/t_m$, $t_m = L/u$, $\Psi = C/C_0$, $Z = z/L$, and $Pe = u_{sl}L/(1-\alpha_g)E_z$. The two extreme cases of mixing were assessed by $Pe \rightarrow 0$ (refers to large dispersion, so a perfect mixed flow) and $Pe \rightarrow \infty$ (characterize a negligible dispersion, therefore plug flow behavior). The axial dispersion coefficient is expressed as

$$E_z = \frac{u_{sl} Z}{(1-\alpha_g) Pe} \tag{5.3}$$

For the closed-closed boundary condition, the analytical solution of the Eq. (5.2), as reported by (Mavros, 1992; Xu et al., 1991)

$$E(\theta) = 4N_D \exp\left(\frac{0.5}{N_D}\right)\sum_{n=1}^{\infty}\left[\frac{\lambda_n(2\lambda_n N_D \cos\lambda_n + \sin\lambda_n)}{4\lambda_n^2 N_D^2 + 4N_D + 1}\right]\exp\left[-\frac{1+4\lambda_n^2 N_D^2}{4N_D}\theta\right] \tag{5.4}$$

where $E(\theta)$ denotes the normalized residence time distribution. The parameter λ_n in Eq. (5.4) refers to the n^{th} positive root of the transcendental equation, which can be expressed as

$$\tan\lambda_n = \frac{4\lambda_n N_D}{4\lambda_n^2 N_D^2 - 1} \tag{5.5}$$

According to the moment method, the variance associated with the Peclet number and the mean residence time is calculated by

$$\sigma_\theta^2 = \frac{\sigma^2}{t_m^2} = \frac{2}{Pe} - \frac{2}{Pe^2}(1 - e^{-Pe}) \tag{5.6}$$

where σ^2, t_m and σ_θ^2 represent the variance, mean residence time, and normalized variance, respectively. The mean residence time (t_m) of the tracer particle is calculated by

$$t_m = \frac{\sum tC\Delta t}{\sum C\Delta t} \tag{5.7}$$

The variance is a measure of the spreadness or the deviation of the system from the mean. The variance (σ^2) of the system is calculated by

$$\sigma^2 = \frac{\sum (t - t_m)^2 C\Delta t}{\sum C\Delta t} \tag{5.8}$$

Similarly, the transverse slurry dispersion coefficient is expressed as

$$E_w = \frac{u_{sl} w}{(1 - \alpha_g) Pe} \tag{5.9}$$

where w is the transverse point in the column from the left edge of the column, as shown in Fig. 5.1b.

5.2.2. Velocity distribution model to analyze dispersion phenomena

The axial dispersion coefficient of the liquid flowing in the column can be described by the equation suggested by Taylor (1953) and Aris (1956) as

$$E_z = \frac{d_c^2 u_0^2}{k D_m} + D_m \tag{5.10}$$

where u_0, k, and D_m are the maximum velocity at the column axis, the velocity distribution characteristics factor, and the molecular diffusion coefficient of the solute, respectively. The Eq. (5.10) is used to analyze the dispersion coefficient of bubble motion based on an assumption: (i) uniform distribution of the gas bubble, (ii) continuous dispersion of liquid and particle throughout the column, (iii) homogeneous flow. Based on the above assumptions, Eq. (5.10) has been reformed by replacing D_b in place of D_m

$$E_z = \frac{d_c^2 u_0^2}{kD_b} + D_b \tag{5.11}$$

where D_b denotes the dispersion coefficient of bubble motion. The maximum velocity at the column axis can be calculated by the correlation proposed by Riquarts (1981)

$$u_0 = 0.2\left(g\sqrt{\frac{4\pi}{A_c}}\right)^{1/2}\left(\frac{u_{sg}^3\rho_l}{g\mu_l}\right)^{1/8} \tag{5.12}$$

The values of k and D_b are estimated by plotting the experimental data of the axial slurry dispersion coefficient (E_z) and fitting them with Eq. (5.11).

5.3. Experimentation

5.3.1. Experimental setup and procedure

In the present work, the experiments were performed at atmospheric pressure and at a temperature of 298.15 K. The experiments were conducted in a Plexiglas microstructured column of 0.63 m length, 0.03 m depth, and 0.19 m width, as shown in Fig. 5.1a, as per the experimental setup described in chapters 2 to 4. The Plexiglas material was chosen for the visual observations of the hydrodynamic characteristics of the column. A single pipe with an inner diameter of 10 mm was used to introduce the slurry at the top of the plexiglass column. The experiments were performed in a range of superficial gas velocity from 0.011 to 0.075 m/s (based on the column cross-sectional area), superficial slurry velocity from 0.018 to 0.058 m/s (based on the column cross-sectional area), particle concentration from 0.5 to 3.0 wt.%, and particle size from 63.01 to 408.31 μm. The superficial slurry velocity in the pipe (based on the cross-sectional pipe area) is in the range of 0.48 – 1.54 m/s. The entire experiments were performed in the presence of 6 ppm Methyl Isobutyl

Carbinol (MIBC) surfactant (supplied by Tokyo Chemical Industry Corporation Limited). For each experiment, the slurry level in the column was maintained at 0.49 m from the base of the column. The slurry pump was used to transport the slurry to the column, and the flow rate of the slurry was measured with an electromagnetic flow meter (make: Adept Fluidyne, model: MagFlow 6410). The range of the flow meter was 0 – 15 ± 0.5% liter/min. A compressor was used to supply the compressed air to the column. The air flow rate was measured using a calibrated rotameter (range: 0 – 10 liters/min). A needle valve was used in the air line to control the air flow rate. The bubble in the column was generated using the stainless steel super porous cylindrical sparger (make: TFI filtration). The pore size of the sparger was 20 μm (given by the manufacturer). The outer diameter, inner diameter, and length of the sparger was 0.0104 m, 0.01 m, and 0.175 m, respectively (as shown in Fig. 5.1d).

Potassium chloride (KCl) was used as a tracer and injected through a high-pressure spring-loaded syringe at the top of the column with the slurry inlet. An amount of 10 ml of 1 molar concentration of KCl was injected smoothly with a high-pressure spring-loaded syringe in about 1 second. The variation in the tracer concentration was measured by the conductivity probe installed at six different positions in the column, as shown in Fig. 5.1b. The conductivity probes were installed axially and transversely in the column. The conductivity probes 1, 2, 3, and 4 are installed at 0.46, 0.32, 0.23, and 0.21 m distance from the tracer inlet position. The corresponding aspect ratio for the conductivity probe in the axial direction is $H/W = 0.89$ (probe 1), $H/W = 1.63$ (probe 2), $H/W = 2.11$ (probe 3), and $H/W = 2.21$ (probe 4). Here AR is the ratio of the probe distance from the bottom of the column to the width of the column. The probes 2, 5, and 6 are installed at 0.10, 0.14, and 0.19 m distance from the left end of the column. The position of the transverse probes (2, 5, and 6) is 0.32 m from the tracer inlet position. The aspect ratio of probes 2, 5, and 6 in the transverse direction are $x/W = 0.53$, $x/W = 0.74$, and $x/W = 1.0$, respectively. All conductivity probes (make: MicroSet, model: MS CD 18, range: 0 – 19.99 mS/cm) were connected to the data logger, which was then connected to the computer via RS 485 cable port. The image of the conductivity probe is shown in Fig. 5.1c. The conductivity meter was calibrated with KCl in the slurry with a known concentration, and the calibration chart was prepared for different particle concentrations. A linear correlation of conductivity with concentration was determined based on the conductivity and concentration data. Since the different particle concentrations and particle sizes were used in this

work, the conductivity meter was calibrated for each slurry concentration.

Fig. 5.1. (a) Schematic diagram of the experimental arrangement along with its aided accessories. 1. Air rotameter, 2. Solenoid valve, 3. Electromagnetic flow meter, 4. Digital online conductivity probes, 5. Air bypass valve (needle valve), 6. Compressor, 7. Slurry line valve, 8. Slurry pump, 9. Storage tank, 10. Column, 11. Level control valve, 12. Computer monitor, 13. central processing unit, 14. Online data logger, (b) Position of conductivity probes, (c) Image of the conductivity probe, (d) Cylindrical porous sparger, and (e) 3-D view of the column. (Copyright material)

The relationship between the conductivity and the concentration for the slurry system can be expressed as follows

$$C = a(K - K_0) \tag{5.13}$$

where C, K, K_0, and a are the concentration of the tracer in kg/m^3, the conductivity of the solution in mS/cm, the conductivity of the water, and the slope of Eq. (5.13), respectively. The conductivity of the water was 0.17 mS/cm. Different values of the slope of the calibration curves are reported in Table 5.1.

Table 5.1 Typical calibration values of a at different particle concentrations.

Particle size, dp (μm)	Concentration, w_s (wt. %)	a (kg. m^{-3}.cm. ms^{-1})
63.01	0.5	0.4373
	1.0	0.4632
	2.0	0.4446
	3.0	0.3325
242.72	0.5	0.5520
	1.0	0.4937
	2.0	0.4613
	3.0	0.4142
408.31	0.5	0.5198
	1.0	0.4937
	2.0	0.4587
	3.0	0.4209

The slurry was prepared with the known quantity of coal particle, surfactant, and water. The density of the coal particle was 1400 kg/m^3. The composition of coal particles was 74.61% carbon and 25.39% ash (mineral particles such as SiO_2, Al_2O_3, Fe_2O_3, etc.). The physical properties of the slurries at various particle concentrations are reported in chapter 2 (as Table 2.2 and Table 2.3). The uncertainty analysis of the experimentally measured quantities is provided in Table 5.2.

Table 5.2 Uncertainty analysis of experimentally measured quantities.

Parameters	Mean × 10^3, $\bar{x}$	$SD \times 10^3$ (–)	$U \times 10^3$ (–)	$U_r \times 10^3$ (%)
E_z	0.91 – 13.72	0.01 – 0.251	0.005 – 0.014	105.87 – 634.45
E_w	1.26 – 14.18	0.004 – 1.0	0.002 – 0.577	209.31 – 4070.0
u_{sg}	47.0 – 74.5	63.22 – 0.5	36.50 – 0.288	387.48 – 77662
u_{sl}	18.0 – 57.33	2.0 – 2.51	1.154 – 1.452	2534.24 – 6415

5.4. Results and discussions

5.4.1. Residence time distribution (RTD)

Typical plots of variation of the tracer concentration with time at different axial and transverse locations in the column are shown in Figs 5.2a and 5.2b. As shown in Fig. 5.2a, the highest and lowest peaks were observed at H/W = 2.21 (probe 4, nearest to the tracer inlet point, as shown in Fig. 5.1b) and H/W = 0.89 (probe 1, farthest to the tracer inlet point), respectively. It is noticed that the peak of the RTD curves shifts to the left side with the axial length. The response and peak

associated with probe 4 are maximum relative to the other probes. Approximately, 16.95% (probe at $H/W = 0.89$), 19.90% (probe at $H/W = 1.63$), 23.37% (probe at $H/W = 2.11$), and 30.93% (probe at $H/W = 2.21$) of the liquid passing the conductivity probe positions within 0 – 30 s. The mean residence times (t_m) corresponding to $H/W = 0.89$, 1.63, 2.11, and 2.21 are 89.53 s, 89.0 s, 84.59 s, and 80.02 s, respectively. The RTD behavior at various x/W (= 0.53, 0.74, and 1.0) in the transverse direction is also shown in Fig. 5.2b. About 17.0% (at $x/W = 0.53$), 17.35% (at $x/W = 0.74$), and 17.29% (at $x/W = 1.0$) of the liquid have crossed the positions of the conductivity probes within 0 – 30 s. The mean residence time (t_m) corresponding to the location at $x/W = 0.53$, 0.74, and 1.0 are 91.0 s, 91.34 s, and 90.3 s, respectively. Internal circulation of the fluid at $x/W = 0.74$ may be more prominent than other locations in the transverse direction. In the center zone, the liquid velocity is maximum, whereas, in the wall region, the velocity is minimum. At the wall region, due to the boundary layer effect, the circulation tends to reduce, whereas, in the center zone of kinetic energy, the fluids tend to induce the liquid to the upward direction. This may enhance the circulatory motion of the fluid particles and results in more residence time of the fluid particles in the region between the wall and centerline.

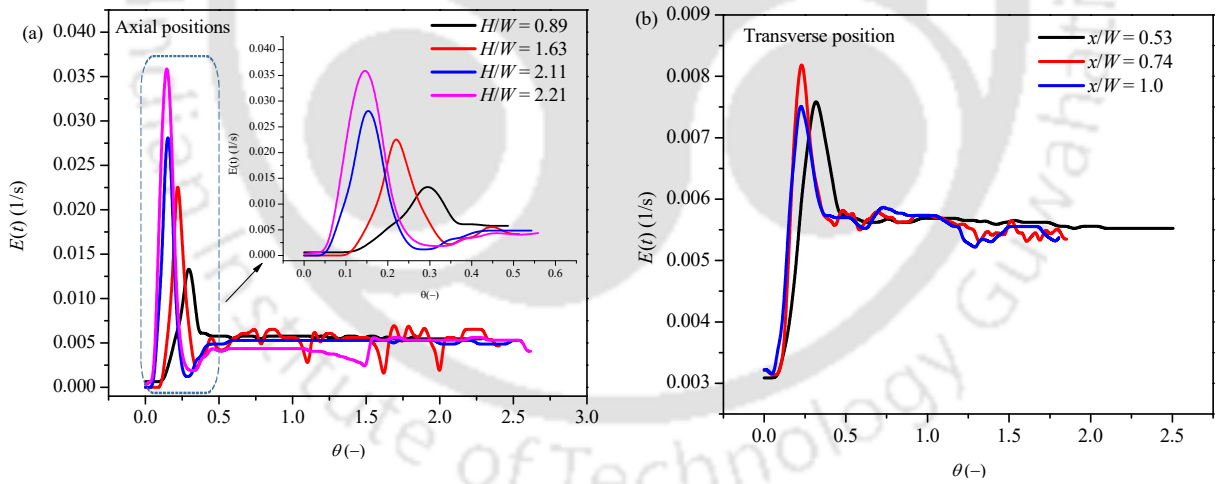

Fig. 5.2 Typical plot of RTD profile as a function of θ at various (a) $H/W = 0.89$, 1.63, 2.11, and 2.21 and (b) $x/W = 0.53$, 0.74, and 1.0.

5.4.2. Influence of different variables on the axial dispersion coefficient

This section shows the influence of different variables on the axial and transverse dispersion coefficient in the three-phase counter-current flow.

5.4.2.1. Effect of superficial gas velocity on the axial slurry dispersion coefficient

The influence of u_{sg} and u_{sl} on the axial dispersion coefficient (for probe 2) at fixed particle concentration (w_s = 0.5 wt.%) and particle size (d_p = 61.30 μm) is shown in Fig. 5.3a. It is noticed that with an increase in both the u_{sg} and the u_{sl}, the axial dispersion coefficient (E_z) increases. This is due to the fact that as the u_{sg} increases, the bubble population increases, thus increasing the turbulence and scattering of the bubbles (Baird and Rice, 1975). As the u_{sl} increases, it enhances the spreading and circulation (increases convection transport) of the gas molecules throughout the column due to turbulence created by the input slurry velocity, thus increasing the E_z. As the u_{sg} increases, more energy is transferred to the system, and the non-uniformity increases, leading to a higher bubble dispersion. In the present experimental analysis, it was found that the E_z varies with the u_{sl} as $E_z \propto u_{sl}^{0.848}$, while with the u_{sg}, it is $E_z \propto u_{sg}^{0.240}$. The impact of the u_{sl} on the axial slurry dispersion coefficient is about 5.05 times the superficial gas velocity.

5.4.2.2. Variation of the axial slurry dispersion coefficient with the axial length

The influence of the axial position (H/W) at superficial gas velocity (u_{sg} = 0.011 – 0.075 m/s) on E_z at a fixed particle concentration (w_s = 3.0 wt. %), the particle size (d_p = 408.31 μm), and the superficial slurry velocity (u_{sl} = 0.034 m/s) is shown in Fig. 5.3b. The E_z is higher at H/W= 0.89 compared to that at H/W = 2.21 for all u_{sg}. The higher bubble slurry interaction in the vicinity of sparger, resulting in a shorter mixing time, increases the E_z. The E_z decreases from 0.003 to 0.001 m^2/s at a u_{sg} of 0.011 m/s when the H/W increases from 0.89 to 2.21. Similarly, at a u_{sg} of 0.075 m/s, the E_z varies from 0.006 to 0.003 m^2/s in the same range of variation of the aspect ratio. It has been observed that E_z varies according to $E_z \propto z^{1.341}$.

5.4.2.3. Effect of particle concentration on the axial slurry dispersion coefficient

The high ranges of slurry velocity cause strong turbulence in the top region (of probe 4 (at H/W = 2.21)). However, the slurry induced turbulence at H/W = 2.21 is lower compared to that at H/W = 0.89 (sparger region). The increase in the slurry velocity enhances the spreading and circulation (increases convection transport) of the gas molecules throughout the column due to turbulence created by the inlet slurry velocity, accordingly, the degree of axial dispersion at the top section of the column results as shown in Figs 5.3b, 5.3d, 5.3f. The influence of the particle concentration on

the E_z as a function of u_{sl} and aspect ratios is shown in Figs 5.3c and 5.3d. It is observed that the E_z decreases due to an increase in particle concentration. As the particle concentration increases, it increases the viscosity of the system, thus reducing the mobility of the bubbles in the column. The reduction of bubble mobility decreases E_z. The influence of the particle concentration on the E_z is also shown in Fig. 5.3d. It is observed that the impact of the particle concentration on the E_z at $H/W = 2.21$ is negligible. It is because the movement of the small gas bubbles is slow and the existence of a larger bubble in this region. In the top region of the column (from $H/W = 2.21$ to 0.89), the difference in E_z at different particle concentrations is noticed. The more reduction in the E_z with an increase in particle concentration is noticed in the bottom region. From the present experimental analysis, it can be concluded that the influence of the smaller bubble above the sparger is more significant on the E_z in comparison to that of the effect of particle concentration. The reduction in E_z is approximately 27.14% (at $H/W = 0.89$) when the particle concentration changes from 0.5 to 2.0 wt.%.

5.4.2.4. Influence of particle size on the axial slurry dispersion coefficient

The influence of particle size on E_z at different experimental conditions is shown in Fig.s 5.3e and 5.3f. It is found that the E_z increases by increasing the particle size for all the experimental conditions. For a given amount of particle, the particle population decreases as the particle diameter increases (Kara et al., 1982). The decrease in the particle concentration per unit volume leads to a decrease in the viscosity and an increase in bubble mobility in the column. Consequently, E_z increases. A similar trend of an increase in E_z is also reported by other researchers (Mills et al., 1992). In the present work, as per the correlation, the functionality between E_z and particle size was found to be as $E_z \propto d_p^{0.083}$.

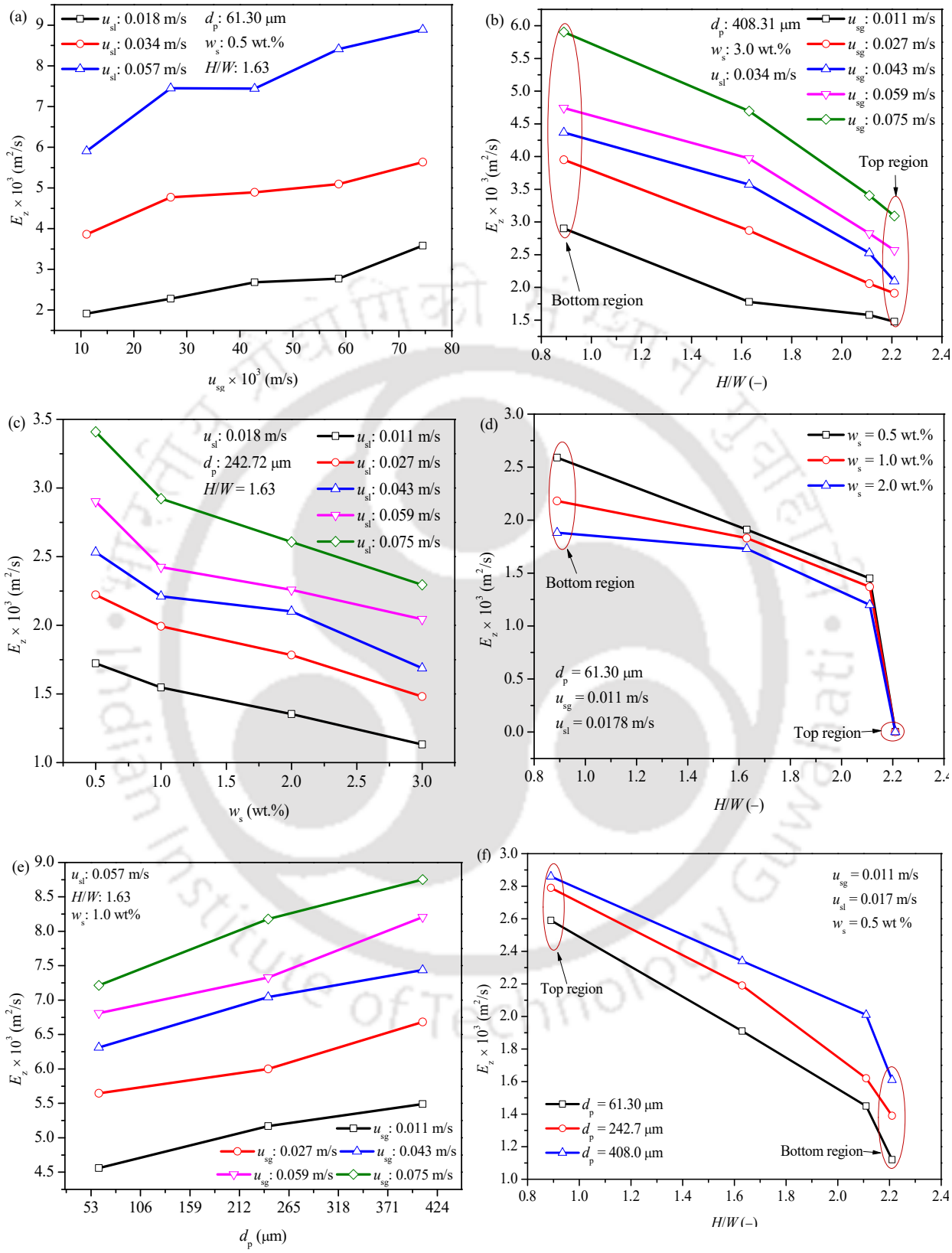

Fig. 5.3 Variation of the axial slurry dispersion coefficient as a function of (a) the superficial slurry and the gas velocity (b) the axial height, (c) and (d) the particle concentration, (e) and (f) the particle size.

5.4.3. Variation of the transverse slurry dispersion coefficient in different experimental conditions

This section explains the influence of superficial gas and slurry velocity, particle concentration, and particle size on the transverse slurry dispersion coefficient (E_w). The E_w at different experimental conditions is shown in Figs 5.4a and 5.4b. The E_w in the middle of the column (i.e., at x/W = 0.53) is higher than that of the other transverse positions, as shown in Fig. 5.4a. The maximum E_w is noticed in the middle section and lowest at the column wall. It is found that the E_w decrease with the increase in the distance from the middle section to the column wall and increases with an increase in the u_{sg}. Many researchers have reported that the gas volume fraction is higher in the central part of the column, and it decreases as approaches to the column wall. The higher gas volume fraction in the middle section of the column demarcates the presence of small bubbles, leading to an enhancement of E_w. In both Figs, 5.4a (at d_p: 61.30 μm, w_s: 3.0 wt.%, u_{sl}: 0.034 m/s) and 5.4b (at d_p: 61.30 μm, w_s: 0.5 wt.%, u_{sl}: 0.018 m/s) the E_w is higher at the higher superficial gas velocity.

The influence of superficial slurry velocity, the particle concentration, and the particle size on the E_w is shown in Figs 5.4c, 5.4d, 5.4e, and 5.4f, respectively. It is seen that the E_w decreases with increasing distance from the center of the column. The E_w increase with an increase in the superficial slurry velocity and the particle diameter, while it decreases by increasing the particle concentration.

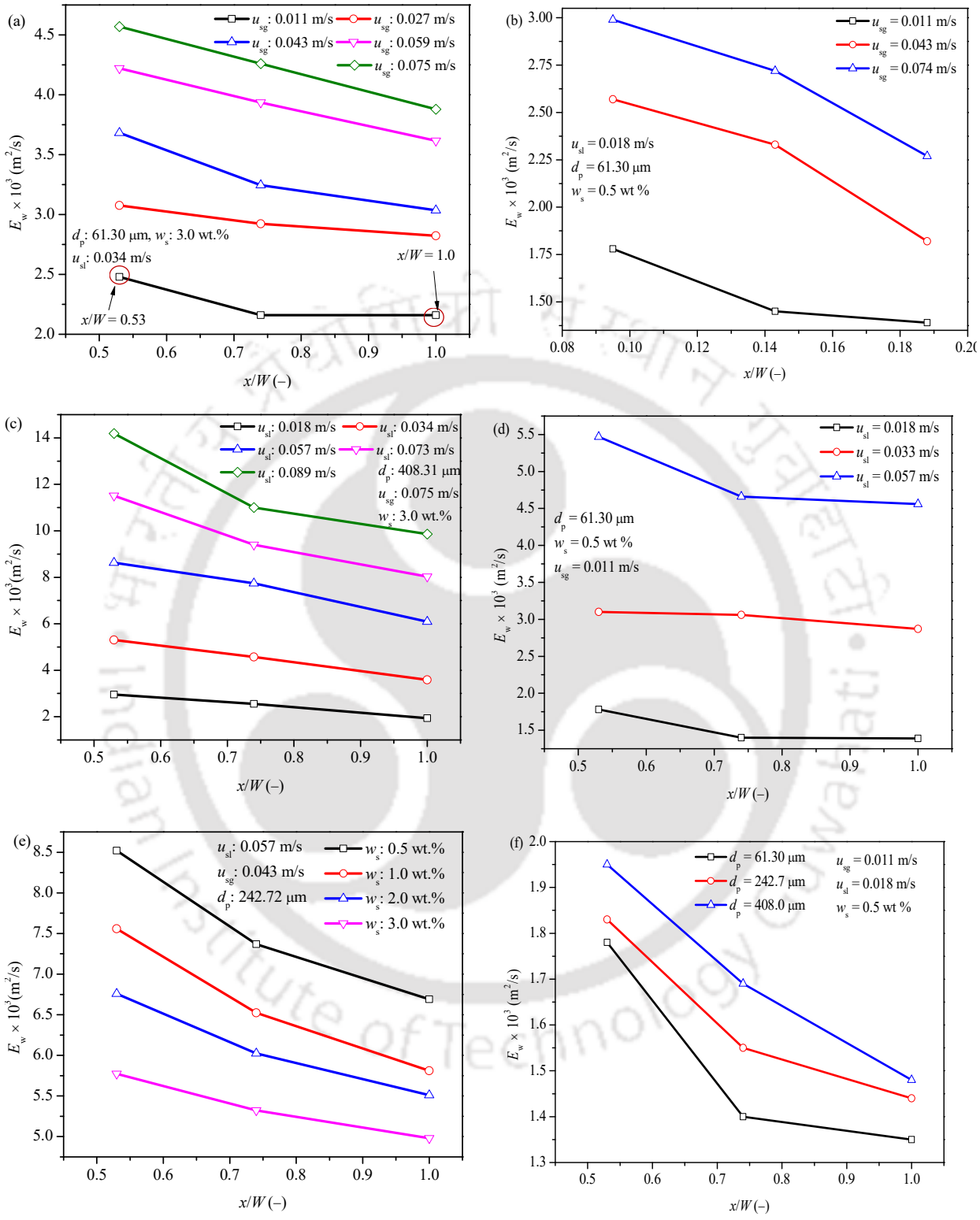

Fig. 5.4 Transverse slurry dispersion coefficient as a function of (a) the column width, (b) the superficial gas velocity, (c) the superficial slurry velocity (at w_s: 3.0 wt.%), (d) the superficial

slurry velocity (at w_s: 0.5 wt.%), (e) the particle concentration (at d_p: 242.72 μm), and (f) the particle size (at u_{sl}: 0.018 m/s).

5.4.4. Correlation for the axial and transverse slurry dispersion coefficient

In the literature, no such correlation is reported for the counter-current slurry bubble column, which exhibits the cumulative influence of important variables on the axial slurry dispersion coefficient. Therefore, an attempt is made to propose a new correlation that takes into account the impact of the variables. The behavior of the slurry dispersion coefficient was observed as a function of the superficial gas (u_{sg}) and the slurry velocities (u_{sl}), the particle diameter (d_p), the slurry surface tension (σ_{sl}), the axial height (z), the slurry density (ρ_{sl}), the column diameter (d_c), and the acceleration due to gravity (g). Therefore, the axial slurry dispersion coefficient as a function of different variables can be written as follows

$$E_z = f(u_{sg}, u_{sl}, d_p, \sigma_{sl}, z, \rho_{sl}, d_c, g) \tag{5.14}$$

After applying Buckingham's Pi theorem of dimensional analysis and multiple linear regression analysis to experimental data, the following correlation is obtained

$$\frac{E_z}{u_{sg} z} = 3.54\times10^{-2}\left(\frac{\rho_{sl} u_{sl}^2 d_p}{\sigma_{sl}}\right)^{0.424}\left(\frac{g d_c}{u_{sg}^2}\right)^{0.380}\left(\frac{z}{d_p}\right)^{0.341} \tag{5.15}$$

The term ($E_z/u_{sg}z$) is known as the inverse of the Bodenstein number ($1/Bo$). As $Bo \rightarrow 0$, it characterizes the complete backmixing (mixed flow behavior) and $Bo \rightarrow \infty$, characterizes no backmixing (plug flow behavior). According to Mirón et al. (2004), perfect mixing takes place when $Bo < 0.1$; however, it shows plug flow behavior when $Bo > 20$.(Chisti, 1989) The terms ($\rho_{sl}u_{sl}^2 d_p/\sigma_{sl}$) and ($g d_c/u_{sg}^2$) are the Weber number ($We$) and the inverse of the Froude number ($1/Fr$), respectively. The correlation presented in the Eq. (5.15) are valid in the range of $2.60\times10^{-4} \le \rho_{sl}u_{sl}^2 d_p/\sigma_{sl} \le 1.95\times10^{-2}$; $91.45 \le g d_c/u_{sg}^2 \le 412248$; and $506.97 \le z/d_p \le 755302$. The absolute average relative error (AARE) between the experimental and predicted axial slurry dispersion coefficient is 9.52%. The correlation coefficient and the standard error of Eq. (5.15) are 0.95 and 0.250, respectively. The parity of the axial slurry dispersion coefficient against the

experimental value is shown in Fig. 5.5 a. Similarly, a correlation is proposed for the transverse slurry dispersion coefficient. The proposed correlation can be represented as

$$\frac{E_w}{u_{sg}w} = 1.640\left(\frac{\rho_{sl}u_{sl}^2 d_p}{\sigma_{sl}}\right)^{0.316}\left(\frac{gd_c}{u_{sg}^2}\right)^{0.376}\left(\frac{w}{d_c}\right)^{-1.175} \tag{5.16}$$

The correlation represented by Eq. (5.16) for the transverse slurry dispersion coefficient is valid in the ranges of $2.60\times10^{-4} \le \rho_{sl}u_{sl}^2 d_p/\sigma_{sl} \le 4.50\times10^{-2}$; $91.45 \le gd_c/u_{sg}^2 \le 412248$; and $1.84 \le w/d_c \le 3.64$. The regression coefficient and the standard error of the Eq. (5.16) are 0.94 and 0.293, respectively. The AARE between the experimental and interpreted transverse slurry dispersion coefficient is approximately 8.84%. The parity of the experimental and predicted transverse slurry dispersion coefficient is shown in Fig. 5.5 b.

5.4.5. Comparison of the experimental axial and transverse slurry dispersion coefficient with the published data

The present experimental E_z values are compared with the published correlations of the different authors, as shown in Fig. 5.5 c. It is seen that the experimental values of E_z (for probe 1, at H/W = 0.95) are close to those calculated by the correlations of Deckwer et al. (1973) (with AARE = 16.114%), Miyauchi et al. (1981a) (with AARE = 16.073%) and Towell and Ackermann (1972) (with AARE = 15.016%). It is also noticed that the E_z obtained from the correlation of Deckwer et al. (1974), Dobby and Finch (1986), Laplante et al. (1988), Kato et al. (1985), and Miyauchi et al. (1981a) are higher than the present experimental values. While the values obtained by correlations of Shawaqfeh (2003), Shah et al. (2012), Cruz (1997), Muroyama et al. (1978), Nedeltchev et al. (2005), Lim et al. (2011), Kang and Kim (1986) and Wadaugsorn et al. (2018) underpredict the E_z. The deviation of the values of the present experiment and the other correlations is due to different experimental conditions, operating variables, physical properties of the system, geometric variable, and operating mode. The AARE between the present experimental and literature data and the correlations is given in Table 5.3. The present experimental values of E_w were compared with the experimental values of Muhsin and Mohammad (2008) and El-Temtamy et al. (1979), as shown in Fig. 5.5 d. In the case of cylindrical geometry, the radial dispersion coefficient (in a two-phase semi-batch) is only about 1 percent (Rubio et al., 2004) and

less than one-tenth (Deckwer, 1992) of the axial dispersion coefficient. In this present geometry, the range of E_w is 1.03 – 1.39 times of the E_z. The axial dispersion coefficient reported by Rubio et al. (2004) was in the range of 150×10^{-4} – 380×10^{-4} m^2/s. The range of E_z in the present experiment was found to be 9.12×10^{-4} – 137.23×10^{-4} m^2/s.

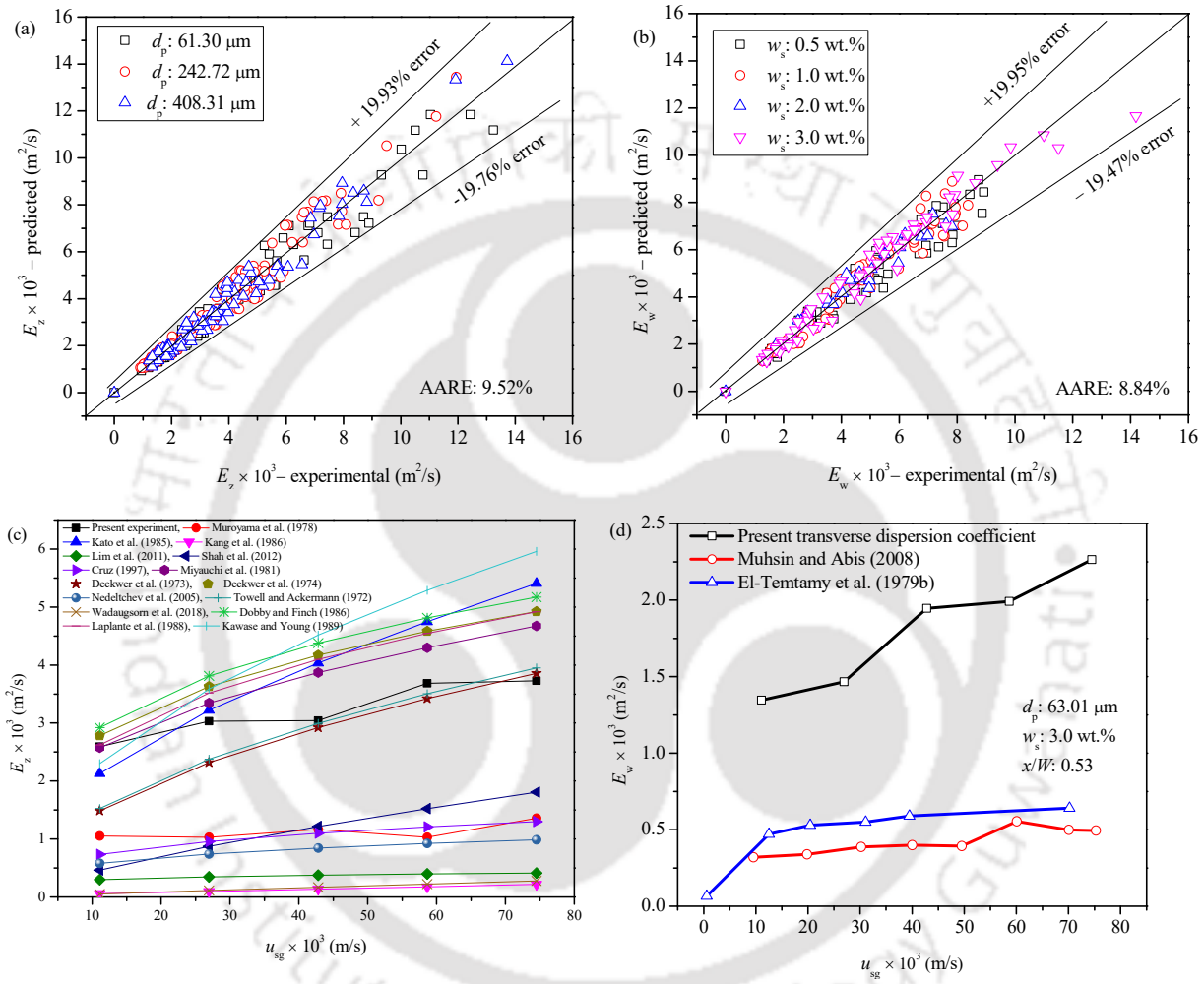

Fig. 5.5 (a) Comparison of the experimental and predicted axial slurry dispersion coefficient, (b) parity of the experimental and predicted transverse slurry dispersion coefficient, (c) comparison of the present experimental axial slurry dispersion coefficient with the published empirical correlation, and (d) comparison of the transverse slurry dispersion coefficient with the published experimental values.

Table 5.3 Absolute average relative error (AARE) between the present experimental and literature data and correlations.

Authors	Absolute average relative error (AARE) (%)	Authors	Absolute average relative error (AARE) (%)
Muroyama et al. (1978)	64.542	Deckwer et al. (1974)	24.088
Kato et al. (1985)	26.129	Nedeltchev et al. (2005)	74.783
Kang and Kim (1986)	95.911	Towell and Ackermann (1972)	15.016
Lim et al. (2011)	88.568	Wadaugsorn et al. (2018)	95.066
Shah et al. (2012)	64.720	Dobby and Finch (1986)	30.336
Cruz (1997)	67.261	Laplante et al. (1988)	21.409
Miyauchi et al. (1981b)	16.073	Kawase and Moo-Young (1989)	36.295
Deckwer et al. (1973)	16.114		

5.4.6. Analysis of the intensity of dispersion by the degree of phase exchange

In order to understand the influence of liquid circulation on the coefficient of dispersion, a mechanistic model has been developed based on the effects of both liquid turbulence and liquid circulation. Two flow regions, such as the up flow in the center of the column (at $x/R = 0.53$) and the down flow in the region between $0.53 < x/R < 1.0$ are shown in Fig. 5.6.

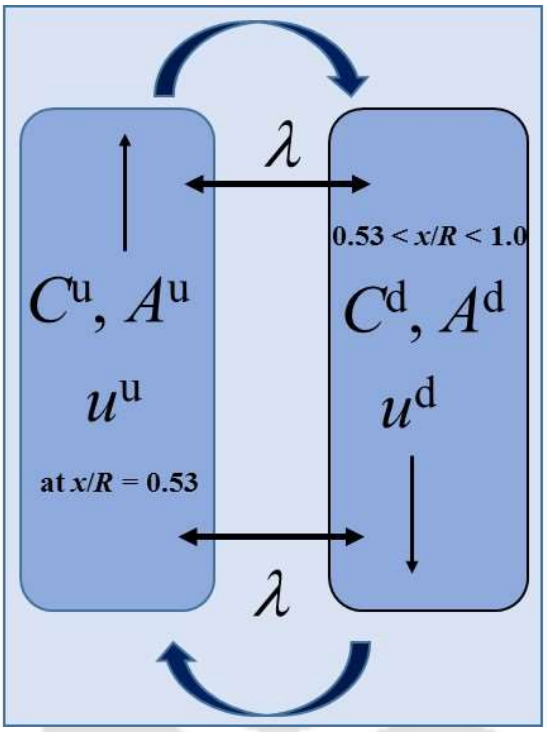

Fig. 5.6 Circulation pattern in a slurry bubble column.

The terms C^u, A^u, and u^u represent the tracer concentration, area, and velocity in the up-flow region, respectively. The superscript u and d refer to the up and down flows, respectively. The slurry exchange between the up and down flow region is taken into account by the slurry exchange parameter (λ). The transport equation for the tracer at any position z for the downstream flow can be written as

$$\frac{\partial C^d}{\partial t} = E^d \frac{\partial^2 C^d}{\partial z^2} - u^d \frac{\partial C^d}{\partial z} - \frac{\lambda S}{A_d}\left(C^u - C^d\right) \tag{5.17}$$

Similarly, for the up flow stream, the transport equation can be expressed as

$$\frac{\partial C^u}{\partial t} = E^u \frac{\partial^2 C^u}{\partial z^2} + u^u \frac{\partial C^u}{\partial z} + \frac{\lambda S}{A_u}\left(C^u - C^d\right) \tag{5.18}$$

The difference in tracer concentration ($C^u - C^d$) will be small if the interaction between the up and down flows streams is significant. The up and down flow axial dispersion coefficient is assumed to be the same and equal to the total axial dispersion coefficient ($E^d \approx E^u = E_z$). Incorporating all assumptions and adding Eq. (5.17) and Eq. (5.18) it can be written as

$$\frac{\partial \widetilde{C}}{\partial t} = E_Z \frac{\partial^2 \widetilde{C}}{\partial z^2} - 0.5 u_{sl} \frac{\partial (C^d - C^u)}{\partial z} \tag{5.19}$$

The area of up and down flow region is considered to be half the area of the cross-section of the column ($A^d \approx A^u = ½A_c$). The average tracer concentration can be expressed as $\widetilde{C} = (C^u/2) + (C^d/2)$. Subtracting Eq. (5.17) from Eq. (5.18) and incorporating all the assumptions yields the following equation

$$u_{sl} \frac{\partial \widetilde{C}}{\partial z} = -\frac{\lambda S}{0.5 A_c} \left(C^u - C^d \right) \tag{5.20}$$

Differentiating Eq. (5.20) with respect to z yields the Eq. (5.21)

$$\frac{\partial \left(C^d - C^u \right)}{\partial z} = -\frac{-A_c u_{sl}}{2\lambda S} \frac{\partial^2 \widetilde{C}}{\partial z^2} \tag{5.21}$$

The circumference between the up and down flow region is equivalent to $S = \pi d_c/\sqrt{2}$. Substituting the expression Eq. (5.21) into Eq. (5.19), and by incorporating the value of S yields the Eq. (5.22)

$$\frac{\partial \widetilde{C}}{\partial t} = \left(E_t + \frac{u_{sl}^2 d_c \sqrt{2}}{16 \lambda} \right) \frac{\partial^2 \widetilde{C}}{\partial z^2} \tag{5.22}$$

The Eq. (5.22) is analogous to the 1-D axial dispersion model, and the term $E_t + u_{sl}^2 d_c \sqrt{2}/16\lambda$ can be expressed by

$$E_z = E_t + E_c = E_t + \frac{\delta}{\lambda} \tag{5.23}$$

where E_t and E_c refer to the dispersion due to turbulence and dispersion due to circulation, respectively. The dispersion because of circulation can be represented as

$$E_c = \frac{u_{sl}^2 d_c \sqrt{2}}{16\lambda} = \frac{\delta}{\lambda} \tag{5.24}$$

where the parameter δ is defined by

$$\delta = \left(\frac{2u_{sl}}{1-\alpha_g} \right)^2 d_c \sqrt{2} \Big/ 16 \tag{5.25}$$

The dispersion coefficient because of turbulence (E_t) and the slurry exchange parameter (λ) was evaluated based on the experimental value of the total slurry dispersion coefficient.

5.4.6.1. Effect of different variables on the dispersion coefficient because of circulation

The dispersion due to circulation (E_c) increases with an increase in the superficial gas and the slurry velocities and particle concentration, as shown in Figs 5.7a and 5.7b. As the slurry or gas velocity increases, it intensifies the circulation of the phases in the column, which in turn increases the slurry dispersion coefficient. The increase in the particle concentration leads to an increase in the slurry viscosity, which inhibits the smooth flow of the slurry, causes phase circulation, and increases the dispersion coefficient. As per Joshi (1980), in the heterogeneous bubbly flow, the intensity of phase dispersion is related to the sum of the superficial liquid velocity and the average liquid circulation velocity. The circulation of the liquid is due to the non-uniform radial gas volume fraction. The formation of a non-uniform radial gas volume fraction results in a difference in density that causes the circulation and backmixing of the phases (Palaskar et al., 2000b). During circulation, a transverse interaction between the phases exchanges a certain amount of slurry with each other. The slurry exchange parameter is strongly influenced by the operating and physical properties of the system, as shown in Fig. 5.7c. The dependency of E_c on u_{sg} and u_{sl} at $H/W = 0.89$ is $E_c \propto u_{sg}^{0.138}$ and $E_c \propto u_{sl}^{2.85}$, respectively. The effect of particle concentration (w_s = 0.5 – 3.0 wt.%) and the superficial gas velocity (u_{sg} = 0.011 – 0.075 m/s) on the slurry exchange parameter (λ) is shown in Fig. 5.7c. The λ increased by increasing w_s and the u_{sg}. The dependency of the slurry exchange parameter on u_{sg} and u_{sl} at $H/W = 0.95$ are $\lambda \propto u_{sg}^{0.096}$ and $\lambda \propto u_{sl}^{0.016}$, respectively. Here, it is seen that the effect of u_{sl} on the λ is dominant compared to that of the u_{sg}. It is about 1.52 times the u_{sg}.

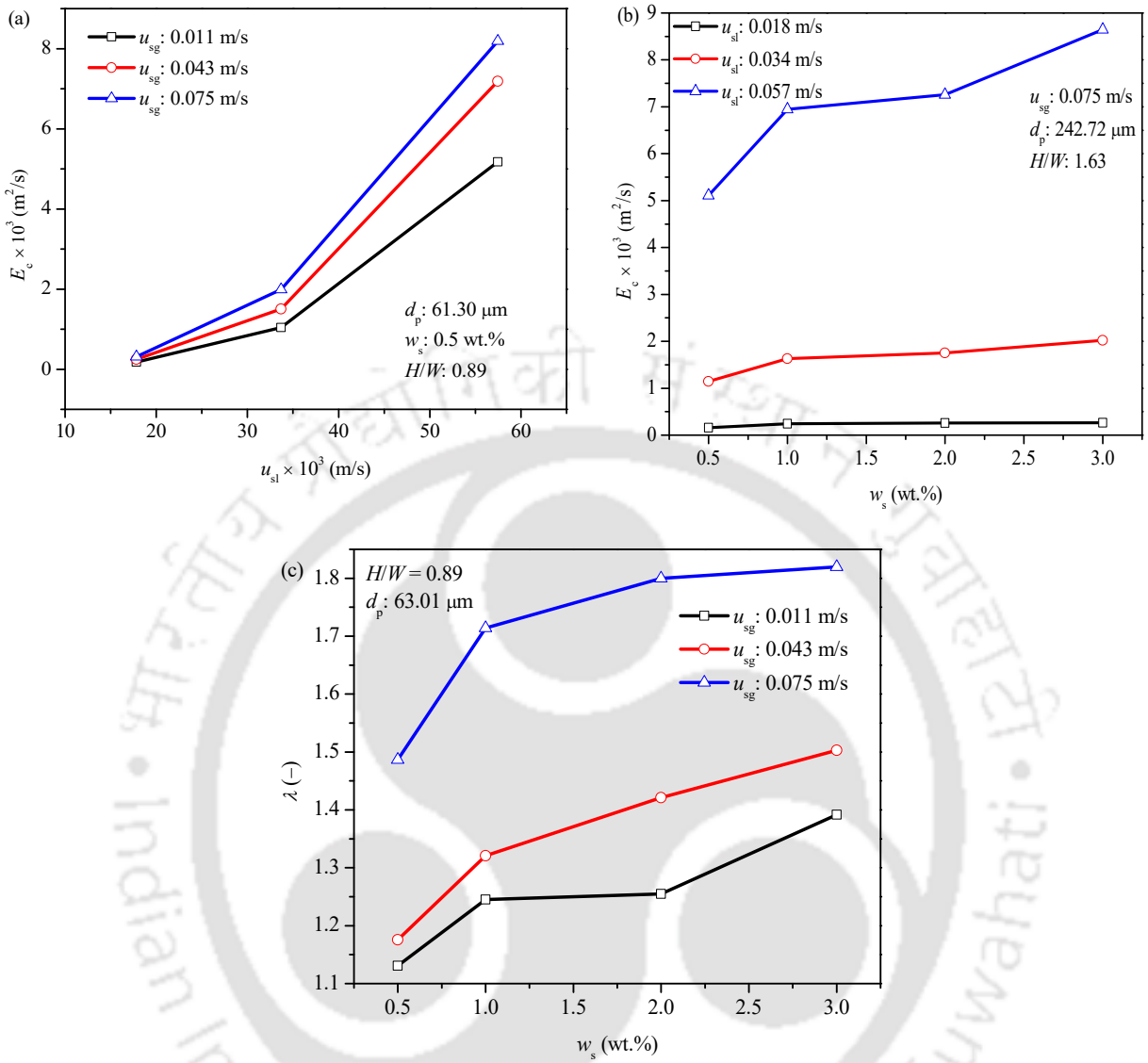

Fig. 5.7 Influence of different variables on (a) the dispersion due to circulation at different superficial slurry and gas velocities, (b) the dispersion due to circulation at different particle concentrations, and (c) the slurry exchange parameter at various particle concentrations and superficial gas velocities.

Correlations are proposed for the interpretation of the slurry exchange parameter and the dispersion due to circulation as defined by Eq. (5.23) and (5.24), respectively, for all the H/W ratios. The proposed correlations are given in Table 5.4.

Table 5.4 Developed correlations for the dispersion due to circulation and slurry exchange parameters at various H/W.

Developed correlations	AARE (%)	H/W (–)
$\frac{E_c}{u_{sg}z} = 1.40\times10^{-4}\left(\frac{\rho_{sl}u_{sl}^2 d_p}{\sigma_{sl}}\right)^{1.425}\left(\frac{gd_p}{u_{sg}^2}\right)^{0.431}\left(\frac{z}{d_p}\right)^{1.882}$, $R^2 = 0.94$	9.14	0.89
$\lambda = 2.28\times10^{-2}\left(\frac{\rho_{sl}u_{sl}^2 d_p}{\sigma_{sl}}\right)^{0.008}\left(\frac{gd_p}{u_{sg}^2}\right)^{-0.048}\left(\frac{z}{d_p}\right)^{-0.062}\left(1-w_s\right)^{-9.651}$, $R^2 = 0.99$	2.71	
$\frac{E_c}{u_{sg}z} = 8.46\times10^{-5}\left(\frac{\rho_{sl}u_{sl}^2 d_p}{\sigma_{sl}}\right)^{1.470}\left(\frac{gd_p}{u_{sg}^2}\right)^{0.444}\left(\frac{z}{d_p}\right)^{1.986}$, $R^2 = 0.93$	8.54	1.63
$\lambda = 3.04\times10^{-2}\left(\frac{\rho_{sl}u_{sl}^2 d_p}{\sigma_{sl}}\right)^{0.008}\left(\frac{gd_p}{u_{sg}^2}\right)^{-0.048}\left(\frac{z}{d_p}\right)^{-0.062}\left(1-w_s\right)^{-9.651}$, $R^2 = 0.99$	1.99	
$\frac{E_c}{u_{sg}z} = 2.26\times10^{-4}\left(\frac{\rho_{sl}u_{sl}^2 d_p}{\sigma_{sl}}\right)^{1.411}\left(\frac{gd_p}{u_{sg}^2}\right)^{0.412}\left(\frac{z}{d_p}\right)^{1.815}$, $R^2 = 0.94$	8.85	2.11
$\lambda = 3.94\times10^{-2}\left(\frac{\rho_{sl}u_{sl}^2 d_p}{\sigma_{sl}}\right)^{0.008}\left(\frac{gd_p}{u_{sg}^2}\right)^{-0.048}\left(\frac{z}{d_p}\right)^{-0.062}\left(1-w_s\right)^{-9.651}$, $R^2 = 0.99$	2.39	
$\frac{E_c}{u_{sg}z} = 8.55\times10^{-5}\left(\frac{\rho_{sl}u_{sl}^2 d_p}{\sigma_{sl}}\right)^{1.474}\left(\frac{gd_p}{u_{sg}^2}\right)^{0.445}\left(\frac{z}{d_p}\right)^{1.999}$, $R^2 = 0.92$	8.08	2.21
$\lambda = 4.52\times10^{-2}\left(\frac{\rho_{sl}u_{sl}^2 d_p}{\sigma_{sl}}\right)^{0.008}\left(\frac{gd_p}{u_{sg}^2}\right)^{-0.048}\left(\frac{z}{d_p}\right)^{-0.062}\left(1-w_s\right)^{-9.651}$, $R^2 = 0.99$	2.81	

The parities of the experimental and predicted dispersion due to circulation and the slurry exchange parameter are shown in Figs 5.8a and 5.8b, respectively.

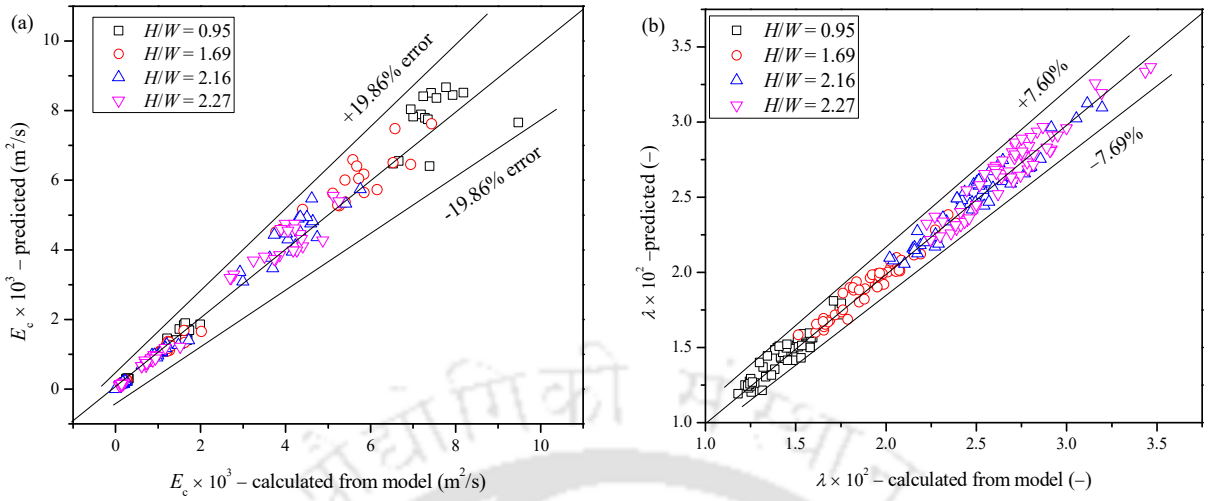

Fig. 5.8 Parity plot of (a) the dispersion due to circulation and (b) the slurry exchange parameter.

5.4.7. Influence of different variables on the dispersion due to bubble motion

The impact of the superficial gas velocity, the particle concentration, and the particle size on the dispersion coefficient of bubble motion (D_b) and velocity distribution characteristics factor (k) as defined by Eq. (5.11) is shown in Figs 5.9a and 5.9b. It is noticed that the D_b increases with the increase in the u_{sg}, while it decreases with the increase in the particle concentration. As the u_{sg} increases, the momentum of the gas bubbles increases, resulting in an increase in the D_b. Increasing the concentration of particles increases the viscosity of the system and also increases the collision between bubbles and particles (Majumder, 2016), hence the D_b decreases. The k was reduced with an increase in the u_{sg}; however, it increases by increasing the concentration of particles. As shown in Fig. 5.9b, the D_b decreases by increasing the particle size; however, the decrease is not significant as the particle size increases. The k increases with increasing particle size. The k depends on the intensity of the turbulence (Majumder, 2008). The increase in the liquid velocity increases the turbulence, which results in a reduction of the k. The functionality ($D_b \propto u_{sg}^{0.26}$) of the u_{sg} at $H/W = 0.89$ on D_b is approximately 4.34 times the u_{sl} ($D_b \propto u_{sl}^{0.06}$). Similarly, in the case of the k, the functionalities are: $k \propto u_{sg}^{-0.18}$ and $k \propto u_{sl}^{-0.002}$, respectively.

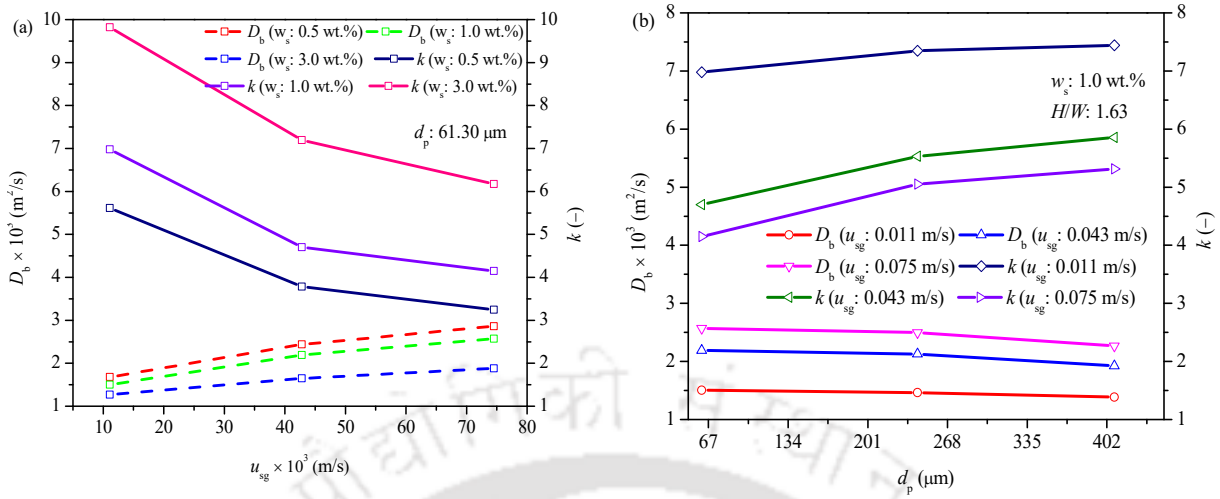

Fig. 5.9 Variation of D_b and k as a function of (a) u_{sg} at different particle concentrations and (b) d_p at different superficial gas velocities.

Correlations for the dispersion due to bubble motion and the velocity distribution characteristics factor are suggested based on the experimental results, as shown in Table 5.5.

Table 5.5 Developed correlations for the dispersion due to bubble motion and the velocity distribution characteristic factor at various H/W.

Developed correlations	AARE (%)	H/W (–)
$\frac{D_{b,pre}}{u_{sg} z} = 6.95\times10^{-3}\left(\frac{\rho_{sl}u_{sl}^2 d_p}{\sigma_{sl}}\right)^{0.030}\left(\frac{g d_p}{u_{sg}^2}\right)^{0.370}\left(\frac{z}{d_p}\right)^{0.406}$, $R^2 = 0.95$	9.435	0.89
$k_{pre} = 4.598\left(\frac{\rho_{sl}u_{sl}^2 d_p}{\sigma_{sl}}\right)^{-0.001}\left(\frac{g d_p}{u_{sg}^2}\right)^{0.090}\left(\frac{z}{d_p}\right)^{0.069}\left(\frac{c_s}{\rho_{sl}}\right)^{0.277}$, $R^2 = 0.94$	7.803	
$\frac{D_{b,pre}}{u_{sg} z} = 7.58\times10^{-3}\left(\frac{\rho_{sl}u_{sl}^2 d_p}{\sigma_{sl}}\right)^{0.030}\left(\frac{g d_p}{u_{sg}^2}\right)^{0.370}\left(\frac{z}{d_p}\right)^{0.406}$, $R^2 = 0.95$	9.013	1.63
$k_{pre} = 11.109\left(\frac{\rho_{sl}u_{sl}^2 d_p}{\sigma_{sl}}\right)^{-0.002}\left(\frac{g d_p}{u_{sg}^2}\right)^{0.101}\left(\frac{z}{d_p}\right)^{0.037}\left(\frac{c_s}{\rho_{sl}}\right)^{0.301}$, $R^2 = 0.94$	6.715	
$\frac{D_{b,pre}}{u_{sg} z} = 8.36\times10^{-3}\left(\frac{\rho_{sl}u_{sl}^2 d_p}{\sigma_{sl}}\right)^{0.030}\left(\frac{g d_p}{u_{sg}^2}\right)^{0.369}\left(\frac{z}{d_p}\right)^{0.406}$, $R^2 = 0.95$	9.309	2.11

$k_{pre} = 14.554\left(\frac{\rho_{sl}u_{sl}^2 d_p}{\sigma_{sl}}\right)^{-0.002}\left(\frac{gd_p}{u_{sg}^2}\right)^{0.088}\left(\frac{z}{d_p}\right)^{0.063}\left(\frac{c_s}{\rho_{sl}}\right)^{0.280}$, $R^2 = 0.94$	8.151	
$\frac{D_{b,pre}}{u_{sg}z} = 8.38\times10^{-3}\left(\frac{\rho_{sl}u_{sl}^2 d_p}{\sigma_{sl}}\right)^{0.030}\left(\frac{gd_p}{u_{sg}^2}\right)^{0.370}\left(\frac{z}{d_p}\right)^{0.406}$, $R^2 = 0.95$	10.252	
$k_{pre} = 15.443\left(\frac{\rho_{sl}u_{sl}^2 d_p}{\sigma_{sl}}\right)^{-0.001}\left(\frac{gd_p}{u_{sg}^2}\right)^{0.091}\left(\frac{z}{d_p}\right)^{0.073}\left(\frac{c_s}{\rho_{sl}}\right)^{0.276}$, $R^2 = 0.94$	7.608	2.21

Parities of D_b and k are shown in Figs 5.10a and 5.10b, respectively. The validity of the velocity distribution model is examined by comparing the experimental axial slurry dispersion and axial slurry dispersion coefficient calculated by Eq. (5.26), as shown in Fig. 5.10c.

$$E_Z = \frac{4d_c^2 u_{sl}^2}{k_{predicted} D_{b,predicted}} + D_{b,predicted} \tag{5.26}$$

To assess the range of experimentally calculated D_b, it is compared with the published experimental values of Kato and Nishiwaki (1971), Deckwer et al. (1974), Hikita and Kikukawa (1974), Yang and Fan (2003), Baird and Rice (1975), and Kawase and Moo-Young (1986) as shown in Fig. 5.10d. It is noticed that the present experimental values of D_b are much smaller than the literature value. The literature value is higher in the two-phase semi-batch or co-current operation in the large diameter column at a higher u_{sg}. The D_b depends on the extent of turbulence and the circulation of phases. However, the present system does not reflect a large amount of backmixing because of the structure of the column. Experimentally obtained k is compared with the values of Hikita and Kikukawa (1974), Deckwer et al. (1974), and Miyauchi et al. (1981a) as shown in Fig. 5.10e. It has been found that the present experimental values of the k increase with an increase in the u_{sg} and also higher than the values published in the literature. The trend of the k is in accordance with the results of other investigators (Sivaiah and Majumder, 2013a). At higher superficial gas velocity (i.e., $u_{sg} > 0.05$ m/s), the values of k reported by Towell and Ackermann (1972), Riquarts (1981), Reith et al. (1968), and Kato and Nishiwaki (1971) are in the same trend as those observed in the present experiment.

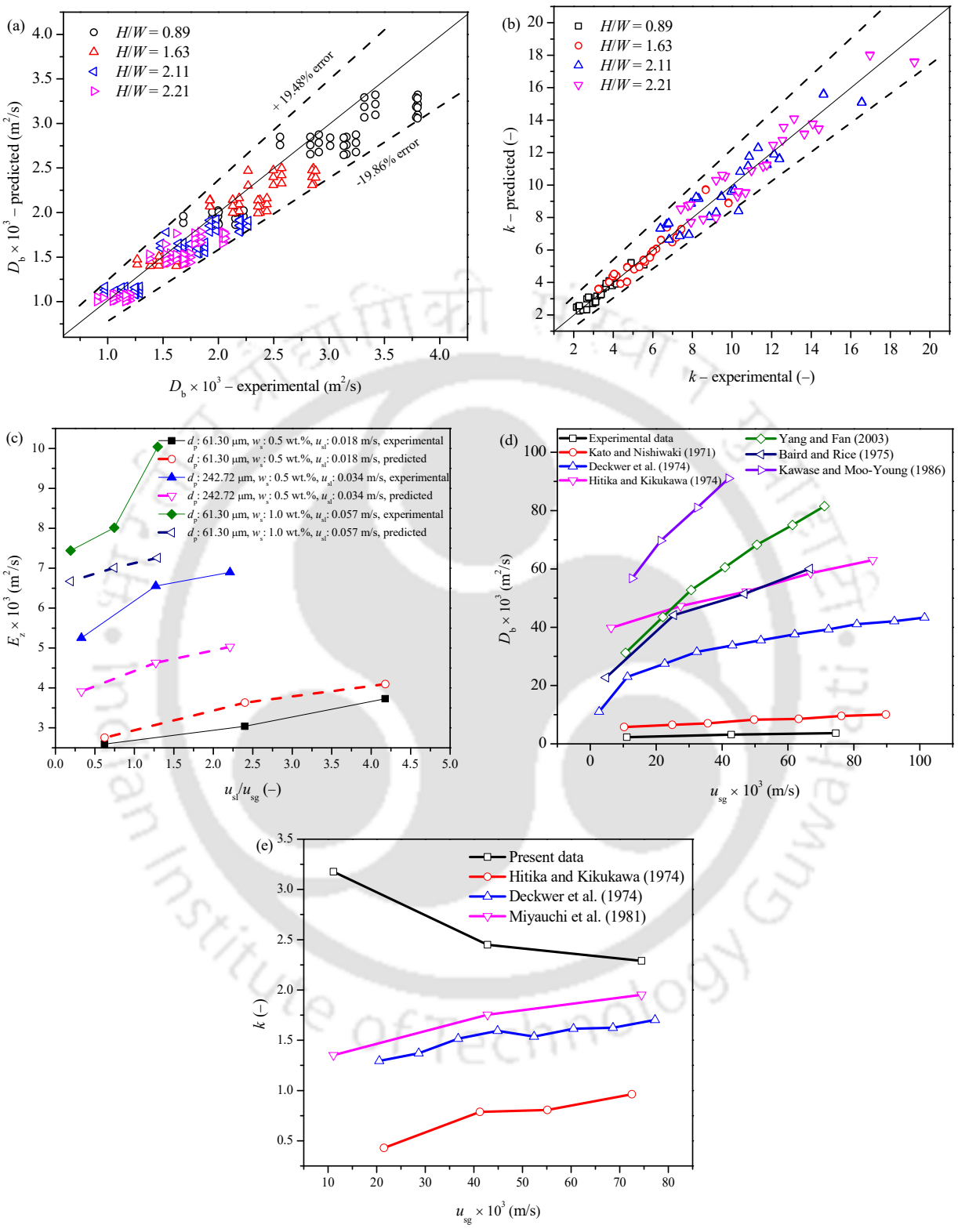

Fig. 5.10 Comparison of (a) the experimental and interpreted dispersion due to bubble motion, (b) the experimental and predicted velocity distribution characteristic factor, (c) the predicted axial

dispersion coefficient based on the velocity distribution model (using Eq. 5.26), and the experimentally measured axial slurry dispersion coefficient, (d) comparison of the dispersion due to the bubble motion with others published experimental data, and (e) comparison of the velocity distribution characteristic factor with others published experimental data.

Some typical values of the axial (at H/W = 1.63) and transverse slurry dispersion (at x/W = 1.0) coefficient, dispersion due to the bubble motion (at H/W = 1.63), dispersion due to circulation (at H/W = 1.63), the velocity distribution characteristics factor (at H/W = 1.63), and the slurry exchange parameter (at H/W = 1.63) are given in Table 5.6.

Table 5.6. Some typical values of axial (at H/W = 1.63) and transverse dispersion (at x/W = 1.0) coefficient, dispersion due to bubble motion (at H/W = 1.63), dispersion due to circulation (at H/W = 1.63), velocity distribution characteristics factor (at H/W = 1.63), and slurry exchange parameter (at H/W = 1.63).

Superficial slurry velocity, $u_{sl} \times 10^3$ (m/s)	Superficial gas velocity, $u_{sg} \times 10^3$ (m/s)	Particle concentration, w_s (wt. %)	Particle diameter, d_p (μm)	Axial dispersion coefficient, $E_z \times 10^3$ (m^2/s)	Tranaverse dispersion coefficient, $E_w \times 10^3$, (m^2/s)	Dispersion due to bubble motion, $D_b \times 10^3$ (m^2/s)	Dispersion due to circulation, $E_c \times 10^3$ (m^2/s)	Velocity distribution characteristic factor, k (–)	Slurry exchange parameter, $\lambda \times 10^3$ (–)
17.83	11.10	0.5	63.01	1.913	1.385	1.675	0.133	5.614	16.364
33.69	42.80	0.5	63.01	4.891	3.894	2.439	1.269	3.784	15.631
57.46	74.50	1.0	63.01	8.889	5.795	2.571	5.586	4.148	29.598
17.83	11.10	0.5	242.72	1.923	1.441	1.632	0.143	5.912	21.402
57.46	11.10	3.0	242.72	4.892	4.448	1.151	5.306	8.671	27.194
33.69	74.50	0.5	408.31	4.464	5.238	2.878	1.236	4.690	29.945
57.46	42.80	1.0	408.31	4.119	6.841	1.923	5.403	4.855	27.838

5.4.8. Conclusions

The present work reports the dispersion characteristics of slurry in the counter-current slurry bubble column. The slurry phase mixing patterns are analyzed in terms of axial and transverse dispersion coefficient, the intensity of dispersion, velocity distribution characteristic factor, and

dispersion due to bubble motion. A thorough study was conducted to quantify the effect of operating variables, geometric variables, and physical properties of the system on the investigated hydrodynamics. Based on the experimental investigation, the following conclusions can be drawn:

- The axial (E_z) and transverse (E_w) dispersion coefficient increases with the superficial gas and slurry velocities and with the particle diameter, but decreases with the particle concentration. The effect of the slurry phase superficial velocity on the axial slurry dispersion coefficient $(E_z \propto u_{sl}^{0.848})$ is more pronounced compared to that of the gas-phase superficial $(E_z \propto u_{sg}^{0.240})$ velocity. Similarly, the effect of the superficial slurry velocity on the transverse dispersion coefficient $(E_w \propto u_{sl}^{0.632})$ is significant compared to that of the superficial gas velocity $(E_w \propto u_{sg}^{0.248})$.

- The axial slurry dispersion coefficient (E_z) is 1.40 – 9.60 times the dispersion coefficient due to circulation (E_c), while it is 1.28 – 3.61 times the dispersion due to bubble motion (D_b). The transverse slurry dispersion coefficient (E_w) was 1.03 – 1.39 times the axial slurry dispersion coefficient (E_z). The transverse dispersion coefficient (E_w) is more in the middle (in the transverse direction) of the column and decreases as it approaches the right section of the column.

- The effect of the superficial slurry velocity has a very strong effect on the dispersion due to circulation (E_c). The effect is 20.65 times the superficial gas velocity. The scales of dispersion due to circulation (E_c) with superficial gas velocity, superficial slurry velocity, and particle size at $H/W = 0.89$ are: $E_c \propto u_{sg}^{0.138}$, $E_c \propto u_{sl}^{2.85}$ and $E_c \propto d_p^{-0.026}$, respectively. It was seen that the influence of superficial gas velocity on the slurry exchange parameter is more pronounced compared to the superficial slurry velocity. The effect of the superficial gas velocity on the slurry exchange parameter is 6 times the superficial slurry velocity. The functionality of the slurry exchange parameter (λ) with the superficial gas velocity, the superficial slurry velocity, and the particle size at $H/W = 0.89$ are $\lambda \propto u_{sg}^{0.096}$, $\lambda \propto u_{sl}^{0.016}$, and $\lambda \propto d_p^{0.022}$, respectively. The effect of the

variation in particle size on the slurry exchange parameter (λ) and the dispersion due to circulation (E_c) is marginal compared to other parameters.

- The velocity distribution model was also used to enunciate the dispersion characteristics. The increase in the superficial gas velocity has a positive effect on the dispersion coefficient of bubble motion (D_b), while it has a negative effect on the velocity distribution characteristic factor (k). The increase in the concentration of the particles leads to a reduction in the dispersion coefficient of bubble motion, while the velocity distribution characteristic factor increases. The increase in the particle size reduces the dispersion coefficient of bubble motion, while the velocity distribution characteristic factor increases. However, the variation in particle size has no significant effect on both parameters. The effect of the superficial gas velocity on dispersion due to bubble motion ($D_b \propto u_{sg}^{0.26}$) is about 4.33 times (at H/W = 0.89), the effect of the superficial slurry ($D_b \propto u_{sl}^{0.06}$) velocity. Similarly, the dependence of the velocity distribution characteristic factor on the superficial gas and slurry velocities is: $k \propto u_{sg}^{-0.18}$ and $k \propto u_{sl}^{-0.002}$, respectively.

The proposed correlations for the hydrodynamic parameters are in good agreement between the experimental and predicted values for all studied experimental conditions. The proposed correlations well predict the experimental values in the ± 20% error range. The proposed correlations can be used to scale-up the system for the further development of the industrial process related to such studies. The results of the mixing can give insight into a further understanding, process intensification, and modeling of the counter-current slurry bubble column.

Chapter 6

Particle Recovery in Microstructured Column

Abstract

The coal particle recovery in a microstructured flotation column is reported in this chapter. The current report is based on the deashing/demineralization of coal particles using the froth/column flotation beneficiation technique. The effect of operating variables on particle recovery, flotation rate constant, efficiency index, ash content, combustible recovery, and induction time is studied. Induction time is enunciated using the phenomenological kinetic model based on the consecutive sub-processes comprising of the bubble-particle collision, attachment, and detachment. The flotation system was optimized by varying the collector as well as surfactant doses.

6.1. Introduction

Coal is one of the largest sources of energy, and perhaps the largest contributor to industrial growth worldwide (Zhu et al., 2020b). Coal is primarily used in the power generation sector (Rawat and Yadav, 2020), iron & steel sector, metallurgical processes (Wang et al., 2017), coke production (Tan et al., 2020) as well as in cement manufacturing units. India produces 157377 MW of electricity through 155 coal-fired power plants using 509.46 MT coal (Rawat and Yadav, 2020). India's energy system relies primarily on the use of coal to generate electricity. Approximately 40% of the world's total electricity production and one-third of the world's steel production is based on coal. As the reserves of high-grade coal are depleted day by day and in many mining processes, the large amounts of fine coal which needs to be beneficiated for use in industries. Owing to the high ash and sulfur content of coal, it is becoming mandatory to demineralize and desulfurize the coal to make it more valuable. Use of inferior coal in coal-fired power plants results in the emission of Hg, NO_x, SO_x, CO_2, trace elements (i.e., As, Se, and Cd), particulate matter, corrodes the surface of the boiler, economizer malfunction, huge ash production (Chang et al., 2019; Steel et al., 2001; Wang et al., 2000; Zhao et al., 2008). Under strict environmental laws, it is of the utmost importance to reduce ash and sulfur minerals from substandard coal.

Several techniques, such as physical, physico-chemical, and chemical techniques are commonly used to beneficiate the coal (Xia et al., 2015). The detailed information on the different techniques regarding coal beneficiation is provided elsewhere (Barma, 2019; Xia et al., 2015). Each technique has its advantages and disadvantages depending on the degree of demineralization, the particle characteristics (particle size, the difference in wettability between carbon-rich and mineral-rich particle or washability, etc.), the chemical consumption, and the environmental policies. Column flotation cell is superior to the mechanical cell, in terms of higher particle recovery with low ash content (Jena et al., 2008; Liaoa et al., 2015), low floor space, low capital and operating cost, and adaptability to automatic control (Hacifazlioglu and Sutcu, 2007; Tian et al., 2017). The present work is focused on the physico-chemical technique in the air-sparged column. The froth flotation technique is regarded to be the physico-chemical technique. This technique depends on the particle properties (i.e., surface morphology, particle size, particle shape, hydrophobicity, crystal structure, roughness), equipment hydrodynamics (i.e., bubble size), mode of operation, physical properties (i.e., surface tension), pH, reagent doses, reagent type, etc. (Hassanzadeh et al., 2018;

Szczerkowska et al., 2018). All the parameters are interdependent, and any change in the design parameters will affect the flotation process. The flotation technique is carried out in a multiphase contacting device where the liquid is in a continuous phase while the gas and fine particles are in the dispersed phase. In counter-current operation, the feed is introduced after conditioning with reagents, entering the flotation column in the middle section or the 2/3 height of the column from the column base where it mixes with the liquid and interacts with the swarm of gas bubbles that are introduced from the bottom of the column through a gas distributor. The relative velocity of particle and gas bubbles decides the probability of the bubble-particle attachment, the power requirement of the process, bubble loading, and the flotation rate. A counter-current operation provides the optimal conditions for the bubble-particle attachment and stability by reducing the rise velocity of the swarm of gas bubbles, thereby increases the retention time in the slurry, and reduces the compressed air requirement. In the counter-current operation, the probability of bubble-particle collision is high because of the large aerated volume in the column, the large distance of travel of the bubble and particle along with the column height and low longitudinal slurry mixing. Collectors are chemicals that absorb on the particle surface and make it hydrophobic. Collector develops a monolayer on the particle surface, which is the thin film of non-polar hydrophobic hydrocarbon, which imparts hydrophobicity. Collector increases the contact angle between the air bubble and particle, thus increases the adherence capacity of the particle surface. Excess concentration of collector limits the recovery of the valuable particle by developing the multilayer on the particle surface, which reduces the hydrophobicity and prevent floatability. Frother or surfactants reduce the surface tension of the liquid and aid in the formation of a large number of stable bubbles and increase the process kinetics.

For the size of coal particles smaller than 0.5 mm, the flotation technique is one of the most efficient processes to enhance the quality of fine coal by removing ash or other mineral matters (Gui et al., 2014). It is a physicochemical technique for separating valuable fine particles (Jena et al., 2008). The flotation technique is based on the wettability property of coal and minerals. It is mainly used to reduce the ash content of coal particles. Ash content mainly consists of inorganic impurities such as quartz (SiO_2), pyrite (FeS_2), aluminum oxide (Al_2O_3), hematite (Fe_2O_3), kaolinite ($Al_2Si_2O_5(OH_4)$), calcite ($CaCO_3$), etc. (Barma et al., 2018a; Barma et al., 2018b; Rahman et al., 2017). The flotation technique is not only capable of reducing the ash content, but it also reduces the sulfur from the coal particles. Sulfur in coal is present in organic (mainly in the

form of mercaptans, thioethers, and thiophenes) and inorganic (pyritic and sulphate) form (Yu et al., 2019). The sulphate sulfur is associated with Ca or Fe, while the pyritic sulfur mainly occurs as high-density inorganic minerals, such as pyrite and marcasite. Inorganic sulfur can be reduced with the flotation technique, while organic is difficult to reduce due to its strong chemical bond (Barma, 2019).

The hydrophobicity of the particle is characterized by the induction time (Zhu et al., 2020a). The most fundamental requirement for efficient flotation is the attachment of the particles on the gas bubble. The attachment of particles on the bubble involves thinning and rupturing of the thin film between the particle and the gas bubble. The minimum length of time required to draining of thin film to the accomplishment of critical thickness and its rupturing and forming the stable bubble-particle aggregate is the induction time (Yoon and Yordan, 1991). Attachment of particles on gas bubbles occurs only when the bubble-particle contact time is larger than the induction time. A detailed review of induction and attachment time is given elsewhere (Albijanic et al., 2010). Zhang et al. (2018) reported the bubble-coal particle induction time using an induction timer. Shorter induction time results in higher recoveries. Smaller particles have a lower induction time compared to larger particles. Shorter induction time (< 20 ms) reflects high grade and strong hydrophobicity of coal particles. Bubble size significantly affects the induction time. The small bubble has a higher interfacial area, which enhances the particle recovery. The induction time for the microbubble-particle attachment is 1000 ms, while in the case of nanobubble, the induction time is reduced to 39 ms. Parmar and Majumder (2016) studied induction time using the phenomenological kinetic model based on the consecutive sub-processes, comprising of the bubble-particle collision efficiency, attachment efficiency, and detachment efficiency. They reported that the induction time is strongly dependent on the slurry circulation velocity, surfactant concentration, and type of surfactant (ie., cationic, anionic, or non-ionic). The reported induction time increases as the slurry circulation velocity increases, while it decreases as the surfactant concentration increases. Zhu et al. (2020a) studied the induction time using two different collectors: (i) mixture of fossil oil and oxygenated compound and (ii) diesel oil. The induction time of coal particles without conditioning with the collector was 100 ms, after conditioning it shortens to 50 ms. The induction time after conditioning with a mixture of fossil oil and oxygen compound was approximately 0 – 10 ms. The induction time of coal particles in acidic, neutral (i.e, deionized water) and the alkaline solution is investigated by Qi et al. (2020). The induction time was 500 ms, 400 ms, and 250 ms in the

alkaline, neutral, and acidic solution, respectively. The induction time of coal particles is also affected by the fresh coal particles. For the fresh coal particles with the collector, the induction time was 10 ms, however, for the aged coal without the collector, it was 11.6 ms (Zhou et al., 2020). The effect of the conventional air bubble and nanobubble on coal recovery is studied by (Chang et al., 2020). The combustible matter recovery in the presence of nanobubble is 10% higher compared to the conventional air bubble.

The literature review indicates that the cleaning of fine coal can be enhanced by the flotation technique. In this study, the cleaning of coal samples has been investigated in a microstructured column to understand the effects of various parameters such as collector and surfactant doses, gas and feed velocity on combustible recovery, the ash content in concentrate, yield, efficiency index, and induction time. An attempt has been made to optimize the reagent doses, and gas and feed velocity in the microstructured column. The phenomenological kinetic model has been used based on the consecutive sub-processes compromising of the bubble-particle collision, attachment, and detachment that has been used to enunciate the induction time. In addition, the correlation for induction time has been proposed in terms of gas and feed Reynolds number.

6.2. Experimental setup and methodology

All the experiments were done at atmospheric pressure (1 atm) and room temperature (298.15 K) in a microstructured flotation column, as shown in Fig. 6.1. The height, width, and depth of the experimental setup were 0.63 m, 0.19 m, and 0.03 m, respectively. For the continuous flow of air in the column, an air compressor was incorporated. Air flow rate was controlled and measured by the needle valve and the calibrated air rotameter (Deluxe Industrial gases, acrylic body, range: 0 – 40 l/m). A cylindrical super porous sparger (SS316, powder sparger, manufactured by TFI Filtration (India) Pvt. Ltd.) with 20 μm was positioned horizontally at the column base to disperse air in the form of a gas bubble in the chamber. For each test, the slurry was prepared in the conditioning tank by taking the known quantity of coal and water. The stirrer was used to mix the coal particles and water thoroughly for approximately 5 minutes. Diesel oil (as a collector), and short branched-chain alcohol, i.e., Methyl-iso-butyl-carbinol ($(CH_3)_2CHCH_2CH(OH)CH_3$, molecular wt.: 105.0 g/mol) (as a frother) were added, respectively at an interval of 5 minutes and mixed thoroughly using the stirrer. MIBC used in the experiment was purchased from the Tokyo Chemical Industry Corporation Limited, while diesel oil was purchased locally. For each test, froth

concentrate generated during the process was collected from the upper lip of the column for 3 minutes. The experiments were carried out in the continuous mode, where the slurry flow was charged continuously wherein the gas flow was dispersed from the base of the column. The feed and gas flowrate was varied from 0.004 to 0.044 m/s and 0.043 to 0.090 m/s, respectively. The experiments were carried out at the ambient pH of the slurry system. The slurry pump was used to feed the slurry from the conditioning tank to the column, while the gravity-driven underflow was collected in the tailing tank. Electromagnetic flow meter (Adept Fluidyne, MagFlow 6410, India) was installed between the slurry pump and feed inlet to the column to measure the feed flow rate. The feed flow rate was controlled using the bypass valve installed between the pump and the electromagnetic flow meter. The slurry concentration of 3.0 wt.% was kept constant for all the experiments. After collection of the froth concentrate and drying in the oven for 105 °C, the concentrate was weighted and sampled for analysis. For the measurement of moisture content, the coal samples were crushed to 230-micron particle size using mortar and pestle. A fixed amount of 1 g coal of this sample was measured in a porcelain crucible, which was put in a hot air oven set at a temperature of 108°C. It is left to dry for 2-3 hours. The loss in weight gives the moisture content of coal. 1 g of 230-micron sample was taken in a high temperature withstanding silica crucibles. The sample was then kept in a muffle furnace (IKON, IK-108). A progressive and constant rate of heating was maintained inside the furnace until the temperature reached 810°C. The sample was maintained at this temperature for the next 1 hour. After that, it was taken out and weighed again. Using the initial and final weight of the coal sample, ash content was estimated. The presence of volatiles in coal favors the coal ignition. The volatile matter was estimated using closed lid cylindrical silica crucibles. 1 g of finely powdered coal (230-micron size) was placed in silica crucibles and kept in the muffle furnace at 910 °C for 10 minutes. To prevent the oxidation of carbon in coal and to allow only volatile matter and moisture to escape, 2-3 drops of benzene was put in coal sample to create an inert atmosphere before putting in a muffle furnace. The sample was taken out and weighed. The difference between the initial and final weight of the sample gives the cumulative weight of moisture and volatiles. After each experiment, the setup was cleaned properly with water to avoid traces of chemicals and other contaminants for the new experiment.

Fig. 6.1. Schematic of the experimental setup. (Copyright material)

The slurry density and viscosity of the slurry was calculated as per the Eq. (6.1) and Eq. (6.2), respectively.

$$\rho_{sl} = \frac{100}{w_s / \rho_s + (100 - w_s) / \rho_l} \tag{6.1}$$

$$\mu_{sl} = \left(1 + k_1 \alpha_s + k_2 \alpha_s^2\right) \mu_l \tag{6.2}$$

where ρ_{sl} and μ_{eff} denote the density and viscosity of the slurry, respectively. The terms w_s, ρ_s, α_s are particle concentration, particle density, and particle holdup. The values of k_1 and k_2 in Eq. (6.2) are 2.5 and 10.05, respectively. The particle holdup is calculated using the following Eq. (6.3)

$$\alpha_s = \frac{m_s / \rho_s}{a_c h_m} \tag{6.3}$$

where m_s, a_c, and h_m refers to the mass of the particle, cross-sectional area of the column, and gas-slurry dispersion height.

6.2.1. Materials and method

The high ash coal sample used in the experiment was taken from the Shillong mine in Meghalaya, India. It was low-rank coal. Four different size fractions (< 150 μm, 150 – 300 μm, 300 – 425 μm, and 425 – 525 μm) of the coal was prepared by the jaw crusher, roll crusher, hammer mill, followed by sieving in mechanical sieve shaker.

Ash analysis was performed for all the four different particle fractions, as shown in Table 6.1. It was observed that ash content is 23.542% for particle fraction of size less than 150 μm. Therefore, raw coal was grinded to this size, and all the experiments were carried out at the same particle fraction. Proximate and ultimate analysis of coal is shown in Table 6.2 and Table 6.3, respectively. The fixed carbon in the proximate analysis was calculated was as fixed carbon (%) = 100 – (%ash + % moisture + % volatile matter). The gross calorific value of coal was measured by the bomb calorimeter. The gross calorific value was found to be 24.41 MJ/kg. Ultimate analysis of coal was performed by carbon-hydrogen-nitrogen-sulfur (CHNS) analyzer (Eurovector EA3000) in Guwahati Biotech Park. The zeta potential of raw coal was also measured by Delsa Nano (Delsa Nano C, Beckman Coulter, Switzerland). The zeta potential of coal particle was found to be – 6.51 mV.

Table 6.1. Ash content in different particle fractions.

Particle fraction	< 150	150 – 300	300 – 425	> 425
% Ash	23.542	25.538	23.707	25.830

Table 6.2. Proximate analysis of coal particle (for d_p < 150 μm).

Proximate analysis	Fixed moisture	Ash content	Volatile matter	Fixed carbon
wt.%	2.751	23.542	37.017	36.69

Table 6.3. Ultimate analysis of coal particle (for d_p < 150 μm).

Ultimate analysis	Carbon	Hydrogen	Nitrogen	Sulfur	Oxygen (by difference)
wt.%	55.585	4.447	1.50	2.756	35.712

The recovery (R) of concentrate was calculated as per the following equation

$$R(\%)=\frac{M_c}{M_f}\times 100 \tag{6.4}$$

The combustible recovery (CR) was calculated using the following expression

$$\mathrm{CR}(\%)=\left[\frac{M_c(100-A_c)}{M_f(100-A_f)}\right]\times 100 \tag{6.5}$$

where A_c, A_f, M_c, and M_f refers to the ash content of concentrate, the ash content of feed coal, the mass of concentrate, and mass of feed, respectively. Percentage ash rejection (AR) of the flotation test was calculated as per the following equation

$$AR(\%)=\left[1-\left(\frac{M_cA_c}{M_fA_f}\right)\right]\times 100 \tag{6.6}$$

The efficiency index (EI) of flotation was estimated as per the following equation

EI = (Combustible recovery (%) + Ash rejection (%)) – 100 (6.7)

6.2.2. Particle characterization

Typical image of coal particles captured by Field Emission Scanning Electron Microscope (FESEM) (make: Zeiss, Model: Sigma) and particle size distribution (measured by laser particle size analyzer) is shown in Fig. 2.2a. and 2.2b, respectively.

6.2.2.1. X-ray fluorescence of coal

X-ray fluorescence (XRF) spectrometry is an instrumental method used for the analysis of major, minor, and trace compounds and elements in the coal samples. The XRF spectrometry (Table 6.4) of raw coal shows that the major constituents of ash in coal are silica (SiO_2 = 42.601%), followed by alumina (Al_2O_3 = 7.919%) and iron oxide (Fe_2O_3 = 7.387%). Cumulatively, all three constitute 57.907% of the ash. In the elemental analysis, all these three (Al, Si, and Fe) contribute 29.271%. The coal also has high sulphur content (SO_3 = 38.128%, S = 15.269%).

Table 6.4. X-ray fluorescence spectrometry of coal.

Element	Concentration (%)	Compound	Concentration (%)
O	52.303	Na_2O	0.627

Na	0.465	MgO	0.434
Mg	0.262	Al_2O_3	7.919
Al	4.191	SiO_2	42.601
Si	19.913	P_2O_5	0.087
P	0.038	SO_3	38.128
S	15.269	Cl	0.230
Cl	0.230	K_2O	1.021
K	0.848	CaO	0.881
Ca	0.629	Ti	0.471
Ti	0.471	Cr	0.069
Cr	0.069	Fe_2O_3	7.387
Fe	5.167	Sr	0.117
Sr	0.117	Zr	0.028
Zr	0.028		

6.2.2.2. XRD of coal

Identification of mineral phases available in coal is helpful to detect the quality of coal and important for its beneficiation. X-ray powder diffraction (XRD) (Make: Bruker, Netherland, Model: D8, Advance) analysis is performed over a 2θ interval and step size of 3 to 90° and 0.02°, respectively. Quartz (SiO_2) and kaolinite ($Al_2Si_2O_5(OH)_4$) are the major mineral phase, as shown in Fig. 6.2a. However, among these two, the maximum peaks of the quartzitic phase reveal its predominance. Quartzitic phase contributes to the majority of crystalline or free silica (SiO_2) matters while kaolinite contributes alumina (Al_2O_3) along with some amount of SiO2. Reduction in the peak intensity (as shown in Fig. 6.2a) of mineral phases indicating the removal of accompanied impurities after flotation.

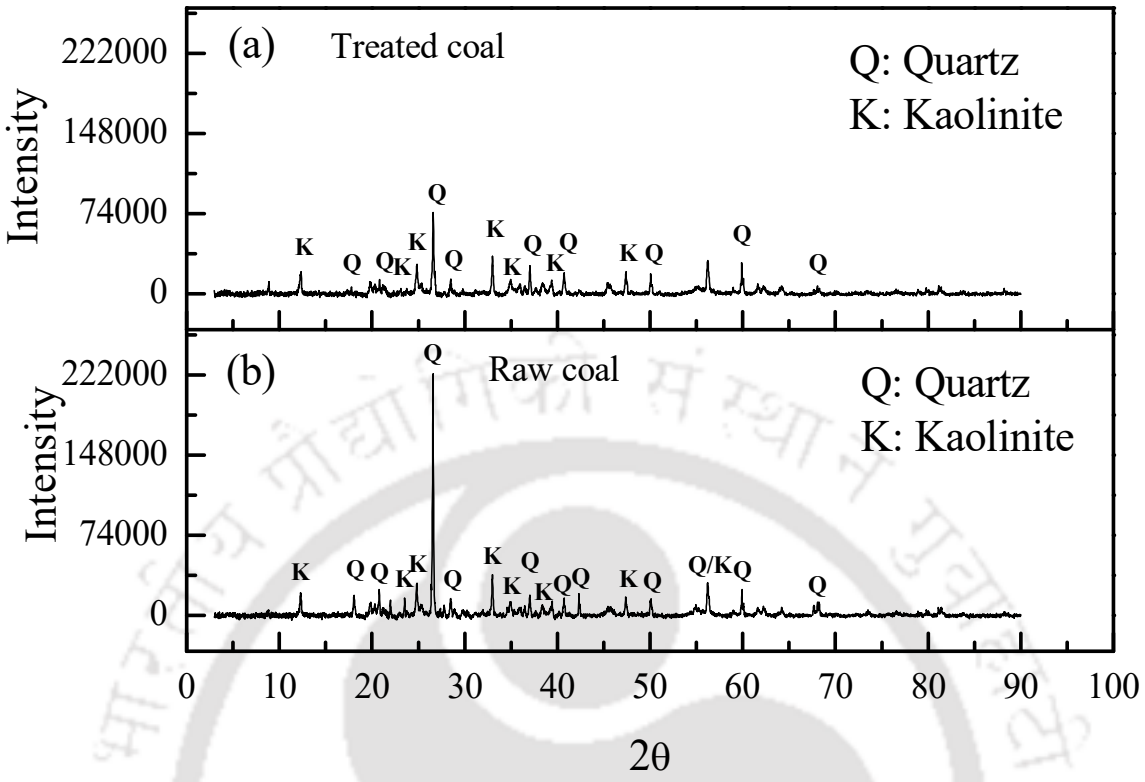

Fig. 6.2. XRD result of coal particles.

6.2.2.3. FESEM-EDX result of coal

Field emission-scanning electron microscope in conjunction with energy-dispersive X-ray spectrometer (FESEM-EDX) (Make: Zeiss, model: Sigma 300) was used to analyze the distribution of mineral matters of raw and treated coal. Feed coal (Fig. 6.3a and Fig. 6.3b) and concentrate (Fig. 6.3c and Fig. 6.3d) show a substantial amount of mineral matters are removed from the raw coal. Fig. 6.3b shows the content of raw coal corresponding to spectrum 3 (Fig. 6.3a), where C (66.1%), O (20.90%), S (3.20%), Si (3.0%), Al (2.5%), Fe (2.30%) and Cl (1.40%) are major components. In Fig. 6.3d, the content of concentrate corresponding to spectrum 25 (Fig. 6.3c) shows that C content increases to 79.60%, while other components such as O, S, Si, Al, Cl, and Fe reduces to 14.20%, 2.0%, 1.60%, 1.40%, 0.80%, 0.10%, respectively. Results show significant removal of mineral content after coal flotation.

Fig. 6.3. EDX spectra of coal: (a) raw coal, (b) EDX of raw coal, (c) treated coal, and (d) EDX result of treated coal. (Copyright material)

6.2.2.4. FTIR analysis of coal

Fourier-transform infrared spectroscopy (FTIR) analysis of powdered samples of coal was performed to identify the functional group of raw and concentrate coal. The analysis was done in the FTIR instrument (Model No.: IRAffinity-1; Make: M/s Shimadzu, Japan) in the range of 400 to 4000 $cm^{-1,}$ as shown in Fig. 6.4. Coal sample of approximately 5 – 7 mg was weighed in a single pan digital balance-weighing machine (Make: MicroSet, model: MS WB-325). The sample was prepared by thoroughly mixing coal particles with dry finely ground spectroscopic grade KBr (approximately 180 -200 mg) in an agate mortar and pestle. FTIR was performed at the 30 scans in an absorbance mode.

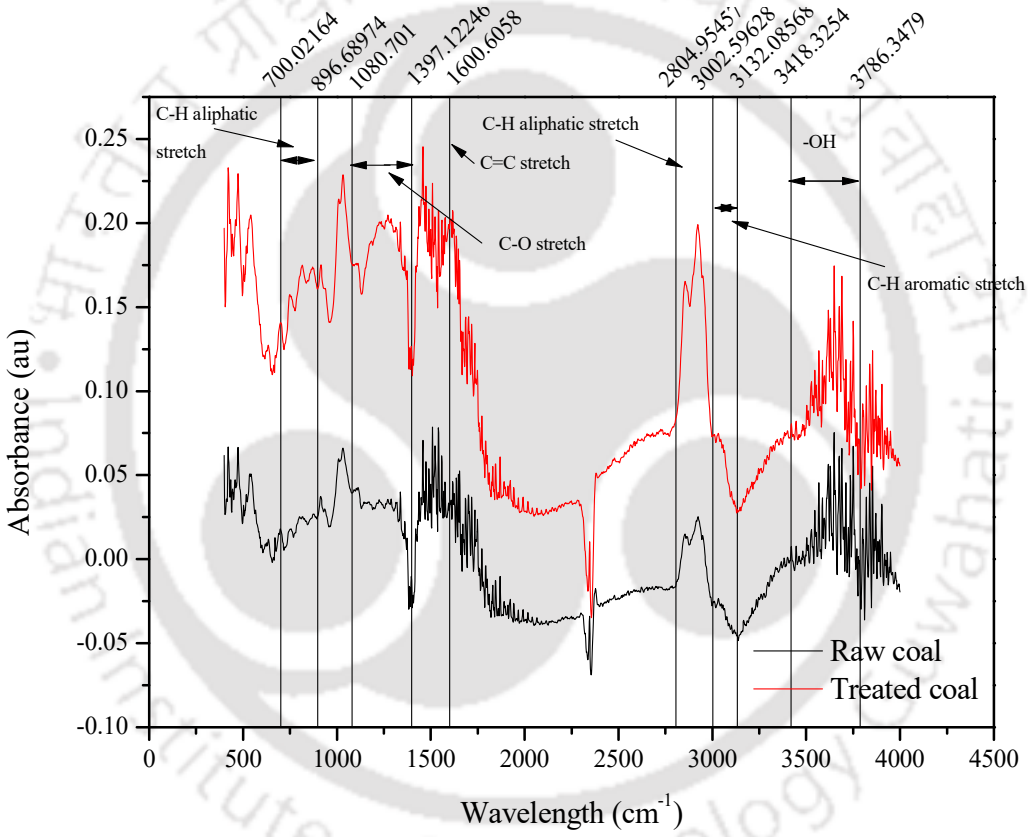

Fig. 6.4. FTIR analysis of coal.

6.3. Results and discussion

6.3.1. Optimization of collector and surfactant doses

The effect of variation of collector and surfactant doses on combustible recovery (*CR*) and efficiency index (*EI*) at 0.004 m/s feed (u_f) and 0.082 m/s gas velocity (u_g) and at fixed surfactant dose of 600 gram per ton (GPT) is shown in Fig. 6.5a and Fig. 6.5b, respectively. In Fig. 6.5a, it

is noticed that as the collector doses increased from 2500 to 3100 gram per ton (GPT), the *CR* increases from 54.275 to 83.66%, and a further increase in the collector doses (from 3400 to 3700 GPT) leads to *CR* more or less constant. The *EI* of the system increases from 24.94% to 35.78% (as the collector doses increase from 2500 to 3100 GPT), and it starts to decrease from 35.78% to 28.47% (as the collector dose increase from 3400 to 3700 GPT). This may be attributed to the non-selectivity of the collector on the coal particles and entrainment of ash containing minerals in the froth concentrate at high collector doses.

The addition of the surfactant stabilizes the gas bubbles and forms the small bubble size. Small bubble size has a high interfacial area that facilitates more bubble-particle interaction and leads to enhance the system performance. The influence of the surfactant dose on CR and EI at 0.004 m/s feed and 0.082 m/s gas velocity at fixed collector doses (at 3100 GPT) is shown in Fig. 6.5b. It is observed that CR increases from 73.88% to 87.67% (as surfactant dose increases from 320 to 540 GPT), and a further increase in the surfactant dose (from 600 to 660 GPT) leads to a slight variation in CR. The maximum *EI* (39.60%) is observed to be at 480 GPT surfactant dose, and an increase in the surfactant dose beyond 480 GPT, the *EI* starts to decrease. The reduction in EI is attributed to a reduction in the growth rate of yield and the increase in the ash content in concentrate caused due to the recovery of high ash content minerals.

The optimization of the collector and surfactant dose is performed based on the EI of the system. From Figs. 6.5a and 6.5b, it is found that the maximum EI is about 39.60% at collector and surfactant dose of 3100 and 480 GPT, respectively. Further experiments were carried out to enunciate the influence of operating variables such as feed and gas velocity at the optimized collector and surfactant dose.

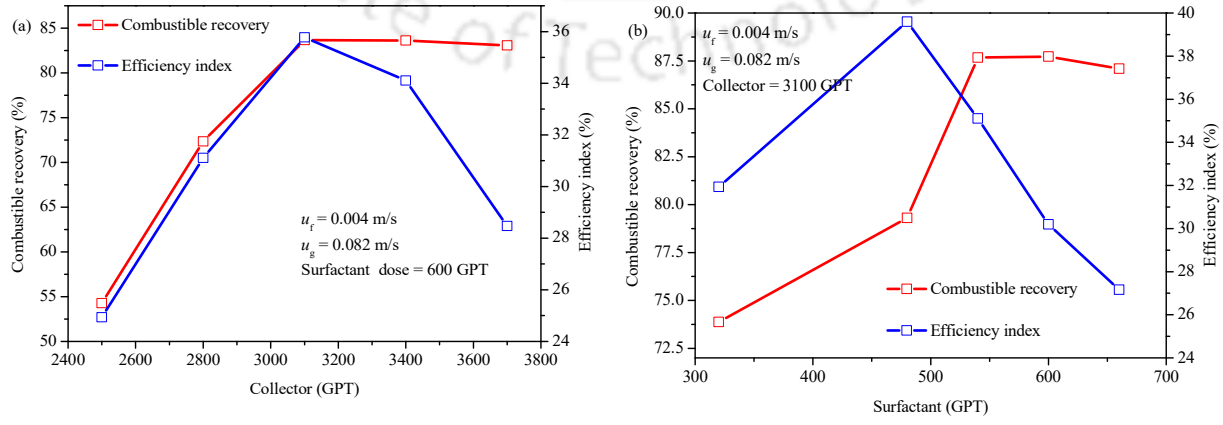

Fig. 6.5. Effect of (a) collector on combustible recovery and efficiency index and (b) surfactant on combustible recovery and efficiency index.

6.3.2. Effect of different variables on combustible recovery, efficiency index, yield, and ash content

The effect of gas velocity on yield at various feed rates (u_f = 0.004 – 0.044 m/s) is shown in Fig. 6.6a. It is observed that the yield is increasing as the gas velocity increases for all the feed rates. It is obvious that as the gas velocity increases, it forces more particles to come to the froth phase, therefore the yield of the system increases.

The increase in the feed velocity reduces the residence time of the slurry. Hence the yield of the system also gets influenced significantly. The yield of the system decreases, owing to a reduction in the residence time of the slurry. The low residence time of the slurry does not facilitate effective bubble-particle interaction, bubble-particle collision, and bubble-particle attachment, which is attributed to reducing the yield of the system. At high feed velocity, from 0.028 – 0.044 m/s, the reduction in yield for all the gas velocity is clearly noticed, however at low feed velocity from 0.004 to 0.020 m/s, the yield curve intersects each other at few gas velocities. It is attributed to the effective interaction of bubble-particle due to the high residence time of slurry in the column. The maximum and minimum yield is found to be approximately 83.22% and 28.40% at 0.09 m/s gas velocity (for u_f = 0.020 m/s) and 0.004 m/s gas velocity (for u_f = 0.044 m/s), respectively. At the maximum feed rate (u_f = 0.044 m/s), as the gas velocity increases from 0.043 to 0.090 m/s, the yield increases from 28.41% to 43.01%, approximately an increase of 51.01%. Similarly, at low feed velocity (u_f = 0.004 m/s), the increase in yield is about 57.85% at the same variation of the gas velocity.

The influence of gas and feed velocity on ash content of concentrate at optimum collector and surfactant dose is shown in Fig. 6.6b. It is noticed that the ash content is increasing as the gas velocity increases for all the feed rates. In actual lower ash content is obtained at the expanse of combustible recovery. As the gas velocity increases, along with desired particles, the entrainment of gangue particles to the froth phase also increases, therefore the ash content. At lower feed velocity, the resistance on the upward carrying of the particle by a gas bubble is low, which leads to a higher yield of the ash containing particle, which leads to an increase the ash in concentrate. At high feed rate (u_f = 0.028 to 0.044 m/s), the throughput of the particles with froth is low.

Therefore, the ash content curve is not clear as it was with u_f < 0.028m/s. At minimum feed velocity, 0.004 m/s, the ash content in concentrate increases from 13.58% to 16.93%, an increase of approximately 24.62%, when the gas velocity increases from 0.043 to 0.090 m/s. Similarly, at maximum feed velocity, the ash content increases from 10.24 to 12.38%, the increase is about 20.92% at the same variation of gas velocity. The minimum increase in the ash content is 10.97 to 12.12%, approximately an increase of 10.53% (at u_f = 0.036 m/s), at the same variation of gas velocity. If looking at the variation of ash content with the feed velocity, for all the gas velocity, the ash content in concentrate decreases with an increase in the feed velocity. For minimum gas velocity, say 0.043 m/s, the ash content decreases from 13.58 to 10.24%, the reduction of about 24.65%, as the feed velocity increases from 0.004 to 0.044 m/s. Similarly, for maximum gas velocity, say 0.090 m/s, the reduction in ash content is about 26.89%, at the same change in the feed velocity.

The variation in combustible recovery (CR) as a function of gas velocity and feed velocity at optimum collector and surfactant concentration is shown in Fig. 6.6c. Combustible recovery is the function of the mass of concentrate, the mass of feed, the ash content in concentrate, and ash content in the feed. Higher recovery and lower ash content in concentrate improve the product quality and combustible recovery. Combustible recovery from the fines of coal particles strongly depends on the hydrophobicity of the fine particles, mineral (ash) distribution, and particle size distribution in the feed (Das et al., 2010). Under the suitable kinetic condition, the CR reaches 80% and also exceeds the value. It is noticed that the CR increases as the gas velocity decreases while it decreases with an increase in the feed velocity. The present CR results are in agreement with the finding of other researchers (Babu et al., 2018). The maximum CR is observed to be 93.65% at 0.090 gas velocity and 0.020 m/s feed velocity. For 0.004 and 0.012 m/s feed velocity, at $u_g \geq$ 0.075 m/s, the CR is greater than 80%, while for the feed velocity 0.020 m/s, CR more than 80% is observed at $u_g \geq$ 0.082 m/s. For other feed and gas velocities, the CR is below 80%.

Efficiency index (EI) is a useful parameter to compare the system performance under various experimental conditions is shown in Fig. 6.6d. EI is dependent on combustible recovery and ash removal from the feed. The maximum EI of 47.70% is observed to be at 0.020 m/s feed velocity and 0.082 m/s gas velocity. Unlike other plots (Fig. 6.6a, 6.6b, and 6.6c), no any particular trend observed with respect to feed and gas velocities. The improvement in EI is about 1.78% (at u_f =

0.004 m/s), 6.06% (at u_f = 0.012 m/s), 42.03% (at u_f = 0.020 m/s), 17.79% (at u_f = 0.028 m/s), 16.22% (at u_f = 0.036 m/s), and 25.68% (at u_f = 0.044 m/s) when the gas velocity changes from 0.043 to 0.090 m/s. Operating the system at gas velocity of 0.082 m/s and feed rate 0.020 m/s will leads to provide the optimum condition for this system in terms of efficiency index.

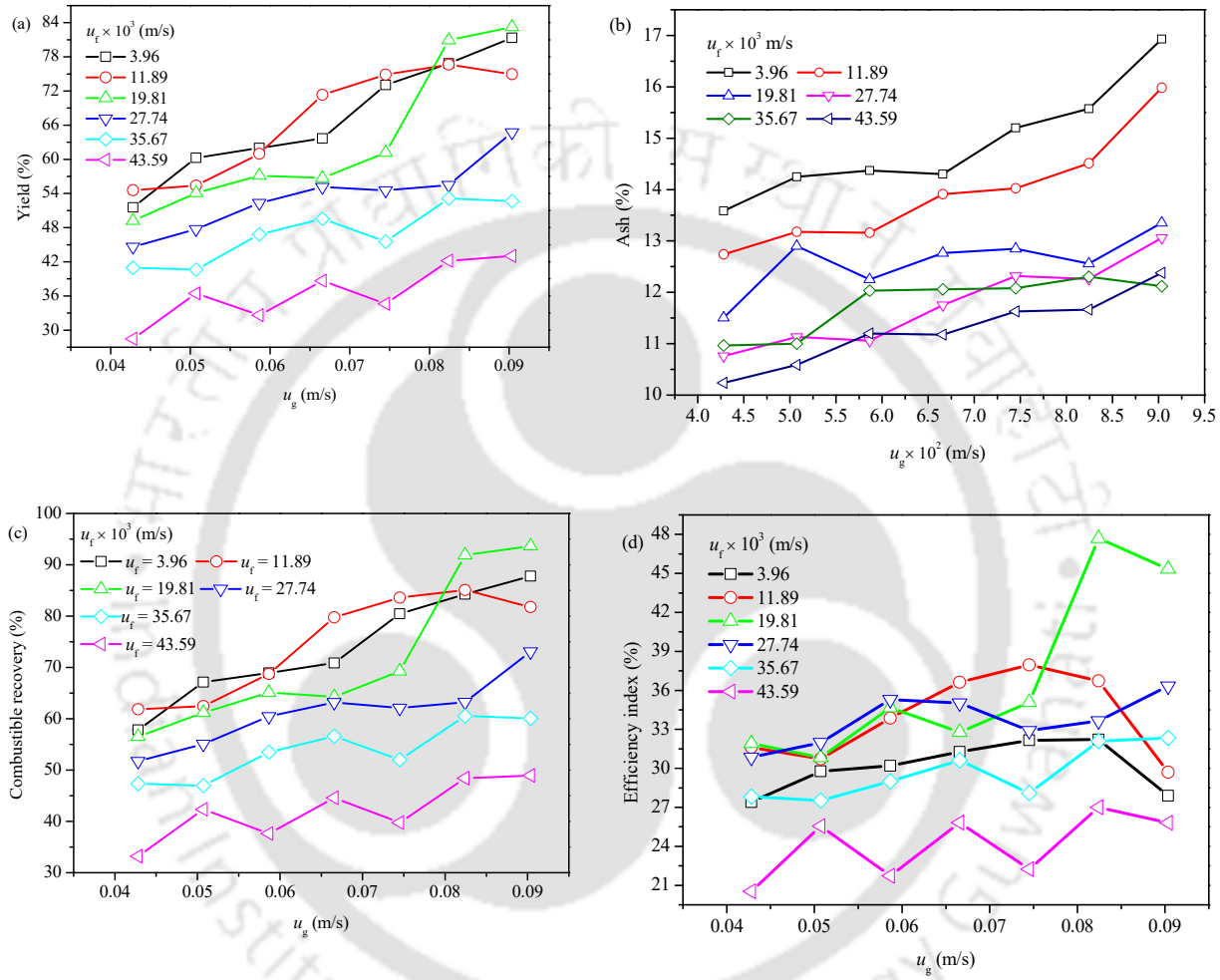

Fig. 6.6. Effect of gas and feed velocity on (a) yield, (b) ash content in concentrate, (c) combustible recovery, and (d) efficiency index.

6.3.3. Variation of particle recovery with time

To understand the science behind the flotation technique and plant design, numerous flotation model have been developed by several researchers (Albijanic et al., 2015; Danoucaras et al., 2013). The flotation process has been shown to follow a rate equation of the type given below.

$$\frac{dC}{dt} = -KC^N \qquad (6.8)$$

where C is the concentration of the floatable mineral in the pulp, $C = M / V$, t is time for which the mineral is allowed to float, and N is the rate of the order. The term M denotes the mass of floatable mineral in the pulp, and V is the volume of the pulp and is kept constant throughout the experiment. If time is the only variable, then

$$\frac{-dC}{dt} = KC(t)^N \tag{6.9}$$

Integrating Eq. (6.9) with $N = 1$ and the appropriate limit of $C = C_0$ at $t = 0$, gives the following equation:

$$\ln C(t) = -Kt + \ln C_0 \tag{6.10}$$

In Eq. (6.10), it is assumed that non –floatable mineral is not present in the cell. However, due to some reasons like insufficient collector concentration or incomplete liberation of mineral, etc. some portion of the mineral in the pulp is non-floatable. So the Eq. (6.9) becomes

$$\ln[C(t) - C_\infty] = -Kt + \ln[C_0 - C_\infty] \tag{6.11}$$

where C_∞ is the concentration of mineral remaining in the pulp after prolonged floatation. Expressing recovery of the valuable mineral as

$$R(t) = \frac{C_0 - C(t)}{C_0} \tag{6.12}$$

After a prolonged time

$$R_\infty = \frac{C_0 - C_\infty}{C_0} \tag{6.13}$$

Combining Eq. (6.12) and (6.13) with Eq. (6.11), the recovery as a function of time can be expressed as

$$R(t) = R_\infty(1 - e^{-Kt}) \tag{6.14}$$

where $R(t)$ and R_∞ refers to the recovery at time t and ultimate recovery (or theoretical maximum recovery), respectively. The ultimate recovery is dependent on the chemical doses

such as collector and surfactant concentration, while the rate constant depends on the process variables such as power input, particle size, and gas velocity (Nguyen and Schulze, 2003). The rate constant reflects the particle floatability (Cheng et al., 2013), and both of these parameters are used to analyze the flotation behavior (Xu, 1998). Flotation kinetics is related to micro sub-process such as collision, attachment, and stability efficiencies, all of these are associated with the transport of the hydrophobic particles to the froth phase. Determination of the flotation rate constant can be divided into three categories: (i) single flotation rate constant, (ii) distributed rate constant (Gamma, rectangular distributions, etc.), and (iii) fractional rate constant type (Alvarez-Silva et al., 2016). Alvarez-Silva et al. (2016) reported that a single flotation rate constant is suitable for the identification of ultimate recovery. Other flotation kinetic model used in flotation is given elsewhere (Drzymała, 2018). The flotation kinetic model brings together all the factors that takes place while flotation (Lazic and Calic, 2000). Flotation running under steady-state condition, the rate constant is dependent on the probability of flotation and bubble surface area flux ($s_b = 6q_g/d_b$).

A typical variation of fractional and cumulative recovery as a function of time at fixed feed velocity (0.004 m/s) and different gas velocities (0.043 – 0.090 m/s) is shown in Fig. 6.7. It is noticed that for each gas velocity, fractional recovery is maximum for the first 30 s and in the later period, it starts to decreases. In the initial period, the affinity of attachment of particles to the gas bubble is high because of the presence of a larger number of hydrophobic particles, and with time quantity of hydrophobic particles reduces in the column, therefore the fractional recovery decreases. Up to 80 s, the little variation of fractional recovery is observed. Beyond this time, the variation in fractional recovery is more or less the same. The flotation rate constant (K) and ultimate recoveries (R_∞) for each experimental condition are evaluated by fitting the Eq. (6.14) using experimental cumulative recovery values as a function of time. Typical values of flotation rate constant and ultimate recoveries are given in Table 6.5.

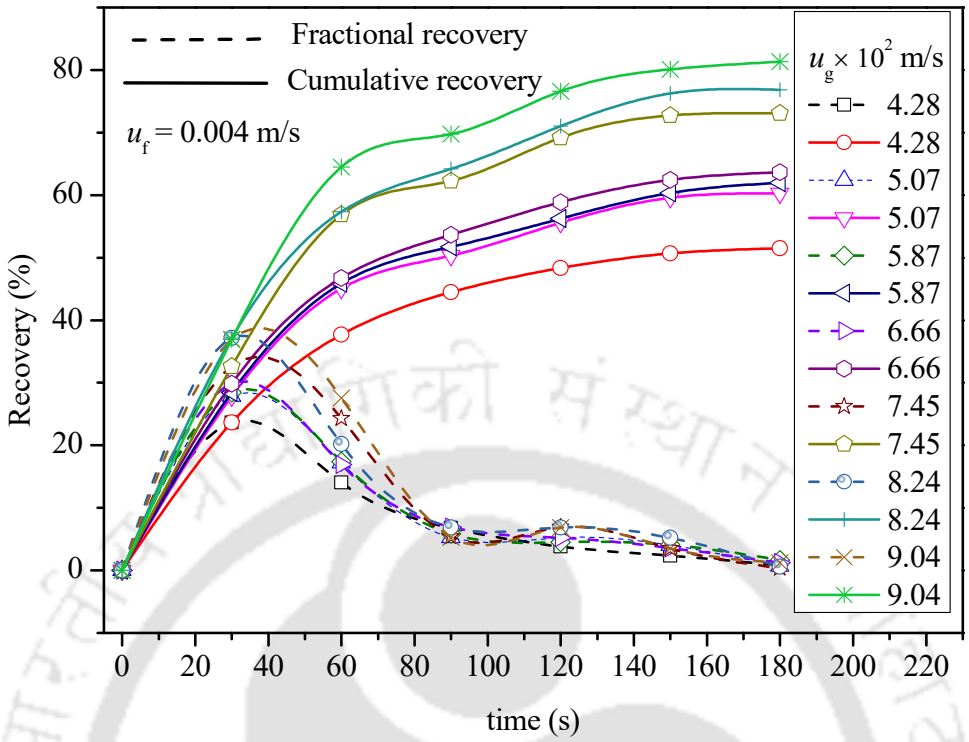

Fig. 6.7. Variation of fractional and cumulative recovery with time at different gas velocities.

Table 6.5. Typical values of rate constant and ultimate recovery.

$u_g \times 10^2$ (m/s)	4.28	5.07	5.87	6.66	7.45	8.24	9.04
$K \times 10^{-2}$ (1/s)	2.0151	2.0357	2.0357	2.0437	2.0648	2.1037	2.0075
R_∞	53.11	61.67	65.18	64.99	75.50	78.25	83.18

6.3.4. Modeling of induction time

The collection efficiency in the flotation process is the function of three sub-processes, such as E_c (particle-bubble collision), E_a (particle-bubble attachment), E_s (stability) efficiencies, also known as a three-zone model (Derjaguin and Dukhin, 1993). The efficiencies are strongly dependent on the particle size, particle shape, particle composition, induction time, pulp viscosity, particle density, particle velocity, holdup characteristics, bubble diameter, bubble velocity, turbulence, etc. (Danoucaras et al., 2013). Any change in these input parameters greatly influences flotation efficiencies. Three sub-processes takes place, and attachment of particle on gas bubbles takes place in a very short period: (i) thinning of liquid film to a critical thickness between the gas bubble and particle, (ii) rupturing of the thin film at critical film thickness and establishment of initial three-

phase contact, and (iii) expansion of initial three-phase contact and formation of the stable wetting perimeter (Albijanic et al., 2010; Basařová et al., 2019; Nguyen et al., 1997; Subasinghe and Albijanic, 2014). Details on the expansion of a three-phase contact line are given elsewhere (Basařová et al., 2019). Considering, these sub-processes are independent of each other, particle and bubble are spherical, and particle size is less than the bubble size, the kinetic relation representing the recovery of the particle is expressed as

$$\frac{dN_P}{dt} = -KN_P = -Z_{pb}E_cE_aE_s \tag{6.15}$$

where N_p is the number of particles, t is time, K is rate constant, and Z_{pb} is particle-bubble collision frequency based on the size of the particle and bubble, and hydrodynamics of the pulp flotation. The particle-bubble collision frequency can be calculated by the expression given by Pyke et al. (2003)

$$Z_{pb} = 5N_PN_b\left(\frac{d_b + d_p}{2}\right)^2\sqrt{\bar{v}_b^2 + \bar{v}_p^2} \tag{6.16}$$

where N_b denotes the number of bubbles per unit volume. Terms v_b and v_p are the roots mean square velocities of bubbles and particles relative to the turbulent fluid velocity. Since, $d_p << d_b$, hence, the root mean square velocity of the particle neglected, and the root mean square velocity of the bubble is expressed by the following equation suggested by (Schubert, 1999)

$$\left(\bar{v}_b^2\right)^{1/2} = 0.33\frac{\varepsilon^{4/9}d_b^{7/9}}{\nu^{1/3}}\left(\frac{\rho_p - \rho_f}{\rho_f}\right)^{2/3} \tag{6.17}$$

where ε denote the dispersion rate of turbulent kinetic energy per unit mass, ν is the kinematic viscosity of the fluid, ρ_p is particle density, and ρ_f is the fluid density. Dispersion rate of turbulent kinetic energy per unit mass can be calculated as per the following equation

$$\varepsilon = \frac{0.85}{L}\left(\frac{\bar{U}_{cx}^2 + \bar{U}_{cy}^2 + \bar{U}_{cz}^2}{2}\right)^{1.5} \tag{6.18}$$

where L refers to the flow length scale, which can be taken as $0.04d_c$. Hence, Eq. (6.18) can be modified as

$$\varepsilon = \frac{12.143}{d_c}\left(\frac{\overline{U}_{cx}^2 + \overline{U}_{cy}^2 + \overline{U}_{cz}^2}{2}\right)^{1.5} \tag{6.19}$$

The root mean square circulation velocity of bubble-particle is assumed to equal to the circulation velocity of the mixture, therefore the Eq. (6.19) can be expressed as

$$\varepsilon = \frac{12.143}{d_c}\left(\frac{\overline{U}_c^2}{2}\right)^{1.5} \tag{6.20}$$

Substituting the Eq. (6.20) into Eq. (6.17), the root mean square velocity of the bubble can be written as

$$\left(\overline{v}_b^2\right)^{1/2} = 0.33\left(\frac{12.143}{d_c}\left(\frac{\overline{U}_c^2}{2}\right)^{1.5}\right)^{4/9} \frac{d_b^{7/9}}{\nu^{1/3}}\left(\frac{\rho_p - \rho_f}{\rho_f}\right)^{2/3} \tag{6.21}$$

The number of bubbles per unit volume can be calculated as

$$N_b = \frac{6\alpha_g}{\pi d_b^3} \tag{6.22}$$

where α_g denote the gas holdup. Substituting Eq. (6.21) and Eq. (6.22), into Eq. (6.16), the final form of the particle-bubble collision frequency equation can be expressed as

$$Z_{pb} = 5N_P \frac{6\alpha_g}{\pi d_b^3}\left(\frac{d_b + d_p}{2}\right)^2 0.33\left(\frac{12.143}{d_c}\left(\frac{\overline{U}_c^2}{2}\right)^{1.5}\right)^{4/9} \frac{d_b^{7/9}}{\nu^{1/3}}\left(\frac{\rho_p - \rho_f}{\rho_f}\right)^{2/3} \tag{6.23}$$

Replacing the expression for particle-bubble collision frequency (Eq. (6.23)) into Eq. (6.15), the expression for rate constant can be given as

$$K = 30.03\frac{\alpha_g}{\pi d_b^3}\left(\frac{d_b + d_p}{2}\right)^2\left(\frac{1}{d_c}\left(\frac{\overline{U}_c^2}{2}\right)^{1.5}\right)^{4/9} \frac{d_b^{7/9}}{\nu^{1/3}}\left(\frac{\rho_p - \rho_f}{\rho_f}\right)^{2/3} E_c E_a E_s \tag{6.24}$$

6.3.4.1. Collision efficiency

In flotation sub-processes, the first process is a bubble-particle collision, where particles will collide with the gas bubble. It is dependent on the hydrodynamic characteristics of the fluid flow

around the bubble-particle encounter. The expression for bubble-particle collision efficiency is given by Dukhin so-called generalized Sutherland (E_c^{GSE}), which can be expressed as (Hassanzadeh et al., 2019)

$$E_c^{GSE} = E_c^{SU} Sin^2\theta_t \exp\left[3K_3 \cos\theta_t \left(\ln\left(\frac{3}{E_c^{SU}} - 1.8\right)\right) - \frac{9K_3\left(\frac{2}{3} + \cos^3\theta_t - \cos\theta_t\right)}{2E_c^{SU} Sin^2\theta_t}\right] \tag{6.25}$$

where E_c^{SU} is given as $3d_p/ d_b$. The maximum possible collision angle (θ_t) of the particle on the bubble surface is given as

$$\theta_t = 2\arcsin\left[2\beta(1+\beta^2)^{0.5} - \beta\right]^{0.5} \tag{6.26}$$

The term K_3 in Eq. (6.25) is defined as

$$K_3 = k_{st}\left(\frac{\rho_p - \rho_f}{\rho_p}\right) \tag{6.27}$$

were k_{st} denote the particle Stokes number, which can be given as

$$k_{st} = \frac{\rho_p u_b d_p^2}{9\mu_{sl} d_b} \tag{6.28}$$

where u_b and μ_{sl} denote the bubble rising velocity and slurry viscosity. The rising velocity is calculated as per the expression given by (Clift et al., 1978)

$$u_b = \left[\frac{2.14\sigma_{sl}}{\rho_{sl} d_{32}} + 0.505 g d_{32}\right]^{0.5} \tag{6.29}$$

The parameter β is calculated as

$$\beta = \frac{2fE_c^{Su}}{9K_3} \tag{6.30}$$

where f is constant and its value is given as 2.034 (Dukhin and Rulev, 1977).

6.3.4.2. Stability efficiency

All the particles attached to the gas bubble does not reach to the froth phase, some of the particles detach and fall back to the pulp phase due to the hydrodynamic effect (Wang and Tao, 2019). The detachment of the particles takes place on the detachment force (i.e., bubble oscillation caused by the bubble-bubble interaction or vigorous interaction among phases due to turbulent condition or backmixing of the phases as a result of non-uniform radial or axial gas holdup characteristics) is more compared to the adhesive forces. The detachment of particles from the bubble as a means of vibration technique is reported by Cheng and Holtham (1995). Other researchers reported that the bubble collision against large particles results in the detachment of many small particles (Kirchberg and Topfer, 1965). The forces acting between bubble particle attachments are Capillary force, the weight of the particle, excess force such as the relative difference between the excess pressure in the bubble, which facilitates attachment and hydrodynamic force, which enables detachment, and drag force (Drzymala, 1994; Ralston et al., 1999a; Ralston et al., 1999b). More hydrophobic particles have a greater stabilizing influence on froth (Klassen and Mokrousov, 1963). Intermediate hydrophobic particle ($\theta \approx 65°$) stabilizes the froth phase, high hydrophobic particle ($\theta > 90°$) actually destabilize and low hydrophobic particle ($\theta < 40°$) have no influence on froth stability (Johansson and Pugh, 1992). Stability efficiency was calculated as per the modified Schulze (1992) model

$$E_s = 1 - \exp\left(A_s \left(1 - \frac{1}{Bo} \right) \right) \tag{6.31}$$

where A_s is constant, its value is taken as 0.5 (Bloom and Heindel, 2002) and Bo denote the Bond number, which can be expressed as (Koh and Schwarz, 2007; Pyke et al., 2003)

$$Bo = \frac{d_p^2 \left[(\rho_p - \rho_f) g + 1.9 \rho_p \varepsilon^{2/3} \left(\frac{d_p + d_b}{2} \right)^{-1/3} \right] + 1.5 d_p \left(\frac{4\sigma_{sl}}{d_b} - d_b \rho_f g \right) \sin^2\left(\pi - \frac{\theta}{2} \right)}{6\sigma_{sl} \sin\left(\pi - \frac{\theta}{2} \right) \sin\left(\pi + \frac{\theta}{2} \right)} \tag{6.32}$$

where θ is the contact angle and σ_{sl} is the slurry surface tension. The contact angle is taken as 62° for coal particles (He et al., 2018).

6.3.4.3. Bubble-particle attachment efficiency

Sufficient hydrophobic particles encounter a gas bubble and thin the liquid film between the particle and gas bubble and finally rupture it as a result of attractive surface forces (Tao, 2005). Ultimately, the particle attaches to the surface of the gas bubble. Experiential and analytical studies show that attachment efficiency improves in the presence of hydrophobic particles while deteriorate as the particle size increases (Dai et al., 1998; Ralston et al., 1999b). The attachment of the particle on the gas bubble will occur only when the induction time is lower compared to the sliding time. Dobby and Finch (1987) model were used to calculate the bubble-particle attachment efficiency. The model is expressed as

$$E_a = \frac{\sin^2 \theta_a}{\sin^2 \theta_t} \tag{6.33}$$

where θ_a is the adhesion angle, which can be expressed as equation given by Dobby and Finch (1987)

$$\theta_a = 2 \arctan \exp\left(-t_{ind} \frac{2(u_p + u_b) + u_b \left(\frac{d_b}{d_b + d_p} \right)^3}{d_b + d_p} \right) \tag{6.34}$$

where t_{ind} is the induction time and u_p is the particle velocity, which can be expressed as (Bruce, 2003)

$$u_p = \frac{20.52 \mu}{\rho d_p} \left[\left(1 + 0.0921 \left(\frac{d_p^3 (\rho_p - \rho_l) \rho_l g}{0.75 \mu^2} \right)^{\frac{1}{2}} \right)^{\frac{1}{2}} - 1 \right]^2 \tag{6.35}$$

In the present work, the induction time is calculated from the experimental values of recovery and fitting the classical first-order kinetic Eq. (6.14).

6.4. Variation of induction time

The concept of induction time was first introduced by Sven-Nilsson (1934), measuring the induction time by moving the bubble towards and away from the flat mineral surface. The time required for the liquid film to thin to a critical film thickness where thin-film ruptures are called as induction time. Particles with shorter induction time will be easily captured by the gas bubbles and said to have higher selectivity (Li et al., 1990). Bubble-particle attachment time is regarded as the sum of induction time (t_i), the time required to thin-film rupture and establish the three-phase contact line (t_r), and time required to the three-phase contact line to expand beyond the nucleus radius to establish a stable wetting perimeter (t_{pc}) (Albijanic et al., 2010). Under normal experimental conditions, t_r is very small of order 1 ms, which is significantly low compared to t_r and t_{pc}. Therefore, it is neglected during the modeling of attachment time. Generally, researchers used both time scales, induction time, and attachment time interchangeably without proper definition. Induction time is a strong function of particle size, particle shape, surface chemistry of bubbles and particles, trajectories of particle and bubble and their relative velocity, bubble size, surface tension, and viscosity of the continuous phase (Albijanic et al., 2010; Li et al., 1990; Verrelli et al., 2014; Verrelli et al., 2011). Attachment of particles on gas bubbles takes place when the contact time between the particle and gas bubble (i.e., sliding time) is low compared to induction time. Induction time is related to surface chemistry, and it has the potential to link the future scope related to changing the chemical environment. In the literature, no correlation between particle recovery and induction time is mentioned. However, variation in induction time with the particle size was studied and mentioned by several researchers (Zhang et al., 2018). The relation exhibiting a change in induction time with particle diameter and contact angle (Dai et al., 1999; Duan et al., 2003), particle and bubble diameter (Li et al., 1990). Other researchers reported the generalized correlation for induction time in terms of circulation velocity, capillary number, Reynolds number, bubble, and particle diameter (Parmar and Majumder, 2016). Induction times vary based on the particle size. Smaller particle size has a shorter induction time. Induction time lower than 20 ms, is considered to be the better coal quality and higher hydrophobicity. Shorter induction time reflects the higher particle recovery (Yoon and Yordan, 1991). The particle hydrophobicity can be characterized by the induction time (Ofori et al., 2014; Wang and Tao, 2019). The variation of induction time (t_i) as a function of gas velocities at different feed velocities are shown in Fig. 6.8. It is noticed that the t_i decreases as the gas velocities increases while it is increased with the feed velocities. The increase in the gas velocity increases the turbulence, as a

result, the rate of rupturing of thin-film between the gas bubble and particle decreases, therefore, the induction time decreases. The increase in the feed velocity reduces the residence time of slurry in the column, as a result, contact time decreases, while the attachment time increases. The reduction in slurry residence time in the column decreases the rate of breakage of the thin film between the particle and the gas bubble. Therefore the induction time increases. Thin film draining time account for 76 – 94% of induction time and influenced by the force acting on it (Drelich et al., 1997; Schulze et al., 2001; Wang et al., 2005). The force acting on the thin-film is Reynolds number. Induction time will be shorter when the energy barrier between particle and gas bubble will be overcome easily by hydrodynamic forces (Feng and Aldrich, 2001).

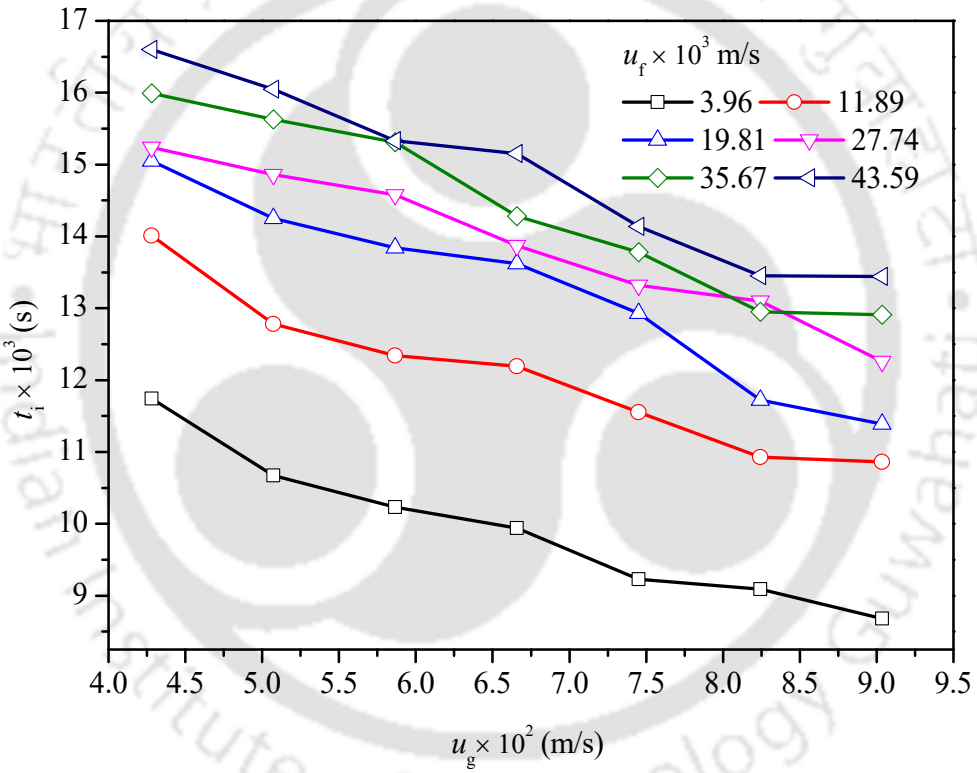

Fig. 6.8. Effect of gas and feed velocities on induction time (t_i).

In the present study, a correlation is developed in terms of operating and physical properties of the system for the interpretation of induction time. Induction time is correlated as follows:

$$t_i = \frac{\lambda}{K}\left(\mathrm{Re}_g\right)^{\phi}\left(\mathrm{Re}_f\right)^{\gamma} \tag{6.36}$$

The values of coefficient (λ) and exponents (ϕ and γ) in Eq. (6.36) is calculated after doing the regression analysis on experimental values. The proposed correlation is expressed as follows:

$$t_i = \frac{1.95\times10^{-4}}{K}\left(\mathrm{Re}_g\right)^{-0.160}\left(\mathrm{Re}_f\right)^{0.160} \tag{6.37}$$

where Re_g (= ($\rho_g \times u_g \times d_c$)/ μ_{air}) and Re_f (= ($\rho_f \times u_f \times d_c$)/ μ_{slurry}) denote the gas and feed Reynolds number. The range of parameters of Eq. (6.37) are $145.180 \le \mathrm{Re}_g \le 306493$; $249.107 \le \mathrm{Re}_f \le 2740.177$. The proposed correlation is suitable to interpret the experimental induction time within the error range of ± 9.27% and absolute average relative error (AARE) of 16.44%. The correlation coefficient and standard error of proposed correlation, Eq. (6.37) is 0.93, and 0.062, respectively. The parity of experimental and predicted induction time is shown in Fig. 6.9.

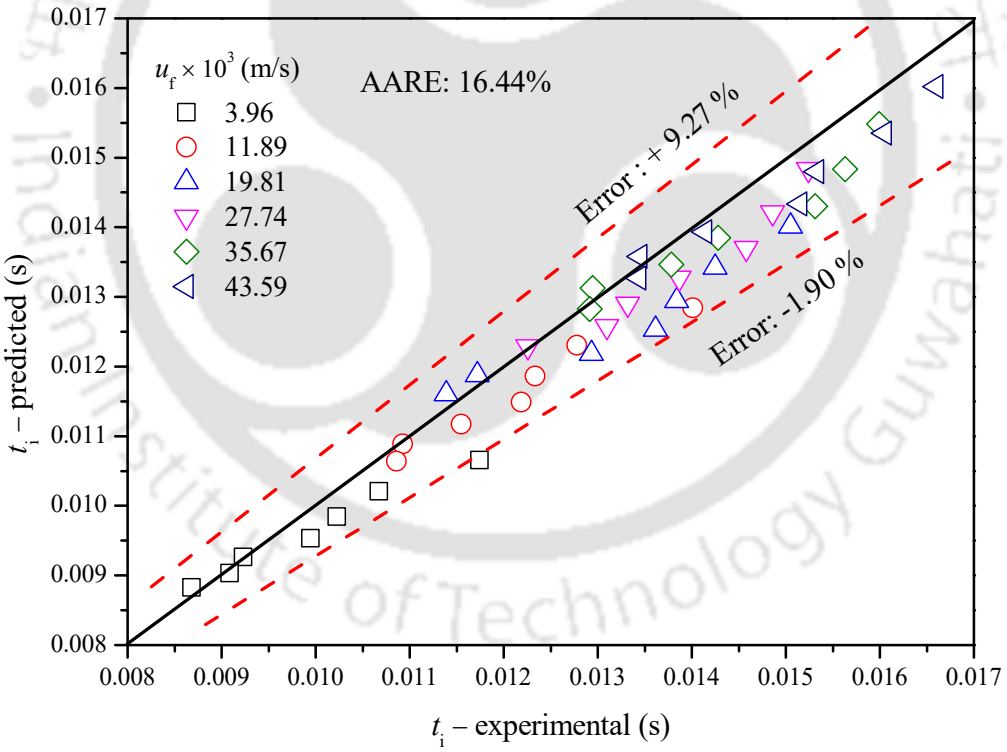

Fig. 6.9. Parity of experimental and predicted induction time.

6.5. Conclusion

Flotation of coal particles was carried out in the counter-current microstructured column using diesel oil and MIBC as a collector and frother, respectively. Production of clean coal can be improved by optimizing the operating and process variables. The performance of the flotation was assessed in terms of flotation parameters such as yield, the ash content in concentrate, combustible recovery, flotation rate constant, and efficiency index. The effect of gas and feed velocities are investigated on the flotation performance parameters. The extent of combustible recovery, ash removal, and efficiency index depends on the selection of optimized collector and surfactant concentration and operating variables such as the gas and feed velocity. The optimization of collector and surfactant doses was done based on the efficiency index at the fixed gas and feed velocity. The increase in the gas velocity improves the yield and combustible recovery, while it decreases with an increase in the feed velocity. The ash content of the concentrate increases as the gas velocity increases, whereas the ash content reduces with the feed velocity. The maximum efficiency index of 47.70% with 91.88% combustible recovery and 12.53% ash content is observed at 0.020 m/s feed velocity and 0.082 m/s gas velocity. Induction time is also enunciated using the phenomenological kinetic model based on the consecutive sub-processes compromising of the bubble-particle collision, attachment, and detachment. The results showed shorter induction time and higher rate constant at higher particle recovery. In addition, correlation is also developed for induction time in terms of the gas and feed Reynolds number.

Chapter 7

Overall Conclusion, Limitation, and Future Recommendation

This chapter provides the overall conclusions, limitations, and future recommendations based on the present research in the three-phase microstructured column.

7.1. Overall conclusion

- The experimental investigation of the gas holdup characteristics in a three-phase counter-current microstructured column is carried out with and without the presence of a surfactant.
- The result shows that the gas holdup is highly dependent on the operating variables and the particle concentration, but only to a small extent on the size of the particles.
- The maximum gas holdup in the column is found to be 38.570% and 33.195% in the presence and absence of the surfactant, respectively.
- It has been found that increasing the concentration of particles reduces gas holdup. Moreover, increasing particle size and superficial gas velocity and superficial slurry velocity increases gas holdup. The effect of superficial gas velocity, superficial slurry velocity, and particles concentration on gas holdup is more pronounced compared to the particle size.
- The analysis of holdup characteristics by the slip velocity model enunciates two critical parameters (u_b and n), demonstrating that the ranges of the two parameters are higher in the three-phase without surfactant as compared to the three-phase with a surfactant. Higher values of the parameter 'n' in the absence of surfactant reflect that the rising bubbles are exposed to more interaction with the neighboring bubbles and surrounding fluids.
- Frictional pressure drop observed to increase with an increase in the superficial gas velocity, the particle concentration, and the bubble size, while it reduces by increasing the superficial slurry velocity and the average particle diameter, respectively. A reduction in the frictional pressure drop was about 34.46% when the superficial slurry velocity increases from 0.018 to 0.057 m/s and an increase was approximately 35.38% when the superficial gas velocity increases from 0.01 to 0.075 m/s (at d_p = 65.29 μm and w_s = 3.0 wt.%). The addition of the surfactant reduces the frictional pressure drop as compared to that of the system without surfactant.

- A considerable change of approximately 15.04% (without surfactant) was noticed in the interfacial shear stress as the particle concentration varied from 0.5 to 3.0 wt.%, but this change is insignificant and reduced to 1.61% in the presence of a surfactant.
- The impact of the bubble size on the rate of energy loss because of a slip of the gas-slurry interface was lower in the case of the surfactant solution. The rate of energy loss because of the gas-slurry interface decreased to about 50.21% as the bubble size increased by 8.01% in the presence of the surfactant.
- The rate of energy loss due to the wetting of a thin liquid layer with the column wall increases to approximately 14% in the particle concentration range of w_s = 0.5 – 3.0 wt.% (at u_{sg} = 0.075 m/s without surfactant), and the increase is less than 1% in the presence of the surfactant.
- An increase in the dispersed phase velocity, the particle concentration led to a rise in Sauter mean bubble diameter, while, it is decreased with an increase in the continuous phase velocity and particle size.
- The aspect ratio of the bubble gradually decreases with an increase in Eötovos number. Here also, it has been observed that the sphericity of the bubbles reduces as the dispersed gas and continuous slurry velocity and particle concentration increase. In the presence of the large particle size, the bubble shape distortion is low compared to that of the small particle size.
- Bubble size distribution became wider and shifted towards the larger bubble diameter as the particle concentration, and dispersed gas velocity increased, whereas it was narrower and moved to a smaller bubble size with an increase in the continuous slurry velocity and particle size.
- Bubble size distribution in the two- and three-phase systems (with and without surfactant) satisfactorily follows the log-logistic distribution function.
- Experimental investigation of the degree of axial and transverse dispersion coefficient, dispersion due to circulation, dispersion due to bubble motion, slurry exchange parameter, and velocity distribution characteristics factor was carried out in the three-phase counter-current column in the presence of the surfactant.

- The axial (E_z) and transverse (E_w) dispersion coefficient increases with the superficial gas and slurry velocities and with the particle diameter, but decreases with the particle concentration.
- The effect of the slurry phase superficial velocity on the axial slurry dispersion coefficient $(E_z \propto u_{sl}^{0.848})$ is more pronounced compared to that of the gas-phase superficial $(E_z \propto u_{sg}^{0.240})$ velocity. Similarly, the effect of the superficial slurry velocity on the transverse dispersion coefficient $(E_w \propto u_{sl}^{0.632})$ is significant compared to that of the superficial gas velocity $(E_w \propto u_{sg}^{0.248})$.

- The axial slurry dispersion coefficient (E_z) is 1.40 – 9.60 times the dispersion coefficient due to circulation (E_c), while it is 1.28 – 3.61 times the dispersion due to bubble motion (D_b). The transverse slurry dispersion coefficient (E_w) was 1.03 – 1.39 times the axial slurry dispersion coefficient (E_z). The transverse dispersion coefficient (E_w) is more in the middle (in the transverse direction) of the column and decreases as it approaches the right section of the column.

- The effect of the superficial slurry velocity has a very strong effect on the dispersion due to circulation (E_c). The effect is 20.65 times the superficial gas velocity. The effect of the superficial gas velocity on the slurry exchange parameter is 6 times the superficial slurry velocity.
- The performance of the coal flotation was assessed in terms of flotation parameters such as yield, the ash content in concentrate, combustible recovery, flotation rate constant, and efficiency index.
- The ash content of the concentrate increases as the gas velocity increases, whereas the ash content reduces with the feed velocity. The maximum efficiency index of 47.70% with 91.88% combustible recovery and 12.53% ash content is observed at 0.020 m/s feed velocity and 0.082 m/s gas velocity.
- Induction time is enunciated using the phenomenological kinetic model based on the consecutive sub-processes compromising of the bubble-particle collision, attachment, and

detachment. The results showed shorter induction time and higher rate constant at higher particle recovery.

- Correlation is proposed for the interpretation of induction time in terms of the gas and feed Reynolds number.

7.2. Future recommendation

This section discusses the future recommendations based on the present research.

- There are mainly two types of flow regime occurs, namely homogeneous (bubbly flow) and heterogeneous (churn turbulent) region. If scale-up is initiated, the first design parameter that significantly changes is the flow regime. In the present research, most of the experiments have been carried out in the bubbly flow region. Thorough characterizations of the hydrodynamic characteristics need to be studied in the heterogeneous regime. Limitation in gas and liquid flow rate, surfactant concentration, particle concentration, and particle size restrict the analysis of the extent of design parameters. The limitations are also in the context of the size of the column, which causes an overflow of the system. Therefore, in the future, a large column needs to be designed following the Wilkinson scale-up criteria (Wilkinson et al., 1992).
- Volume expansion and phase isolation technique are one of the most efficient technique to determine the average or overall holdup characteristics of the system. However, this technique fails to measure the radial or transverse and axial holdup profile and holdup at a point in the column. Other techniques such as dynamic gas disengagement, differential pressure, conductometric method, and electrical resistance tomography technique can be used to enunciate the radial or transverse and axial gas holdup profile of holdup.
- Studies on frictional pressure drop and bubble-slurry interfacial shear stress in a heterogeneous flow regime are missing. Further, frictional pressure drop characteristics can be analyzed using the different models (i.e., Lockhart and Martinelli model, Kato model, Bankoff model, Davis model, Akoi, and Inoue model, Baroczy model, Chisholm model, etc.) available in the literature. A mechanistic model can be developed. The present developed mechanistic model could be modified and extended for the scale-up condition.
- Despite time-consuming, photographic technique is proved to be efficient for the measurement of bubble size in bubbly and dense bubbly flow. This technique measures the

bubble size near the wall in the presence of sufficient light source. Bubbles in the central region is cannot be measured due to a lack of proper visualization. The probe technique can be used to measure the bubble size in the central region of the column, and this technique is time-efficient. In the future, bubbles size & its distribution and bubble aspect ratio can be studied in the heterogeneous flow. Bubble size and gas holdup are useful parameters, which required to physically estimate the bubble interfacial area, however, this can be also done using the chemical technique, and the disparity between these two techniques can be compared. Probe technique can be used to estimate the bubble diameter at the higher particle concentration and a wider range of experimental conditions. Moreover, transport efficiency is better in the presence of a small bubble, i.e., micro or nanobubble. Micro and nanobubble can be achieved using the pressure dissolution technique. The oscillatory air supply can also produce small gas bubbles, which can be produced using the microfluidic device (fluidic oscillator). Oscillatory gas flow device is suitable to produce significantly small bubbles compared to the other gas bubbles generation techniques such as cavitation, plunging jets, sparging, agitation, electrolysis, etc.

- The present research is limited to the interpretation of axial and transverse slurry dispersion characteristics in a lab-scale column. Lab-scale column restricts wide variations of particle concentration, particle size, surfactant concentration, superficial gas, and superficial slurry velocity. Therefore, it is recommended to study the mixing characteristics in the scaled-up column. The Wilkinson scale-up criteria (Wilkinson et al., 1992) can be followed for scale-up purposes. The presently developed mechanistic model for the determination of the intensity of dispersion based on the turbulence and circulation should be modified to use for the scaled-up column. The present work can be extended to measure the quality of mixing based on the information entropy theory.
- Optimization of collector and surfactant concentration is performed based on the combustible recovery and efficiency index during the flotation of coal particles. Detail analysis can be also conducted in the presence of different collectors and surfactants. The phenomenological kinetic model was used to enunciate the induction time based on the best fitting of the experimental flotation rate constant. However, the induction can be measured experimentally with the aid of an induction timer setup and a high-speed camera.

In this work, induction time is measured using the sub-processes of flotation, such as collision, attachment, and stability efficiency. Several researchers have suggested sub-processes. Numerous investigators have proposed several suitable expressions for each sub-processes, therefore it is of paramount importance to analyze which set of expressions provides better results. The proposed two sets of expressions are: (I) generalized Sutherland equation (for collision), modified Dobby-Finch model (for attachment), and modified Schulze model (for stability), and (ii) Yoon–Luttrell collision model, Yoon–Luttrell attachment model, and modified Schulze stability model. Two sets of equations can be used to identify the suitable combination and better interpretation of induction time.

- Studied design parameters can be further continued using the computational fluid dynamics (CFD) for the bubbly and heterogeneous flow conditions at the wider variation of operating and physical properties of the system.

Nomenclature

Chapter 2

AARE	Absolute average relative error (%)
A_c	Column cross-sectional area (m^2)
c_s	Particle concentration (kg/m^3)
c_f	Surfactant concentration (ppm)
d_p	Particle diameter (m)
d_o	Pore diameter of sparger (mm)
d_n	Number of pores in sparger (–)
d_{be}	Equivalent column diameter (m)
d_c	Column diameter (m)
g	Acceleration due to gravity (m/s^2)
h_c	Column height (m)
h_l	Initial liquid height (m)
h_m	Gas-slurry or gas-liquid mixture height (m)
m_s	Mass of particle (kg)
P	Pressure (MPa)
STDEV	Standard deviation (–)
s	Sample size (–)
T	Temperature (K)
u_{sg}	Superficial gas velocity (m/s)
u_{sl}	Superficial slurry velocity (m/s)

u_l	Superficial liquid velocity (m/s)
u_s	Slip velocity (m/s)
u_b	Bubble rise velocity (m/s)
U	Standard uncertainties (–)
U_r	Relative uncertainties (%)
w_s	Particle concentration (wt.%)
$\bar{x}$	Mean of experimental quantities

Greek letters

μ_{eff}	Effective viscosity of slurry (Pa.s)
μ_l	Liquid viscosity (Pa.s)
μ_{sl}	Slurry viscosity (Pa.s)
σ_{sl}	Slurry surface tension (N/m)
ρ_m	Slurry density (kg/m^3)
ρ_g	Gas density (kg/m^3)
ρ_l	Liquid density (kg/m^3)
ρ_s	Particle density (kg/m^3)
ρ_{sl}	Slurry density (kg/m^3)
α_g	Gas holdup (–)
$\alpha_{g,\ slip}$	Gas holdup as per slip velocity model (–)
α_l	Liquid holdup (–)
α_s	Particle holdup (–)

Chapter 3

A_c	Column cross-sectional area (m^2)
c_d	Drag coefficient (–)
c_f	Surfactant concentration (ppm)
c_s	Particle concentration (kg/m^3)
c_v	Particle concentration (volume %)
d	Depth of column (m)
d_p	Average particle diameter (μm)
d_{32}	Sauter mean bubble diameter (m)
d_{be}	Equivalent column diameter (m)
E_g	Rate of frictional energy dissipation due to gas flow (Nm/s)
E_{sl}	Rate of frictional energy dissipation due to slurry flow (Nm/s)
E_{slip}	Rate of energy dissipation due to slip of gas-slurry interface (Nm/s)
E_b	Rate of energy dissipation due to bubble formation (Nm/s)
E_w	Rate of energy dissipation due to wetting of solid wall (Nm/s)
f_{sl0}	Friction factor due to slurry flow (–)
f_{fg0}	Friction factor due to gas flow (–)
f_T	Three-phase effective friction factor (–)
g	Acceleration due to gravity (m/s^2)
G	Gas mass flux (kg/m^2s)
h	Length of the column (m)
h_m	Gas-liquid-solid mixture height (m)
L_s	Slurry mass flux (kg/m^2s)
m_s	Mass of particle (kg)
Mo	Morton number (–)
N_b	Rate of bubble formation (1/s)
N	Total number of data points (–)
ΔP_f	Frictional pressure drop (bar (g))
ΔP_h	Hydrostatic pressure drop (bar (g))

ΔP_a	Acceleration pressure drop (bar (g))
ΔP_T	Total pressure drop (bar (g))
ΔP_{fsl}	Frictional pressure drop due to slurry flow (bar (g))
ΔP_{fsl0}	Frictional pressure drop due to slurry flow (bar (g))
ΔP_{fg0}	Frictional pressure drop due to gas flow (bar (g))
Δp_{fg}	Frictional pressure drop due to gas flow (bar (g))
ΔP_{FD}	Pressured drop due to phase interaction (bar (g))
Q_m	Gas-slurry mixture flow rate (m^3/s)
Re_b	Bubble Reynolds number (–)
St	Stokes number (–)
$STDEV$	Standard deviation (–)
u_{sg}	Superficial gas velocity (m/s)
u_{sl}	Superficial slurry velocity (m/s)
u_l	Superficial liquid velocity (m/s)
u_s	Slip velocity (m/s)
U	Standard uncertainties (–)
U_r	Relative uncertainties (%)
w	Width of the column (m)
w_s	Particle concentration (wt.%)
$\bar{x}$	Mean of experimental quantities
x_i	Each of the values of the data (–)
ΔZ	Distance between the two pressure port (m)

Greek Letter

τ_i	Bubble-slurry interfacial shear stress (N/m^2)
τ_b	Bubble response time (s)
τ_k	Kolmogorov time scale (s)

μ_{eff}	Effective viscosity of slurry (Pa.s)
μ_l	Liquid viscosity (Pa.s)
μ_{sl}	Slurry viscosity (Pa.s)
σ_{sl}	Slurry surface tension (N/m)
ρ_m	Slurry density (kg/m^3)
ρ_g	Gas density (kg/m^3)
ρ_l	Liquid density (kg/m^3)
ρ_s	Particle density (kg/m^3)
ρ_{sl}	Slurry density (kg/m^3)
α_g	Gas holdup (–)
α_l	Liquid holdup (–)
α_s	Particle holdup (–)
α_{sl}	Parameter equal to ($\alpha'_{sl}\alpha''_{sl}$) (–)
α'_{sl}	Parameter equal to (f_{slg}/f_{sl0}) (–)
β_g	Parameter equal to ($\alpha'_g\alpha''_g$) (–)

Chapter 4

AARE	Absolute average relative error $\left(\frac{1}{n}\sum_{i=1}^{n}\frac{\lvert\text{Pre}-\text{Exp}\rvert}{\text{Exp}}\times 100\right)(\%)$
AR	Aspect ratio (–)
A_c	Column cross-sectional area (m^2)
c_f	Surfactant concentration (ppm)
d	Depth of the rectangular column (m)
d_p	Particle diameter (μm)
d_{pore}	Pore diameter (mm)

d_{32}	Sauter mean bubble diameter (mm)
d_{be}	Equivalent column diameter (m)
d_c	Column diameter (m)
d_{eq}	Equivalent bubble diameter (mm)
d_b	Bubble diameter (mm)
$d_{b,\,max}$	Major length of bubble (mm)
$d_{b,\,min}$	Minor length of bubble (mm)
$F(d_b)$	Bubble distribution function (–)
g	Acceleration due to gravity (m/s^2)
h_m	Gas-slurry mixture height (m)
L_c	Length of the column (m)
$M_{Position}$	Measurement position (m)
m_s	Mass of Particle (kg)
n_i	Number of bubbles with diameter d_{bi} (–)
n_c	Number of bins (–)
P	Pressure (MPa)
Q_{sl}	Slurry flow rate (l/s)
RF	Relative frequency (%)
r/R	Radial position (–)
s	Sample size (–)
T	Temperature (K)
u_{sg}	Dispersed gas velocity (m/s)

u_{sl}	Continuous slurry velocity (m/s)
u_l	Superficial liquid velocity (m/s)
u_b	Bubble rise velocity (m/s)
w	Width of the rectangular column (m)
w_s	Particle concentration (wt.%)

Non-dimensional number

Eo	Eötovos number $\left(\frac{g(\rho_l-\rho_g)d_b^2}{\sigma_l}\right)$ (–)
Mo	Morton number $\left(\frac{g(\rho_l-\rho_g)\mu_l^4}{\rho_l^2\sigma_l^3}\right)$ (–)
Re	Reynolds number $\left(\frac{\rho_l u_t d_b}{\mu_l}\right)$ (–)

Greek letters

ϕ	Aspect ratio (–)
μ_{eff}	Effective viscosity of slurry (kg/ms)
μ_l	Liquid viscosity (kg/ms)
μ_{sl}	Slurry viscosity (kg/ms)
σ_{sl}	Slurry surface tension (N/m)
σ_l	Liquid surface tension (N/m)
ρ_m	Mixture density (kg/m^3)
ρ_g	Gas density (kg/m^3)
ρ_l	Liquid density (kg/m^3)

ρ_p	Particle density (kg/m^3)
ρ_{sl}	Slurry density (kg/m^3)
α	Bubble shape parameter (–)
β	Scale parameter (–)
α_l	Liquid holdup (–)
α_s	Particle holdup (–)
λ	Ratio between the bubble and column diameter (–)

Chapter 5

a	Slope of Eq. (5.13) (kgm^{-3}.cm ms^{-1})
A_c	Column cross-sectional area (m^2)
AARE	Absolute average relative error (–)
A^u	Area of up flow region (m^2)
A^d	Area of downflow region (m^2)
Bo	Bodenstein number (–)
C	Tracer concentration (kg/m^3)
C_0	Initial Tracer concentration (kg/m^3)
$C(t_i)$	Tracer concentration of the collected sample at time t_i second (kg/m^3)
C^u	Tracer concentration in up flow region (kg/m^3)
C^d	Tracer concentration in down flow region (kg/m^3)
D_b	Dispersion coefficient of bubble motion (m^2/s)
d_{32}	Sauter mean bubble diameter (m)

d_p	Particle size (μm)
d_c	Column diameter (m)
E_z	Axial dispersion coefficient (m^2/s)
E_t	Dispersion coefficient due to turbulence (m^2/s)
E_c	Dispersion coefficient due to circulation (m^2/s)
E_w	Transverse dispersion coefficient (m^2/s)
E^u	Dispersion coefficient in up flow region (m^2/s)
E^d	Dispersion coefficient in down flow region (m^2/s)
g	Acceleration due to gravity (m/s^2)
k	Velocity distribution Characteristic factor (-)
K	Conductivity of solution (mS/cm)
K_0	Conductivity of tap water (mS/cm)
h_m	Gas-slurry mixture height (m)
m_s	Mass of the Particle (kg)
N	Total number of variables (-)
Pe	Peclet number (-)
S	Circumference between up flow and down flow region (m)
t	Time (s)
Δt	Time interval of conductivity measurement (s)
t_m	Mean residence time (s)
u_o	Maximum velocity at the column axis (m/s)

u_{sl}	Superficial slurry velocity (m/s)
u_{sg}	Superficial gas velocity (m/s)
u^{u}	Velocity in up flow region (m/s)
u^{d}	Velocity in down flow region (m/s)
w_s	Particle concentration (wt.%)
w	Probe distance from left side of the column (m)
z	Distance of the probe from the tracer inlet (m)
Z	Dimensionless distance of a probe from tracer inlet (-)
σ_{sl}	Surface tension of slurry (N/m)
θ	Dimensionless time (–)
Ψ	Dimensionless concentration, C/C_0 (–)
μ_{eff}	Effective viscosity of slurry (kg/m.s)
μ_l	Liquid viscosity (kg/m.s)
α_s	Particle volume fraction (–)
α_g	Gas volume fraction (–)
α_l	Liquid volume fraction (–)
σ_{sl}	Slurry surface tension (N/m)
ρ_m	Mixture density (kg/m^3)
ρ_{sl}	Slurry density (kg/m^3)
ρ_s	Particle density (kg/m^3)
ρ_g	Gas density (kg/m^3)
ρ_l	Liquid density (kg/m^3)

t_m	Mean residence time (s)
λ	Slurry exchange parameter (–)
δ	Parameter in Eq. (5.25) (–)
σ^2	Variance (–)
σ_θ^2	Normalized variance or dimensionless variance function (–)

Chapter 6

AR	Ash rejection (%)
A_c	Ash content in concentrate (%)
a_c	Cross-sectional area of column (m^2)
A_f	Ash content in feed (%)
Bo	Bond number (–)
CR	Combustible recovery (%)
C	Concentration of the floatable mineral (kg/m^3)
C_0	Initial concentration mineral (kg/m^3)
C_∞	Concentration of mineral remaining in the pulp after prolonged floatation (kg/m^3)
d_p	Particle size (μm)
d_b	Equivalent bubble diameter (m)
d_{32}	Sauter mean bubble diameter (m)
d_c	Column diameter (m)
E_c	Particle-bubble collision efficiency (–)
E_a	Particle-bubble attachment efficiency (–)
E_s	Particle-bubble stablity efficiency (–)
EI	Efficiency index (%)
E_c^{GSE}	Generalized Sutherland collision efficiency (–)
E_c^{SU}	Sutherland collision efficiency (–)

f	Constant in Eq. (6.30) (–)
g	Gravitational constant (m/s^2)
h_m	Gas-slurry dispersion height (m)
K	Rate constant (1/s)
k_1, k_2	Constant in Eq. (6.2) (–)
K_3	Parameter in Eq. (6.25) (–)
k_{st}	Particle stokes number (–)
L	Flow length scale (m)
m_s	Mass of Particle (kg)
M_c	Mass of concentrate (gm)
M_f	Mass of feed (gm)
M	Mass of floatable mineral (gm)
N	Rate of order (–)
N_P	Number of particles (–)
N_b	Number of bubbles per unit volume (1/m^3)
R	Recovery (%)
Re_g	Gas Reynolds number (–)
Re_f	Feed Reynolds number (–)
R_∞	Ultimate recovery (%)
t_i	Induction time (s)
t	Time (s)
u_f	Feed velocity (m/s)
u_g	Gas velocity (m/s)
U_c	Circulation velocity (m/s)
u_b	Bubble rise velocity (m/s)

u_p	Particle velocity (m/s)
V	Volume of pulp (kg/m^3)
v_b	root mean square velocity of bubble relative to the turbulent fluid velocity (m/s)
v_p	root mean square velocity of particles relative to the turbulent fluid velocity (m/s)
w_s	Particle concentration (wt.%)
Z_{pb}	Particle-bubble collision frequency (–)

Greek letter

ρ_p	Particle density (kg/m^3)
ρ_f	Fluid density (kg/m^3)
ε	Dispersion rate of turbulent kinetic energy per unit mass (m^2/s^3)
ν	Kinematic viscosity of fluid (m^2/s)
α_g	Gas holdup (–)
β	Parameter in Eq. (6.26) (–)
θ_t	Maximum possible collision angle ()
θ	Contact angle (radian)
θ_a	Adhesion angle (radian)
μ_{sl}	Slurry viscosity (kg/m.s)
μ_l	Liquid viscosity (kg/m.s)
σ_{sl}	Slurry surface tension (N/m)
α_g	Gas holdup (–)
α_s	Particle holdup (–)

Appendix A

Uncertainty analysis

The experiments were repeated three times for each experimental condition. The mean of the experimental values are calculated as per the given expression ($\bar{x}$)

$$\bar{x} = \frac{1}{N}\sum_{i=1}^{N} x_i \tag{A1}$$

where ($\bar{x}$) refers to the mean of the data points. The standard deviation (*STDEV*) is evaluated as

$$STDEV = \sqrt{\frac{\sum_{1}^{N}(x_i - \bar{x})^2}{N-1}} \tag{A2}$$

where x_i and N refer the i^{th} element of variables and the total number of variables, respectively. The expression for evaluation of standard uncertainty (U) can be given as

$$U = \frac{STDEV}{\sqrt{N}} \tag{A3}$$

The relative uncertainty (U_r) of the repeated experimental data points is determined by

$$U_r = \frac{U}{\bar{x}} \times 100\,\% \tag{A4}$$

Appendix B

Calculation Procedure for Typical Multiple Regression

For Eq. (2.11)

The regression equation is

$$\alpha_g = c_1 u_{sg}^{\ b_1}, u_{sl}^{\ b_2}, \sigma_{sl}^{\ b_3}, \rho_{sl}^{\ b_4}, d_p^{\ b_5}, d_c^{b_6}, g^{b7} \quad \text{(B1)}$$

Taking logarithm on both sides of Eq. (B1), one get

$$\begin{aligned} Log(\alpha_g) &= Log(c_1) + b_1 Log(u_{sg}) + b_2 Log(u_{sl}) \\ &+ b_3 Log(\sigma_{sl}) + b_4 Log(\rho_{sl}) + b_5 Log(d_p) + b_6 Log(d_c) + b_7 Log(g) \end{aligned} \quad \text{(B2)}$$

The Eq. (B2) can be written as

$$Y = b_0 + b_1 X_1 + b_2 X_2 + b_3 X_3 + b_4 X_4 + b_5 X_5 + b_6 X_6 + b_7 X_7 + e \quad \text{(B3)}$$

where Y = Log (α_g), X_1=Log (u_{sg}), X_2 = Log(u_{sl}), X_3 = Log(σ_{sl}), X_4 = Log(ρ_{sl}), X_5 = Log(d_p), X_6 = Log(d_c), X_7 = Log(g) and b_0 = Log (c_1). Here, e is the error term, which has to be minimized to estimate the regression model as

$$\hat{Y} = b_0 + b_1 X_1 + b_2 X_2 + b_3 X_3 + b_4 X_4 + b_5 X_5 + b_6 X_6 + b_7 X_7 \quad \text{(B4)}$$

$\hat{Y}$ is the predicted value of Y

The intercept b_0 and coefficients b_1, b_2, b_3, b_4, b_5, b_6, and b_7 have been estimated by multiple regression analysis by "Data Analysis Tool" of Software "Microsoft Excel".

The software gives the outputs based on the following calculation

The equation A3 can be written as matrix form for n (here n = 557) observations and k (here k = 7) variables as

$$\begin{bmatrix} Y_1 \\ Y_2 \\ : \\ : \\ Y_n \end{bmatrix} = \begin{bmatrix} 1 & X_{11} & X_{12} & .. .. & X_{1k} \\ 1 & X_{21} & X_{22} & .. .. & X_{2k} \\ : & : & : & .. .. & : \\ : & : & : & .. .. & : \\ 1 & X_{n1} & X_{n2} & .. .. & X_{nk} \end{bmatrix} \times \begin{bmatrix} b_0 \\ b_1 \\ : \\ : \\ b_k \end{bmatrix} + \begin{bmatrix} e_1 \\ e_2 \\ : \\ : \\ e_n \end{bmatrix} \quad \text{(B5)}$$

$\Rightarrow$ **Y = X × B + e**

Regression Statistics

		Explanation
Multiple R	0.993	R = square root of R^2
R Square	0.987	R^2 = coefficient of determination
Adjusted R Square	0.987	Adjusted R^2 used if more than one X variable
Standard Error	0.099	This is the estimate of the st. dev. of the error *e*
Observations	557	Number of observations used in the regression (n)

Analysis of Variance

	Degrees Of freedom	Sum of Square	Mean Sum of Square	F-stat
Regression	2	407.614	203.807	20629.48
Residual	543	5.364	0.009	
Total	545	412.978		

Where

$$\text{Regression Sum of Square} = B'X'Y - n\overline{Y}^2$$

$$\text{Total Sum of Square} = Y'Y - n\overline{Y}^2$$

Residual Sum of Square = Total Sum of Square – Regression Sum of Square

$$R^2 = \frac{\text{Regression Sum of Square}}{\text{Residual Sum of Square}}$$

$$F - stat = \frac{R^2/(k-1)}{(1-R^2)/(n-k)}$$

$$Adjusted\, R^2 = 1-(1-R^2)\frac{n-1}{(n-k)}$$

$$\text{Standard Error} = \sqrt{\frac{\text{Residual Sum of Square}}{n-k}}$$

$$Y' = [Y_1 \quad Y_2 \quad \ldots\ldots\ldots Y_n]$$

$$B' = [B_0 \quad B_1 \quad \ldots\ldots\ldots B_k]$$

The F-stat gives the overall F-test of null hypothesis *H0*: $b_i = 0$. The F-stat gives the associated Probability-value. Since it is greater than 0.05 at the 5% significance level, we do not reject null hypothesis for the goodness of fit.

REFERENCES

Abdulrahman, M. W., 2016. Experimental studies of gas holdup in a slurry bubble column at high gas temperature of a helium− water− alumina system. Chemical Engineering Research and Design 109, 486-494.

Abdulrazzaq, B. S., 2015. Gas holdup and axial liquid dispersion in three phase bubble columns. Journal of Engineering and Sustainable Development 19, 132-146.

Acharya, A., Mashelkar, R. A., Ulbrecht, J., 1977. Mechanics of bubble motion and deformation in non-Newtonian media. Chemical Engineering Science 32, 863-872.

Ahmadi, G., Zhang, X., 2005. Three-phase liquid-gas-solid flows in a bubble column, ASME Fluids Engineering Division Summer Meeting, June 19–23. American Society of Mechanical Engineers Digital Collection, Houston, Texas, USA, pp. 761-765.

Akagawa, K., Takenaka, N., Fuji, T., Minamiyama, T., Takagi, N., Koike, T., Nishizaki, K., 1989. Experimental study on gas–non-Newtonian liquid two-phase flow in a vertical tube, Proceedings of the 2nd International Symposium on Multiphase Flow and Heat Transfer, pp. 48-57.

Akita, K., Yoshida, F., 1973. Gas holdup and volumetric mass transfer coefficient in bubble columns. Effects of liquid properties. Industrial & Engineering Chemistry Process Design and Development 12, 76-80.

Al-Oufi, F. M., 2011. An investigation of gas void fraction and transition conditions for two-phase flow in an annular gap bubble column. © Fahd Aloufi.

Albijanic, B., Ozdemir, O., Nguyen, A. V., Bradshaw, D., 2010. A review of induction and attachment times of wetting thin films between air bubbles and particles and its relevance in the separation of particles by flotation. Advances in Colloid and Interface Science 159, 1-21.

Albijanic, B., Subasinghe, N., Park, C. H., 2015. Flotation kinetic models for fixed and variable pulp chemical conditions. Minerals Engineering 78, 66-68.

Aliyu, M. A., Lao, L., Yeung, H., Almabrok, A. A., 2015. A comparative analysis of interfacial friction factor correlation for adiabatic co-current gas-liquid annular two-phase flow in large diameter pipes, Proc., World Congress on Mechanical, Chemical and Material Engineering, Barcelona, Spain, July, Barcelona, Spain, pp. 20-21.

Alvarez-Silva, M., Vinnett, L., Langlois, R., Waters, K. E., 2016. A comparison of the predictability of batch flotation kinetic models. Minerals Engineering 99, 142-150.

Anastasiou, A. D., Kazakis, N. A., Mouza, A. A., Paras, S. V., 2010. Effect of organic surfactant additives on gas holdup in the pseudo-homogeneous regime in bubble columns equipped with fine pore sparger. Chemical Engineering Science 65, 5872-5880.

Ansari, M., Turney, D. E., Yakobov, R., Kalaga, D. V., Kleinbart, S., Banerjee, S., Joshi, J. B., 2018. Chemical hydrodynamics of a downward microbubble flow for intensification of gas-fed bioreactors. AIChE Journal 64, 1399-1411.

Aoyama, S., Hayashi, K., Hosokawa, S., Tomiyama, A., 2016. Shapes of ellipsoidal bubbles in infinite stagnant liquids. International Journal of Multiphase Flow 79, 23-30.

Aoyama, S., Hayashi, K., Hosokawa, S., Tomiyama, A., 2018. Shapes of single bubbles in infinite stagnant liquids contaminated with surfactant. Experimental Thermal and Fluid Science 96, 460-469.

Aris, R., 1956. On the dispersion of a solute in a fluid flowing through a tube. Proceedings of the Royal Society of London. Series A. Mathematical and Physical Sciences 235, 67-77.

Ata, S., Ahmed, N., Jameson, G. J., 2003. A study of bubble coalescence in flotation froths. International journal of mineral processing 72, 255-266.

Auton, T. R., 1987. The lift force on a spherical body in a rotational flow. Journal of fluid Mechanics 183, 199-218.

Azad, M. A. K., Syeda, S. R., 2006. A numerical model for bubble size distribution in turbulent gas-liquid dispersion. Journal of Chemical Engineering 24, 25-34.

Azgomi, F., Gomez, C. O., Finch, J. A., 2007. Correspondence of gas holdup and bubble size in presence of different frothers. International journal of mineral processing 83, 1-11.

Babu, K. P., Patnaik, K. R., Sunder, R. S., 2018. Effects of operating Parameters on Recovery of non-floatable Coal by Column flotation. International Journal of Applied Engineering Research 13, 10462-10469.

Bahri, Z., Shafaei, S. Z., Karamoozian, M., 2013. Investigation of effective parameters on the gas holdup in column flotation of a coal tailing sample. International Journal Of Coal Preparation And Utilization 33, 47-58.

Baird, M. H. I., Rice, R. G., 1975. Axial dispersion in large unbaffled columns. The Chemical Engineering Journal 9, 171-174.

Bakshi, B. R., Zhong, H., Jiang, P., Fan, L. S., 1995. Analysis of flow in gas-liquid bubble-columns using multiresolution methods. Chemical engineering research & design 73, 608-614.

Banisi, S., Finch, J. A., Laplante, A. R., Weber, M. E., 1995a. Effect of solid particles on gas holdup in flotation columns—I. Measurement. Chemical Engineering Science 50, 2329-2334.

Banisi, S., Finch, J. A., Laplante, A. R., Weber, M. E., 1995b. Effect of solid particles on gas holdup in flotation columns—II. Investigation of mechanisms of gas holdup reduction in presence of solids. Chemical Engineering Science 50, 2335-2342.

Barghi, S., Prakash, A., Margaritis, A., Bergougnou, M. A., 2004. Flow regime identification in a slurry bubble column from gas holdup and pressure fluctuations analysis. The Canadian Journal of Chemical Engineering 82, 865-870.

Barma, S. D., 2019. Ultrasonic-assisted coal beneficiation: A review. Ultrasonics sonochemistry 50, 15-35.

Barma, S. D., Baskey, P. K., Biswal, S. K., 2018a. Chemical beneficiation of high-ash indian noncoking coal by alkali leaching under low-frequency ultrasonication. Energy & Fuels 32, 1309-1319.

Barma, S. D., Sathish, R., Baskey, P. K., 2018b. Ultrasonic-assisted cleaning of Indian low-grade coal for clean and sustainable energy. Journal of cleaner production 195, 1203-1213.

Bartrand, T. A., Farouk, B., Haas, C. N., 2009. Countercurrent gas/liquid flow and mixing: Implications for water disinfection. International Journal of Multiphase Flow 35, 171-184.

Basařová, P., Zawala, J., Zedníková, M., 2019. Interactions between a Small Bubble and a Greater Solid Particle during the Flotation Process. Mineral Processing and Extractive Metallurgy Review 40, 410-426.

Behkish, A., Lemoine, R., Sehabiague, L., Oukaci, R., Morsi, B. I., 2007. Gas holdup and bubble size behavior in a large-scale slurry bubble column reactor operating with an organic liquid under elevated pressures and temperatures. Chemical Engineering Journal 128, 69-84.

Besagni, G., Deen, N. G., 2019. Aspect ratio of bubbles in different liquid media: a novel correlation. Chemical Engineering Science, 115383.

Besagni, G., Di Pasquali, A., Gallazzini, L., Gottardi, E., Colombo, L. P. M., Inzoli, F., 2017a. The effect of aspect ratio in counter-current gas-liquid bubble columns: Experimental results and gas holdup correlations. International Journal of Multiphase Flow 94, 53-78.

Besagni, G., Guédon, G., Inzoli, F., 2014. Experimental investigation of counter current air-water flow in a large diameter vertical pipe with inners, Journal of Physics: Conference Series. IOP Publishing, p. 012024.

Besagni, G., Inzoli, F., 2016a. Bubble size distributions and shapes in annular gap bubble column. Experimental Thermal and Fluid Science 74, 27-48.

Besagni, G., Inzoli, F., 2016b. Comprehensive experimental investigation of counter-current bubble column hydrodynamics: Holdup, flow regime transition, bubble size distributions and local flow properties. Chemical Engineering Science 146, 259-290.

Besagni, G., Inzoli, F., 2017a. The effect of electrolyte concentration on counter-current gas–liquid bubble column fluid dynamics: Gas holdup, flow regime transition and bubble size distributions. Chemical Engineering Research and Design 118, 170-193.

Besagni, G., Inzoli, F., 2017b. The effect of liquid phase properties on bubble column fluid dynamics: Gas holdup, flow regime transition, bubble size distributions and shapes, interfacial areas and foaming phenomena. Chemical Engineering Science 170, 270-296.

Besagni, G., Inzoli, F., 2019. Bubble sizes and shapes in a counter-current bubble column with pure and binary liquid phases. Flow Measurement and Instrumentation 67, 55-82.

Besagni, G., Inzoli, F., De Guido, G., Pellegrini, L. A., 2017b. The dual effect of viscosity on bubble column hydrodynamics. Chemical Engineering Science 158, 509-538.

Besagni, G., Inzoli, F., Zieghenein, T., Lucas, D., 2019. Experimental study of liquid velocity profiles in large-scale bubble columns with particle tracking velocimetry, Journal of Physics: Conference Series. IOP Publishing, p. 012036.

Bhatia, B., Nigam, K. D. P., Auban, D., Hebrard, G., 2004. Effect of a new high porosity packing on hydrodynamics and mass transfer in bubble columns. Chemical engineering and processing: Process intensification 43, 1371-1380.

Bhunia, K., Kundu, G., Mukherjee, D., 2017. Gas holdup characteristics in a flotation column with different solids. Separation science and technology 52, 1298-1309.

Bińi, A. K., Duczmal, B., Machniewski, P., 2001. Hydrodynamics and ozone mass transfer in a tall bubble column. Chemical Engineering Science 56, 6233-6240.

Biria, S., 2013. Prediction of pressure drop in vertical air/water flow in the presence/absence of sodium dodecyl sulfate as a surfactant. University of Dayton.

Bloom, F., Heindel, T. J., 2002. On the structure of collision and detachment frequencies in flotation models. Chemical Engineering Science 57, 2467-2473.

Bozzano, G., Dente, M., 2001. Shape and terminal velocity of single bubble motion: a novel approach. Computers & Chemical Engineering 25, 571-576.

Bruce, H. K., 2003. Modeling of hindered-settling column separations. A PhD Thesis in Mineral Processing, The Pennsylvania State University, 11-13.

Buchholz, R., Zakrzewski, W., Schugerl, K., 1979. Techniques for determining the properties of bubbles in a bubble columns. Chemie Ingenieur Technik 51, 568-575.

Buwa, V. V., Ranade, V. V., 2003. Mixing in bubble column reactors: role of unsteady flow structures. The Canadian Journal of Chemical Engineering 81, 402-411.

Camarasa, E., Vial, C. H., Poncin, S., Wild, G., Midoux, N., Bouillard, J., 1999. Influence of coalescence behaviour of the liquid and of gas sparging on hydrodynamics and bubble characteristics in a bubble column. Chemical engineering and processing: Process intensification 38, 329-344.

Cao, C., Dong, S., Geng, Q., Guo, Q., 2008. Hydrodynamics and axial dispersion in a gas−liquid−(solid) EL-ALR with different sparger designs. Industrial & Engineering Chemistry Research 47, 4008-4017.

Chandrakar, S. K., Biswas, M. N., Mitra, A. K., 1985. Two-phase gas non-Newtonian liquid flow in vertical pipe with improved gas dispersion, Second International Conference on Multiphase Flow, London, pp. 197-213.

Chang, G., Xing, Y., Zhang, F., Yang, Z., Liu, X., Gui, X., 2020. Effect of Nanobubbles on the Flotation Performance of Oxidized

Coal. ACS Omega 5, 20283-20290.

Chang, L., Yang, J., Zhao, Y., Liu, H., Zhang, J., Zheng, C., 2019. Behavior and fate of As, Se, and Cd in an ultra-low emission coal-fired power plant. Journal of cleaner production 209, 722-730.

Charton, S., Thebault, M., Winn, S., Roussel, H., Lamadie, F., Hlawitschka, M. W., Korb, C., Bart, H.-J., 2017. Hydrodynamics of pulsed columns: The effect of new parameters affecting the pressure drop. Chemical Engineering Research and Design 125, 483-493.

Chaumat, H., Billet-Duquenne, A. M., Augier, F., Mathieu, C., Delmas, H., 2005. Mass transfer in bubble column for industrial conditions—effects of organic medium, gas and liquid flow rates and column design. Chemical Engineering Science 60, 5930-5936.

Cheng, G., Ma, L. Q., Gui, X. H., Liu, J. T., Wang, Y. T., 2013. Study on kinetic modelling for fine coal flotation. International Journal Of Coal Preparation And Utilization 33, 12-25.

Cheng, T.-W., Holtham, P. N., 1995. The particle detachment process in flotation. Minerals Engineering 8, 883-891.

Chilekar, V. P., Warnier, M. J. F., Van Der Schaaf, J., Kuster, B. F. M., Schouten, J. C., Van Ommen, J. R., 2005. Bubble size estimation in slurry bubble columns from pressure fluctuations. AIChE Journal 51, 1924-1937.

Chisti, M. Y., 1989. Airlift Bioreactors, Elsevier Applied Science. London and New York 1.

Chung, J. S., Yarim, G., Savasci, H., 1998. Shape effect of solids on pressure drop in a 2-phase vertically upward transport: Silica sands and spherical beads, The Eighth International Offshore and Polar Engineering Conference. International Society of Offshore and Polar Engineers.

Clift, R., Grace, J. R., Weber, M. E., 1978. Bubbles, Drops and Particles, Academic Press, New York.

Cruz, E. B., 1997. A comprehensive dynamic model of the column flotation unit operation. Virginia Polytechnic Institute and State University, USA.

Dai, Z., Dukhin, S., Fornasiero, D., Ralston, J., 1998. The inertial hydrodynamic interaction of particles and rising bubbles with mobile surfaces. Journal of Colloid and Interface Science 197, 275-292.

Dai, Z., Fornasiero, D., Ralston, J., 1999. Particle–bubble attachment in mineral flotation. Journal of Colloid and Interface Science 217, 70-76.

Danoucaras, A. N., Vianna, S. M., Nguyen, A. V., 2013. A modeling approach using back-calculated induction times to predict recoveries in flotation. International journal of mineral processing 124, 102-108.

Darton, R. C., Harrison, D., 1975. Gas and liquid hold-up in three-phase fluidisation. Chemical Engineering Science 30, 581-586.

Das, A., Sarkar, B., Ari, V., Roy, S., 2010. Efficient recovery of combustibles from coking coal fines. Mineral Processing & Extractive Metallurgy Review 31, 236-249.

de Andrade Lima, L. R. P., 2006. Liquid axial dispersion and holdup in column leaching. Minerals Engineering 19, 37-47.

De Guido, G., Pellegrini, L. A., 2017. Prediction of the gas hold-up in a large-diameter bubble column with liquid mixtures and electrolytes. Chemical Engineering Research and Design 124, 283-298.

Deckwer, W.-D., 1985. Grundlagen der Chemischen Technik, Reaktionstechnik in Blasensäulen. 1. Aufl., Salle und Sauerländer, Frankfurt/Main 21.

Deckwer, W.-D., 1992. Bubble Column Reactors. Wiley: Chichester, UK.

Deckwer, W.-D., Burckhart, R., Zoll, G., 1974. Mixing and mass transfer in tall bubble columns. Chemical Engineering Science 29, 2177-2188.

Deckwer, W., Graeser, U., Langemann, H., Serpemen, Y., 1973. Zones of different mixing in the liquid phase of bubble columns. Chemical Engineering Science 28, 1223-1225.

Derjaguin, B. V., Dukhin, S. S., 1993. Theory of flotation of small and medium-size particles. Progress in Surface Science 43, 241-266.

Descamps, M. N., Oliemans, R. V. A., Ooms, G., Mudde, R. F., 2008. Air–water flow in a vertical pipe: experimental study of air bubbles in the vicinity of the wall. Experiments in Fluids 45, 357-370.

Dobby, G. S., Finch, J. A., 1986. Flotation column scale-up and modelling. CIM Bulletin 79, 89-96.

Dobby, G. S., Finch, J. A., 1987. Particle size dependence in flotation derived from a fundamental model of the capture process. International journal of mineral processing 21, 241-260.

Dong, H., Wang, X., Liu, L., Zhang, X., Zhang, S., 2010. The rise and deformation of a single bubble in ionic liquids. Chemical Engineering Science 65, 3240-3248.

Drelich, J., Miller, J. D., Li, J. S., Wan, R. Y., 1997. Bubble attachment time measurements at a chalcopyrite surface using a high-speed video system, XX International Mineral Processing Congress, pp. 53-64.

Drzymala, J., 1994. Characterization of materials by Hallimond tube flotation. Part 2: maximum size of floating particles and contact angle. International journal of mineral processing 42, 153-167.

Drzymała, J., 2018. Mineral processing. Foundations of theory and practice of minerallurgy 2nd ed. Ofic. Wyd. PWr, Wroclaw Poland.

Duan, J., Fornasiero, D., Ralston, J., 2003. Calculation of the flotation rate constant of chalcopyrite particles in an ore. International journal of mineral processing 72, 227-237.

Dukhin, S. S., Miller, R., Loglio, G., 1998. Physico-chemical hydrodynamics of rising bubble, Studies in Interface Science. Elsevier, pp. 367-432.

Dukhin, S. S., Rulev, N. N., 1977. Hydrodynamic interaction between a solid spherical-particle and a bubble in elementary act of flotation. COLLOID JOURNAL OF THE USSR 39, 231-236.

Einstein, A., 1906. Eine neue bestimmung der moleküldimensionen. Annalen der Physik 324, 289-306.

Eissa, S. H., Schügerl, K., 1975. Holdup and backmixing investigations in cocurrent and countercurrent bubble columns. Chemical Engineering Science 30, 1251-1256.

Ekambara, K., Dhotre, M. T., 2010. CFD simulation of bubble column. Nuclear Engineering and Design 240, 963-969.

Ekambara, K., Joshi, J. B., 2003. CFD simulation of mixing and dispersion in bubble columns. Chemical Engineering Research and Design 81, 987-1002.

El-Temtamy, S. A., El-Sharnoubi, Y. O., El-Halwagi, M. M., 1979. Liquid dispersion in gas—liquid fluidized beds: Part II: Axial and radial dispersion. The dispersed plug-flow model. The Chemical Engineering Journal 18, 161-168.

Fahad, M. K., Prakash, R., Majumder, S. K., Ghosh, P., 2019a. Frictional pressure drop in a flotation column: an experimental investigation in a continuous mode and its prediction by general model. Multiphase Science and Technology 31, 1-20.

Fahad, M. K., Prakash, R., Majumder, S. K., Ghosh, P., 2019b. Gas holdup in the gas-liquid-coal slurry flow in a flotation column in presence of surface active agent. Multiphase Science and Technology 31, 199-214.

Fahad, M. K., Prakash, R., Majumder, S. K., Ghosh, P., 2020. Dispersion characteristics in a gas-liquid-coal slurry flotation column and its analysis by the velocity distribution model. Journal of Dispersion Science and Technology.

Fan, L.-S., Hemminger, O., Yu, Z., Wang, F., 2007. Bubbles in nanofluids. Industrial & Engineering Chemistry Research 46, 4341-4346.

Fan, L.-S., Yang, G. Q., Lee, D. J., Tsuchiya, K., Luo, X., 1999. Some aspects of high-pressure phenomena of bubbles in liquids and liquid–solid suspensions. Chemical Engineering Science 54, 4681-4709.

Fan, L. S., Tsuchiya, K., 1990. Bubble Wake Dynamics in Liquid and Liquid-Solid Suspensions,. Butter-worth-Heinemann Series in Chemical Engineering, Stoneham, U.S.A.

Feng, D., Aldrich, C., 2001. Influence of pulp pulsation on the batch flotation of galena. Chemical Engineering Communications 186, 205-215.

Ferre, A. L., Shook, C. A., 1998. Coarse particle wall friction in vertical slurry flows. Particulate Science and Technology 16, 125-133.

Finch, J. A., Dobby, G. S., 1990. Column Flotation. Pergamon Press: Oxford, UK.

Finch, J. A., Xiao, J., Hardie, C., Gomez, C. O., 2000. Gas dispersion properties: bubble surface area flux and gas holdup. Minerals Engineering 13, 365-372.

Fontaine, A. A., Deutsch, S., Brungart, T. A., Petrie, H. L., Fenstermacker, M., 1999. Drag reduction by coupled systems: microbubble injection with homogeneous polymer and surfactant solutions. Experiments in Fluids 26, 397-403.

Forret, A., Schweitzer, J. M., Gauthier, T., Krishna, R., Schweich, D., 2006. Scale up of slurry bubble reactors. Oil & Gas Science and Technology-Revue d'IFP Energies nouvelles 61, 443-458.

Fujiwara, A., Minato, D., Hishida, K., 2004. Effect of bubble diameter on modification of turbulence in an upward pipe flow. International Journal of Heat and Fluid Flow 25, 481-488.

Fujiwara, H., 2007. Spectroscopic ellipsometry: principles and applications. John Wiley & Sons.

Fukano, T., Furukawa, T., 1998. Prediction of the effects of liquid viscosity on interfacial shear stress and frictional pressure drop in vertical upward gas–liquid annular flow. International Journal of Multiphase Flow 24, 587-603.

Fukuma, M., Muroyama, K., Yasunishi, A., 1987. Properties of bubble swarm in a slurry bubble column. Journal of chemical engineering of Japan 20, 28-33.

Gandhi, B., Prakash, A., Bergougnou, M., 1999a. Hydrodynamic behavior of slurry bubble column at high solids concentrations. Powder Technology 103, 80-94.

Gandhi, B., Prakash, A., Bergougnou, M. A., 1999b. Hydrodynamic behavior of slurry bubble column at high solids concentrations. Powder Technology 103, 80-94.

Gao, Y., Muzzio, F. J., Ierapetritou, M. G., 2012. A review of the residence time distribution (RTD) applications in solid unit operations. Powder Technology 228, 416-423.

Giusti, A., Lucci, F., Soldati, A., 2005. Influence of the lift force in direct numerical simulation of upward/downward turbulent channel flow laden with surfactant contaminated microbubbles. Chemical Engineering Science 60, 6176-6187.

Godfrey, J. C., Slater, M. J., 1991. Slip velocity relationships for liquid-liquid extraction columns. Transactions of the Institution of Chemical Engineers 69, 130-141.

Gomez, C. O., Cortes-Lopez, F., Finch, J. A., 2003. Industrial testing of a gas holdup sensor for flotation systems. Minerals Engineering 16, 493-501.

Gomez, C. O., Finch, J. A., 2007. Gas dispersion measurements in flotation cells. International journal of mineral processing 84, 51-58.

Gorain, B. K., Franzidis, J. P., Manlapig, E. V., 1997. Studies on impeller type, impeller speed and air flow rate in an industrial scale flotation cell. Part 4: Effect of bubble surface area flux on flotation performance. Minerals Engineering 10, 367-379.

Götz, M., Lefebvre, J., Mörs, F., Ortloff, F., Reimert, R., Bajohr, S., Kolb, T., 2017. Novel gas holdup correlation for slurry bubble column reactors operated in the homogeneous regime. Chemical Engineering Journal 308, 1209-1224.

Götz, M., Lefebvre, J., Mörs, F., Reimert, R., Graf, F., Kolb, T., 2016. Hydrodynamics of organic and ionic liquids in a slurry bubble column reactor operated at elevated temperatures. Chemical Engineering Journal 286, 348-360.

Grace, J. R., 1976. Shapes and velocities of single drops and bubbles moving freely through immiscible liquids. Chemical Engineering Research and Design 54, 167-173.

Grau, R. A., Heiskanen, K., 2005. Bubble size distribution in laboratory scale flotation cells. Minerals Engineering 18, 1164-1172.

Griffith, P., 1962. Two-phase flow in pipes. Special Summer Program, Massachusetts Institute of Technology, Cambridge, Massachusetts.

Guet, S., Luther, S., Ooms, G., 2005. Bubble shape and orientation determination with a four-point optical fibre probe. Experimental Thermal and Fluid Science 29, 803-812.

Guet, S., Ooms, G., Oliemans, R. V. A., Mudde, R. F., 2003. Bubble injector effect on the gaslift efficiency. AIChE Journal 49, 2242-2252.

Gui, X., Liu, J., Cao, Y., Cheng, G., Li, S., Wu, L., 2014. Flotation process design based on energy input and distribution. Fuel Processing Technology 120, 61-70.

Guin, M. M., Kato, H., Yamaguchi, H., Maeda, M., Miyanaga, M., 1996. Reduction of skin friction by microbubbles and its relation with near-wall bubble concentration in a channel. Journal of Marine Science and Technology 1, 241-254.

Gupta, R., Wanchoo, R. K., 2009. Motion of a single Newtonian liquid drop through quiescent immiscible visco-elastic liquid: shape and eccentricity. Journal of Fluids Engineering 131, 021301.

Hacifazlioglu, H., Sutcu, H., 2007. Optimization of some parameters in column flotation and a comparison of conventional cell and column cell in terms of flotation performance. Journal of the Chinese Institute of Chemical Engineers 38, 287-293.

Han, O.-H., Kim, M.-K., Kim, B.-G., Subasinghe, N., Park, C.-H., 2014. Fine coal beneficiation by column flotation. Fuel Processing Technology 126, 49-59.

Hanratty, T. J., Engen, J. M., 1957. Interaction between a turbulent air stream and a moving water surface. AIChE Journal 3, 299-304.

Hansen, G. M., 1985. Mie scattering as a technique for the sizing of air bubbles. Applied Optics 24, 3214-3220.

Harrison, M., 1952. An experimental study of single bubble cavitation noise. The Journal of the Acoustical Society of America 24, 776-782.

Hassanzadeh, A., Azizi, A., Kouachi, S., Karimi, M., Celik, M. S., 2019. Estimation of flotation rate constant and particle-bubble interactions considering key hydrodynamic parameters and their interrelations. Minerals Engineering 141, 105836.

Hassanzadeh, A., Firouzi, M., Albijanic, B., Celik, M. S., 2018. A review on determination of particle–bubble encounter using analytical, experimental and numerical methods. Minerals Engineering 122, 296-311.

Hatate, Y., Nomura, H., Fujita, T., Tajiri, S., Hidaka, N., Ikari, A., 1986. Gas holdup and pressure drop in three-phase vertical flows of gas-liquid-fine solid particles system. Journal of chemical engineering of Japan 19, 56-61.

He, J., Liu, C., Yao, Y., 2018. Flotation intensification of the coal slime using a new compound collector and the interaction mechanism between the reagent and coal surface. Powder Technology 325, 333-339.

Heindel, T. J., 2002. Bubble size in a cocurrent fiber slurry. Industrial & Engineering Chemistry Research 41, 632-641.

Hernandez-Alvarado, F., Kalaga, D. V., Banerjee, S., Kawaji, M., 2016. Comparison of gas hold-up profiles in co-current, counter-current and batch bubble column reactors measured using gamma densitometry and surface of revolution method, ASME 2016 Fluids Engineering Division Summer Meeting collocated with the ASME 2016 Heat Transfer Summer Conference and the ASME 2016 14th International Conference on Nanochannels, Microchannels, and Minichannels. American Society of Mechanical Engineers Digital Collection.

Hikita, H., Kikukawa, H., 1974. Liquid-phase mixing in bubble columns: Effect of liquid properties. The Chemical Engineering Journal 8, 191-197.

Holland, D. J., Blake, A., Tayler, A. B., Sederman, A. J., Gladden, L. F., 2012. Bubble size measurement using Bayesian magnetic resonance. Chemical Engineering Science 84, 735-745.

Honkanen, M., Saarenrinne, P., Stoor, T., Niinimäki, J., 2005. Recognition of highly overlapping ellipse-like bubble images. Measurement Science and Technology 16, 1760.

Hooshyar, N., Hamersma, P. J., Mudde, R. F., van Ommen, J. R., 2010a. Gas fraction and bubble dynamics in structured slurry bubble columns. Industrial & Engineering Chemistry Research 49, 10689-10697.

Hooshyar, N., Hamersma, P. J., Mudde, R. F., van Ommen, J. R., 2010b. Intensified operation of slurry bubble columns using structured gas injection. The Canadian Journal of Chemical Engineering 88, 533-542.

Huang, C., Wang, L., Chen, X., Wei, X., Liang, J., 2018. The rising behaviors of single bubbles in stagnant turpentine and pine resin solutions. Experimental Thermal and Fluid Science 98, 170-180.

Hughmark, G. A., Pressburg, B., 1961. Holdup and pressure drop with gas-liquid flow in a vertical pipe. AIChE Journal 7, 677-682.

Ityokumbul, M. T., Kosaric, N., Bulani, W., 1995. Effect of fine solids and frother on gas hold-up and liquid mixing in a flotation column. Minerals Engineering 8, 1369-1380.

Jakobsen, H. A., Lindborg, H., Dorao, C. A., 2005. Modeling of bubble column reactors: progress and limitations. Industrial & Engineering Chemistry Research 44, 5107-5151.

Jamialahmadi, M., Müller-Steinhagen, H., 1991. Effect of solid particles on gas hold-up in bubble columns. The Canadian Journal of Chemical Engineering 69, 390-393.

Jamshidi, N., Mostoufi, N., 2017. Measurement of bubble size distribution in activated sludge bubble column bioreactor. Biochemical Engineering Journal 125, 212-220.

Janssen, L. P. B. M., Hollander, R. W., Spoor, M. W., Smith, J. M., 1979. Residence time distributions in a plasticating twin screw extruder. AIChE Journal 25, 345-351.

Jena, M. S., Biswal, S. K., Das, S. P., Reddy, P. S. R., 2008. Comparative study of the performance of conventional and column flotation when treating coking coal fines. Fuel Processing Technology 89, 1409-1415.

Jin, H., Yang, S., He, G., Wang, M., Williams, R. A., 2010. The effect of gas-liquid counter-current operation on gas hold-up in bubble columns using electrical resistance tomography. Journal of Chemical Technology & Biotechnology 85, 1278-1283.

Jin, H., Yang, S., Wang, M., Williams, R. A., 2007. Measurement of gas holdup profiles in a gas liquid cocurrent bubble column using electrical resistance tomography, AIP Conference Proceedings. American Institute of Physics, pp. 869-876.

Johansson, G., Pugh, R. J., 1992. The influence of particle size and hydrophobicity on the stability of mineralized froths. International journal of mineral processing 34, 1-21.

Joshi, J. B., 1980. Axial mixing in multiphase contactors-a unified correlation. Transactions of the Institution of Chemical Engineers 58, 155-165.

Joshi, J. B., Veera, U. P., Prasad, C. V., Phanikumar, D. V., Deshphande, S. H., Thakre, S. S., Thorat, B. N., 1998. Gas hold-up structure in bubble column reactors. PINSA 64, 441-567.

Kang, Y., Kim, S. D., 1986. Radial dispersion characteristics of two-and three-phase fluidized beds. Industrial & Engineering Chemistry Process Design and Development 25, 717-722.

Kantarci, N., Borak, F., Ulgen, K. O., 2005. Bubble column reactors. Process Biochemistry 40, 2263-2283.

Kara, S., Kelkar, B. G., Shah, Y. T., Carr, N. L., 1982. Hydrodynamics and axial mixing in a three-phase bubble column. Industrial & Engineering Chemistry Process Design and Development 21, 584-594.

Kato, Y., Morooka, S., Koyama, M., Kago, T., Yang, S.-Z., 1985. Longitudinal dispersion coefficient of liquid in three-phase fluidized bed for gas-liquid-solid systems. Journal of chemical engineering of Japan 18, 313-318.

Kato, Y., Nishiwaki, A., 1971. Longitudial Dispersion Coefficient of Liquid in Bubble Column. Kagaku Kogaku Ronbunshu 35, 912-916.

Kato, Y., Nishiwaki, A., Fukuda, T., Tanaka, S., 1972. The behavior of suspended solid particles and liquid in bubble columns. Journal of chemical engineering of Japan 5, 112-118.

Kawamura, T., Fujiwara, A., Takahashi, T., Kato, H., Matsumoto, Y., Kodama, Y., 2004. The effects of the bubble size on the bubble dispersion and skin friction reduction, Proceeding of the 5th Symposium on Smart Control of Turbulence, Tokyo, pp. 145-151.

Kawase, Y., Moo-Young, M., 1986. Liquid phase mixing in bubble columns with Newtonian and non-Newtonian fluids. Chemical Engineering Science 41, 1969-1977.

Kawase, Y., Moo-Young, M., 1989. Turbulence intensity in bubble columns. The Chemical Engineering Journal 40, 55-58.

Kawatra, S., Eisele, T., 1988a. Rheological effects in grinding circuits. International Journal of Mineral Processing 22, 251-259.

Kawatra, S. K., Eisele, T. C., 1988b. Rheological effects in grinding circuits. International journal of mineral processing 22, 251-259.

Kelkar, B. G., Shah, Y. T., Carr, N. L., 1984. Hydrodynamics and axial mixing in a three-phase bubble column. Effects of slurry properties. Industrial & Engineering Chemistry Process Design and Development 23, 308-313.

Khare, A. S., Joshi, J. B., 1990. Effect of fine particles on gas hold-up in three-phase sparged reactors. The Chemical Engineering Journal 44, 11-25.

Kim, H. S., Kim, J. H., Lee, C. G., Kang, S. H., Woo, K. J., Jung, H. J., Kim, D. W., 2014. Bubble and heat transfer phenomena in viscous slurry bubble column. Advances in Chemical Engineering and Science 4, 417-429.

Kim, J. Y., Kim, B., Nho, N.-S., Go, K.-S., Kim, W., Bae, J. W., Jeong, S. W., Epstein, N., Lee, D. H., 2017. Gas holdup and hydrodynamic flow regime transition in bubble columns. Journal of Industrial and Engineering Chemistry 56, 450-462.

Kim, Y. H., Tsutsumi, A., Yoshida, K., 1987. Effect of particle size on gas holdup in three-phase reactors. Sadhana 10, 261-268.

Kirchberg , H., Topfer, E., 1965. The miner alizati on of air bubbl es in flotation, In Proc. VII Min. Process. Congress, Gordon and Breach: New York, pp. 157-168.

Klassen, V. I., Mokrousov, V. A., 1963. An introduction to the theory of flotation. Butterworths.

Kluytmans, J. H. J., van Wachem, B. G. M., Kuster, B. F. M., Schouten, J. C., 2001. Gas holdup in a slurry bubble column: influence of electrolyte and carbon particles. Industrial & Engineering Chemistry Research 40, 5326-5333.

Koh, P. T. L., Schwarz, M. P., 2007. CFD modelling of bubble–particle attachments in flotation cells. Minerals Engineering 19, 619-626.

Kracht, W., Moraga, C., 2016. Acoustic measurement of the bubble Sauter mean diameter d32. Minerals Engineering 98, 122-126.

Kuan, S. H., Finch, J. A., 2010. Impact of talc on pulp and froth properties in F150 and 1-pentanol frother systems. Minerals Engineering 23, 1003-1009.

Kulkarni, A. A., Joshi, J. B., 2005. Bubble formation and bubble rise velocity in gas− liquid systems: a review. Industrial & Engineering Chemistry Research 44, 5873-5931.

Kumar, R., Pant, H. J., Goswami, S., Sharma, V. K., Dash, A., Mishra, S., Bhanja, K., Mohan, S., Mahajani, S. M., 2017. Investigation of holdup and axial dispersion of liquid phase in a catalytic exchange column using radiotracer technique. Applied Radiation and Isotopes 121, 51-60.

Kumar, S., Khanna, A., 2014. Experimental analysis and development of correlations for gas holdup in high pressure slurry co-current bubble columns. Korean Journal of Chemical Engineering 31, 1964-1972.

Kumar, S., Kumar, R. A., Munshi, P., Khanna, A., 2012. Gas hold-up in three phase co-current bubble columns. Procedia Engineering 42, 782-794.

Kumar, S. B., Moslemian, D., Duduković, M. P., 1997. Gas-holdup measurements in bubble columns using computed tomography. AIChE Journal 43, 1414-1425.

Lage, P. L. C., Espósito, R. O., 1999. Experimental determination of bubble size distributions in bubble columns: prediction of mean bubble diameter and gas hold up. Powder Technology 101, 142-150.

Lakhdissi, E. M., Soleimani, I., Guy, C., Chaouki, J., 2019. Simultaneous effect of particle size and solid concentration on the hydrodynamics of slurry bubble column reactors. AIChE Journal.

Lapidus, L., Elgin, J. C., 1957. Mechanics of vertical-moving fluidized systems. AIChE Journal 3, 63-68.

Laplante, A. R., Yianatos, J. B., Finch, J. A., 1988. On the mixing characteristics of the collection zone in flotation columns, In column flotation '88. Proceedings of the International Symposium, ed. K. V. S. Sastry. Littleton (Colorado): Society of Mining Engineers, Phoenix (Arizona), pp. 69-79.

Lau, R., Mo, R., Sim, W. S. B., 2010. Bubble characteristics in shallow bubble column reactors. Chemical Engineering Research and Design 88, 197-203.

Lau, Y. M., Sujatha, K. T., Gaeini, M., Deen, N. G., Kuipers, J. A. M., 2013. Experimental study of the bubble size distribution in a pseudo-2D bubble column. Chemical Engineering Science 98, 203-211.

Lazic, P., Calic, N., 2000. Boltzmann's model of flotation kinetics. Proc. XXI IMPC (Rome), vol. B, 87-93.

Legendre, D., Zenit, R., Velez-Cordero, J. R., 2012. On the deformation of gas bubbles in liquids. Physics of Fluids 24, 043303.

Leonard, C., Ferrasse, J.-H., Boutin, O., Lefevre, S., Viand, A., 2015. Bubble column reactors for high pressures and high temperatures operation. Chemical Engineering Research and Design 100, 391-421.

Li, D., Fitzpatrick, J. A., Slattery, J. C., 1990. Rate of collection of particles by flotation. Industrial & Engineering Chemistry Research 29, 955-967.

Li, H., Liu, Z., Chen, J., Sun, B., Guo, Y., He, H., 2017a. Correlation of aspect ratio and drag coefficient for hydrate-film-covered methane bubbles in water. Experimental Thermal and Fluid Science 88, 554-565.

Li, H., Prakash, A., 1997. Heat transfer and hydrodynamics in a three-phase slurry bubble column. Industrial & Engineering Chemistry Research 36, 4688-4694.

Li, H., Prakash, A., 2000. Influence of slurry concentrations on bubble population and their rise velocities in a three-phase slurry bubble column. Powder Technology 113, 158-167.

Li, S., Han, R., Zhang, A. M., Wang, Q. X., 2016. Analysis of pressure field generated by a collapsing bubble. Ocean Engineering 117, 22-38.

Li, S., Huang, S., Fan, J., 2017b. Effect of surfactants on gas holdup in shear-thinning fluids. International Journal of Chemical Engineering 2017.

Li, W., Zhong, W., Jin, B., Xiao, R., Lu, Y., He, T., 2013. Study of the particle size effect on bubble rise velocities in a three-phase bubble column. World Academy of Science, Engineering and Technology, International Journal of Chemical, Molecular, Nuclear, Materials and Metallurgical Engineering 7, 971-975.

Liaoa, Y., Caoa, Y., Hub, Z., Taoc, X., 2015. A new preparation scheme for a difficult-to-float coking coal by column flotation following grinding. Journal of the Southern African Institute of Mining and Metallurgy 115, 161-164.

Lim, H. O., Seo, M. J., Kang, Y., Jun, K. W., 2011. Particle fluctuations and dispersion in three-phase fluidized beds with viscous and low surface tension media. Chemical Engineering Science 66, 3234-3242.

Liu, L., 2014. The phenomenon of negative frictional pressure drop in vertical two-phase flow. International Journal of Heat and Fluid Flow 45, 72-80.

Liu, L., Li, X., Tong, L., Liu, Y., 2014. Effect of surfactant additive on vertical two-phase flow. Journal of Petroleum Science and Engineering 115, 1-10.

Lu, J., Tryggvason, G., 2007. Effect of bubble size in turbulent bubbly downflow in a vertical channel. Chemical Engineering Science 62, 3008-3018.

Luewisutthichat, W., Tsutsumi, A., Yoshida, K., 1997. Bubble characteristics in multi-phase flow systems: bubble sizes and size distributions. Journal of chemical engineering of Japan 30, 461-466.

Luo, X., Lee, D. J., Lau, R., Yang, G., Fan, L. S., 1999. Maximum stable bubble size and gas holdup in high-pressure slurry bubble columns. AIChE Journal 45, 665-680.

Luo, X., Zhang, J., Tsuchiya, K., Fan, L.-S., 1997. On the rise velocity of bubbles in liquid-solid suspensions at elevated pressure and temperature. Chemical Engineering Science 52, 3693-3699.

Majumder, S. K., 2008. Analysis of dispersion coefficient of bubble motion and velocity characteristic factor in down and upflow bubble column reactor. Chemical Engineering Science 63, 3160-3170.

Majumder, S. K., 2016. Hydrodynamics and transport processes of inverse bubbly flow. Elsevier, Amsterdam.

Majumder, S. K., 2018. Hydrodynamics and mass transfer in downflow slurry bubble columns. Apple Academic Press. Inc.

Majumder, S. K., 2019. Hydrodynamics and mass transfer in downflow slurry bubble columns. CRC Press, New York.

Majumder, S. K., Ghosh, S., Kundu, G., Mitra, A. K., 2011. Frictional pressure drop of gas-Newtonian and gas-non Newtonian slug flow in vertical pipe. International Journal of Chemical Reactor Engineering 9.

Majumder, S. K., Kundu, G., Mukherjee, D., 2006. Prediction of pressure drop in a modified gas–liquid downflow bubble column. Chemical Engineering Science 61, 4060-4070.

Majumder, S. K., Kundu, G., Mukherjee, D., 2007. Pressure drop and bubble–liquid interfacial shear stress in a modified gas non-Newtonian liquid downflow bubble column. Chemical Engineering Science 62, 2482-2490.

Maldonado, M., Quinn, J. J., Gomez, C. O., Finch, J. A., 2013. An experimental study examining the relationship between bubble shape and rise velocity. Chemical Engineering Science 98, 7-11.

Mandal, A., Kundu, G., Mukherjee, D., 2004. Studies on frictional pressure drop of gas-non-Newtonian two-phase flow in a cocurrent downflow bubble column. Chemical Engineering Science 59, 3807-3815.

Manjrekar, O. N., Dudukovic, M. P., 2015. Application of a 4-point optical probe to a Slurry Bubble Column Reactor. Chemical Engineering Science 131, 313-322.

Manjrekar, O. N., Hamed, M., Dudukovic, M. P., 2018. Gas hold-up and mass transfer in a pilot scale bubble column with and without internals. Chemical Engineering Research and Design 135, 166-174.

Marrucci, G., 1969. A theory of coalescence. Chemical Engineering Science 24, 975-985.

Massinaei, M., Kolahdoozan, M., Noaparast, M., Oliazadeh, M., Yianatos, J., Shamsadini, R., Yarahmadi, M., 2009. Hydrodynamic and kinetic characterization of industrial columns in rougher circuit. Minerals Engineering 22, 357-365.

Mavros, P., 1992. Technical note validity and limitations of the closed-vessel analytical solution to the axial dispersion model. Minerals Engineering 5, 1053-1060.

Meikap, B. C., 2000. Abatement of particulate laden sulphur in a modified multistage bubble column scrubber PhD dissertation. Chemical Engineering Department, IIT, Kharagpur, India.

Mena, P. C., Ruzicka, M. C., Rocha, F. A., Teixeira, J. A., Drahoš, J., 2005. Effect of solids on homogeneous–heterogeneous flow regime transition in bubble columns. Chemical Engineering Science 60, 6013-6026.

Meng, J., Tabosa, E., Xie, W., Runge, K., Bradshaw, D., Manlapig, E., 2016. A review of turbulence measurement techniques for flotation. Minerals Engineering 95, 79-95.

Merkle, C. L., Deutsch, S., 1989. Microbubble drag reduction, Frontiers in Experimental Fluid Mechanics. Springer, pp. 291-335.

Miller, D. N., 1980. Gas holdup and pressure drop in bubble column reactors. Industrial & Engineering Chemistry Process Design and Development 19, 371-377.

Mills, P. J. T., Yianatos, J. B., O'Connor, C. T., 1992. The mixing characteristics of solid and liquid phases in a flotation column. Minerals Engineering 5, 1195-1205.

Mirón, A. S., García, M.-C. C., Camacho, F. G., Grima, E. M., Chisti, Y., 2004. Mixing in bubble column and airlift reactors. Chemical Engineering Research and Design 82, 1367-1374.

Mittal, G. S., Zhang, J., 2007. Friction factor prediction for Newtonian and non-Newtonian fluids in pipe flows using neural networks. International Journal of Food Engineering 3.

Miyauchi, T., Furusaki, S., Morooka, S., Ikeda, Y., 1981a. Transport phenomena and reaction in fluidized catalyst beds, Advances in Chemical Engineering. Elsevier, pp. 275-448.

Miyauchi, T., Furusaki, S., Morooka, S., Ikeda, Y., 1981b. Transport phenomena and reaction in fluidized catalyst beds. Advances in Chemical Engineering 11, 275-448.

Mokhtari, M., Chaouki, J., 2019. New technique for simultaneous measurement of the local solid and gas holdup by using optical fiber probes in the slurry bubble column. Chemical Engineering Journal 358, 831-841.

Moshtari, B., Moghaddas, J. S., Gangi, E., 2007. A hydrodynamic experimental study of slurry bubble column, Studies in Surface Science and Catalysis. Elsevier, pp. 67-72.

Moustiri, S., Hebrard, G., Thakre, S. S., Roustan, M., 2001. A unified correlation for predicting liquid axial dispersion coefficient in bubble columns. Chemical Engineering Science 56, 1041-1047.

Mu, B., Thompson, M. R., 2012. Examining the mechanics of granulation with a hot melt binder in a twin-screw extruder. Chemical Engineering Science 81, 46-56.

Muhsin, H. A. A.-k., Mohammad, F. A., 2008. Experimental study of liquid dispersion in bubble column. Diyala Journal of Engineering Sciences 1, 56-85.

Muroyama, K., Hashimoto, K., Kawabata, T., Shiota, M., 1978. Axial liquid mixing in three-phase fluidized beds. Kagaku Kogaku Ronbunshu 4, 622.

Muroyama, K., Imai, K., Oka, Y., Hayashi, J. i., 2013. Mass transfer properties in a bubble column associated with micro-bubble dispersions. Chemical Engineering Science 100, 464-473.

Myint, W., Hosokawa, S., Tomiyama, A., 2007. Shapes of single drops rising through stagnant liquids. Journal of Fluid Science and Technology 2, 184-195.

Nagarajan, K., Renganathan, T., Krishnaiah, K., 2016. Hydrodynamics of a continuous countercurrent liquid–solid system: experiments and modeling. RSC Advances 6, 35486-35497.

Nedeltchev, S., Ookawara, S., Ogawa, K., 2005. The effect of superficial gas velocity and aerated liquid height on the spatial distribution of local liquid-phase axial dispersion coefficients in a bubble column. Journal of chemical engineering of Japan 38, 1-11.

Nguyen, A., Schulze, H. J., 2003. Colloidal science of flotation. CRC Press.

Nguyen, A. V., Schulze, H. J., Ralston, J., 1997. Elementary steps in particle—bubble attachment. International journal of mineral processing 51, 183-195.

Nouri, N. M., Motlagh, S. Y., Navidbakhsh, M., Dalilhaghi, M., Moltani, A. A., 2013. Bubble effect on pressure drop reduction in upward pipe flow. Experimental Thermal and Fluid Science 44, 592-598.

Ofori, P., O'Brien, G., Hapugoda, P., Firth, B., 2014. Distributed flotation kinetics models–A new implementation approach for coal flotation. Minerals Engineering 66, 77-83.

Ojima, S., Hayashi, K., Tomiyama, A., 2014. Effects of hydrophilic particles on bubbly flow in slurry bubble column. International Journal of Multiphase Flow 58, 154-167.

Ojima, S., Sasaki, S., Hayashi, K., Tomiyama, A., 2015. Effects of particle diameter on bubble coalescence in a slurry bubble column. Journal of chemical engineering of Japan 48, 181-189.

Okawa, T., Tanaka, T., Kataoka, I., Mori, M., 2003. Temperature effect on single bubble rise characteristics in stagnant distilled water. International Journal of Heat and Mass Transfer 46, 903-913.

Orvalho, S., Hashida, M., Zednikova, M., Stanovsky, P., Ruzicka, M. C., Sasaki, S., Tomiyama, A., 2018. Flow regimes in slurry bubble column: effect of column height and particle concentration. Chemical Engineering Journal 351, 799-815.

Otake, T., Tone, S., Shinohara, K., 1981. Gas holdup in the bubble column with cocurrent and countercurrent gas-liquid flow. Journal of chemical engineering of Japan 14, 338-340.

Palaskar, S., De, J., Pandit, A., 2000a. Liquid phase RTD studies in sectionalized bubble column. Chemical Engineering & Technology: Industrial Chemistry-Plant Equipment-Process Engineering-Biotechnology 23, 61-69.

Palaskar, S. N., De, J. K., Pandit, A. B., 2000b. Liquid phase RTD studies in sectionalized bubble column. Chemical Engineering & Technology: Industrial Chemistry-Plant Equipment-Process Engineering-Biotechnology 23, 61-69.

Pallapothu, S. K., Taweel, A. M. A., 2012. Effect of contaminants on the gas holdup and mixing in internal airlift reactors equipped with microbubble generator. International Journal of Chemical Engineering 2012.

Pandit, A. B., Joshi, J. B., 1984. Three phase sparged reactors—some design aspects. Reviews in Chemical Engineering 2, 1-84.

Pareek, V. K., Yap, Z., Brungs, M. P., Adesina, A. A., 2001. Particle residence time distribution (RTD) in three-phase annular bubble column reactor. Chemical Engineering Science 56, 6063-6071.

Parisien, V., Farrell, A., Pjontek, D., McKnight, C. A., Wiens, J., Macchi, A., 2017. Bubble swarm characteristics in a bubble column under high gas holdup conditions. Chemical Engineering Science 157, 88-98.

Parmar, R., Majumder, S. K., 2014. Hydrodynamics of microbubble suspension flow in pipes. Industrial & Engineering Chemistry Research 53, 3689-3701.

Parmar, R., Majumder, S. K., 2016. Mineral beneficiation by ionic microbubble in continuous plant prototype: Efficiency and its analysis by kinetic model. Chemical Engineering Science 142, 42-54.

Parthasarathy, R., Ahmed, N., 1994. Bubble size distribution in a gas sparged vessel agitated by a Rushton turbine. Industrial & Engineering Chemistry Research 33, 703-711.

Passos, A. D., Voulgaropoulos, V. P., Paras, S. V., Mouza, A. A., 2015. The effect of surfactant addition on the performance of a bubble column containing a non-Newtonian liquid. Chemical Engineering Research and Design 95, 93-104.

Peker, S. M., Helvaci, S. S., Yener, H. B., Ikizler, B., Alparslan, A., 2008. Solid-liquid two phase flow. Elsevier.

Pjontek, D., Parisien, V., Macchi, A., 2014. Bubble characteristics measured using a monofibre optical probe in a bubble column and freeboard region under high gas holdup conditions. Chemical Engineering Science 111, 153-169.

Prakash, R., Majumder, S. K., Singh, A., 2018a. Flotation technique: Its mechanisms and design parameters. Chemical Engineering and Processing-Process Intensification 127, 249-270.

Prakash, R., Majumder, S. K., Singh, A., 2018b. Gas holdup and frictional pressure drop contributions in microstructured two-and three-phase bubbling bed with Newtonian and non-Newtonian liquids: Effect of coarse and fine particles with surface active agent. Chemical Engineering and Processing-Process Intensification 133, 40-57.

Prakash, R., Majumder, S. K., Singh, A., 2019. Particle-laden bubble size and its distribution in microstructured bubbling bed in presence and absence of a surface active agent. Industrial & Engineering Chemistry Research 58, 3499 - 3522.

Prakash, R., Majumder, S. K., Singh, A., 2020. Bubble size distribution and specific bubble interfacial area in two–phase microstructured dense bubbling bed. Chemical Engineering Research and Design 156, 108-130.

Pyke, B., Fornasiero, D., Ralston, J., 2003. Bubble particle heterocoagulation under turbulent conditions. Journal of Colloid and Interface Science 265, 141-151.

Qi, X., Li, X., Liang, Y., Wang, H., Guo, W., Cong, X., Lv, F., Zhang, H., 2020. Surface structure-dependent hydrophobicity/oleophilicity of pyrite and its influence on coal flotation. Journal of Industrial and Engineering Chemistry.

Rabha, S., Schubert, M., Hampel, U., 2013a. Intrinsic flow behavior in a slurry bubble column: a study on the effect of particle size. Chemical Engineering Science 93, 401-411.

Rabha, S., Schubert, M., Wagner, M., Lucas, D., Hampel, U., 2013b. Bubble size and radial gas hold-up distributions in a slurry bubble column using ultrafast electron beam X-ray tomography. AIChE Journal 59, 1709-1722.

Rahman, M., Pudasainee, D., Gupta, R., 2017. Review on chemical upgrading of coal: Production processes, potential applications and recent developments. Fuel Processing Technology 158, 35-56.

Ralston, J., Dukhin, S. S., Mishchuk, N. A., 1999a. Inertial hydrodynamic particle–bubble interaction in flotation. International journal of mineral processing 56, 207-256.

Ralston, J., Fornasiero, D., Hayes, R., 1999b. Bubble–particle attachment and detachment in flotation. International journal of mineral processing 56, 133-164.

Rampure, M. R., Kulkarni, A. A., Ranade, V. V., 2007. Hydrodynamics of bubble column reactors at high gas velocity: experiments and computational fluid dynamics (CFD) simulations. Industrial & Engineering Chemistry Research 46, 8431-8447.

Rawat, K., Yadav, A. K., 2020. Characterization of coal and fly ash (generated) at coal based thermal power plant. Materials Today: Proceedings 26, 1406-1411.

Rayleigh, L., 1917. On the pressure developed in a liquid during the collapse of a spherical cavity: Philosophical Magazine Series 6, 34, 94–98.

Raymond, F., Rosant, J.-M., 2000. A numerical and experimental study of the terminal velocity and shape of bubbles in viscous liquids. Chemical Engineering Science 55, 943-955.

Reith, T. h., Renken, S., Israel, B. A., 1968. Gas hold-up and axial mixing in the fluid phase of bubble columns. Chemical Engineering Science 23, 619-629.

Reitz, E., Podhaisky, H., Ely, D., Thommes, M., 2013. Residence time modeling of hot melt extrusion processes. European Journal of Pharmaceutics and Biopharmaceutics 85, 1200-1205.

Richardson, J. F., Zaki, W. N., 1954. Sedimentation and fluidisation: Part I. Transactions of the Institution of Chemical Engineers 32, 35-37.

Riquarts, H. P., 1981. A physical model for axial mixing of the liquid phase for heterogeneous flow regime in bubble columns. German Chemical Engineering 4, 18-23.

Rollbusch, P., Becker, M., Ludwig, M., Bieberle, A., Grünewald, M., Hampel, U., Franke, R., 2015. Experimental investigation of the influence of column scale, gas density and liquid properties on gas holdup in bubble columns. International Journal of Multiphase Flow 75, 88-106.

Rubio, F. C., Mirón, A. S., García, M.-C. C., Camacho, F. G., Grima, E. M., Chisti, Y., 2004. Mixing in bubble columns: a new approach for characterizing dispersion coefficients. Chemical Engineering Science 59, 4369-4376.

Ruthiya, K. C., van der Schaaf, J., Kuster, B. F. M., Schouten, J. C., 2006. Influence of particles and electrolyte on gas hold-up and mass transfer in a slurry bubble column. International Journal of Chemical Reactor Engineering 4.

Sada, E., Kumazawa, H., Lee, C., Iguchi, T., 1986a. Gas holdup and mass-transfer characteristics in a three-phase bubble column. Industrial & Engineering Chemistry Process Design and Development 25, 472-476.

Sada, E., Kumazawa, H., Lee, C. H., 1986b. Influences of suspended fine particles on gas holdup and mass transfer characteristics in a slurry bubble column. AIChE Journal 32, 853-856.

Sarhan, A. R., Homadi, A. M., Naser, J., 2020. Modelling detachment rates of hydrophobic particles from bubbles in a froth phase. Separation and Purification Technology 235, 116200.

Sarhan, A. R., Naser, J., Brooks, G., 2016. CFD simulation on influence of suspended solid particles on bubbles' coalescence rate in flotation cell. International journal of mineral processing 146, 54-64.

Sarhan, A. R., Naser, J., Brooks, G., 2017a. CFD analysis of solid particles properties effect in three-phase flotation column. Separation and Purification Technology 185, 1-9.

Sarhan, A. R., Naser, J., Brooks, G., 2017b. CFD modeling of three-phase flotation column incorporating a population balance model. Procedia engineering 184, 313-317.

Sarhan, A. R., Naser, J., Brooks, G., 2018a. CFD model simulation of bubble surface area flux in flotation column reactor in presence of minerals. International Journal of Mining Science and Technology 28, 999-1007.

Sarhan, A. R., Naser, J., Brooks, G., 2018b. CFD modeling of bubble column: Influence of physico-chemical properties of the gas/liquid phases properties on bubble formation. Separation and Purification Technology 201, 130-138.

Sarhan, A. R., Naser, J., Brooks, G., 2018c. Effects of particle size and concentration on bubble coalescence and froth formation in a slurry bubble column. Particuology 36, 82-95.

Schäfer, R., Merten, C., Eigenberger, G., 2002. Bubble size distributions in a bubble column reactor under industrial conditions. Experimental Thermal and Fluid Science 26, 595-604.

Schmidt, L. D., 1998. The engineering of chemical reactions. Oxford University Press, USA.

Schubert, H., 1999. On the turbulence-controlled microprocesses in flotation machines. International journal of mineral processing 56, 257-276.

Schulze, H. J., 1992. Probability of particle attachment on gas bubbles by sliding. Advances in Colloid and Interface Science 40, 283-305.

Schulze, H. J., Stöckelhuber, K. W., Wenger, A., 2001. The influence of acting forces on the rupture mechanism of wetting films—nucleation or capillary waves. Colloids and Surfaces A: Physicochemical and Engineering Aspects 192, 61-72.

Seger, M. A., Oliveira, C., Rodrigues, R. T., 2019. Development of a laboratory-scale flotation column with inlet bubble size measurement. Minerals Engineering 142, 105936.

Sehabiague, L., Basha, O. M., Hong, Y., Morsi, B., Shi, Z., Jia, H., Weng, L., Men, Z., Liu, K., Cheng, Y., 2015. Assessing the performance of an industrial SBCR for F ischer–T ropsch synthesis: Experimental and modeling. AIChE Journal 61, 3838-3857.

Sehabiague, L., Morsi, B. I., 2013. Hydrodynamic and mass transfer characteristics in a large-scale slurry bubble column reactor for gas mixtures in actual Fischer–Tropsch cuts. International Journal of Chemical Reactor Engineering 11, 83-102.

Senapati, P. K., Panda, D., Parida, A., 2009. Predicting viscosity of limestone–water slurry. Journal of Minerals and Materials Characterization and Engineering 8, 203.

Shah, M., Kiss, A. A., Zondervan, E., Van der Schaaf, J., De Haan, A. B., 2012. Gas holdup, axial dispersion, and mass transfer studies in bubble columns. Industrial & Engineering Chemistry Research 51, 14268-14278.

Shaikh, A., Al-Dahhan, M. H., 2007. A review on flow regime transition in bubble columns. International Journal of Chemical Reactor Engineering 5.

Shannak, B. A., 2008. Frictional pressure drop of gas liquid two-phase flow in pipes. Nuclear Engineering and Design 238, 3277-3284.

Shawaqfeh, A. T., 2003. Gas holdup and liquid axial dispersion under slug flow conditions in gas–liquid bubble column. Chemical engineering and processing: Process intensification 42, 767-775.

Sheikhi, A., Sotudeh-Gharebagh, R., Zarghami, R., Mostoufi, N., Alfi, M., 2013. Understanding bubble hydrodynamics in bubble columns. Experimental Thermal and Fluid Science 45, 63-74.

Shen, X., Ceccio, S. L., Perlin, M., 2006. Influence of bubble size on micro-bubble drag reduction. Experiments in Fluids 41, 415-424.

Shollenberger, K. A., Torczynski, J. R., Adkins, D. R., O'hern, T. J., Jackson, N. B., 1997. Gamma-densitometry tomography of gas holdup spatial distribution in industrial-scale bubble columns. Chemical Engineering Science 52, 2037-2048.

Shukla, S. C., Kukade, S., Mandal, S. K., Kundu, G., 2008. Coal–oil–water multiphase fuel: Rheological behavior and prediction of optimum particle size. Fuel 87, 3428-3432.

Shukla, S. C., Kundu, G., Mukherjee, D., 2010. Study of gas holdup and pressure characteristics in a column flotation cell using coal. Minerals Engineering 23, 636-642.

Sines, J. N., Hwang, S., Marashdeh, Q. M., Tong, A., Wang, D., He, P., Straiton, B. J., Zuccarelli, C. E., Fan, L.-S., 2019. Slurry bubble column measurements using advanced electrical capacitance volume tomography sensors. Powder Technology 355, 474-480.

Sivaiah, M., Majumder, S. K., 2012. Gas holdup and frictional pressure drop in a modified slurry bubble column. International Journal of Chemical Reactor Engineering 10.

Sivaiah, M., Majumder, S. K., 2013a. Hydrodynamics and mixing characteristics in an ejector-induced downflow slurry bubble column (EIDSBC). Chemical Engineering Journal 225, 720-733.

Sivaiah, M., Majumder, S. K., 2013b. Mass Transfer and Mixing in an Ejector-Induced Downflow Slurry Bubble Column. Industrial & Engineering Chemistry Research 52, 12661-12671.

Smith, J. S., Burns, L. F., Valsaraj, K. T., Thibodeaux, L. J., 1996. Bubble column reactors for wastewater treatment. 2. The effect of sparger design on sublation column hydrodynamics in the homogeneous flow regime. Industrial & Engineering Chemistry Research 35, 1700-1710.

Smith, T. N., Tait, R. W. F., 1964. Interfacial waves in horizontal gas-liquid flow. Australian Journal of Applied Science 15, 247.

Smith, T. N., Tait, R. W. F., 1966. Interfacial shear stress and momentum transfer in horizontal gas-liquid flow. Chemical Engineering Science 21, 63-75.

Son, S. M., Shin, I. S., Kang, S. H., Kang, Y., Kim, S. D., 2007. Pressure fluctuations and bubble size in viscous three-phase circulation fluidized bed bioreactors. Korean Journal of Chemical Engineering 24, 866-871.

Sriram, K., Mann, R., 1977. Dynamic gas disengagement: A new technique for assessing the behaviour of bubble columns. Chemical Engineering Science 32, 571-580.

Steel, K. M., Besida, J., O'Donnell, T. A., Wood, D. G., 2001. Production of ultra clean coal: Part I—Dissolution behaviour of mineral matter in black coal toward hydrochloric and hydrofluoric acids. Fuel Processing Technology 70, 171-192.

Stegeman, D., Knop, P. A., Wijnands, A. J. G., Westerterp, K. R., 1996. Interfacial area and gas holdup in a bubble column reactor at elevated pressures. Industrial & Engineering Chemistry Research 35, 3842-3847.

Stewart, C. W., 1969. Energy dissipation by pulsating air bubbles in a viscoelastic medium. Journal of Polymer Science Part A-2: Polymer Physics 7, 143-151.

Subasinghe, G. K. N., Albijanic, B., 2014. Influence of the propagation of three phase contact line on flotation recovery. Minerals Engineering 57, 43-49.

Sugihara, K., Sanada, T., Shirota, M., Watanabe, M., 2007. Behavior of single rising bubbles in superpurified water. Kagaku Kogaku Ronbunshu 33, 402-408.

Sven-Nilsson, I., 1934. Effect of contact time between mineral and air bubbles on flotation. Kolloid 69, 230-232.

Szczerkowska, S., Wiertel-Pochopien, A., Zawala, J., Larsen, E., Kowalczuk, P. B., 2018. Kinetics of froth flotation of naturally hydrophobic solids with different shapes. Minerals Engineering 121, 90-99.

Takahashi, T., Miyahara, T., Izawa, H., 1976. Drag coefficient and wake volume of single bubbles rising through quiescent liquid. Kagaku Kogaku Ronbunshu 2, 480-487.

Tan, J., Liang, L., Peng, Y., Xie, G., 2020. Challenges of using froth features to predict clean coal ash content in coal flotation. International Journal Of Coal Preparation And Utilization, 1-37.

Tang, C. C., Tiwari, S., Ghajar, A. J., 2013. Effect of void fraction on pressure drop in upward vertical two-phase gas-liquid pipe flow. Journal of Engineering for Gas Turbines and Power 135, 022901.

Tao, D., 2005. Role of bubble size in flotation of coarse and fine particles—a review. Separation science and technology 39, 741-760.

Tavera, F. J., Escudero, R., Finch, J. A., 2001. Gas holdup in flotation columns: laboratory measurements. International journal of mineral processing 61, 23-40.

Taylor, G. I., 1953. Dispersion of soluble matter in solvent flowing slowly through a tube. Proceedings of the Royal Society of London. Series A. Mathematical and Physical Sciences 219, 186-203.

Thomas, D. G., 1965. Transport characteristics of suspension: VIII. A note on the viscosity of Newtonian suspensions of uniform spherical particles. Journal of Colloid Science 20, 267-277.

Tian, Q., Wang, Y., Li, G., 2017. Application of special collectors and flotation column for beneficiation low rank coal slimes. Physicochemical Problems of Mineral Processing 53, 553-568.

Tian, Z., Cheng, Y., Li, X., Wang, L., 2019. Bubble shape and rising velocity in viscous liquids at high temperature and pressure. Experimental Thermal and Fluid Science 102, 528-538.

Tomiyama, A., Tamai, H., Zun, I., Hosokawa, S., 2002. Transverse migration of single bubbles in simple shear flows. Chemical Engineering Science 57, 1849-1858.

Towell, G. D., Ackermann, G. H., 1972. Axial mixing of liquid and gas in larger bubble reactors, In Chemical Reaction Engineering: Proceedings of the Fifth European /Second International Symposium on Chemical Reaction Engineering, Amsterdam, 2, 3 and 4 May, 1972. B3-1 to B3-13. Elsevier, Amsterdam and New York.

Trivedi, R., Renganathan, T., Krishnaiah, K., 2018. Hydrodynamics of countercurrent bubble column: Experiments and predictions. Chemical Engineering Journal 338, 636-650.

Tsutsumi, A., Chen, W., Kim, Y.-H., 1999. Classification and characterization of hydrodynamic and transport behaviors of three-phase reactors. Korean Journal of Chemical Engineering 16, 709-720.

Tsutsumi, A., Nieh, J.-Y., Fan, L.-S., 1991. Particle wettability effects on bubble wake dynamics in gas—liquid—solid fluidization. Chemical Engineering Science 46, 2381-2384.

Turney, D. E., Ansari, M., Kalaga, D. V., Yakobov, R., Banerjee, S., Joshi, J. B., 2019. A micro-jet array for economic intensification of gas transfer in bioreactors. Biotechnology progress 35, e2710.

Tyagi, P., Buwa, V. V., 2017. Dense gas–liquid–solid flow in a slurry bubble column: Measurements of dynamic characteristics, gas volume fraction and bubble size distribution. Chemical Engineering Science 173, 346-362.

Uchida, S., Tsuyutani, S., Seno, T., 1989. Flow regimes and mass transfer in counter-current bubble columns. The Canadian Journal of Chemical Engineering 67, 866-869.

Uribe-Salas, A., De Lira-Gomez, P., Perez-Garibay, R., Nava-Alonso, F., Magallanes-Hernandez, L., Lara-Valenzuela, C., 2003. Overloading of gas bubbles in column flotation of coarse particles and effect upon recovery. International journal of mineral processing 71, 167-178.

Uribe-Salas, A., Pérez-Garibay, R., Nava-Alonso, F., 2008. Dynamic and Geometrical Models to Estimate the Density of Fully-Loaded Bubbles in the Column Flotation of Silica Sand. The Open Mineral Processing Journal 1, 1-5.

Vadlakonda, B., Mangadoddy, N., 2017. Hydrodynamic study of two phase flow of column flotation using electrical resistance tomography and pressure probe techniques. Separation and Purification Technology 184, 168-187.

Vadlakonda, B., Mangadoddy, N., 2018. Hydrodynamic study of three-phase flow in column flotation using electrical resistance tomography coupled with pressure transducers. Separation and Purification Technology 203, 274-288.

Vakhrushev, I. A., Efremov, G. I., 1970. Interpolation formula for computing the velocities of single gas bubbles in liquids. Chemistry and Technology of Fuels and Oils 6, 376-379.

Vazirizadeh, A., Bouchard, J., Chen, Y., 2016. Effect of particles on bubble size distribution and gas hold-up in column flotation. International journal of mineral processing 157, 163-173.

Veera, U. P., Joshi, J. B., 1999. Measurement of gas hold-up profiles by gamma ray tomography: effect of sparger design and height of dispersion in bubble columns. Chemical Engineering Research and Design 77, 303-317.

Verrelli, D. I., Bruckard, W. J., Koh, P. T. L., Schwarz, M. P., Follink, B., 2014. Particle shape effects in flotation. Part 1: Microscale experimental observations. Minerals Engineering 58, 80-89.

Verrelli, D. I., Koh, P. T. L., Nguyen, A. V., 2011. Particle–bubble interaction and attachment in flotation. Chemical Engineering Science 66, 5910-5921.

Vinaya, M., Varma, Y. B. G., 1996. Gas holdup-slip velocity relationship in multistage bubble column. Bioprocess Engineering 15, 105-108.

Vinnett, L., Ledezma, T., Alvarez-Silva, M., Waters, K., 2016. Gas holdup estimation in flotation machines using image techniques and superficial gas velocity. Minerals Engineering 96, 26-32.

Vitankar, V. S., Dhotre, M. T., Joshi, J. B., 2002. A low Reynolds number k–ε model for the prediction of flow pattern and pressure drop in bubble column reactors. Chemical Engineering Science 57, 3235-3250.

Wadaugsorn, K., Limtrakul, S., Vatanatham, T., Ramachandran, P. A., 2018. Mixing characteristics of gas and liquid phases in bubble column reactors from virtual tracer simulation. Industrial & Engineering Chemistry Research 57, 14064-14079.

Wallis, G. B., 1969. One-dimensional two-phase flow.

Wang, J., Wang, L., Hanotu, J., Zimmerman, W. B., 2017. Improving the performance of coal flotation using oscillatory air supply. Fuel Processing Technology 165, 131-137.

Wang, Q., Shen, W., Ma, Z., 2000. Estimation of mercury emission from coal combustion in China. Environmental Science & Technology 34, 2711-2713.

Wang, S., Tao, X., 2019. Investigation of the attachment interaction between low-rank coal particles and bubbles. Energy Sources, Part A: Recovery, Utilization, and Environmental Effects, 1-15.

Wang, T., Wang, J., Yang, W., Jin, Y., 2001. Bubble behavior in gas–liquid–solid three-phase circulating fluidized beds. Chemical Engineering Journal 84, 397-404.

Wang, W., Zhou, Z., Nandakumar, K., Masliyah, J. H., Xu, Z., 2005. An induction time model for the attachment of an air bubble to a hydrophobic sphere in aqueous solutions. International journal of mineral processing 75, 69-82.

Weijenberg, D. C., Mulder, J. J., Drinkenburg, A. A. H., 2000. Froth Processes and the Design of Column Flotation Cells.

Wellek, R. M., Agrawal, A. K., Skelland, A. H. P., 1966. Shape of liquid drops moving in liquid media. AIChE Journal 12, 854-862.

Wilkinson, P. M., Spek, A. P., van Dierendonck, L. L., 1992. Design parameters estimation for scale-up of high-pressure bubble columns. AIChE Journal 38, 544-554.

Wilson, K. C., 1989. Two mechanisms for drag reduction. Drag reduction in fluid flows, techniques for friction control, 1-8.

Wilson, K. C., Addie, G. R., Sellgren, A., Clift, R., 2006. Slurry transport using centrifugal pumps, 3rd ed. Springer Science & Business Media.

Winkel, E. S., Ceccio, S. L., Dowling, D. R., Perlin, M., 2004. Bubble-size distributions produced by wall injection of air into flowing freshwater, saltwater and surfactant solutions. Experiments in Fluids 37, 802-810.

Wongsuchoto, P., Charinpanitkul, T., Pavasant, P., 2003. Bubble size distribution and gas–liquid mass transfer in airlift contactors. Chemical Engineering Journal 92, 81-90.

Wongwises, S., Kongkiatwanitch, W., 2001. Interfacial friction factor in vertical upward gas-liquid annular two-phase follow. International Communications in Heat and Mass Transfer 28, 323-336.

Wu, C., Suddard, K., Al-dahhan, M. H., 2008. Bubble dynamics investigation in a slurry bubble column. AIChE Journal 54, 1203-1212.

Wu, Y., Cheng, Z.-M., Huang, Z.-B., 2009. Backmixing reduction of a bubble column by interruption of the global liquid circulation. Industrial & Engineering Chemistry Research 48, 6558-6563.

Xia, W., Xie, G., Peng, Y., 2015. Recent advances in beneficiation for low rank coals. Powder Technology 277, 206-221.

Xia, W., Yang, J., Wang, Y., 2011. Reliability of gas holdup measurements using the differential pressure method in a cyclone-static micro-bubble flotation column. Mining Science and Technology (China) 21, 797-801.

Xu, M., 1998. Modified flotation rate constant and selectivity index. Minerals Engineering 11, 271-278.

Xu, M., Finch, J. A., Laplante, A. R., 1991. Numerical solution to axial dispersion model in flotation column studies. Canadian Metallurgical Quarterly 30, 71-77.

Xu, X., Zhang, J., Liu, F., Wang, X., Wei, W., Liu, Z., 2017. Rising behavior of single bubble in infinite stagnant non-Newtonian liquids. International Journal of Multiphase Flow 95, 84-90.

Xue, J., Al-Dahhan, M., Dudukovic, M. P., Mudde, R. F., 2008. Bubble velocity, size, and interfacial area measurements in a bubble column by four-point optical probe. AIChE Journal 54, 350-363.

Yang, G. Q., Du, B., Fan, L. S., 2007. Bubble formation and dynamics in gas–liquid–solid fluidization—A review. Chemical Engineering Science 62, 2-27.

Yang, G. Q., Fan, L. S., 2003. Axial liquid mixing in high-pressure bubble columns. AIChE Journal 49, 1995-2008.

Yang, Y. B., Devanathan, N., Duduković, M. P., 1992. Liquid backmixing in bubble columns. Chemical Engineering Science 47, 2859-2864.

Yao, C., Li, H., Xue, Y., Liu, X., Hao, C., 2018. Investigation on the frictional pressure drop of gas liquid two-phase flows in vertical downward tubes. International Communications in Heat and Mass Transfer 91, 138-149.

Yerushalmi, J., Cankurt, N. T., 1979. Further studies of the regimes of fluidization. Powder Technology 24, 197-201.

Yianatos, J. B., Bergh, L. G., Díaz, F., Rodríguez, J., 2005. Mixing characteristics of industrial flotation equipment. Chemical Engineering Science 60, 2273-2282.

Yianatos, J. B., Finch, J. A., Dobby, G. S., Xu, M., 1988. Bubble size estimation in a bubble swarm. Journal of Colloid and Interface Science 126, 37-44.

Yoon, R.-H., Yordan, J. L., 1991. Induction time measurements for the quartz—amine flotation system. Journal of Colloid and Interface Science 141, 374-383.

Yoshida, Y., Katsumoto, T., Taniguchi, S., Shimosaka, A., Shirakawa, Y., Hidaka, J., 2013. Prediction of viscosity of slurry suspended fine particles using coupled DEM-DNS simulation. Chemical Engineering Transactions 32, 2089-2094.

Yu, X., Luo, Z., Gan, D., 2019. Desulfurization of high sulfur fine coal using a novel combined beneficiation process. Fuel 254, 115603.

Zhang, C., Li, S., Wang, Z., Shen, Y., Wei, F., 2019. Model and experimental study of relationship between solid fraction and back-mixing in a fluidized bed. Powder Technology.

Zhang, K., Qi, N., Jin, J., Lu, C., Zhang, H., 2010. Gas holdup and bubble dynamics in a three-phase internal loop reactor with external slurry circulation. Fuel 89, 1361-1369.

Zhang, L.-j., Li, T., Ying, W.-y., Fang, D.-y., 2008. Rising and descending bubble size distributions in gas–liquid and gas–liquid–solid slurry bubble column reactor. Chemical Engineering Research and Design 86, 1143-1154.

Zhang, Z., Zhuang, L., Wang, L., Gao, H., Zhao, L., 2018. The relationship among contact angle, induction time and flotation recovery of coal. International Journal Of Coal Preparation And Utilization, 1-9.

Zhao, Y., Wang, S., Duan, L., Lei, Y., Cao, P., Hao, J., 2008. Primary air pollutant emissions of coal-fired power plants in China: Current status and future prediction. Atmospheric Environment 42, 8442-8452.

Zhen, T., Cheng, Y., Li, X., Wang, L., 2019. Bubble shape and rising velocity in viscous liquids at high temperature and pressure. Experimental Thermal and Fluid Science 102, 528-538.

Zhou, Y., Albijanic, B., Tadesse, B., Wang, Y., Yang, J., Zhu, X., 2020. Surface properties of aged coal and their effects on bubble–particle attachment during flotation. Advanced Powder Technology.

Zhou, Z. A., Plitt, L. R., Egiebor, N. O., 1993. The effects of solids and reagents on the characteristics of coal flotation in columns. Minerals Engineering 6, 291-306.

Zhu, C., Xing, Y., Wang, Y., Li, G., Gui, X., 2020a. Flotation intensification of low-rank coal using a new compound collector. Powder Technology.

Zhu, H., Valdivieso, A. L., Zhu, J., Min, F., Song, S., Corona Arroyo, M. A., 2019. Air dispersion and bubble characteristics in a downflow flotation column. Mineral Processing and Extractive Metallurgy Review 40, 224-229.

Zhu, X., Wei, H., Hou, M., Wang, Q., You, X., Li, L., 2020b. Thermodynamic behavior and flotation kinetics of an ionic liquid microemulsion collector for coal flotation. Fuel 262, 116627.